UNIVERSITY OF OKLAHOMA

GRADUATE COLLEGE

SURFACTANT AGGREGATE MORPHOLOGY ON SURFACES: INSIGHTS FROM MOLECULAR SIMULATIONS

A DISSERTATION

SUBMITTED TO THE GRADUATE FACULTY

in partial fulfillment of the requirements for the

Degree of

DOCTOR OF PHILOSOPHY

By

NAGA RAJESH TUMMALA
Norman, Oklahoma
2010

SURFACTANT AGGREGATE MORPHOLOGY ON SURFACES: INSIGHTS FROM MOLECULAR SIMULATIONS

A DISSERTATION APPROVED FOR THE
SCHOOL OF CHEMICAL, BIOLOGICAL AND MATERIALS ENGINEERING

BY

Dr. Alberto Striolo, Chair

Dr. Jana Shen

Dr. Daniel E. Resasco

Dr. Edgar A. O'Rear III

Dr. Brian P. Grady

Dedication

To my parents and brother

for their endless love and

their encouragement to pursue my interests

and for the valuable words of wisdom

and

To all those who without being overwhelmed

by the results of work, keep working…..

and finally to all teachers

Acknowledgements

It had been wonderful experience working with students, staff, and faculty as a doctoral student at the University of Oklahoma, Norman. I would like to express my sincere gratitude to my academic advisor, Dr. Alberto Striolo, University of Oklahoma, Norman. His methodological and creative way of thinking and the extensive knowledge in the field of my dissertation have been of great value to help improve the quality of my research. Without his constant feedback and encouragement this dissertation would have been really difficult to finish.

Also, I would like to take this opportunity to thank my committee members Dr. Jana Shen, Dr. Brian Grady, Dr. Edgar O'Rear III, and Dr. Daniel Resasco for their support and inputs during the development of this dissertation. I would like to take this opportunity to extend my sincere thanks to Dr. Brian Grady for the helpful discussions and guidance during the initial phases of my doctoral studies, and also Dr. Daniel Resasco for the helpful suggestions regarding the simulations of surfactants on carbon nanotubes. I would also like to extend my gratitude to Dr. Henry Neeman from University of Oklahoma Super Computing Center for Education and Research (OSCER) for his constant help with respect to super-computing and teaching us the introduction to the super-computing.

I would like to thank Brian Morrow, Dimitrios Argyris and Liu Shi for the fruitful discussions and successful collaborations we had over the years. I would like to thank my friends and others who had directly and indirectly supported me during my dissertation and who had made my doctoral studies, a memorable period. My deepest gratitude goes to my family for their unflagging love and support throughout my life;

this dissertation would have been impossible without them. Lastly, I am thankful to Harika and Appu for their support in difficult times.

I also acknowledge financial support from the United States Department of Energy through Carbon Nanotube Technology Center (CANTEC) at University of Oklahoma, and from the Oklahoma State Regents for Higher Education. Generous allocations of computing time were provided by the OSCER and by the National Energy Research Scientific Computing Center (NERSC) at Lawrence Berkeley National Laboratory.

Table of Contents

List of Tables

List of Figures

Abstract

Surfactant Aggregate Morphology on Surfaces: Insights from Molecular Simulations

(July 2010)

Naga Rajesh Tummala

Doctor of Philosophy- University of Oklahoma, Norman, Oklahoma

Chair of the Advisory Committee: Dr. Alberto Striolo

Surfactants are an important class of molecules used in number of applications at a range of length scales. Oil recovery, mineral recovery, detergency are applications that have been using surfactants for decades, whereas colloidal dispersions of nano-particles, preparation of nano-porous materials, dispersing carbon nanotubes are new applications of surfactants that are currently gaining prominence. The aggregate structure of surfactants plays an important role in determining the structure of nano-porous materials, ability of surfactants to disperse colloidal particles, carbon nanotubes and graphene nanosheets. To better understand such mechanisms at the nanoscale, we employed molecular dynamics simulations to study aggregation structure of surfactants (anionic sodium dodecyl sulfate (SDS)) at vacuum-water, water-graphite, water-silica, water-graphene and water-carbon nanotube interfaces. We also performed simulations of non-ionic mono dodecyl hexaethylene glycol ($C_{12}E_6$) at vacuum-water and water-silica interfaces for the purpose of comparing the results to those obtained for SDS at those interfaces. The results from the SDS aggregate morphologies at water-graphite (hydrophobic) and water-silica (hydrophilic) interfaces indicate that the aggregate morphology of SDS surfactants changes drastically with the change in the nature of the

substrate. The comparison of results from water-graphite and water-graphene nanosheets and water-graphene nanoribbons indicate that lateral confinement effects are predominant at length scales comparable to the size of the SDS molecules, and diminish gradually as the substrate size increases. The effect of the substrate curvature on the SDS surface aggregate structure has been studied by simulating SDS at water-single walled carbon nanotube (SWNT) interfaces on SWNTs of different diameters and inside SWNTs. The results indicate that curvature, and also the surface coverage of the SDS surfactants influence the aggregate morphology. We also studied the aggregate structure of the flavin mononucleotide (FMN) molecules at water-SWNT interfaces. Finally, we predicted the effective interaction between two SWNTs in presence of SDS surfactants and FMN molecules at two different surface coverages. The knowledge of the effect of the different surfactant molecules on the effective interaction between nanotubes in aqueous dispersions will aid in the design of better surfactants to enhance the SWNTs dispersion and separation.

1. Introduction

"SURFace ACTive AgeNTs" are called surfactants. These are also called amphiphilic molecules as these molecules contain molecular moieties that like and dislike solvent particles. Solvo-philic or lyophilic groups are those that like solvent and solvo-phobic or lyophobic are the groups that have no preferential affinity towards the solvent. At the molecular level no preferential affinity between two compounds corresponds to the fact that the interactions are only due to Van der Waals forces. Surfactants, due to the presence of the two different groups on the same molecule, have tendency to accumulate at surfaces or self-aggregate in the solution.

Amphiphilic molecules are used in a variety of applications that deploy their ability to self-assemble, such applications include the fabrication of porous materials,[1] structured materials,[2] and also tuning the effective interactions between latex spheres in aqueous solution.[3] Surfactants are used in detergency, oil-recovery, mineral recovery, and in many other technological applications, for their ability to aid in the formation of emulsions.[4]

It has been long known that surfactant self-assembly or aggregation is favored due to hydrophobic attraction between the tailgroups. The surfactants aggregates in solutions are usually refereed to as "micelles". Surfactants in solution aggregate above a critical concentration called critical micelle concentration (cmc). The size of the headgroup, that of the counterion, and the length of the tailgroup play an important role in determining the shape of the surfactant micellar aggregate both in aqueous solutions and at interfaces. The shape of micelles can be spherical, cylindrical, lamellar, or

reverse micelle depending on the area of the headgroup, the length of the tail and the nature of the solvent.[5] At liquid-liquid interfaces, nature of the solvent plays an important role in determining the orientation of the surfactant molecules.

Thermodynamic models to study the aggregation of surfactants in solution have been proposed by many researchers.[6-12] These empirical models are based on the experimentally observed critical micelle concentrations[4] and involve calculating free energy of micellization from all the contributions involved in the process of micellization.[6] At low concentrations, it has been suggested that surfactants move towards the interface. The interfacial concentration increases with the increase in bulk concentration. At concentrations closer to cmc, micelles in bulk solvent are observed. The micelles are in equilibrium with the interfacial surfactant aggregates and with the single surfactant molecules within the solution.[4] Recently, thermodynamic models were formulated with the input (free energy o solvation of one molecule, chemical potential at infinite dilution, hydrated and non-hydrated sections of surfactants, etc) taken from molecular dynamic simulations.[13-16] These models were generated for ionic, non-ionic, and zwitterionic surfactants. In chapter 2, we study the behavior of sodium dodecyl sulfate (SDS), an anionic surfactant, and $C_{12}E_6$ (mono dodecyl hexaethylene glycol), a non-ionic surfactant, at the vacuum-water interface. We found, as expected, that the differences in the headgroups can strongly affect the aggregation and interfacial properties of surfactants.

Studies of surfactant adsorption on solid surfaces date back to the 1960's and the classic papers of Fuerstenau.[17-21] Because of the commercial importance of applications such as mineral flotation and detergency, many pioneering studies focused on surfactant

adsorption on small particulate solids.[22-31] The development of the atomic force microscope (AFM) promoted a significant breakthrough in the area of surfactant adsorption. The results from AFM experiments during the 1990's have revealed the hemicylindrical aggregate structure of ionic surfactants on hydrophobic substrates.[32-35] It is now clear that the morphology of surfactants self-assembled structures varies as the critical packing shape and available surface area for the amphiphilic molecule change.[36]

A number of amphiphilic molecules are known which self-assemble yielding bilayers, hemi-cylinders and hemi-spheres.[35,37-38] A number of theoretical calculations and simulations to study the adsorption of surfactants on surfaces and are reported in chapter 3. For example, it has been known that SDS yields hemicylinders on graphite.[35] However, the exact molecular orientation of headgroups, tailgroups, and counterions within the surface aggregate is not well understood, although it can be important for nano-patterning applications.[39] We studied the aggregate morphology of SDS on graphite, and also the effect of counterions on the morphology of SDS surface aggregate. We also performed a parametric study to evaluate the effect of headgroup hydrophilicity on the surface aggregate structure. The results are discussed in chapter 3.

Graphite is an example of hydrophobic surface, whereas many applications in mineral recovery, biology, and geology deal with hydrophilic surfaces. To understand the surfactant surface aggregates on hydrophilic surfaces, we performed MD simulations for SDS on silica (the (1 1 1) surface of β-cristobalite). It has been experimentally verified that SDS does not adsorb significantly on silica surfaces[40-41] but the molecular level understanding has been missing. For comparison purposes we also simulated the aggregate structure of $C_{12}E_6$ surfactants on silica. The effect of change in

the degree of hydroxylation of silica surface on the surface aggregates of both SDS and $C_{12}E_6$ and presented in chapter 4. In this chapter we also present the properties of water molecules next to the silica surfaces, rendered amphiphilic by the surfactants. We report the change in orientation and density distribution of water due to the presence of surfactants. This study emphasizes that one has to consider the discrete surface charge distribution on the solid substrate to be able to predict the orientation of the surfactants and the kind of morphologies they yield.

Understanding the aggregate structure of surfactants on infinitely wide graphite sheets and silica surfaces helped us understand the role of substrate on the aggregate morphology. At the nanoscale the assumption of infinitely long surfaces, or in that matter surfaces that are few orders of magnitude greater than the surfactants, are hard to find. To study the effect of such lateral size confinements on the aggregate morphology, we performed MD simulations with finite-sized graphene sheets as substrates for aqueous SDS. The gain in prominence of the non-covalent functionalization to disperse graphene nanoribbons (GNRs) and graphene nanosheets (GNs)[42-44] was also an important motivation for us to study the aggregate structure of SDS on graphene sheets and ribbons. The results are reported in chapter 5.

There has been renewed interest within the research community to model the surfactants at coarse grained level and be able to predict the micellization properties of surfactants through coarse-grained models. [45-58] Most of the coarse-grained models require data from all-atom simulations. [59] Some methods are iterative schemes that employ inverse Boltzmann techniques. Algorithms differ in various methods employed to reproduce the aggregate structures. Such algorithms include equating chemical

potential,[45-46] force matching technique, [48-49,51] and others predicting thermodynamic properties of interest. After studying the surface aggregate structure of SDS on a variety of substrates including graphite, graphene, and silica we could have opted to model the same systems at coarse grain level and able to study the aggregation phenomenon at large length and time scales. Instead, we ventured on to finding the interactions between nanotubes in presence of surfactant surface aggregates. Dispersion and separation of single walled carbon nanotubes (SWNTs/SWNTs) by the use of density gradient centrifugation is a promising method to separate nanotubes based on chirality and diameter,[60-68] although the molecular level knowledge regarding the aggregate structure of surfactants and how precisely the surfactants play a role in differentiating the nanotubes of different diameter and chirality is presently lacking.

One is easily tempted to extrapolate the behavior of SDS molecules at vacuum-water interface and water-graphite interface to that observed at water-SWNT interface. However as we show in chapter 6 and chapter 7, the curvature of SWNT surfaces introduces non-intuitive changes in the aggregate morphology of SDS molecules on carbonaceous substrates.[69-70] Change in the aggregate morphology of SDS with the change in SDS surface coverage on graphite are discussed in References [71-72], and hence such effects are not explicitly discussed herein. Instead, the results from the study of SDS on graphite are compared to the aggregate structures on single walled carbon nanotubes of small diameter and also with the aggregate structures within large diameter SWNTs. The results are discussed in chapter 7. The effect of SDS surface coverage on carbonaceous substrates of different curvature is also discussed in chapter 7. With the knowledge of aggregate morphology, we investigated the effective potential

between SWNTs in presence of strongly self-aggregating SDS molecules and weakly aggregating heterocyclic biological molecule flavin mononucleotide (FMN). The results are presented in chapter 8.

Although the application of nano-particles in biological environments has been on the rise due to the wide variety of nano-particles that can be synthesized to suit specific application,[73-74] the cytotoxicity of such nano-particles is not yet fully understood.[74-75] The effective potential computed between approaching SWNTs in presence of SDS, FMN can be used to shed light on the aggregation properties of SWNTs in different biological membranes. Further study is necessary to completely understand the mechanism of such aggregation of SWNTs and nano-particles within a cellular membrane. We are currently working on calculating the effective potential between SWNTs in phospholipid bilayer. The details and results are not included in this dissertation.

2. C12E6 and SDS Surfactants Simulated at the Vacuum-Water Interface

The material presented below has been published in volume 26, issue 8 of the journal Langmuir in the year 2010.

2.1. Abstract

The effect of surface coverage on the aggregate structure for the nonionic hexaethylene glycol monododecyl ether ($C_{12}E_6$) and anionic sodium dodecyl sulfate (SDS) surfactants at vacuum-water interface has been studied using molecular dynamics simulations. We report the aggregate morphologies and various structural details of both surfactants as a function of surface coverage. Our results indicate that $C_{12}E_6$ tail groups orient less perpendicularly to the vacuum-water interface compared to SDS ones. Interfacial $C_{12}E_6$s show a transition from gas-like to liquid-like phases as the surface density increases. However, even at the largest coverage considered, interfacial $C_{12}E_6$ aggregates show more disordered structures compared to SDS ones. Both surfactants exhibit a non-monotonic change in the planar mobility as the available surface area per molecule varies. The results are interpreted on the basis of the molecular features of both surfactants, with particular emphasis on the properties of the surfactant heads, which is nonionic, long, and flexible for $C_{12}E_6$, as opposed to ionic, compact, and rigid for SDS.

2.2. Introduction

The surfactant behavior at interfaces plays an important role in many applications, including detergency, mineral flotation, corrosion inhibition, solid dispersion, oil recovery, nanoparticle dispersion, etc.[76] All these applications continue to motivate efforts towards describing surfactant aggregates and surfactant monolayers at various interfaces.[69-70,77-83] Surfactant adsorption properties depend on the balance between hydrophilic and hydrophobic forces, which in turn are governed by the ratio between the properties of tail and head groups. Thus it is important to understand the influence of the head groups' features on the aggregation properties of surfactants not only for molecular-based understanding of the observed phenomena, but also to design surfactants for specific applications, such as the stabilization of carbon nanotube dispersions.[69-70,84-87] Molecular simulations are ideal for these purposes because each molecular parameter can be changed at will.

In this work we compare the behavior of hexaethylene glycol monododecyl ether ($C_{12}E_6$) and sodium dodecyl sulfate (SDS) at vacuum-water interfaces. $C_{12}E_6$ belongs to the family of alkylpolyethylene glycol ethers, known as C_mE_n.[88] These surfactants have chemical formula $C_mH_{2m+1}(OC_2H_4)_nOH$, with a nonpolar hydrocarbon tail group C_mH_{2m+1} ("C_m") and a polar nonionic and long hydrophilic head group $(OC_2H_4)_nOH$ ("E_n"). C_mE_n is atoxic and widely used for detergency, cosmetics and pharmaceutical formulations. The other surfactant employed in this work is the anionic SDS. The tail groups of SDS and $C_{12}E_6$ are identical. As opposed to the long nonionic head group of $C_{12}E_6$, in SDS the head group consists of one anionic sulfate group. The counter-ion is sodium.

A number of experiments have been conducted to study C_mE_n surfactants at solid-liquid interfaces.[38,89-92] Grant et al.[89] reported that on graphite $C_{14}E_6$ forms rod-like structures while $C_{10}E_6$ forms flat layers; on an organic hydrophilic surface both surfactants form flat layers. Our group[83,90] has studied adsorption isotherms of $C_{12}E_6$ on hydrophilic gold surfaces using the quartz crystal microbalance. The results suggest the formation of monolayer-like structures. Less is known about the structure of C_mE_n surfactants at air-liquid interfaces. Among the few experimental results available, Thomas and co-workers[93-97] successfully employed neutron reflection to assess the structure of adsorbed $C_{12}E_n$ aggregates at the air-water interface in a wide concentration range, from dilute conditions to the critical micelle concentration (cmc). The experiments were performed on surfactants with different number of ethylene oxide groups, from n=1 to n=12 ("E_n"). It was observed that the extent of overlap between the alkyl chain and ethylene group increases as n increases, the surfactant layers are molecularly rough, and that both alkyl and glycol groups are tilted at the interfaces. Thomas and co-workers also studied the interfacial properties of SDS at interfaces using neutron reflection.[98-102] At the air-water interface it has been reported that the SDS tail groups are oriented less perpendicularly to the interface than dodecanol tail groups, and also that the thickness of interfacial dodecanol layer is larger than that of SDS.[99]

Of particular importance in surfactant studies is the concept of surface tension, γ. The γ-A, or π-A, isotherm diagram, in which the surface pressure π is a function of the surface area per head group, A, represents the phase diagram for the self-assembled surfactant aggregates. Several phases are typically observed, including dilute gas-like (G), liquid-like (L), liquid-condensed (LC) and solid-like (S) phases. The various

phases are characterized by different morphologies of the two-dimensional fluid, which strongly affects the surface tension.[5]

Lu et al.[94-95] conducted a number of experiments, correlating the surface tension at the air-water interface to the C_mE_n concentration, from infinite dilution to the cmc. SDS, as any other surfactant, reduces the surface tension at air-water interfaces as its concentration increases.[103,104] Strangely, however, it has been noticed that SDS solutions even with small amounts of impurities reach the minimum surface tension at concentrations larger than the cmc.[101,105-107] However, we do not expect such behavior in simulations. Several molecular dynamics (MD) simulation studies have assessed the properties of surfactants at various interfaces.[108-114] Cuny et al.[115-116] investigated the structural and dynamic properties of $C_{12}E_5$ aggregates at air-water interfaces. They reported that both polar glycol head groups and alkyl chains are mobile and exhibit tilted orientations, consistent with neutron reflection experiments.[94] Chanda and Bandyopadhyay simulated complete monolayers of $C_{12}E_2$[117] and $C_{12}E_6$[118] at air-water interfaces for 3 and 5.5 ns, respectively. They found that the longer polar glycol surfactants head groups are more tilted towards the aqueous phase than the shorter ones, because of hydrogen-bonded structures formed between water molecules and oxygen atoms of the head groups. SDS at air-water and water-CCl_4 interfaces has been studied using molecular dynamics by Berkowitz and coworkers.[103,119] MD simulations are also capable of predicting surface tension.[120-123] Baoukina et al.[124] and Laing et al.[125] conducted large scale and long time MD simulations to study π-A isotherms of dipalmitoyl-phosphatidylcholine lipid monolayers, obtaining comparable results with

experiments. To the best of our knowledge, no MD simulation result has been reported for the surface tension of $C_{12}E_6$ at the air-water interface.

In this work we employ MD simulations to study $C_{12}E_6$ and SDS surfactants at vacuum-water interfaces for a large range of interface coverages (surface area per molecule). The results, in general agreement with experiments, are discussed in terms of morphological and dynamical properties, as well as of surface tension. Differences between the results obtained for $C_{12}E_6$ and those for SDS are interpreted based on the atomic-scale properties of the surfactants head groups. The remainder of the manuscript is organized as follows: in section 3 we discuss the simulation details. In section 4 we present our results, including density profiles, quantification of the aggregate thickness, surfactants orientation, morphological properties of the aggregates, and surfactants mobility at the interface. In section 5 we summarize our results.

2.3. Simulation Methodology

MD simulations were performed at the vacuum-water interface. Water molecules were modeled using the extended simple point charge (SPC/E) potential.[126] Bond lengths and angles were maintained fixed using the SETTLE algorithm.[127] The nonionic $C_{12}E_6$ surfactant contains one hydrophobic tail (T) of 12 alkyl groups, and one hydrophilic head (H) of 6 ethylene oxide (EO) moieties and 1 terminal OH group (see Figure 2-i). The alkyl groups were modeled as united atoms, whereas the oxygen atoms in the EO groups as well as oxygen and hydrogen atoms in the terminal OH groups were modeled explicitly. The tail alkyl groups were modeled by the TRaPPE-UA force field.[128] The oxyethylene groups were modeled implementing the OPLS force field.[129-130] Following Berkowitz,[119] we allowed bonds and angles to oscillate from their equilibrium values, thus modifying the original TRaPPE-UA and OPLS recipes.

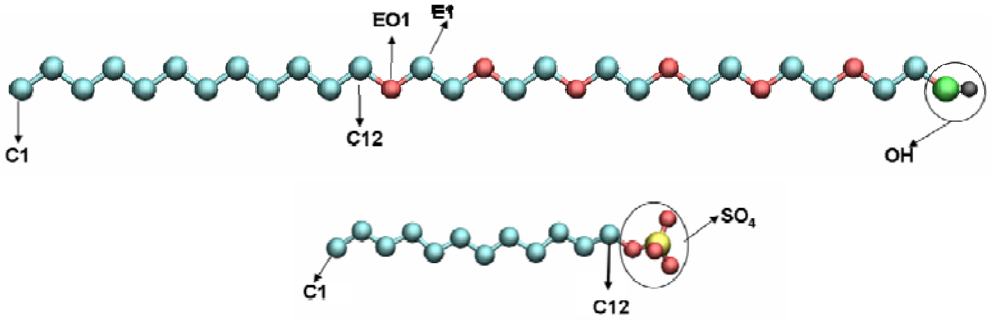

Figure 2-i: Schematic representations of $C_{12}E_6$ (top) and SDS (bottom) surfactants according to the ball-and-stick formalism. Top: C1 represents the 1st alkyl group in the tail, C12 is the 12th alkyl group in tail, EO1 is the oxygen in the 1st ethylene glycol group, E1 is the ethylene in the first ethylene glycol group, and OH is the terminal OH group. Bottom: SDS has the same number of alkyl groups in its tails $C_{12}E_6$ does, but its head group is composed by one sulfur and four oxygen atoms. Color code: the alkyl groups in SDS and $C_{12}E_6$ and ethylene groups in $C_{12}E_6$ are represented as cyan spheres; the oxygen atoms in the ethylene oxide chain of $C_{12}E_6$ and in the sulfate group of SDS are represented as red spheres; the sulfur atom in SDS is a yellow sphere; the oxygen and hydrogen atoms of the terminal OH group in $C_{12}E_6$ are green and black spheres, respectively.

Harmonic potentials were used to model bond stretching:

$$E_{bond} = K_b (r - r_O)^2 \tag{2.1}$$

In Eq. (2.1), K_b is the elastic constant, r is the instantaneous distance between the bonded atoms, and r_O is the equilibrium distance between them.

The harmonic potential was used to model angle bending potentials:

$$E_{ang} = K_\theta (\theta - \theta_O)^2 \tag{2.2}$$

In Eq. (2.2), E_{ang} is the bending energy, K_θ is the force constant, θ_O and θ are the equilibrium and the instantaneous angles, respectively. The force constants in the harmonic bond stretching and angle bending potentials were borrowed from Ref. [[119]]. The bond lengths and angles involving the terminal OH group in $C_{12}E_6$ surfactants were held fixed by the LINCS algorithm.[131]

Following the Ryckaert-Bellemans (RB)[132] dihedral implementation, dihedral angles in the tail groups and the terminal OH group were constrained according to:

$$E_{dihedral} = \sum_{k=0}^{3} c_k \cos^k(\phi) \tag{2.3}$$

The dihedral angles involving oxyethylene group were constrained using harmonic potentials:

$$E_{dihedral} = K_\phi (1 + \cos(n\phi - \phi_s)) \tag{2.4}$$

In Eq. (2.4) n is an integer, ϕ_s is the equilibrium dihedral angle. All the force field parameters employed in our simulations are described in

Table 2-A. The force field implemented for SDS is described in Chapter 3 and also in an article published by our group.[77]

The GROMACS [133-135] MD simulation package was used to integrate the equations of motion using the leap-frog algorithm[136] with a time step of 2 fs. All simulations were conducted in the canonical ensemble in which the number of particles (N), the box volume (V) and the temperature (T) were kept constant. T was maintained constant using the Nose-Hoover thermostat with a relaxation time of 100 fs. All simulations were conducted at T=300 K. Dispersive forces were computed using the Lennard-Jones potential with an inner cutoff of 0.8 nm and outer cutoff of 1.0 nm. Long range electrostatic interactions were treated using the Particle Mesh Ewald (PME) method.[137] Periodic boundary conditions were employed in all three dimensions. 15,000 water molecules were inserted in a simulation box of size 10.08x9.60x30.00 (see Figure 2-ii). All simulations were carried out for 32 ns. Equilibration was considered completed when no change was observed in the calculated density profiles within a 2 ns interval. We found that 30 ns of simulation were necessary to equilibrate the system at the largest surfactant concentrations considered, although shorter runs were sufficient for systems at low surfactant concentration. For consistency, the production run consisted in the last 2ns of each simulation, although we used the last 10ns of simulations to calculate the mean square displacement for the simulated surfactants. During production, the positions of the surfactant atoms were stored every 2 ps and used for all subsequent calculations.

Table 2-A: Parameters used to implement the force fields in Eqs. (2.1), (2.2), (2.3), and (2.4).

Lennard-Jones and Electrostatic Interaction Potential Parameters

ATOMS (or GROUPS)	σ (Angstrom)	ε (Kcal mole^{-1})	*q (e)*
CH_3	3.905	0.175000	0.0000
CH_2	3.905	0.118000	0.0000
CH_2 (in -O-CH_2- CH_2-)	3.905	0.118000	0.2500
CH_2 (in -CH_2-O-H)	3.905	0.118000	0.2650
O (in -O-CH_2- CH_2-)	3.000	0.170000	-0.5000
O (in -OH)	3.150	0.200000	-0.7000
H (in -OH)	3.150	0.200000	0.4350
H (in H_2O)	0.000	0.000000	0.4238
O (in H_2O)	3.166	0.155402	-0.8476

Bond Stretching Potential Parameters

BOND	K_b (kcal mol^{-1} Å^{-2})	r_o (Angstroms)
CH_3-CH_2	620.000	1.540
CH_2-CH_2	620.000	1.540
CH_2-O	600.000	1.410
CH_2-O (in CH_2-O-H)	900.000	1.430
O-H	N/A	0.945

Angle Bending Potential Parameters

ANGLE	K_θ(kcal mol^{-1} rad^{-2})	Θ_O(deg)
CH_3-CH_2-CH_2	124.190	114.000
CH_2-CH_2-CH_2	124.190	114.000
CH_2-CH_2-O	124.190	112.000
CH_2-O-CH_2	124.190	112.000
CH_2-CH_2-O (O in OH)	124.190	108.000
CH_2-O-H	N/A	108.500

Bond Torsion Potential Parameters

DIHEDRAL	K (Kcal mol^{-1})	n	φ	
CH_2-CH_2-CH_2-O	4.184	3	0.0	
CH_2-CH_2-O-CH_2	3.138	3	0.0	
DIHEDRAL	**C_1(Kcal mol^{-1})**	**C_2**	**C_3**	**C_4**
CHn-CH2-CH2-CH2	8.3970	16.7854	1.1339	-26.3160
CH2-CH2-O-H	2.8220	2.9430	0.1160	-6.25090

We report in Figure 2-ii one representative simulation snapshot. We conducted a number of simulations with varying number of surfactants on the two interfaces. The surface coverages of surfactants are randomly chosen from infinite dilution to the concentration necessary to form a monolayer. The thickness of the water film is large enough to prevent undesired interactions between surfactant molecules adsorbed in the opposing vacuum-water interfaces from occurring. The surface areas per $C_{12}E_6$ molecules considered are: 9684, 1936, 691, 358, 293, 179, 136, 115, 92, 77, 64, and 52 Å^2 per surfactant. 52 Å^2 per surfactant corresponds to full coverage.[138] We performed simulations for SDS at 4 surface coverages (~700, 196, 96 and 52 Å^2 per surfactant). The full SDS coverage corresponds to ~40-45 Å^2 per surfactant, conditions simulated previously by Schweighofer et al.[119]

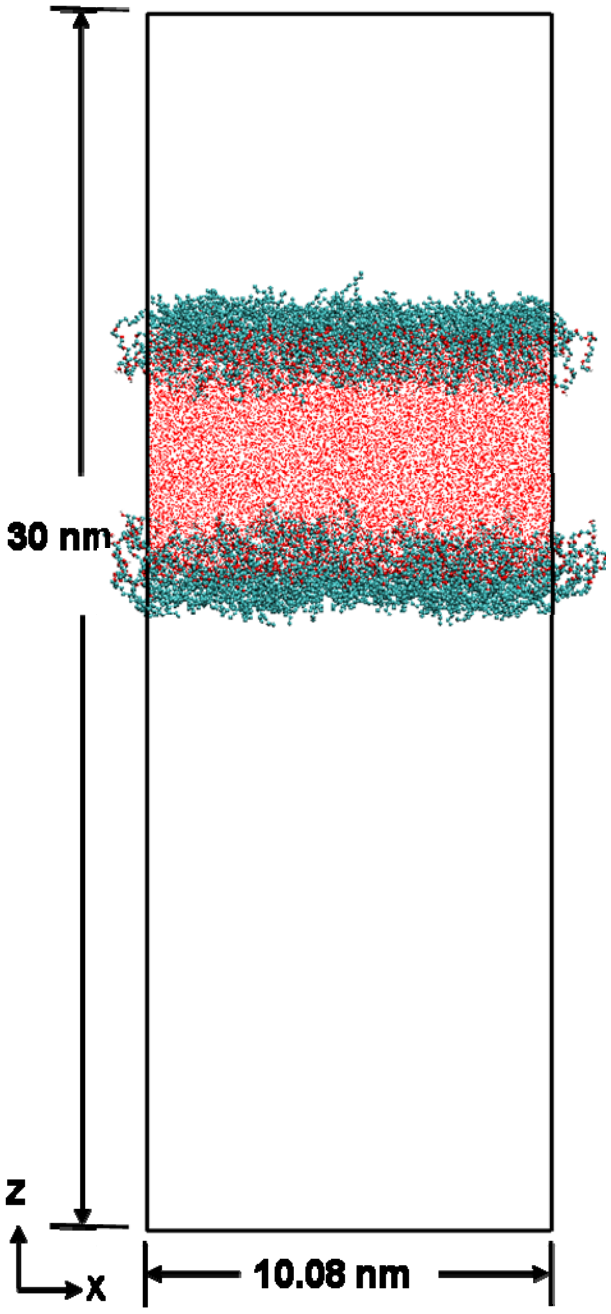

Figure 2-ii: Schematic representation of the simulation box. The color code is the same as in Figure 2-i. Additionally, the red dots between the two surfactant layers represent water in the wire-frame formalism.

2.4. Results and Discussions

2.4.1. Density Profiles

We provide the number density profiles of entire $C_{12}E_6$ chains (E), heads (H) and tails (T) as a function of the distance along the z direction in Figure 2-iii. The density profiles for the entire surfactants (E) correspond to the density profiles of the surfactants center of mass. The density profiles for heads (H) and tails (T) are instead the density distributions of head and tail segments, respectively. The z=0 position corresponds to the center of mass of the simulated systems.

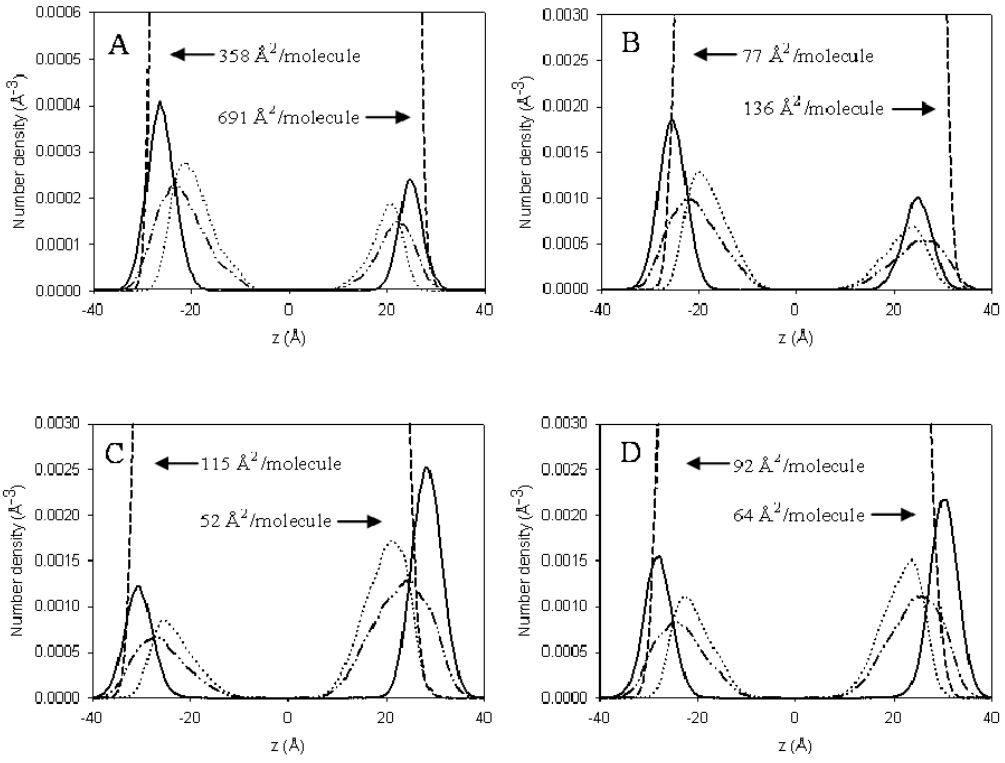

Figure 2-iii**:** Number density profiles perpendicular to the vacuum-water interface at equilibrium for representative systems at different surface coverage: water (dashed line); tails (solid line); heads (dot line); and entire $C_{12}E_6$ surfactants (dot-dot-dash line). The water number density reaches ~ 0.033 $Å^{-3}$ in the center of each system considered (not shown).

For brevity, only the number density profiles obtained from 4 systems (8 interfaces) are shown. It is clear that the surfactant molecules accumulate at both vacuum-water interfaces with the head groups at contact with the water phase and the tail groups away from it. The intensity of the peaks increases as the surface area per molecule decreases (the interface coverage increases). At high surface area per surfactant (691 $Å^2$/molecule) some alkyl groups of the surfactant tails remain at contact with the water phase (right part of panel A), which is due to the low surface coverage considered. At low surface area per head group (52 $Å^2$/molecule) the tail groups are found away from the water phase, towards the gas phase (right part of panel C). The atomic number density for water reaches about 0.033 $Å^{-3}$ in the center of the simulation box (not shown), consistent with the density of bulk liquid water at ambient conditions.

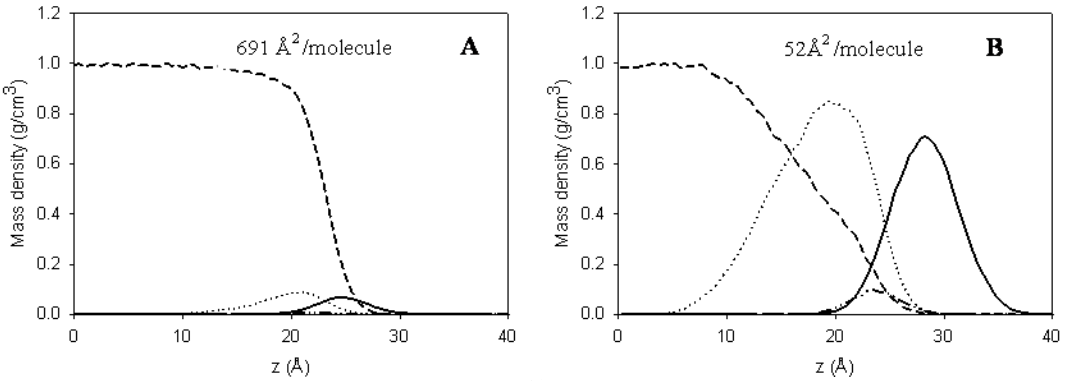

Figure 2-iv**:** Mass density profiles for $C_{12}E_6$ at 691 $Å^2$/molecule (panel A) and 52 $Å^2$/molecule (panel B). Results are for water (dashed line); tails (solid line); heads (dot line); and EO1 groups (dot-dot-dash line).

Because of the large size difference of water molecules compared to $C_{12}E_6$ surfactants, we calculated the mass density profiles of $C_{12}E_6$ at 691 $Å^2$/molecule and 52 $Å^2$/molecule to obtain a better visualization of the interfacial behavior. The results are shown in Figure 2-iv. At low surface coverage (691 $Å^2$/molecule, panel A), the

surfactant tail groups are close to the water phase. At high surface coverage (52 $Å^2$/molecule, panel B), not only the majority of tail groups are out of the water phase, but even part of the head groups are pulled away from water, towards the hydrophobic vacuum. We point out that at high surface coverage (panel B) the mass density profile for water decreases from the bulk value to zero smoothly, but the curve shows a small, yet noticeable change in inflection within the surfactant layers, probably because of surfactant head-water excluded-volume effects. In Figure 2-iv we also report the density profile observed for the EO1 group (see Figure 2-i for details). This group roughly identifies the molecular mid-point for the $C_{12}E_6$ surfactant. Our results show that when the surfactant surface concentration is 52 $Å^2$/molecule the EO1 group is located in between the interfacial layers formed by the head and the tail groups. At lower surface concentration, e.g., 691 $Å^2$/molecule, the EO1 group position fluctuates significantly along the z direction. This is because the surfactant molecules possess more degrees of freedom at low surface coverage. Some simulation snapshots collected at low surfactant concentration even show configurations in which some surfactants form hairpin-type turns. To visualize these results, representative simulation snapshots for $C_{12}E_6$ surfactants at the vacuum-water interface at 691 $Å^2$/molecule and 52 $Å^2$/molecule are shown in Figure 2-v(center and bottom panels, respectively). At high surface coverage the tail groups of $C_{12}E_6$ effectively pull away the long, partially hydrophobic $C_{12}E_6$ head groups from the water phase. Simultaneously, as can be seen from the bottom panel in Figure 2-v, packing of the long $C_{12}E_6$ head groups squeezes water away from the surfactant heads (i.e., because more surfactant head groups are present, less room is available for interfacial water). At 1936 $Å^2$ /molecule (top panel in Figure 2-v) we

highlight the formation of hairpin turns by the $C_{12}E_6$ surfactant. For clarity, only 2 of the total 5 $C_{12}E_6$ surfactants present at the interface are shown in the top panel.

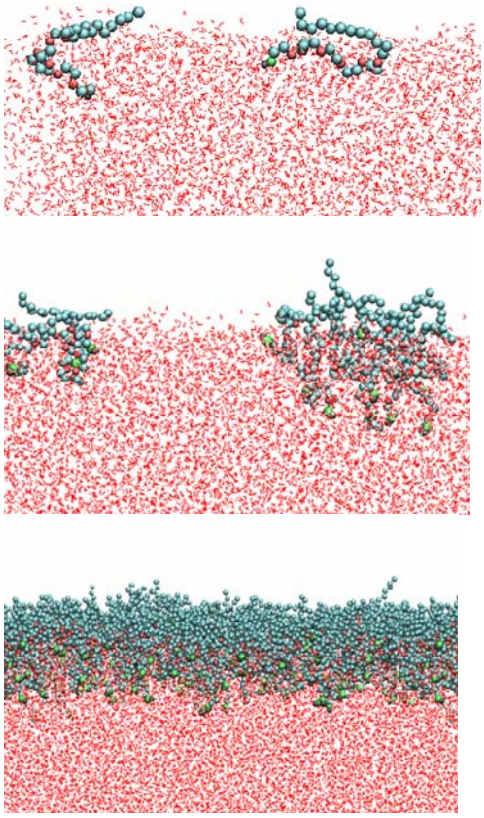

Figure 2-v**:** Representative simulation snapshots for $C_{12}E_6$ at vacuum-water interface. The top panel shows hairpin-type surfactants observed at 1936Å^2 /molecule, the center panel is for 691Å^2 /molecule, and the bottom panel for 52Å^2 /molecule.

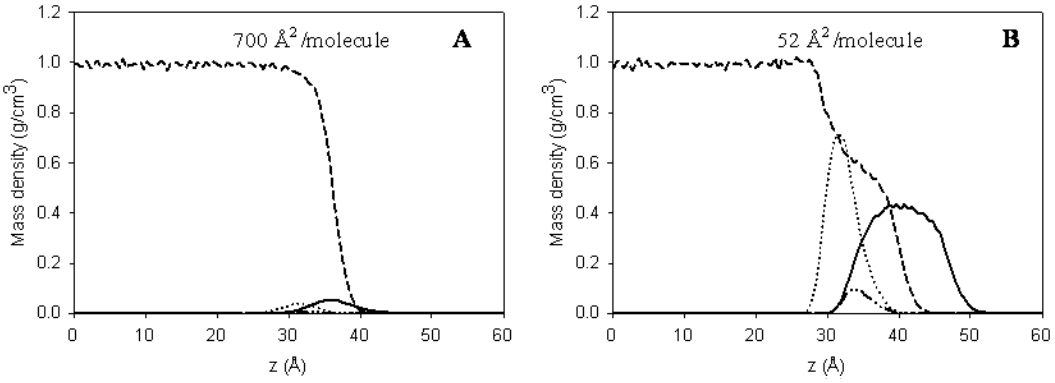

Figure 2-vi**:** Mass density profiles for SDS at 700 $Å^2$/molecule (panel A) and 52 $Å^2$/molecule (panel B). Data are shown for water (dashed line); tails (solid line); heads (dot line); and C12 groups (dot-dot-dash line).

For comparison, we calculated the mass density profiles for SDS surfactants at 700 $Å^2$/molecule and 52 $Å^2$/molecule. The results are shown in Figure 2-vi. At high surface area per molecule the results are qualitatively similar to those observed for $C_{12}E_6$. At low surface area per head group, contrary to that observed for $C_{12}E_6$, the SDS head groups are fully immersed in water and only the surfactant tail groups move away from the water phase. This observation denotes the different hydration properties between the head groups of $C_{12}E_6$ and SDS. The sulfate groups of SDS heads have strong hydration due to electrostatic interactions. The $C_{12}E_6$ head contains both hydrophilic (oxygenated groups) and hydrophobic (ethylene groups) parts. When the $C_{12}E_6$ molecules pack together to form a monolayer, the ethylene groups in the center of the surfactants may repel water molecules, and consequently water molecules are squeezed out of the interfacial region. The different features between $C_{12}E_6$ and SDS head groups result in a different water density profile, which decreases rather gradually from liquid-like to zero across the interface in the case of $C_{12}E_6$, and more abruptly in the case of SDS. In Figure 2-vi we also report the density profile for the C12 group (see

Figure 2-i for details). As in the case of the group EO1 for $C_{12}E_6$ (see Figure 2-iv), the position of the C12 group helps us identify where the SDS head and tail groups meet. Consistent with our previous data for $C_{12}E_6$, the density profiles for the C12 group peak in the region between the interfacial layers formed by SDS head and tail groups. More interestingly, the position of the C12 group corresponds to a significant change in inflexion in the water density profile, suggesting that this unexpected feature of the water density is due to excluded-volume effects near the SDS head groups. To compare SDS vs. $C_{12}E_6$ surfactants, in Figure 2-vii we provide representative simulation snapshots for SDS surfactants self-assembled at the vacuum-water interface. Because the head group of SDS is shorter and over-all less flexible than that of $C_{12}E_6$, no hairpin-type configuration is observed for the former even at low surfactant concentration.

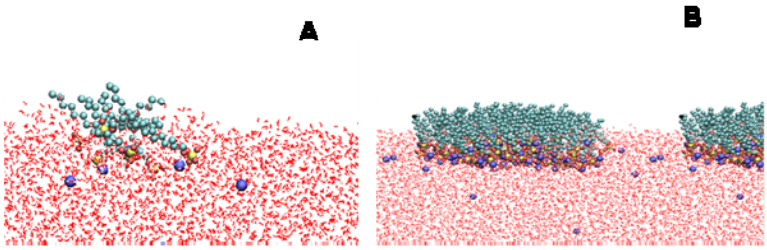

Figure 2-vii**:** Representative simulation snapshots for SDS at vacuum-water interface. Panel A is for 700 $Å^2$ /molecule; panel B is for 52$Å^2$ /molecule.

In all cases considered, for both $C_{12}E_6$ and SDS, our results show that the density profiles for tail groups overlap those of head groups, reflecting the lack of complete segregation between heads and tails. The reason for this behavior was found to be the fluctuation of surfactants along the direction perpendicular to the interface. These

fluctuations occur at all conditions considered because of thermal motion. This observation is consistent with recent quantifications on the density fluctuations for water at hydrophobic interfaces.[139-140] Such density fluctuations become even more pronounced at vapor-liquid interfaces. Structural fluctuations for micelles of C_8E_5 surfactants in water have been observed by Garde et al., who reported that such fluctuations are so pronounced that they lead the C_8E_5 tail group to frequently come in contact with the head groups, and sometimes even with water molecules.[141]

In Figure 2-viii we compare representative simulation snapshots obtained for $C_{12}E_6$ (panel A) and SDS (panel B) at the largest coverage simulated here (52 $Å^2$/molecule in both cases). Note that at this surface coverage $C_{12}E_6$ yields a complete monolayer while SDS forms a monolayer at 40-45 $Å^2$/molecule, a situation studied by Schweighofer et al.[119] For clarity, only parts of the surfactant head groups are shown. In the case of $C_{12}E_6$, we only show EO1 and E1 groups (see Figure 2-i for details), in the case of SDS the entire head groups are shown. The results highlight the staggering of surfactant head groups along the direction perpendicular to the interface. The staggering of head groups along the direction perpendicular to the interface occurs within a region of ~ 1 nm for $C_{12}E_6$, and of ~0.5 nm in the case of SDS. The reason for the wider staggering amplitude in the case of $C_{12}E_6$ is related to the chemical nature of its head groups. For example, the E1 group, which is located between the tail and the head (see Figure 2-i for details, and Figure 2-iv for the density distribution results), can interact with any hydrophobic ethylene groups in either the surfactant head or the surfactant tail. On the contrary, the SDS head group is composed by only one sulfate group, and it can only associate favorably with other sulfates. Also of importance is the flexibility and

length of the $C_{12}E_6$ head groups as opposed to the compactness and rigidity of SDS heads. Because of their flexibility, the $C_{12}E_6$ head groups can rearrange easily at the vacuum-water interface, while the SDS ones cannot. This different aggregate packing at the interface is probably responsible for the different propensity of the two surfactants to lower the surface tension.

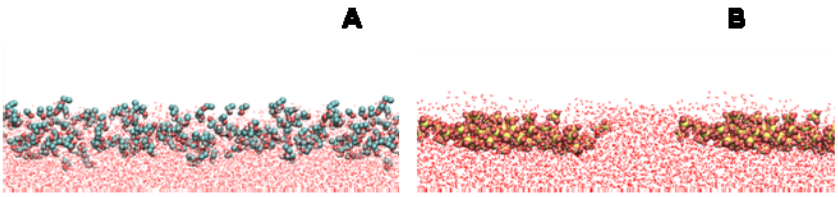

Figure 2-viii**:** Expanded side view of representative simulation snapshots that highlight the surfactant head groups at vacuum-water interface. Results are for EO1 and E1 of $C_{12}E_6$ surfactants in panel A; sulfate groups of SDS surfactants in panel B.

In order to quantify the characteristics of the interfacial structure, we fit the density profiles of entire $C_{12}E_6$ chains (E), head groups (H), and tail groups (T) to Gaussian functions:[142]

$$\rho(z) = n^0 \exp\left[\frac{-4\ln 2(z - z^0)^2}{\sigma^2}\right] \tag{2.5}$$

In Eq. (2.5) n^0, σ and z^0 are the distribution height, distribution width at half-height, and peak position, respectively. The presence of a small asymmetry in the density profiles introduces a bias in fitting the curves to a single Gaussian function, which we consider not relevant for our analysis. The values of σ_E, σ_H, and σ_T as a function of surface area per surfactant head group are reported in Figure 2-ix. As the distribution width increases, the surfactants yield a thicker layer at the vacuum-water

interface. The results show that all values for σ decrease as the surface area per surfactant increases. However, particularly in the case of σ_E, the thickness of the entire surfactant layer and therefore the most important of the results shown in Figure 2-ix, the change is not monotonic and the curve can be divided into 3 regions with decreasing surface area per head group. In region I, the value of σ increases almost linearly from an infinite dilute interface coverage to ~293 $Å^2$ / $C_{12}E_6$ molecule. In Region II, from ~293 $Å^2$ / molecule to ~77 $Å^2$ / molecule, the value of σ remains ~ constant. In region III, when the surface area per head group is lower than ~77$Å^2$/molecule, we observe a significant increase of σ as the surface area per molecule decreases (this is particularly evident when data for σ_E are considered). We relate this observation to the classic π-A isotherm.[5] Region I corresponds to the "gas-like" (G) phase, where the available area per molecule is large compared to the dimensions of the surfactant. Region III, in which the surface is almost completely covered by $C_{12}E_6$, corresponds to L, LC or S phases. Based on the distribution of $C_{12}E_6$ observed in our snapshots (Figure 2-v and Figure 2-viii), we argue that region III corresponds to a liquid-like phase for $C_{12}E_6$ surfactants. Between regions I and III, the plateau region observed in Figure 2-ix indicates a liquid-gas phase transition. Unfortunately, we did not collect sufficient data to provide the entire σ-A phase diagram for SDS.

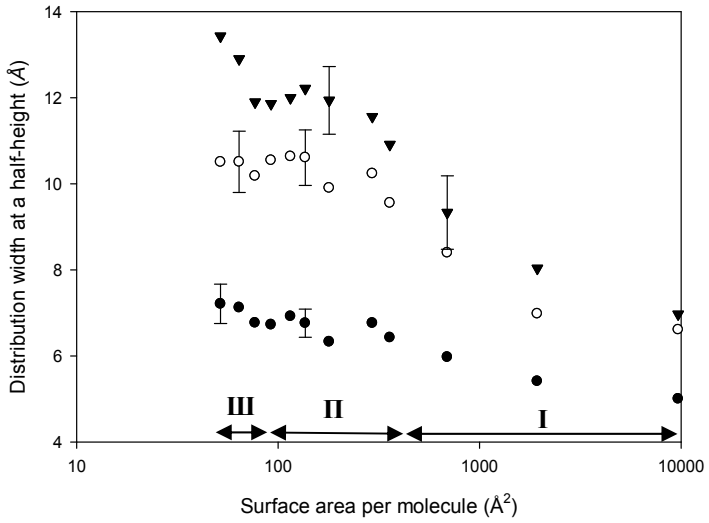

Figure 2-ix**:** Values of the distribution widths at half-height as a function of surface area per molecule. Results shown are for the entire surfactant layer, σ_E, the head groups, σ_H, and the tail groups, σ_T. Symbols ▼, ○, and ● are for σ_E, σ_H, and σ_T, respectively.

The thickness of the self-assembled surfactant structure at the largest surface coverage considered is comparable to those obtained from neutron reflection experiments. At 55 Å^2 per surfactant the experimental data for the width of the surface aggregate reported by Lu et al. is 13.5 ±1 Å, which is close to the value of 13.4±0.9 Å found in our simulation for the system with 52 Å^2 /molecule.[95-96] Good agreement between experiments and simulations is also found for the thickness of head and tail layers, as summarized in Table 2-B (note that the thicknesses reported in Table 2-B are twice the widths reported in Figure 2-ix). Analyzing the results we notice that the sum of the head and tail thicknesses is greater than the thickness of the layer formed by $C_{12}E_6$, which is also in agreement with the experimental data of Lu et al.[44,95-96] This is due to the extensive interpenetration of head and tail layers within the surface aggregates. The main difference between our results and experimental data comes from the thickness of the layer formed by the tail groups. The value reported in Table 2-B

was obtained by Lu et al. fitting the experimental data by a single uniform-layer model. When a Gaussian function was used to fit the experimental data, a thickness of ~16±1 Å was obtained for the layer of surfactant tails.[95] This discrepancy is due, in part, to the difficulty of interpreting uniquely the accurate experimental data. When we consider that the fully-extended length of the $C_{12}E_6$ tail group is ~16 Å and that the tails are slant at the interfaces (see below), we believe that our estimates of ~15.2±0.9 Å for the thickness of the layer of surfactant tails is quite reasonable.

Table 2-B Comparison of the thickness formed by $C_{12}E_6$ headgroups, $C_{12}E_6$ tailgroups, and full $C_{12}E_6$ surfactant obtained from our simulations as opposed to those from neutron reflection experiments.

	Experiment (Å) [95-96]	**MD Simulation (Å)**
Entire Surfactant	26.5±2	26.8±1.8
Tails	19±1	15.2±0.9
Heads	19.5±1	21±1.6

2.4.2. Surfactant End-to-End Distance

The calculated distribution width at half-height shown in Figure 2-ix only provides information of interfacial aggregate thickness along the z direction. To obtain more detailed information, we calculated the average end-to-end distance for the surfactants (details are shown schematically in Figure 2-x).

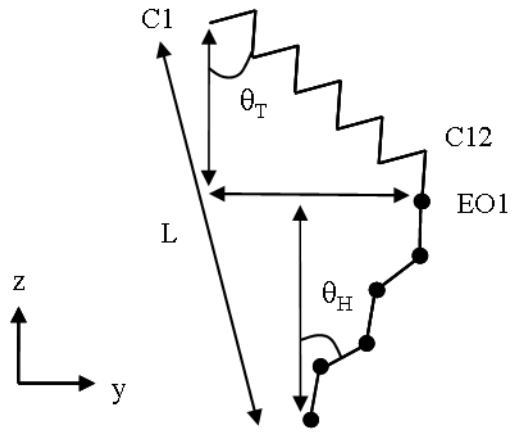

Figure 2-x**:** Schematic representation for a $C_{12}E_6$ surfactant at the water (bottom)-vacuum (top) interface. L is the end-to-end distance of $C_{12}E_6$ surfactant molecules; θ_T and θ_H are the tail and head tilt angles with respect to the direction z, perpendicular to the interface.

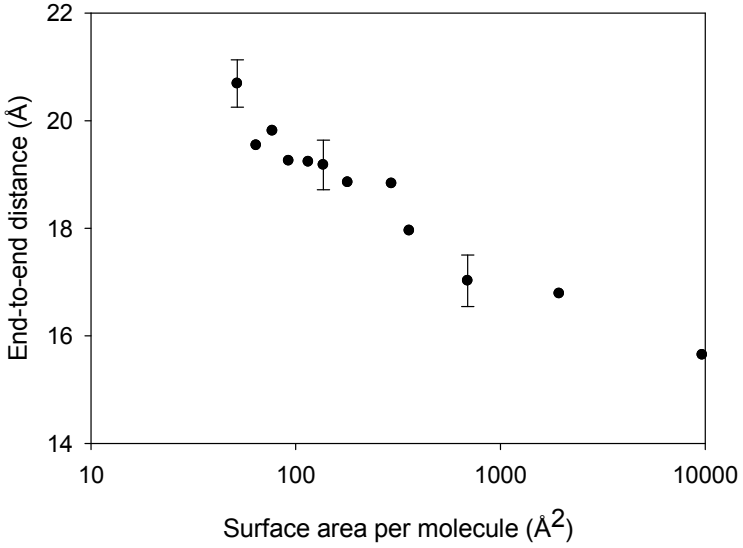

Figure 2-xi**:** Average end-to-end distances for $C_{12}E_6$ surfactants at the vacuum-water interface as a function of the surface area per molecule. Only representative error bars are shown for clarity.

We report the average end-to-end distance of $C_{12}E_6$ molecules as a function of the surface area per molecule in Figure 2-xi. The end-to-end distance increases from 15.8 Å at lowest surface coverage to 20.8Å at full monolayer coverage, i.e., the end-to-

end distance increases as the surface area available for $C_{12}E_6$ decreases. The results in Figure 2-xi follow a trend similar to that observed in Figure 2-ix, although the identification of liquid-like and gas-like phases is obscured by statistical uncertainty. We reiterate that, because the surfactants are staggered along the z direction, the end-to-end distance (which is an average property for the single surfactant molecules) is always shorter than the thickness of the surfactant aggregate (which is a collective property of the aggregate).

2.4.3. Surfactant Orientation at the Interface

Tilt angles for both head groups and alkyl tails (θ_H and θ_T) are defined in Figure 2-x. The values of θ_H and θ_T are between 0° and 90°. When θ is equal to 0°, the group is perpendicular to the vacuum-water interface. When θ equals to 90°, the group is parallel to the interface. The tilt angles for SDS tail groups are calculated by considering the C1 and the sulfur atom of the head group rather than the C1 and C12 groups as in the case of $C_{12}E_6$. θ_H cannot be calculated for SDS due to the geometry of its head group.

In Figure 2-xii we report the average tilt angles of head and tail groups as a function of surface area per $C_{12}E_6$ molecule. The tilt angles of both head and tail groups decrease as the surface area per $C_{12}E_6$ molecule decreases, indicating that at low surface coverage both heads and tails lie nearly parallel to the vacuum-water interface and that the head and tail groups become more perpendicular to the interface as the surface coverage increases. The tail groups tilt angles are always larger than those of head groups, indicating that the surfactant heads are more perpendicular to the interface than the tails are. This is due to the flexibility of the hydrophilic glycol groups in water, which assume several conformations to increase the system entropy without losing

favorable interactions with water. The results in Figure 2-xii show a change in slope as a function of surface coverage, which is consistent with the results of Figure 2-ix. This corroborates a change in aggregation structure for the interfacial surfactants as the coverage varies. At high coverage, the average value of the tilt angle of tail groups, 54º, is slightly larger than the experimental value, 45º.[96] Cuny et al.[115] studied the monolayer structure of the nonionic surfactant $C_{12}E_5$ by simulation and found that when A=64 $Å^2$/molecule, $\theta_T \approx 63º$ and $\theta_H \approx 51º$, which is in reasonable good agreement with our results at 64 $Å^2$/molecule (θ_T = ~58º and θ_H = ~51º), when we consider that our simulations are for $C_{12}E_6$ surfactants.

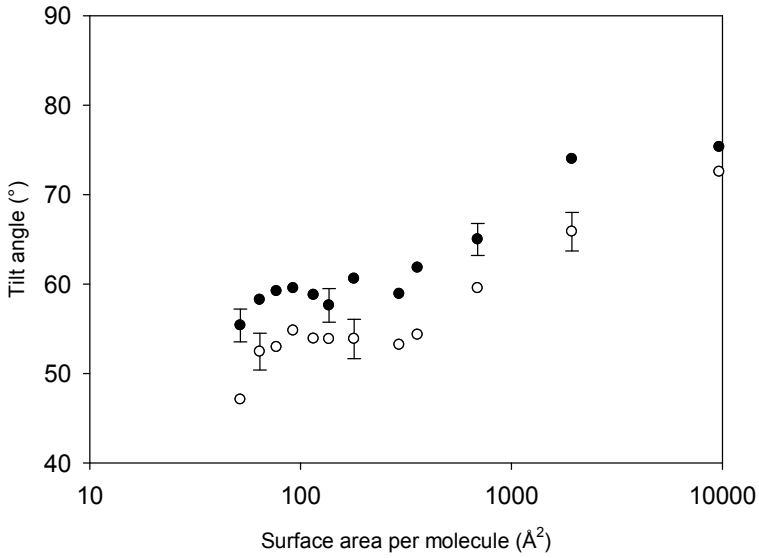

Figure 2-xii**:** Average tilt angles for $C_{12}E_6$ tail and head groups as a function of surface area per molecule. Filled and empty circles stand for θ_T and θ_H, respectively. Only representative error bars are shown for clarity.

In Figure 2-xiii we compare the simulation results for θ_T obtained for $C_{12}E_6$ to those obtained for SDS as a function of surface coverage. When the surface area available per molecule is large, the tail groups of both surfactants remain quite parallel to the interface. As the surface area per surfactant decreases, the tilt angle of SDS tail groups drops much more dramatically compared to $C_{12}E_6$ surfactants, indicating that the SDS tail groups become more quickly perpendicular to the interface than $C_{12}E_6$ ones do as the surface coverage increases. This different behavior is probably due to the different properties of the surfactant head groups, and how they interact with the aqueous film. The compact, rigid, and charged SDS head groups, because of counter-ion condensation phenomena,[77] strongly associate with each other as soon as their surface density allows them to. This aggregation forces the SDS tail groups to become perpendicular to the interface because of excluded-volume effects. On the contrary, the long, flexible, and nonionic $C_{12}E_6$ head groups easily interact with water molecules, but do not yield a compact self-assembled aggregate. Consequently the $C_{12}E_6$ tails do not need to orient perpendicularly to the interface until the surface coverage is very large, approaching the value necessary to form a complete monolayer. The different packing of SDS vs. $C_{12}E_6$ surfactants at the interface is probably responsible for differences observed in surface tensions, as discussed below. When SDS and $C_{12}E_6$ surfactants are compared one should remember that the head group of $C_{12}E_6$ is much larger than that of SDS (see Figure 2-i). The head group of SDS may be comparable in size to that of $C_{12}E_3$ (both surfactants yield a complete mono-layer at surface densities of ~40-45 $Å^2$ per surfactant).[138] However, the experimental data reported by Lu et al. show that the alkyl chain thickness at the air-water interfaces remains ~constant for $C_{12}E_n$ surfactants

with n<8 as long as the experiments are performed at constant surface densities.[94] Thus, the structural properties obtained for the tail groups of $C_{12}E_6$ surfactants should be similar to those obtained for $C_{12}E_3$ ones.

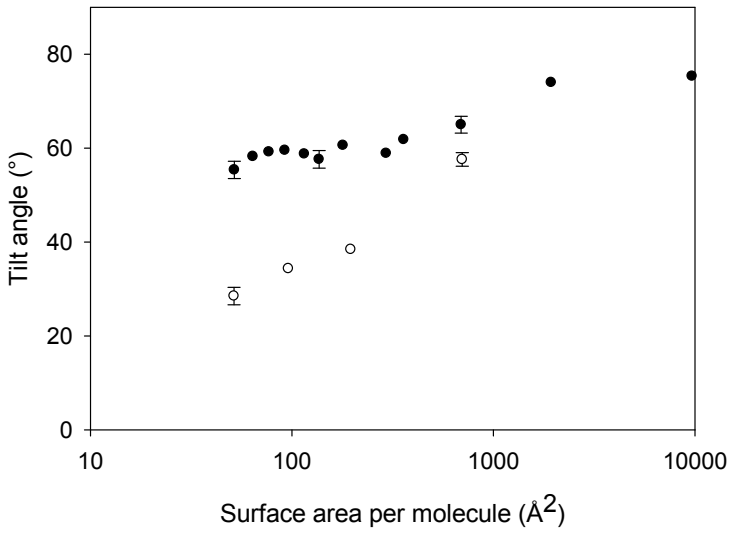

Figure 2-xiii**:** Average tilt angles of tail groups as a function of surface area per head group. Filled and empty symbols represent results for $C_{12}E_6$ and SDS, respectively. Only representative error bars are shown for clarity.

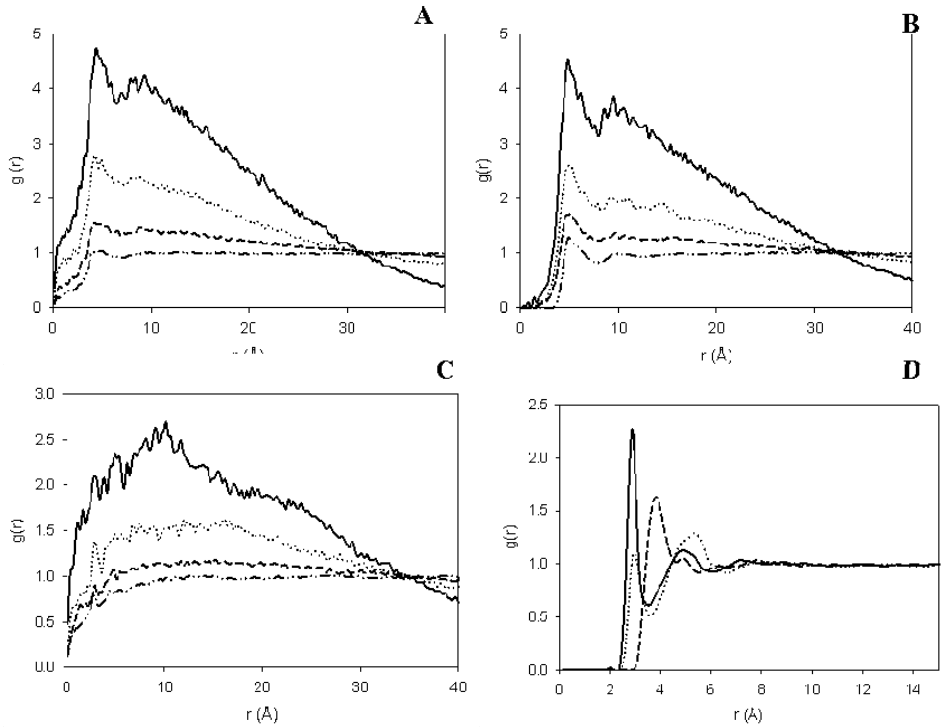

Figure 2-xiv: Two-dimensional radial distribution functions between surfactants functional groups at the vacuum-water interface. For clarity, only 3 functional groups are shown: C1-C1 (panel A); EO1-EO1 (panel B) and OH-OH (panel C). See Figure 2-i for molecular details. Results are obtained at various surface coverages: 293 $Å^2$/molecule (solid line); 179 $Å^2$/molecule (dot line); 92 $Å^2$/molecule (dashed line); and 52 $Å^2$/molecule (dash-dot-dot line). In panel D we report the 2D RDF between $C_{12}E_6$ terminal head groups and the oxygen atom in water at 52 $Å^2$/molecule. Results are shown for OH-water (solid line); EO6-water (dot line); E6-water (dashed line). See Figure 2-i to identify the surfactant functional groups.

2.4.4. Surfactant Aggregates Structure

To quantify the interfacial aggregate morphology we calculated two-dimensional radial distribution functions (2D RDF) between functional groups of $C_{12}E_6$ and SDS surfactants. Representative results obtained as a function of surface coverage are reported in Figure 2-xiv. Panels A, B and C report the 2D RDFs for C1-C1, EO1-EO1 and OH-OH groups of interfacial $C_{12}E_6$ aggregates, respectively. At low surface coverage the 2D RDFs are representative of gas-like structures. We also observe that the 2D RDF is less than unity at large distances. This happens because at low surface

coverage $C_{12}E_6$ surfactants are not evenly distributed, but rather form small interfacial aggregates (see snapshot in panel A of Figure 2-v). As the surface area per $C_{12}E_6$ decreases (i.e., as the surface coverage increases), the 2D RDFs change from gas-like to condensed-phase-like ones. However, $C_{12}E_6$ aggregates never yield crystalline 2D RDFs, not even at the largest surface coverage considered (52 $Å^2$/molecule). The lack of long-range order in the 2D RDFs shown in Figure 2-xiv corroborates our earlier interpretation that region III in Figure 2-ix corresponds to a 2D liquid-like phase. Comparing the 2D RDFs in panel A, B, and C of Figure 2-xiv at the largest coverage considered (dot-dot-dash line), we find that the functional groups in the center of the surfactant molecules (EO1-EO1) show 2D RDFs with more intense first peaks than the functional groups at either ends of the surfactants (C1-C1 and OH-OH). This result suggests that the surfactants are relatively closely packed in their middle sections, and quite sparse at their extremities. This is clearly due to the flexibility of the $C_{12}E_6$ surfactants.

To understand why terminal OH groups in $C_{12}E_6$ surfactant do not densely pack, the 2D RDFs between water and terminal OH, EO6 and E6 are shown in panel D of Figure 2-xiv. For water and terminal OH group only the oxygen atoms are considered. The solid line (water-OH) shows a clear first peak at about 2.8Å, representative of the first hydration shell. The dot line (water-EO6) shows a small peak at the same position, whose intensity is weaker than that for water-OH. The first peak of the dashed line (water-E6) moves to larger distances due to the hydrophobic nature of ethylene and because of excluded-volume effects. These data are consistent with the formation of a well defined hydration layer around the $C_{12}E_6$ head groups. The hydration layers form

easily because the head groups are loosely packed with each other, a consequence of their high flexibility. Our simulations suggest that this hydration layer is in part responsible for preventing the terminal OH groups from densely packing at the interface.

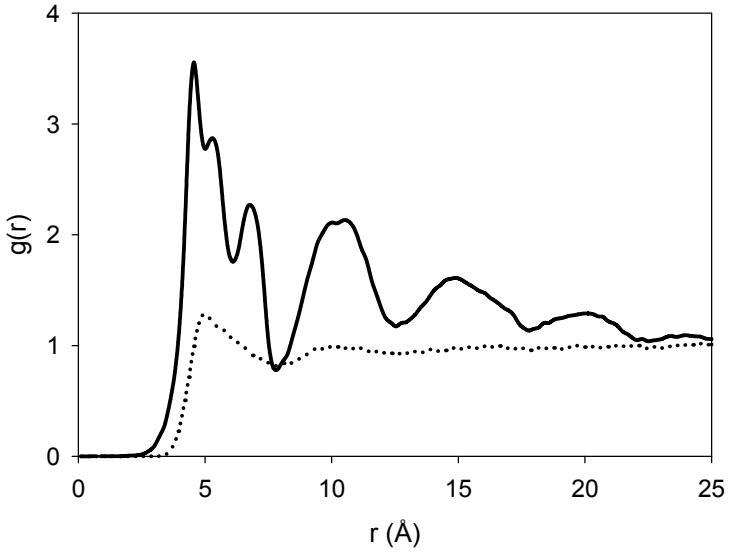

Figure 2-xv: Two-dimensional radial distribution functions between head groups of SDS (solid line) and between the EO1 groups of $C_{12}E_6$ surfactants (dot line) at 52 $Å^2$ per head group. See Figure 2-i for molecular details.

For comparison, we calculated the 2D RDF between sulfur groups of SDS. The results, including those from $C_{12}E_6$, are shown in Figure 2-xv. Contrary to what observed for $C_{12}E_6$, the 2D RDF for SDS aggregates shows regular peaks as r increases, suggesting a more densely packed structure than that obtained with $C_{12}E_6$. The seemingly periodic peaks at 5, 10, 15, and 20 Å suggest a solid-like structure, almost hexagonal (visual inspection of simulation snapshots, not shown for brevity, confirms the formation of a regular structure, but excludes that of a perfect crystalline arrangement). Even though the SDS coverage is not sufficient to form one complete monolayer, the 2D RDF data in Figure 2-xv corroborate the propensity of the SDS head

groups to strongly self assemble, because of counter-ion condensation effects.[77] The counterion condensation phenomenon responsible for close packing of SDS aggregates is not possible with any $C_{12}E_n$ surfactants, and hence we believe that the intensity of the peak observed for 2D RDF in Figure 2-xv for head groups of $C_{12}E_n$ would not be comparable to that observed for SDS head groups.

2.4.5. Surface Tension

The surface tension, γ, was computed from our simulations as:[143]

$$\gamma(A) = (\frac{L_Z}{2})\left[< P_{zz} > -(\frac{< P_{xx} > - < P_{yy} >}{2}) \right] \quad (2.6)$$

In Eq. 6, L_Z is the box size along the direction z, perpendicular to the vacuum-water interface. The factor $1/2$ outside the bracket takes into account the fact that there are two interfaces in the system. $P_{\alpha\alpha}$ are pressure tensors along the α direction.[123] To calculate the surface tension the simulated systems were arranged so that the same number of surfactants was placed on both vacuum-water interfaces (see Figure 2). The corresponding surface pressure-area isotherm (π-A) was obtained as:

$$\pi(A) = \gamma_0 - \gamma(A) \quad (2.7)$$

where γ_0 denotes the surface tension of the vacuum-water interface.

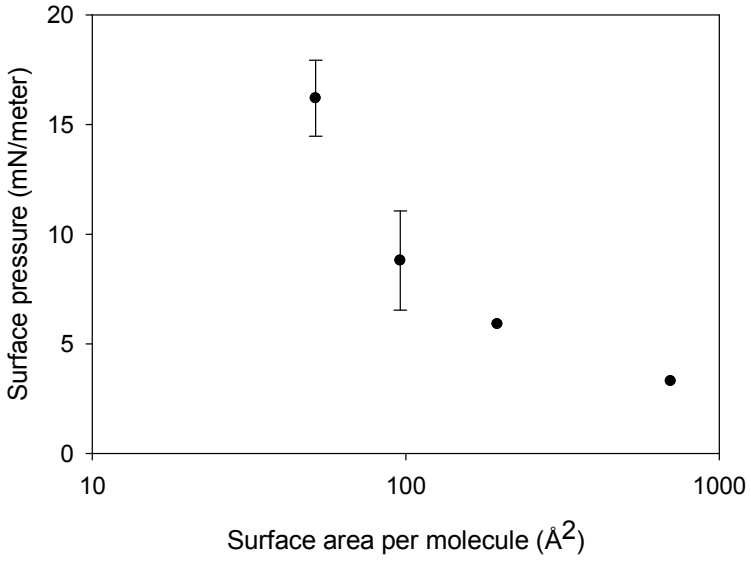

Figure 2-xvi**:** Surface pressure as a function of surface area per SDS surfactant.

The results for SDS are shown in Figure 2-xvi. The surface pressure increases as the surface area per head group decreases, in semi-quantitative agreement with experimental data.[107] On the contrary, our calculation for the surface tension in the presence of $C_{12}E_6$ surfactants showed values only slightly smaller than those obtained at the vacuum-water interface at all surfactant concentrations considered. Although experimental data show that SDS is more effective in reducing the water-air surface tension than $C_{12}E_6$ (surface tension of SDS at cmc is 32.5 mN/m whereas $C_{12}E_6$ yields a value of 41 mN/m),[144-145] we were expecting to observe a more significant effect for our simulated $C_{12}E_6$ systems than those obtained. One possible reason for the discrepancy between simulated and experimental data could be the size of the simulation box. However, several simulation results are available in the literature that report data for biological systems and other surfactants that are in good agreement with experiments despite using simulation boxes significantly smaller than those used herein.[120,123-124]

Prior simulation results showed that appropriately accounting for long-ranged electrostatics is necessary to achieve good agreement between simulated and experimental surface tension data.[123] Because our results for SDS (anionic surfactants) are in good agreement with experiments, and because $C_{12}E_6$ is overall a neutral molecule, it appears that our treatment of long-ranged electrostatics forces is satisfactory. The last possible explanation for the unexpected results for $C_{12}E_6$ is to be found in deficiencies in the implemented force fields. For example, it has been reported previously that although TRaPPE force field parameters yield satisfactory structural and thermodynamic properties, they not always accurately predict interfacial and surface tensions.[146] To test if this was the reason for our unexpected results, we conducted sample simulations in which only the tail groups of $C_{12}E_6$ surfactants (i.e., only dodecane) were simulated at the water-vacuum interface. At surface coverages correspondent to 52 $Å^2$ per dodecane we obtained a ~4% decrease in the surface tension compared to that of the vacuum-water interface, indicating that the TRaPPE force field, used to model the surfactants tails, yields reasonable, yet not always accurate estimates for the surface tension (the NERD force field is known to perform better).[146] On the contrary the force field we implemented to simulate the $C_{12}E_6$ head groups (OPLS, although with some modifications) does not provide good surface tension predictions. We note that the sulfate group parameters used to simulate SDS were fitted to predict the free energy of solvation, along with other thermodynamic properties,[147] while those implemented to describe the $C_{12}E_6$ head groups were fitted to other thermodynamic properties without explicitly considering solvation.[129] Hence we attribute our failure to reproduce experimental surface tension data for $C_{12}E_6$ systems to inefficiency of the

employed force field. Necessary calculations should be performed to increase the accuracy of force fields before any such attempts are undertaken to compute the surface tension data for C_mE_n systems.

2.4.6. Surfactant Mobility

To evaluate the surfactant mobility at the vacuum-water interface we calculated the two-dimensional mean square displacement (2D MSD) for surfactants along the plane parallel to the interface.

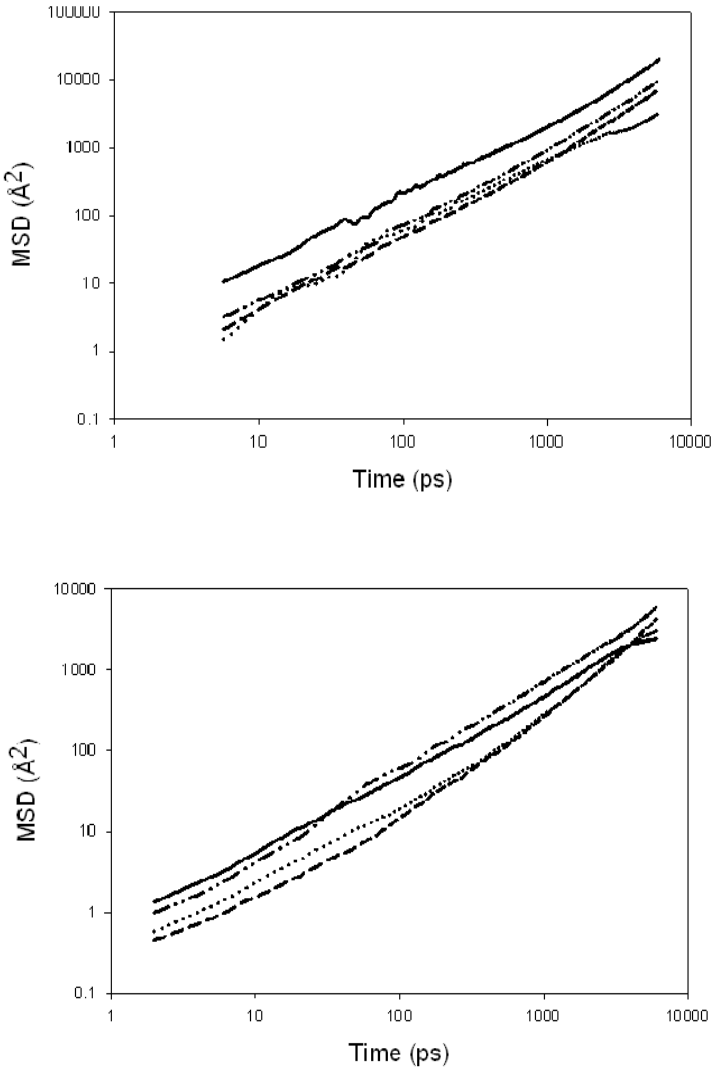

Figure 2-xvii**:** Two-dimensional mean square displacement for surfactants as a function of time. The top panel is for $C_{12}E_6$ surfactants at various surface coverages [9684 $Å^2$/molecule (solid line); 358$Å^2$/molecule (dot line); 92$Å^2$/molecule (short dashed line); 52$Å^2$/molecule (dot-dot-dash line)].The bottom panel is for SDS at various coverages [700 $Å^2$/molecule (solid line); 196$Å^2$/molecule (dot line); 96$Å^2$/molecule (dashed line); 52 $Å^2$/molecule (dot-dot-dash line)].

In Figure 2-xvii we report the results obtained for $C_{12}E_6$ and SDS surfactants at different surface coverages. Our analysis extends to much longer simulation times and to a wider range of surface coverages compared to previous data reported by Chanda[118] and Bandyopadhyay.[117] Our data suggest that Fickian-type diffusion is established when

only 1 surfactant is at the interface, and when a full monolayer is simulated. When the surfactants are simulated at concentrations at which small aggregates form, the diffusion is anomalous because the surfactants are effectively 'confined' within the surface aggregates. More interesting, however, is the fact that the results in the top panel of Figure 2-xvii show that at the lowest surface coverage (correspondent to only 1 $C_{12}E_6$ at the interface) the 2D MSD increases more quickly as a function of time than at any other surface coverage considered. These data suggest that the surfactants move on the interface very quickly when they are not associated with other surfactants. As the surfactant aggregates increase in size, each individual surfactant in the aggregate shows slower mobility because the entire aggregate needs to move simultaneously to avoid disaggregation. When the surfactant aggregate is large enough to span the entire interface, then the individual surfactants can easily move within the aggregate and the slope of the 2D MSD as a function of time increases. Our findings are in apparent contradiction with those of Cuny et al.,[115] who reported that the mobility of interfacial surfactants (expressed as the slope of 2D MSD vs. time) does not change as the surface coverage varies. However, we point out that Cuny et al.[115] considered coverages close to those necessary to form a complete surfactant monolayer, whereas we consider surface coverages ranging from very low, to the one necessary to form the complete monolayer. Because at the largest coverage considered here the results for 2D MSD vs. time are similar to those reported by Cuny et al.,[115] our simulations complement rather than contradict those reported earlier. On the bottom panel of Figure 2-xvii we report the data obtained for SDS. Although we do not have data for 1 SDS chain at the surface, the behavior is qualitatively similar to that described for $C_{12}E_6$, suggesting that the

properties of the surfactant head groups do not affect significantly the surfactant mobility. Our results seem to suggest that the hydrophobic tails are responsible for the formation of surfactant self assemblies at the vacuum-water interface, that the hydrophilic head groups determine the morphological properties of the aggregates, and that the size of the self-assembled aggregate is responsible for the mobility of the individual surfactant molecule at the interface.

2.5. Conclusions

We employed molecular dynamic simulations to characterize the behavior of $C_{12}E_6$ and SDS surfactants at the vacuum-water interface. The aggregate structures of $C_{12}E_6$ at the interface predicted from our simulations are in agreement with data obtained from neutron scattering experiments. Our simulations also indicate that the surfactant structure at the vacuum-water interface strongly depends on the surface density. At high surface area per molecule, the tail groups of $C_{12}E_6$ lie almost parallel to the interface and are located in close proximity to the water phase. At low surface area per molecule, the tail groups remain almost completely segregate from the water phase and show a tilt angle of about 50°. The head groups orient more perpendicularly to the vacuum-water interface than tail groups do at all coverages. At low surface area per head group, not only the tail groups of $C_{12}E_6$ remain out of the water phase, but also part of the ethylene oxide groups at the center of the surfactant molecules move away from the aqueous phase. The tail groups of SDS are more perpendicular to the vacuum-water interface in comparison with $C_{12}E_6$ ones, and the sulfate head groups of SDS are always immersed in water. An overlap between the interfacial layers formed by head and tail groups is observed for all surface coverages studied for both $C_{12}E_6$ and SDS

surfactants, indicating that the surfactant aggregates fluctuate along the direction perpendicular to the interface. Due to these fluctuations the observed thickness of the interfacial surfactant layer is larger than the surfactant end-to-end distance. Due to its long, flexible and partially hydrophobic head groups, the packing of $C_{12}E_6$ head groups is less dense compared to that of SDS head groups.

The surfactants mobility at the vacuum-water interface depends strongly on surface coverage. The mobility is high at infinite dilution, decreases as the surfactant aggregates increase in size, reaches a minimum, and increases when the surface coverage is sufficiently large that the surfactant aggregates cover, albeit with some defects, the entire vacuum-water interface.

3. The Role of Counterion Condensation in the Self-Assembly of SDS Surfactants at the Water-Graphite Interface

The material presented below has been published in volume 112, issue 7 of the journal The Journal of Physical Chemistry B in the year 2008.

3.1. Abstract

The aggregate structure of sodium dodecyl sulphate (SDS) adsorbed at the graphite-water interface has been studied with the aid of molecular dynamics (MD) simulations. As expected, our results show that adsorbed SDS yields hemi-cylindrical micelles. The hemi-cylindrical aggregates in our simulations closely resemble all structural and morphological details provided by previous solution atomic force microscopy (AFM) experiments. More interestingly, our data indicate that SDS head groups do not provide a complete shield to the hydrophobic tails. Instead we found regions in which the hydrophobic tails are exposed to the aqueous solution. By conducting a parametric study for SDS-like nonionic surfactants we show that electrostatic interactions between SDS head groups and counterions are responsible for the unexpected result. Our interpretation is corroborated by density profiles, analysis of the coordination states, and mean square displacement data for both the adsorbed SDS surfactants and the counterions in solution. Counterion condensation appears to be a physical phenomenon that could be exploited to direct the assembly of advanced nano-structured materials.

3.2. Introduction

Amphiphilic molecules are used in a variety of applications that employ their ability to self-assemble, including the fabrication of porous materials,[1] structured materials,[2] and also tuning the effective interactions between latex spheres in aqueous solution.[3] Surfactants are amphiphilic molecules with relatively long (8-24 carbon atoms) hydrophobic tails and short hydrophilic heads. Studies of surfactant adsorption on solid surfaces date back to the 1960's and the classic papers of Fuerstenau.[17-21] Because of the commercial importance of applications such as mineral flotation processes and detergency, many pioneering studies focused on surfactant adsorption on small particulate solids.[22-31] Development of atomic force microscopy (AFM) promoted a significant breakthrough in the area of surfactant adsorption. The results from AFM experiments during the 1990's revealed the hemicylindrical aggregate structure of ionic surfactants on hydrophobic substrates.[32-35] It is now clear that the morphology of surfactants self-assembled structures varies as the critical packing shape and available surface area for the amphiphilic molecule change.[36] A number of amphiphilic molecules are known which self-assemble yielding bilayers, hemi-cylinders and hemi-spheres.

The structural properties of surfactant systems have been investigated via theoretical techniques.[148-149] Leermakers and coworkers[150-153] discussed in a series of articles the results obtained from self-consistent field theory (SCF) for surfactants confined between surfaces. The calculations suggest that for ionic surfactants on amphiphilic surfaces at close enough separation distances (e.g., *the removal point*), one of the two adsorbed layers desorbs due to the presence of the other. In addition, at distances smaller than the removal point, the amount of surfactant adsorbed on one

surface is not only larger than that adsorbed on the other surface, but also than that on free-standing surface. Thus frontal confinement affects how much surfactant is adsorbed at wall-wall separations comparable to the surfactant length. Simulations have been performed at a coarse-grained (CG) level to describe, for example, bulk surfactant solutions[154] or the adsorption of anionic surfactants,[155] and that of diblock copolymers on solid surfaces,[156-157] either homogeneous or heterogeneous.[158-164] CG simulations provide general trends, such as the dependency of the adsorbed amount and adsorbate structure on the adsorption energy and the head/tail ratio.[165-176] Wijmans and Linse showed that self assembly at the surface occurs at bulk concentrations lower than the critical micelle concentration (CMC)[155] because the surfactant concentration is higher near the surface than it is in the bulk solution. Also, the adsorption isotherm on a surface presents a plateau when the bulk concentration is larger than CMC.[177] All-atom simulations are required within molecular dynamics (MD) algorithms[178-179] to better understand the molecular-level mechanism of interfacial phenomena related to surfactant aggregation. It should however be clear that the current computing infrastructures allow researchers to conduct all-atom MD studies for only up to a few tens of nanoseconds. Despite this limitation, all-atom MD can be used, for example, to study surfactants at air-water[119] and at water-CCl_4 interfaces,[103] the structure of reverse micelles,[180] the adsorption of surfactants on scheelite,[181] or the self assembly of water/surfactant/CO_2 systems.[182-184] Shah *et al*. studied aqueous solutions of n-dodecyltrimethylammonium bromide in contact with hydrophilic silica surfaces.[185] The authors were able to show that the compact spherical or elliptical micellar structure observed for the surfactants in bulk solution evolves to flat elliptical structures at

contact with silica surfaces, in agreement with experiments. Bandyopadhyay *et al*. showed that cetyltrimethylammoniumbromide (CTAB) surfactants on graphite form stable hemicylindrical aggregates, in agreement with experimental observations.[186] Dominguez recently reported MD simulation results for sodium dodecyl sulfate (SDS) surfactants at graphite-water interfaces.[187] The results show the formation of hemi-cylinders at surface coverage of 0.45 nm^2 per head group and full cylinders with water near the graphite surface at surface coverage of 0.20 nm^2. Bruce *et al*.[188] provided data for the distribution of counterions in SDS micelles in solution.

We are here interested in the morphology of SDS self-assembled aggregates at the graphite-water interface. We monitor the relative arrangement of surfactant heads and surfactant tails (which is difficult, at best, to obtain experimentally), the role of counterion condensation on the surface aggregate morphology, and the effect of frontal confinement in the structure and dynamics of the self-assembled structures. Our results compare semi-quantitatively to AFM experimental data provided by Wanless and Ducker[35] which show that hemi-cylindrical structures form at bulk concentration well below the CMC, and that the periodicity of the surface aggregates changes with the concentration of salts in solution and decreases as the SDS concentration increases. In Section 3 we provide simulation details and algorithms; in Section 4 we discuss our main results; and in Section 5 we summarize our conclusions.

3.3. Simulation Methodology

Our goal is to study the morphology of SDS aggregates at the graphite-water interface. The entire process of surfactant adsorption from solution cannot be simulated by standard all-atom MD techniques within the limitations of the current computational

resources. In fact, the typical time scale for surfactant adsorption/desorption from a micelle is ~1 μs.[148] Thus it is customary to arrange a given number of surfactant molecules on a surface and then to conduct MD simulations to assess their equilibrium properties.[186-187] Because the results depend on the surface density of the surfactants, it is necessary to employ experimentally-relevant data to initiate the MD calculations. Optical measurements for SDS on graphon indicate that the surface area per head group is ~ 0.40 nm^2 at a bulk concentration of 7 mM SDS.[189] This is the surface area per head group considered in this work. To increase statistical accuracy, two opposing graphite surfaces were considered to gather most of the results discussed below. Sufficient SDS molecules were placed on each graphite surface, and water, with sodium counterions, was placed in the region in between them. The overall density between the graphite surfaces was ~0.94 gm/cc, and the water density at the center of the simulation box was ~ 1.0 gm/cc.

Water was simulated using the simple point charge/extended (SPC/E) model.[126] Carbon atoms in highly ordered pyrolitic graphite (HOPG) were held stationary during the simulation and modeled as Lennard-Jones (LJ) spheres. The LJ parameters to describe carbon-carbon interactions were those of Cheng and Steele.[190] One SDS surfactant is composed of one hydrophobic tail of 12 carbon atoms (one CH_3 and eleven CH_2 groups) and one hydrophilic head of chemical composition SO_4. Following Berkowitz and coworkers,[119] who successfully simulated SDS surfactants at a number of fluid-fluid interfaces, the CH_n- groups in SDS were modeled as united-atom LJ groups. Bond lengths and bond angles were constrained by harmonic potentials. The CH_n-CH_n bond length is constrained through the harmonic potential:

$$E_{bond} = K_b (r - r_O)^2 \tag{3.1}$$

In Eq. (3.1) E_{bond} is the potential energy associated with the bond stretching and contraction, K_b is the elastic constant of the bond, r_O is the equilibrium distance between the bonded atoms, and r is the instantaneous distance between them.

All the angles in one surfactant are constrained by the harmonic potential

$$E_{ang} = K_\theta (\theta - \theta_O)^2 \tag{3.2}$$

In Eq. (3.2) E_{ang} is the potential energy associated with the angle bending, K_θ is the force constant, θ_O is the equilibrium angle, and θ is the instantaneous angle.

Dihedral angles are constrained through the Ryckaert and Bellemans potential[132] given by:

$$E_{dihedral} = \sum_{k=0}^{5} c_k \cos^k(\phi) \tag{3.3}$$

In Eq. (3.3) c_k are the energy constants, φ is the dihedral angle, and $E_{dihedral}$ is the potential energy. The dihedral angles along the backbone of surfactant (CH_n-CH_2-CH_2-CH_2, CH_2-CH_2-CH_2-O^*, CH_2-CH_2-O^*-S and CH_2-O^*-S-O) were constrained using the parameters shown in Table 3-A. The head group in each surfactant molecule was explicitly modeled. Sulfur and oxygen atoms in the head group are described as LJ spheres which bear partial charges. The S-O and CH_2-O^* bonds are constrained through the harmonic potential expressed in Eq. (3.1) with appropriate values for the constants K_b and r_O. The O-S-O and CH_2-O^*-S angles are constrained through the angular potential of Eq. (3.2), with the appropriate choice of constants.

Sodium ions are modeled following the model of Schweighofer *et al.*[119] Chlorine atoms, when present, are modeled as described by Cummings and coworkers.[191] Cesium ions, used to study the effect of counterion size on the surface

aggregates, were described following Smith and Dang[192] but without polarizability, for consistency with the other potentials used here. LJ interaction parameters for unlike atom pairs were computed from those of like pairs using Lorentz-Berthelot mixing rules. In Table 3-A we report all values for the like-pairs parameters used in our simulations.

As mentioned above, all-atom models are too computationally expensive to study the spontaneous formation of micelles at surfactant concentrations at or above the bulk CMC. Bruce *et al*.,[188] using the model implemented in the present work, studied the morphological properties of one micelle composed by 60 SDS molecules in a system corresponded to a SDS concentration of 0.4M, but the micelle was prepared as input for the simulation. Gao *et al*.[193] introduced a simplified model for both SDS and water that allowed them to study the spontaneous formation of micelles from an aqueous solution containing SDS molecules. The SDS concentrations considered were between 0.4 and 1.1 M (well above the bulk SDS CMC). The micelles obtained were rod-like, in qualitative agreement with experimental observation. Although it is not clear whether or not these SDS models predict the bulk CMC concentration in water, the studies just summarized suggest that they are adequate to study the morphology of surfactant aggregates formed at concentrations above the bulk CMC. Because we are interested in capturing atomic-level details that are probably due to the formation of hydrogen bonds and salt bridges between interfacial water molecules, surfactant heads, and counter ions, we implemented the all-atom model of Berkowitz and coworkers rather than the simplified version of Gao *et al*. The correct implementation of the model was validated by comparing the average hydration number of head groups at the water-

vapor interface with neutron-scattering experimental data.[98] The hydration number from our simulations is 8.67, obtained by integrating the sulfur-oxygen (water) radial distribution function up to the first local minima (located at ~0.55 nm from the sulfur atom). The experimental hydration number is 7 +/- 1.[98] We also reproduced the density profiles at the water interface for water, head groups and tails obtained from MD simulation by Schweighofer *et al*.[119]

Table 3-A*:* Parameters used to implement the force fields discussed in Eqs. (3.1), (3.2), and (3.3). O^* is the oxygen atom that bridges the CH_2 group and the S atom in SDS surfactants.

ATOMS (or GROUPS)	**σ (Angstrom)**	**ε (Kcal/mole)**	***q (e)***
CH_3	3.905	0.175000	0.0000
CH_2	3.905	0.118000	0.0000
CH_2 (in CH_2-O-S)	3.905	0.118000	0.1370
S	3.550	0.250000	1.2840
O^* (in CH_2-O-S)	3.000	0.170000	-0.4590
O (in SO_3)	3.150	0.200000	-0.6540
H (in H_2O)	0.000	0.000000	0.4238
O (in H_2O)	3.166	0.155402	-0.8476
C	3.400	0.055700	0.0000
Na^+	2.275	0.115300	+1.000
Cs^+	3.831	0.10000	+1.000
Cl^-	4.401	0.10000	-1.000
BOND	**K_b (kcal mol^{-1} Å^{-2})**	**r_o (Angstroms)**	
CH_3-CH_2	620.000	1.530	
CH_2-CH_2	620.000	1.530	
CH_2-O^*	600.000	1.420	
O^*-S	600.000	1.580	
O-S	900.000	1.460	
ANGLE	**K_θ(kcal mol^{-1} rad^{-2})**	**Θ_O(deg)**	
CH_3-CH_2-CH_2	124.300	111.000	
CH_2-CH_2-CH_2	124.300	111.000	
CH_2-CH_2-O^*	124.300	109.500	
CH_2-O^*-S	124.300	112.600	
O^*-S-O	102.000	102.600	
O-S-O	102.000	115.400	

Dihedral	C_0 (kcal/ mol)	C_1	C_2	C_3	C_4	C_5
CH_n-CH_2-CH_2-CH_2	2.2176	2.905	-3.136	-0.731	6.271	-7.527
CH_2-CH_2-CH_2-O^*	2.2176	2.905	-3.136	-0.731	6.271	-7.527
CH_2-CH_2-O^*-S	2.2176	2.905	-3.136	-0.731	6.271	-7.527
CH_2-O^*-S-O	2.2176	2.905	-3.136	-0.731	6.271	-7.527

The simulation package LAMMPS[194] was employed to integrate the equations of motion. In our simulations we maintained the number of particles (N), the simulation box volume (V), and the temperature (T) constant. In all simulations the time step was 2 fs. The Nose-Hoover thermostat with velocity Verlet algorithm was implemented with a relaxation time constant of 100 fs.[194] Dispersive attractions and repulsive interactions were treated with an inner cutoff of 0.8 nm and outer cutoff of 1.0 nm. Long range electrostatic interactions were treated using the Ewald summation method.[194] Bond lengths and angles in water were maintained fixed using the SHAKE algorithm.

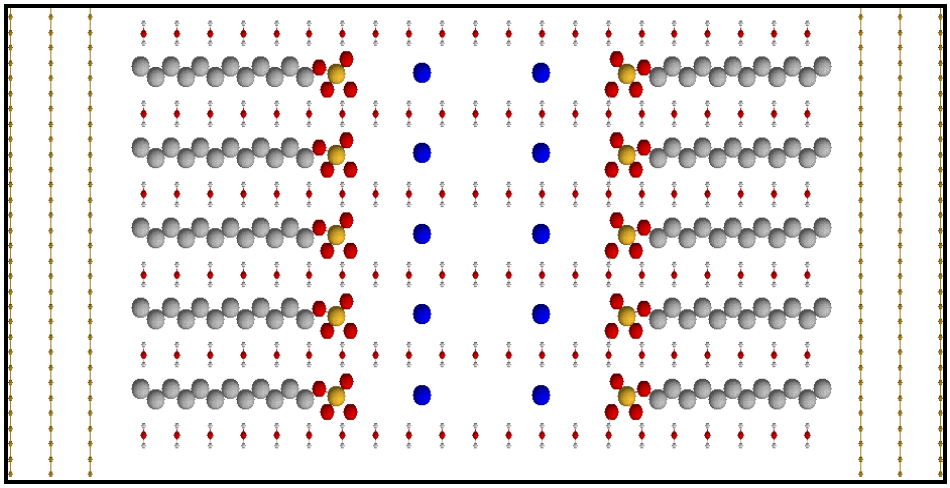

Figure 3-i: Side view of the initial configuration of SDS at the graphite-water interface. CH_n- groups that belong to the surfactant tails, sulfur, oxygen and sodium counterions are shown as grey, orange, red, and blue spheres respectively. Water is represented by small red and white spheres (oxygen and hydrogen atoms respectively). The graphite surfaces are separated by H= 6.5 nm and graphite atoms are depicted as yellow spheres.

Simulations were initialized in a system consisting of two graphite slabs separated by a distance of 6.5 nm. Each graphite slab is composed of three carbon layers, separated by 0.335 nm from each other. The X and Y dimensions of the simulation box are 3.94 and 2.56 nm, respectively. To reach the desired surface area per head group of 0.40 nm^2 we placed 25 SDS surfactants on each graphite slab. In the initial arrangement the SDS surfactants were in the all-trans configuration, and perpendicular to the surface. One positively charged sodium counterion was placed at a distance of 0.5 nm from each surfactant head. Sufficient water molecules (1260) were then inserted to reach the desired density (~1 gm/cc) within the simulation box. The initial configuration is shown in Figure 3-i periodic boundary conditions were implemented in three dimensions. To decrease unrealistic interactions between mirror images in the Z direction, 12.1 nm of empty space was placed after the three layers of graphite in the Z direction. Thus the simulation box was of size $3.94 \times 2.56 \times 20.00$ nm^3. The simulations were initiated by conducting NVT runs at 600 K for 1 ns to ensure that the results were not affected by the initial configuration. The system was then instantaneously brought to 300 K and the simulations were continued in the NVT ensemble for an additional 2 ns. To further ensure that the results were independent of the initial simulation setup, all the sodium counterions were dragged 2 nm away from the head groups in the Z-direction. NVT simulations were then conducted for 12 ns. Even though the system energy reached a plateau after ~ 1 ns, we only used the molecular trajectories of the last 2 ns to obtain the results presented here.

We performed a number of simulations by varying distance H between the graphite slabs. To initiate these simulations we used the final configuration obtained from the simulation conducted at H = 6.5 nm and removed (or inserted) the necessary amount of water from (or in) the central region of the simulation box.

We computed distribution functions, mean square displacements (MSD) and population distributions to characterize and analyze the results. The distribution function was computed using the following expression:[195]

$$Df(r) = \frac{\left(n_{his}(b) \Big/ N \times \tau_{run} \right)}{\frac{4}{3}\pi\left[(r + \delta r)^3 - r^3 \right]} \tag{3.4}$$

where $n_{his}(b)$ represents number of elements in the bth histogram, N is the number of particles considered, τ_{run} are the number of output steps recorded during the simulation, r is the center-to-center distance between the atoms, δr is the width of each histogram bin. In computing distribution functions we do not divide the local density of particles by the average density of the particles within the box. This allowed us to compare the distribution functions in different simulations, irrespectively of the volume of the simulation box.

The MSD, a function of time, is defined by the expression[195]

$$MSD(t) = \left\langle \left| r_i(t) - r_i(0) \right|^2 \right\rangle \tag{3.5}$$

where $r_i(t)$ is the position vector of particle at time 't' and $r_i(0)$ is the initial position vector of the particle. Angular brackets indicate ensemble averages. The MSD yields the distance traveled by a particle during the time interval considered.

The population distribution of surfactant lengths is defined by the following equation

$$P(r) = \left(n_{his}(b) \Big/ N \times \tau_{run} \right) \tag{3.6}$$

where $n_{his}(b)$ represents number of elements in the b^{th} histogram, N and τ_{run} are defined as in Eq. (3.4).

3.4. Results and Discussion

3.4.1. Frontal confinement

We provide here the results from simulations conducted at graphite-graphite separation distances H=4.055, 4.50, 6.50, 8.00, 10.00, 12.00, and 14.00 nm. We report the distribution function between sodium and sulfur atoms in Figure 3-ii. The statistical error is ~5%. Although the curves shown in Figure 3-ii are similar to each other, they present interesting differences as a function of the graphite-graphite separation distance H. A sharp peak is evident in all S-Na distribution functions at a distance r~0.35 nm. This well-pronounced peak corresponds to the association of the counterions to the surfactant heads. We notice that this peak is present for all graphite-graphite separations considered. However, the peak intensity for the distribution function obtained at H=4.05 nm is larger when compared to that obtained when H=4.5nm. It is possible that when the graphite-graphite distance is reduced from H=4.5 nm to H=4.05 nm the surface aggregates adsorbed on the two opposing surfaces interact with each other. The fact that the $Df_{S\text{-}Na}(r)$ peak at 0.35 nm increases suggests that Na^+ may form ion bridges between the surfactant heads which belong to the two opposing surfaces. When the

graphite-graphite separation distance H increases from 4.05 to 6.50 nm the intensity of the $Df_{S\text{-}Na}(r)$ peak at 0.35 nm decreases monotonically. It is interesting to note that the peak at 0.35 nm obtained at H=6.5 nm and that obtained at H=8.0 nm are indistinguishable from each other. As H further increases to values above 8.0 nm the peak intensity does not change, but the peak location shifts to larger S-Na separations. At S-Na separations larger than 0.40 nm we observe smooth oscillatory behavior of the distribution function which does not indicate significant structuring between the surfactant heads and the counterions. However, we point out that the second weak peak in the distribution function, located at r=0.55 nm, becomes slightly more intense as the graphite-graphite separation decreases. This behavior is different from what is observed for SDS surfactant micelles in aqueous solution, in which case a significant second peak for S-Na radial distribution function is observed at ~0.43 nm which corresponds to the second shell of counterions around the surfactant heads.[188] Interestingly, while in the case of micelles 50% of the counterions distribute between the first and second shell around the surfactant heads, our results indicate that in the case of SDS aggregates on graphite about 75% of the Na^+ counterions accumulate within the first solvation shell. This result is in qualitative agreement with experimental data obtained by Bitting and Harwell for Li^+, Na^+, K^+, and Cs^+ salts of dodecyl sulfate aggregates on alumina, which suggest that 'apparent' counterion-surfactant head binding on surface aggregates can be up to 85-95% depending on solution conditions.[196] We also detect a small peak at short separations (0.32 nm). The peak is well pronounced when H is larger than 4.5 nm, and it becomes but a shoulder at H=4.05 nm. At H greater than 8.0 nm this peak shifts from ~0.32 to ~0.34 nm, as indicated in Figure 3-ii by the distance between the continuous

and dotted vertical lines. This small peak may be due to the presence of the Na^+ sandwiched between two next-neighbor SDS surfactant heads, suggesting the possibility of counterion bridging, as documented in the next section.

To investigate the packing of SDS molecules within the surface aggregates we calculated sulfur-sulfur distribution functions. A hemi-cylindrical arrangement should yield a distribution function characterized by broad peaks located at regular intervals. Our results (not shown for brevity) indicate that the head groups are associated with each other only for distances lower than 0.8 nm. The first peak, which does not change as H varies, is observed at S-S distances of 0.45 nm, and a second broad peak, which becomes less intense as H increases, is observed at S-S distance of ~0.7 nm. The second peak suggests some degree of ordering between the head groups, although it does not necessarily imply the formation of any specific supra-molecular structure (e.g., hemi-cylinders).

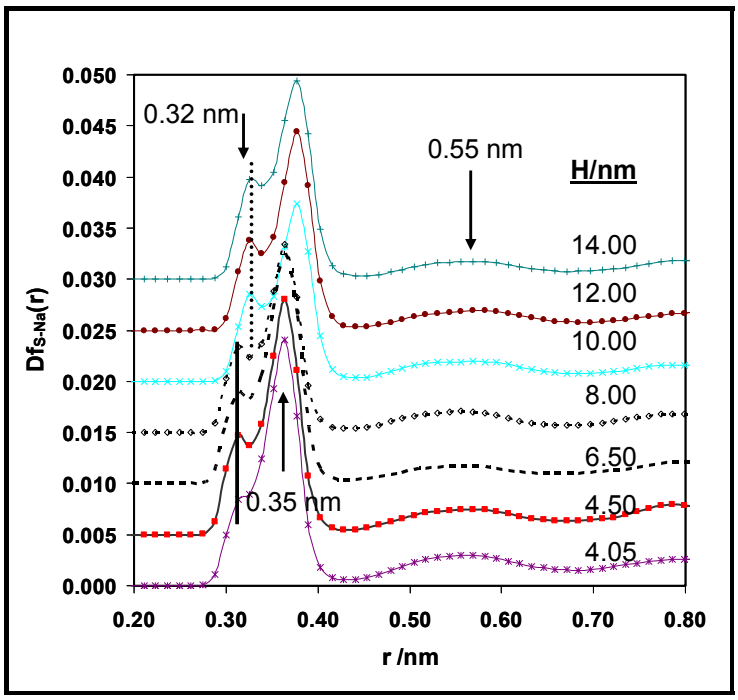

Figure 3-ii: Distribution function between sulfur and sodium for the simulations conducted at different graphite-graphite separations H. From bottom to top the different lines are for H=4.05, 4.5, 6.5, 8.0, 10.0, 12.0 and 14.0 nm. The vertical lines and arrows indicate the observed peaks. Two vertical lines (continuous and dotted) highlight the shift of the ~0.32 nm peak to longer S-Na distances when H increases above 8.0 nm. Individual plots are shifted 0.005 units along the Y axis to ease visualization.

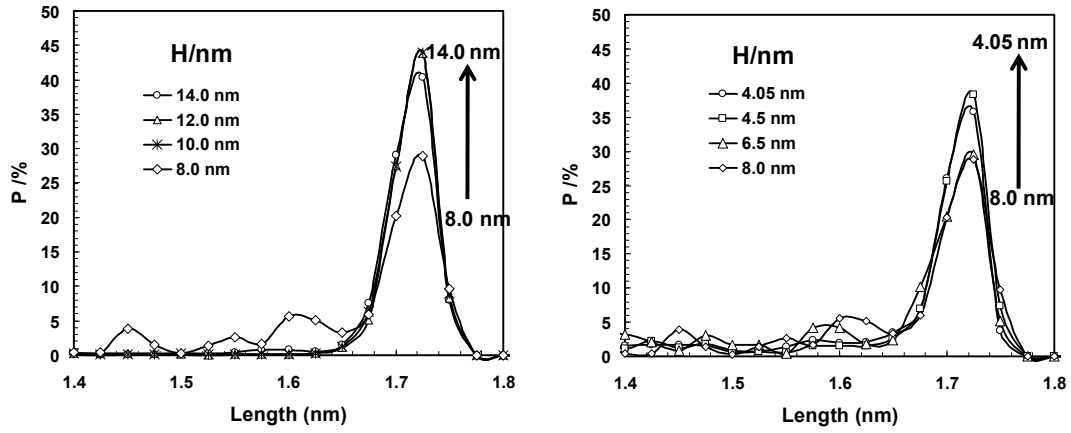

Figure 3-iii: Population distribution of surfactant lengths. The different curves depict the distribution of surfactant lengths in the simulations conducted at different graphite-graphite separations H.

The results shown so far suggest that the properties of the SDS surface aggregates depend on the graphite-graphite separation. It is possible that when H

approaches twice the thickness of the surface aggregate effective forces act between the aggregates, thus affecting the equilibrium structure of the aggregates. To test this hypothesis we calculated the population distribution of the surfactant lengths as a function of H. The surfactant length is calculated as the distance between the CH_3 group in the surfactant tail and the farthest oxygen atom in the surfactant head. The results, whose statistical error is less than 5%, are shown in Figure 3-iii. On the right panel we display the results obtained for graphite-graphite separations H ranging from 4.05 to 8.00 nm. We notice that the pronounced peak for surfactant length of ~1.7 nm increases significantly as H decreases. It is particularly interesting to note that the data sets obtained for H=6.50 nm and H=8.00 nm almost coincide. On the left panel of Figure 3-iii we display the results obtained when H increases from 8.0 nm to 14.0 nm. In contrast to what is observed at smaller H values, we notice that the percentage of surfactant molecules of length 1.7 nm increases as H increases from 8.0 nm to 10.0 nm and larger separations. These results suggest that as the graphite surfaces approach from H=14.0 nm to H=6.5-8.0 nm the surfactant molecules are compressed, as evidenced by the decreasing probability of observing surfactants of length 1.7 nm, possibly indicating an effective repulsion between the surfactant aggregates adsorbed on the two opposing graphite surfaces. As the graphite surfaces further approach, the surfactants begin to stretch, possibly indicating an attraction between the surfactant aggregates adsorbed on the two opposing surfaces. We point out that during our simulations we never observed desorption of the surfactant molecules from one surface followed by the adsorption onto the opposing surface, as could have been expected based on the SCF calculations of

Leermakers and coworkers.[150] It is possible that such phenomena can be observed for longer simulations, which are at present prohibitive.

The results discussed until now suggest that when the graphite slabs are closer than 6.5-8.0 nm there may be a significant attraction between the surfactant aggregates on the two surfaces. This is in qualitative agreement with the observations of Wanless and Ducker,[35] who reported that AFM tips 'feel' the presence of SDS surface aggregates on graphite when they are at a distance of ~10 nm or less from the solid surface. Based on our results, in order to study the behavior of independent SDS aggregates at the water-graphite interface H should be at least greater than 8.0 nm, although this distance may vary depending upon the type of head group, surfactant length and ionic strength of the system. To further test our hypothesis, we focus on the diffusion of the surfactant aggregates on the two opposing surfaces. In the presence of a strong aggregate-aggregate attraction (as well as repulsion), we expect that the aggregates on the opposing surfaces move in a coordinated fashion. If the two aggregates are not influenced by the presence of each other, then the surface displacement of each should be independent from that of the other. We calculated the mean square displacement (MSD) for the sulfur atom in the surfactant head group. We report the results in Figure 3-iv. In the case when graphite surfaces are separated by 4.05 nm (left panel), we observe that the surface aggregates on both surfaces move in a highly coordinated manner along both the X and Y directions. In fact, the MSD calculated for the surfactant aggregate on the top surface is not distinguishable from that calculated for the surface aggregate on the bottom surface, confirming our hypothesis of strong attraction between the surface aggregates. On the other hand the MSD data

obtained at H=14.0 nm (right panel) show significant deviation between the results obtained for the surfactants aggregates adsorbed on top and bottom surfaces, respectively. This uncoordinated behavior suggests that the surface aggregates on each surface are not influencing each other. Our complete set of results (not shown for brevity) indicate that the diffusion of the surface aggregates on the two opposing surfaces is somewhat correlated even at H=4.5 nm. It is interesting to note, from the results in Figure 3-iv, that the MSD along the Y-direction is oscillatory. The amplitude of these oscillations along the hemi-cylinders axis is ~ 1 order of magnitude less than the MSD along the X direction measured in ~1.5 ns of simulation. We point out that the MSD, even that along the X direction, is not sufficiently large to yield accurate estimates for self-diffusion coefficients, thus we do not attempt such calculations.

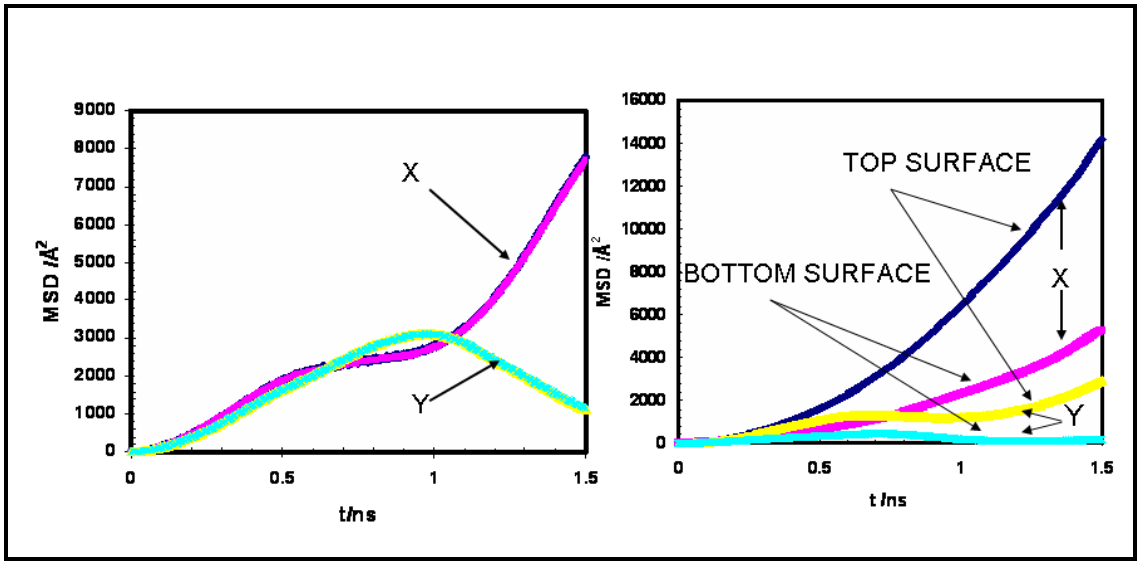

Figure 3-iv: Left: MSD vs time for sulfur atoms within the surface aggregate when graphite-graphite distance H=4.05nm. Right: MSD vs time for sulfur atoms within the surface aggregate with H=14.00 nm between the graphite surfaces. Blue and pink lines are for MSD along the X direction for top and bottom surface aggregates, respectively; yellow and green lines are for MSD data along the Y direction for top and bottom surface aggregates, respectively. Blue and pink lines, as well as yellow and green lines, are indistinguishable in the left panel.

3.4.2. Equilibrium structure

We now discuss the morphological details of SDS surface aggregates. In Figure 3-v we show the equilibrium structure of surface aggregates for various graphite-graphite distances (H) by means of representative simulation snapshots. We report surface aggregates obtained for H=4.05 nm, H=4.50 nm and for H=14.0 nm. Based on the results discussed above, at H=4.05 nm and H=4.50 nm the surface aggregates strongly feel the presence of each other, but at H=14.0 nm the surface aggregates are expected to be non-interacting.

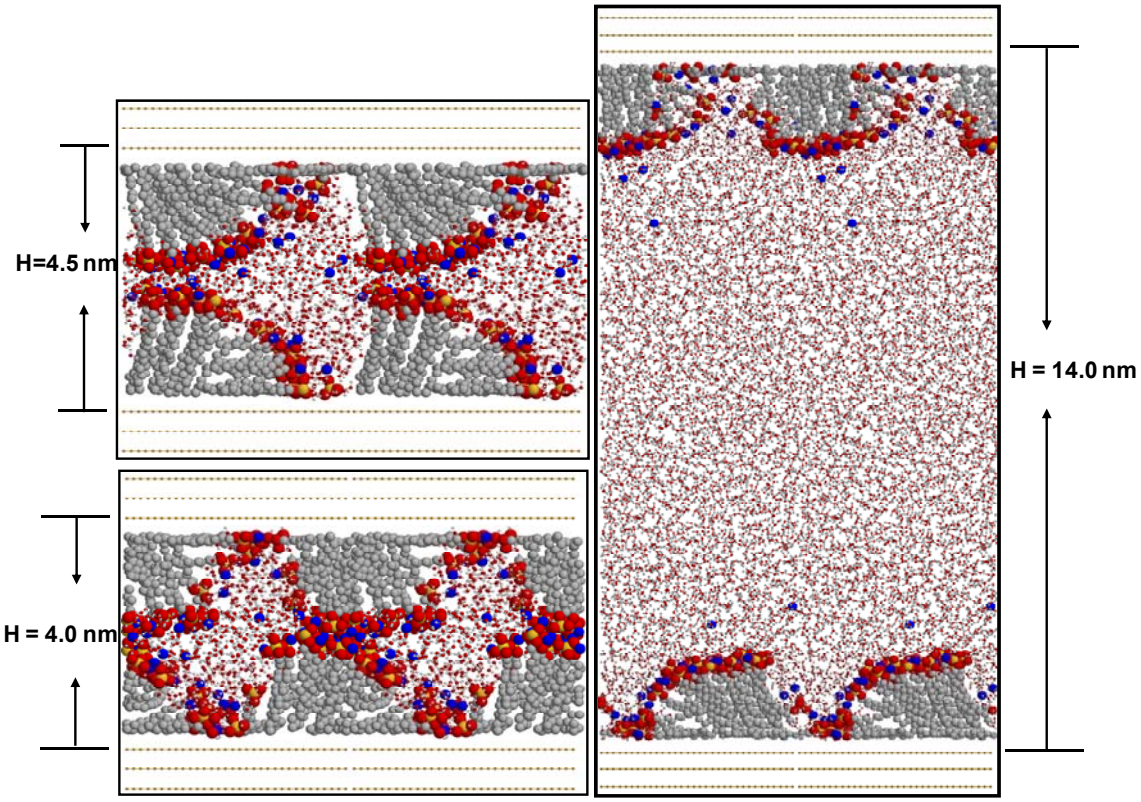

Figure 3-v: Side view of representative simulation snapshots obtained at various graphite-graphite separations H. CH_n- groups in surfactant tails, sulfur, oxygen and sodium counterions are shown as grey, orange, red, and blue spheres, respectively. Water is represented by small red and white dots (oxygen and hydrogen atoms, respectively). Graphite atoms are shown as yellow spheres. The simulation box is replicated twice along the X direction for visualization purposes.

All the snapshots shown in Figure 3-v, as well as all the others not shown for brevity, indicate that SDS surfactants adsorbed on the graphite-water interface yield hemi-cylindrical aggregates at the conditions considered here. More interestingly, we always find regions within the SDS aggregates in which the hydrophobic surfactant tails are exposed to water. It is evident from the snapshots of Figure 3-v that this is due to the fact that head groups closely pack with each other and with sodium counterions.

Although the qualitative morphology of the surface aggregates does not change as H decreases, we note in Figure 3-v that the surfactant aggregates which are adsorbed on the opposing surfaces interact strongly with each other. The surface aggregates on the opposing surfaces resemble each other when H=4.05 nm. The head groups of the surface aggregate are found very close to each other rather than distant as it would be expected because of electrostatic repulsions between like-charged head groups. A few Na^+ counterions are found sandwiched between surfactants which belong to the aggregates of the two opposing surfaces. This counterion condensation results in an effective attraction between the head groups of opposing surface aggregates. In the snapshot obtained for H=4.5 nm the surface aggregates from opposing surfaces seem to stretch in an attempt to touch each other. This structure, along with the larger population distribution observed for surfactants with length 1.7 nm shown in Figure 3-iii, suggests that attractive forces act between the surface aggregates adsorbed on the opposing graphite surfaces. We did not attempt to quantify these forces. When H=14.0 nm the surface aggregates on the opposing surfaces are not identical, and the surface aggregate on the bottom surface looks similar to those observed when H=4.05 nm and H=4.5 nm (note that these snapshots were obtained after at least 10 ns of simulation time). We also

notice that morphological distortion from perfect hemi-cylindrical structure, which are always observed during our simulations, are more pronounced when the two graphite surfaces are at small distance from each other, probably because under those circumstances the surfactant aggregates on the two opposing surfaces strongly attract each other. A complete understanding of the molecular origin for this phenomenon could allow us to tailor the self-assembly of amphiphilic molecules of practical interest.

Because of periodic boundary conditions and because of confinement effects it is possible that the results just discussed are affected by the simulation box size along the X direction (which constrains the distance between two adjacent hemi-cylinders) and of the density of water within the simulation box (which determines the pressure of the system). To assess the reliability of our calculations we performed additional simulations in two representative cases. In the first case study we addressed the effect of box size on the structure and morphology of SDS aggregates. The initial simulation box was replicated twice along the X direction, and the box was further 'grown' in that direction until the X size was 8.36 nm. One of the two opposing graphite surfaces, and the surface aggregates on that surface, were removed. The resultant system contained 3455 water molecules, 50 SDS, and 50 Na^+ ions. The available surface area per surfactant molecule was 0.42 nm^2. Because the X and Y dimensions of the simulation box were maintained equal to those discussed in Section 2, the system simulated now exhibits one vacuum-water interface. As customary, periodic boundary conditions were implemented in all 3 directions.

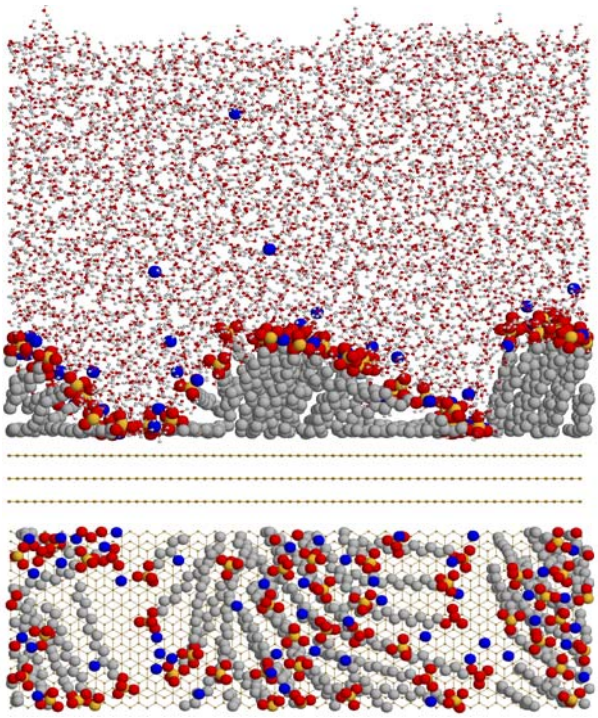

Figure 3-vi**:** Lateral (top) and top view (bottom) of the simulation snapshot obtained after 10 ns in a box of size X=8.36 and Y=2.56 nm. The lateral view is qualitative identical to that obtained in the simulation box of size X=3.94 nm (see Figure 3-v). The top view (from which water molecules are deleted) provides details on the morphological arrangement of the aggregates.

After 10 ns of simulation time, the SDS molecules yield two hemi-cylindrical aggregates one adjacent to the other. As can be seen from the final simulation snapshot shown in Figure 3-vi, the morphology of each aggregate was similar to the one obtained in the original simulation box (Figure 3-v). Further, density profiles and distribution functions computed from both simulations (Figure 3-v and Figure 3-vi) were not distinguishable, within computational accuracy. These comparisons suggest that the simulation box of X = 3.94 nm is sufficiently wide to obtain reliable morphological information. The experimental AFM results of Wanless and Ducker[35] show that the distance between two adjacent SDS hemi-cylindrical aggregates at the graphite-water interface decreases as the SDS surface coverage increases. It ranges from ~7.0 nm at 2

mM SDS bulk concentration to ~5.2 nm at 100 mM. Although our results, dictated in part by the simulation box X dimension, are in reasonable agreement with experiments, our simulation protocol is not adequate to predict the equilibrium aggregate-aggregate separation as a function of surface coverage. Much larger, and at present untractable systems are required for these purposes.

The second case study was conducted by implementing an NPT (constant number of particles, pressure and temperature) algorithm in which one of the two opposing graphite surfaces, along with the surface aggregate on that surface, was removed. Because of periodic boundary conditions in the Z direction, the vacuum-water interface of Figure 3-vi is replaced by a graphite-water interface. To maintain the pressure constant at atmospheric conditions the simulation box height (Z direction) was allowed to fluctuate. After 15 ns, the simulation yielded similar structural and morphological details as those observed when H= 8.0 nm in the simulations described above. Based on the results obtained in the two latter case studies, and how they favorably compare to the results obtained within the original simulation box, we are confident that within the accuracy of the force fields implemented in this work, the morphological results shown in Figure 3-v are representative of the self-association of SDS surfactants at the graphite-water interface at room conditions. The results discussed in the remainder of the manuscript are obtained in the small simulation box.

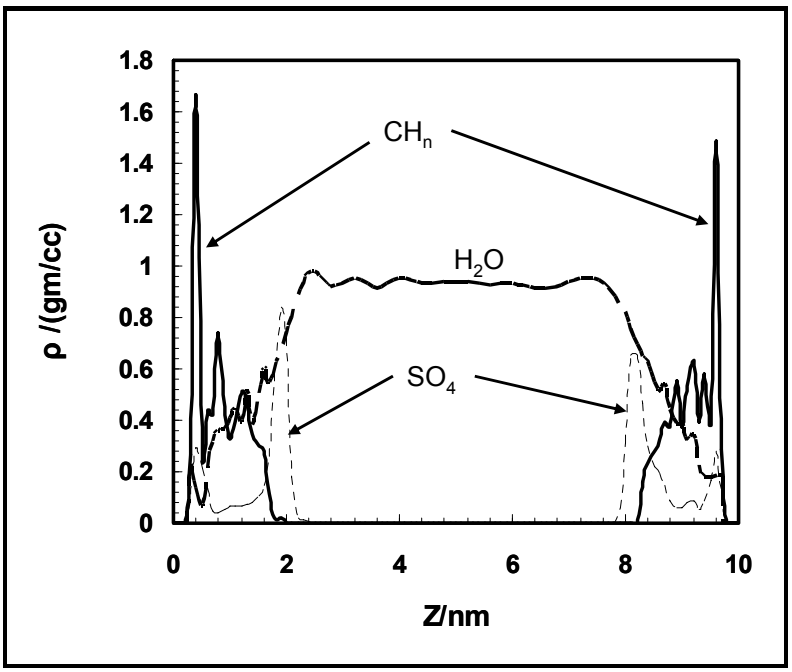

Figure 3-vii: Density profiles for surfactant tails (continuous grey line), surfactant head groups (broken grey line) and water molecules (broken black line) as a function of the distance from the graphite surface.

Density profiles across the simulation box obtained from the equilibrium surface aggregates are reported in Figure 3-vii. We include the density profiles of surfactant tail groups, head groups and water molecules along the Z direction when the distance between the graphite surfaces is 10.0 nm, *i.e.* when the interactions between surfactant aggregates on opposing surfaces are negligible. We did not observe any significant difference in density profiles calculated for surfactant head groups and tails among all the simulations performed for graphite-graphite separations larger than 8.0 nm. Concerning the density profile of head groups (broken grey line) we observe a clear, albeit small, peak at ~0.4 nm. This result is quite surprising (hydrophilic heads are not expected to lie close to the graphite surface), but is due to the parallel orientation of a few surfactant molecules on the surface, as suggested by the peaks in the results for the tail groups density profiles. The number of SDS molecules that lie completely on the

graphite surface are computed by averaging the surfactants that are always within less than 0.6 nm from the graphite surface. We found that always 20-30 % of the surfactant molecules lie parallel to graphite. From the results of Wanless and Ducker[35] we expect that 7 surfactants are present in each cross section of one SDS hemi-cylinder, out of which at least 2 should lie parallel to graphite (i.e., ~28%). The head groups density is the highest at ~1.84 nm from the graphite surfaces, value which corresponds to the thickness of the aggregate structure. This result is in reasonable agreement with the AFM experiments of Wanless and Ducker which indicate an aggregate thickness of 1.7 +/- 0.5 nm.[35] Our result is also in agreement with the recent MD simulations of Dominguez.[187] One would expect the density profile of water to gradually decrease from one in the center of the simulation box to zero at the hydrophobic graphite surface. However, as we can notice in Figure 3-vii (broken black line) the results for the water density profiles are more interesting. For example, we notice the presence of a small peak at about 0.4 nm from the graphite surfaces, indicating the presence of water molecules near the graphite surface. This unexpected result is due to the presence of few surfactant head groups on the graphite surface, which in turn attract water molecules to the surface. In Figure 3-vii we observe a very sharp intense peak at 0.4 nm from either graphite surface for the density profile of surfactant tail groups (continuous grey line). This peak suggests that a few surfactant tails are adsorbed completely parallel to the surface. We also notice that the density profile for tail groups shows several peaks at distances larger than ~1.0 nm from the graphite surface indicating the presence of not regularly adsorbed tails. This suggests the formation of structures in

which the tail groups are neither completely parallel to the graphite surface nor perpendicular to it.

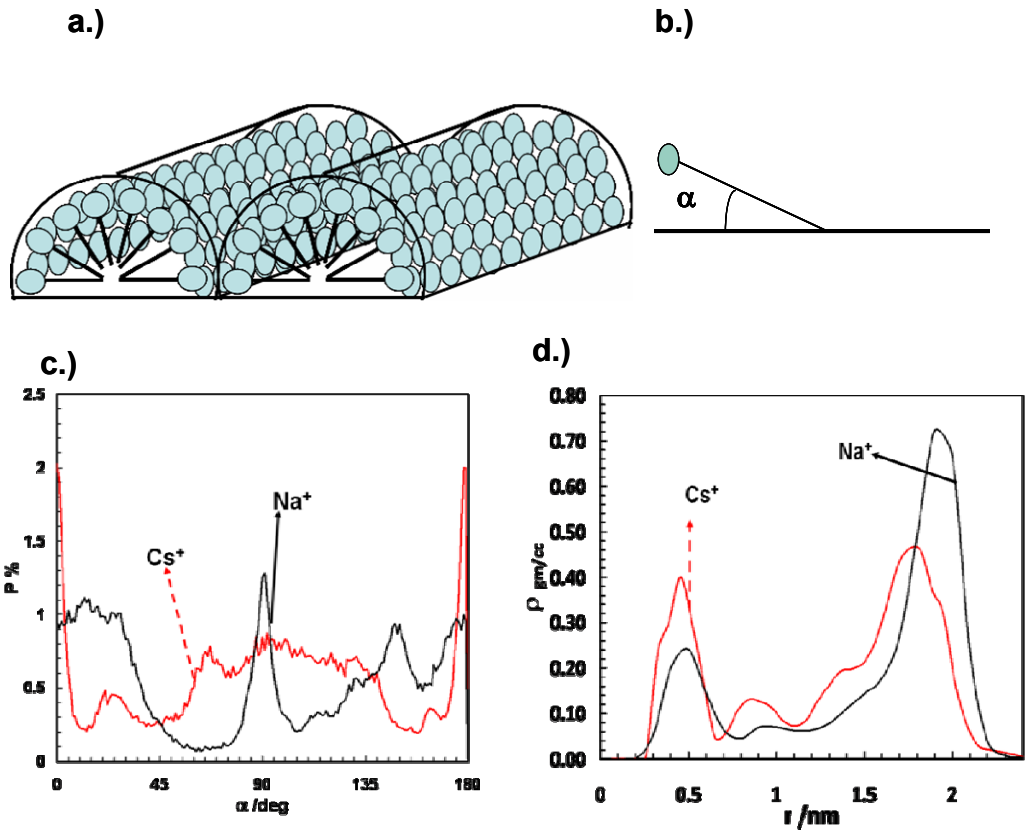

Figure 3-viii: a.) Schematic representation of perfect surfactant hemi-cylindrical aggregates on hydrophobic surfaces. The light blue spheres represent the head groups. In this idealization the surfactant head groups shield the hydrophobic tails from the aqueous solvent. b.) Schematic of the angle α formed between one surfactant molecules and the X direction of the simulation box. c.) Population distribution of angle α. d.) Density profiles of surfactant head groups. In both panels (c) and (d) continuous black lines represent results obtained with Na^+ counterions, dotted red line for those obtained with Cs^+ counterions.

In our simulations the SDS molecules do not yield perfect hemi-cylindrical structures. Perfect hemi-cylinders are shown schematically in Figure 3-viii.a. In such structures it is possible to define the angle α formed between the X direction of the simulation box and the vector obtained by connecting the first and the last methyl group in one SDS molecule (see schematic in Figure 3-viii.b). When α=0 or 180°, the

surfactant is parallel to the X surface direction. When α~90°, the surfactant is perpendicular to the surface. Surfactant organized in perfect hemi-cylinders should yield symmetric distributions of angles α with peaks at 0, 90, and 180°. Instead, we see (black continuous line in Figure 3-viii.c) that SDS surfactants at the graphite-water interface are either perpendicular or parallel to the surface, but the angles in between are not often observed. In agreement with this observation, an enlargement of the density profiles for the surfactant head groups (black continuous line in Figure 3-viii.d) shows that most of the surfactant heads are either located next to the surface or located at ~1.7-2.0 nm from it.

Both the simulation snapshots shown in Figure 3-v and the head group density profiles shown in Figure 3-vii and Figure 3-viii.d suggest that the head groups for SDS surfactants at graphite-water interfaces are not uniformly distributed. Instead, we find that the head groups form few dense patches within the surface aggregate, which cause some of the surfactant tails to be exposed to the aqueous environment. To further highlight this phenomenon we present in Figure 3-ix the top view of one simulation snapshot obtained for SDS aggregates at the graphite-water interface.

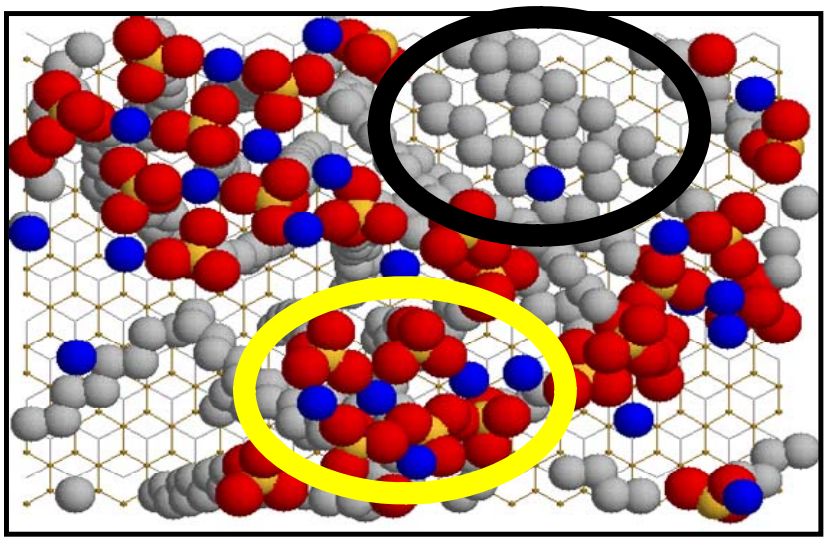

Figure 3-ix: Top view of the surface aggregates of SDS formed on graphite surfaces. The color code is the same as that used in Figure 3-v. The black circle highlights an area in which the hydrophobic surfactant tails are exposed to water. The yellow circle indicates one dense patch composed by head groups and counterions.

The presence of sporadic dense patches formed by counterions and head groups is apparent from Figure 3-ix (highlighted by the yellow circle). Because of the presence of these dense patches, some of the hydrophobic surfactant tails remain exposed to the aqueous environment, as evidenced by the black circle in Figure 3-ix. The dense patches of surfactant heads are also the reason for the noticeable contrast between the snapshots shown in Figure 3-v and Figure 3-vi and the schematic representation proposed in Figure 3-viii.a, *i.e.* the surfactant head groups completely shield the hydrophobic tails from water in Figure 3-viii.a but do not do so in Figure 3-v and Figure 3-vi.

To assess the role played by the counterion condensation in the results shown above, we report an enlargement of one simulation snapshot in Figure 3-x. This figure allows us to highlight the counterion-bridging phenomenon observed in all surface aggregate structures discussed so far. In Figure 3-x the distances between the sodium

counterion and the sulfur atom of two adjacent surfactants are at 0.30 nm and 0.348 nm**.** These distances give rise to the two peaks observed in the S-Na distribution function Figure 3-ii. The sodium counterion associate simultaneously with several surfactant heads, neutralizing the charge-charge repulsion expected between the ionic heads, and instead inducing an effective attraction. This attraction is strong enough to cause the formation of the hydrophilic dense patches discussed in Figure 3-v and Figure 3-ix.

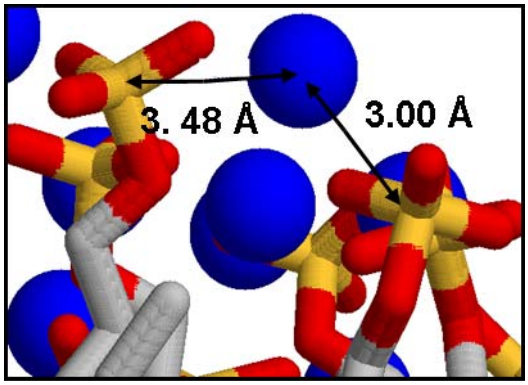

Figure 3-x: Counterion bridging as observed within the SDS surface aggregate. The color code is the same as that of Figure 3-v. In the cartoon the atoms are connected using the stick model. The distance between counterion and adjacent head groups are indicated (3.48 Å and 3.00 Å are the distances form the left and right head groups to the Na^+ counterion, respectively)

Based on the discussion relative to Figure 3-x, we may expect that the morphology of the SDS aggregates at the graphite-water interface is affected by the size of the counterions. Namely, if counterions bigger than Na^+ were considered, the patches of surfactant heads and counterions should become bigger, and therefore provide wider shields to the hydrophobic surfactant tails from the aqueous environment. To test this hypothesis we conducted a series of simulations in which the Na^+ counterions were substituted by the much larger Cs^+ ones. In Figure 3-xi we report the equilibrium simulation snapshot obtained in this latter case. Confirming our hypothesis regarding the importance of counterion-condensation phenomena in the formation of the hemi-

cylindrical aggregates of Figure 3-v (in which hydrophobic tails are exposed to water), the snapshot shown in Figure 3-xi indicates that when Cs^+ ions are considered, the surface SDS aggregates become perfect hemi-cylinders in which the hydrophilic heads act as a perfect shield to the hydrophobic tails. The aggregates in Figure 3-xi were characterized by computing the probability distribution of the angle α (see Figure 3-viii.b), and the head groups density profile away from the graphite surface. We report the results in Figure 3-viii.c and Figure 3-viii.d, respectively, where we directly compare them to those obtained when Na^+ were the counterions. In the case of Cs^+ (red dotted lines) the probability distribution of the angle α shows peaks at 0, 90, and 180°, but the the angles in between are sampled with some probability, as expected for quasi-perfect hemi-cylindrical aggregates. Further, the density distribution of head groups (red dotted line in Figure 3-viii.d) shows a somewhat homogeneous distribution, as expected from the snapshot in Figure 3-xi.

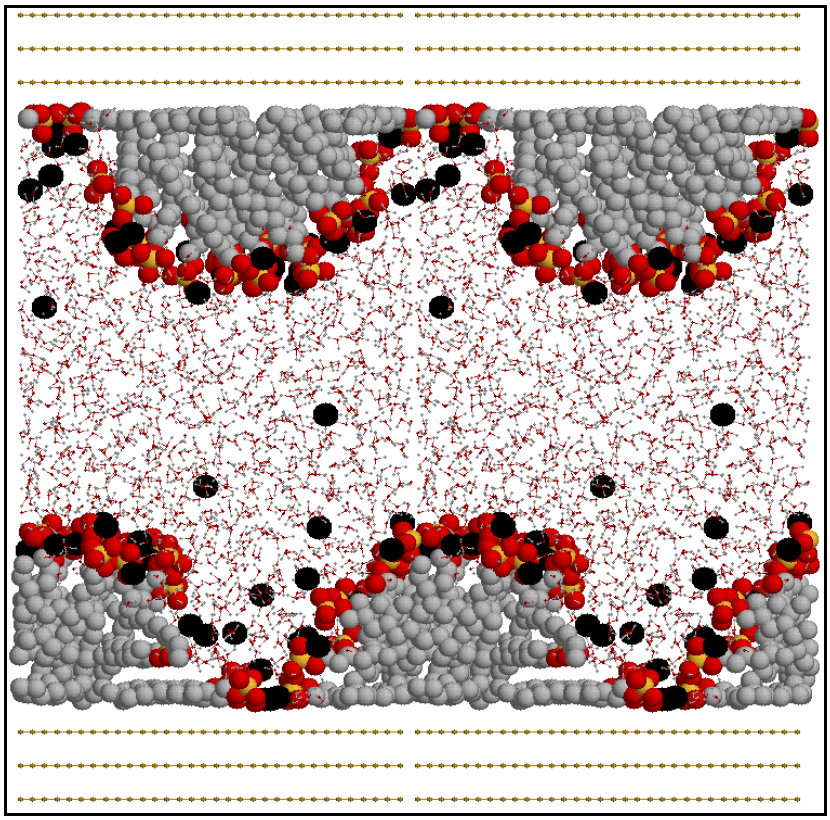

Figure 3-xi: Side view of one representative simulation snapshot obtained when the counterion is cesium rather than sodium at H=6.5 nm. The color code is the same as that used in Figure 3-v, except for cesium atoms, which are represented by black spheres. The simulation box is replicated twice along the X direction for visualization purposes.

The results discussed so far indicate that the presence of sodium counterions in the vicinity of head groups influences the morphology of the self-assembled aggregates. We studied the MSD of sodium counterions to differentiate their behavior when they are associated with surfactant aggregates compared to when they are in the bulk aqueous solution. The comparison of MSD results of the sulfur atoms (representing head groups) to that of all the counterions present in the simulation box suggests that the surfactant head group and counterion movements are highly correlated, but not completely identical. Instead, if we compare the MSD obtained for the sulfur atoms to that of the MSD obtained for only those counterions found within the first shell around

the surfactant head groups (within center-to-center distance of ~0.41 nm), we find identical behavior. These results (not shown for brevity) further indicate that counterions are strongly associated with the head groups. Further, only a few Na^+ or Cs^+ counterions (~25% of the total) are found in the bulk solution during our simulation. The MSD obtained for these ions is larger than that obtained for the counterions found near the surfactant head groups.

3.4.3. Nonionic SDS-like surfactants

The manifestation of phenomena such as counterion bridging and condensation in the surface aggregate structure induced us to reexamine the aggregate structure closely and study the driving forces for such aggregation on surfaces using a parametric study. We report in what follows the results of a series of simulations conducted for nonionic SDS-like surfactants. The goal of these simulations is to unveil the physical origin of the results discussed so far. In particular we are interested in understanding why SDS surfactants form hemi-cylinders at the graphite-water interface and also why some of the hydrophobic tails remain exposed to the aqueous environment. The final configuration from the simulation of SDS at graphite-water interface in which the graphite surfaces are separated by 6.50 nm was used as the initial configuration for the nonionic SDS-like surfactants. The coulombic charge of the atoms present in the SDS head group was set to zero, and the hydrophilicity of the head groups was regulated by increasing the inter-atomic LJ interaction parameters between all head group atoms (which were S and O in the case of SDS) and water. Anionic chlorine atoms were introduced within the simulation box for the purpose of attaining electrical neutrality. Simulations were performed with inter-atomic interaction parameter set to ε_1, $2\varepsilon_1$, 2.5

ε_1, $3\varepsilon_1$, $3.5\varepsilon_1$ and $4\varepsilon_1$, where ε_1 corresponds to the LJ well-depth obtained from the Lorentz-Berthelot mixing rules for LJ parameters of the head group atoms and the oxygen atom in water using the values reported in Table 3-A. Thus, for example, when the simulations were conducted for $4\varepsilon_1$, the LJ energy parameter to determine S-O (water) interaction was 0.78842 kcal/mol whereas the LJ energy parameter for the S-O pair in the simulations conducted for SDS was 0.19710 kcal/mol.

For the weakest head group-water interactions corresponding to the interaction parameter of ε_1 we observe multiple layers of the surfactant on the graphite surface (see top left panel in Figure 3-xii). The formation of multiple layers is justified by energetic reasons. Because of the weak attraction between the head group and water, the entire surfactant molecule acts essentially as a hydrophobic chain. Thus the surfactant molecules partition preferentially at the graphite surface in an effort to minimize the contact with water molecules. The surface aggregate structure depicted on the top right panel of Figure 3-xii is obtained when the LJ interaction parameter used is $2\varepsilon_1$. The increase in the head groups' hydrophilicity is responsible for changing the morphology of the surface aggregates, which now resemble straightened multiple layers. Further increasing the head group-water interaction strength, we observed gradual transition of the surface aggregate structure from multiple layers to 'raising pancakes' obtained for LJ parameters of $3\varepsilon_1$ (lower left panel) and to perfect hemi-cylindrical aggregates obtained for LJ parameters of $4\varepsilon_1$, as depicted in the lower right panel of Figure 3-xii.

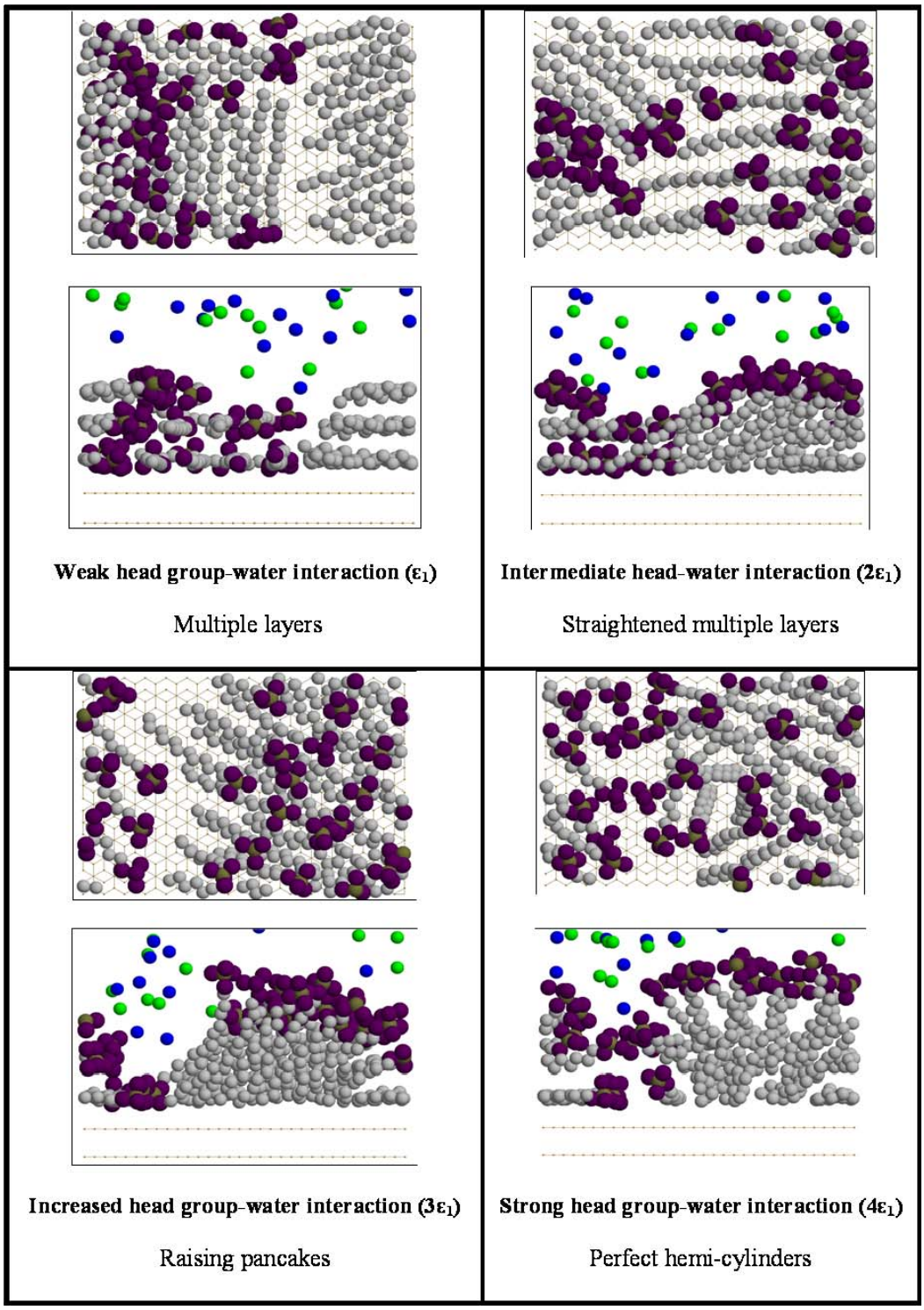

Figure 3-xii: Representative simulation snapshots for nonionic SDS-like surfactants with varying head group-water interactions. In each panel we provide a top (above) and lateral (bottom) view of the simulation snapshot obtained for nonionic SDS-like surfactants on graphite surface. Carbon, sulfur, oxygen, sodium and chlorine atoms are shown as grey, olive green, maroon, blue and green colored spheres respectively.

Perfect hemi-cylinders are observed only when strong head group-water van der Waals interactions are considered. In this case the water molecules are strongly attracted to the surfactant heads, thus the effective area for head groups increases when compared to the simulations of SDS reported above. In the case of SDS surfactant the coulombic charges present on the head groups introduce hydrophilicity, but the effective surface area per head group decreases due to the counterion-condensation phenomenon illustrated in Figure 3-ix and Figure 3-x.

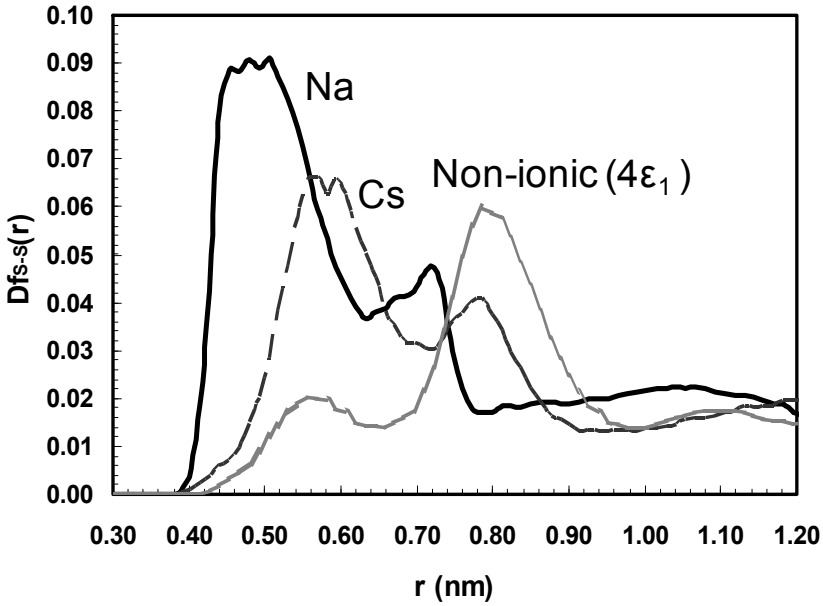

Figure 3-xiii: Sulfur – sulfur distribution function. Continuous black line represents the distribution function obtained for the surface aggregate with sodium counterion, dotted black line for cesium counterion and continuous grey line for nonionic SDS-like with strong head group-water attraction ($4\varepsilon_1$) respectively.

To quantify the differences between the surface aggregates obtained for SDS surfactants in the presence of Na^+ counterions or in the presence of Cs^+, as opposed to those obtained in the case of nonionic SDS-like surfactants with strong head group –

water interactions (4 ε_1), we calculated the S-S distribution function, which is reported in Figure 3-xiii. It is evident from Figure 3-xiii that the distribution functions obtained in the three simulations differ both in location and intensity of the peaks. The first peak is more intense than the second in the case of SDS surfactants in presence of Na^+ and Cs^+ counterions, while the second peak is more intense than the first in the case of SDS-like nonionic surfactants. The effect of counterion size can be observed from the difference in the location of the first peak when counterions are either sodium or cesium. In fact, the position of the first peak in the presence of sodium counterion is ~0.45 nm and it increases to ~0.56 nm in the presence of cesium counterions, suggesting that the 'effective' size of the surfactant heads depends on the nature of the counterions. When the nonionic SDS-like surfactants are considered, the first peak in the S-S distribution function is not well pronounced, a result that we ascribe to the absence of counterion-condensation phenomena. Because the head groups strongly attract water molecules, not many head groups can be found within a distance of 0.45 nm from a sulphur atom, which corresponds to the location of the first peak. The presence of few surfactants at smaller center-to-center distances results in an intense second peak which appears at center-to-center distances of ~0.8 nm.

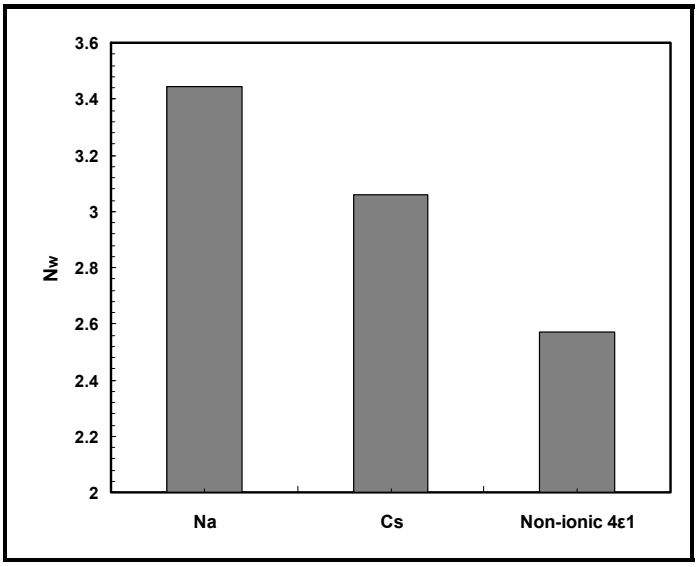

Figure 3-xiv: Average number of water molecules (N_w) within a radius of 0.5 nm from any of the 5 methyl groups farthest away from the surfactant heads. N_w for SDS surfactants in the presence of Na^+ and Cs^+ counterions, is compared to that for nonionic SDS-like surfactants with strong head group – water interactions ($4\varepsilon_l$).

We also computed the number of water molecules present within the first shell of the head groups (referred to as the hydration number) for both ionic and nonionic surfactants. This was done by integrating the sulfur (surfactant head)-oxygen (water) radial distribution function to its first local minima. The hydration number for SDS at graphite-water interface in the presence of sodium counterions yields 10.5 water molecules within the first shell. The increase in hydration number for surface aggregates on graphite compared to the air-water interface is due to the curvature of the aggregate on graphite surface. When the sodium counterions are replaced by cesium ions the hydration number drops to 7.25, indicating that, because of the larger size of Cs^+ compared to Na^+ ions, fewer water molecules can fit near the surfactant heads. The hydration numbers for nonionic SDS-like surfactants strongly depend on the head group-water interaction strength. Our results indicate that 2.4 water molecules are found within the first solvation shell when the well-depth is ε_1, 7.4 when well-depth is

$2\varepsilon_1$, 13.2 for $3\varepsilon_1$, and 20.0 when well-depth is $4\varepsilon_1$. These results are quite interesting because they suggest that the effective size of the surfactant heads (which is due to the association of water and/or counterions to the surfactant heads) determines the morphology of the surfactant aggregate at solid-liquid interfaces.

We finally quantified the average number of water molecules found in contact with the last 5 methyl groups in the surfactant tails in the various cases considered. The results are shown in Figure 3-xiv. The nonionic SDS-like surfactant with the strongest head group-water interaction is compared to the SDS surfactant when sodium or cesium ions act as counterions. As expected from the simulation snapshots shown above (compare Figure 3-v to Figure 3-xi and to Figure 3-xii), the average number of water molecules in contact with the hydrophobic surfactant tails decreases as the surface aggregates resemble more and more the perfect hemi-cylinders of Figure 3-viii.a.

3.5. Conclusions

We conducted a number of molecular dynamics simulations to study the self assembly of SDS surfactants at the graphite-water interface. We reported a comprehensive set of results obtained for surfactants adsorbed on two opposed graphite surfaces as the distance between the surfaces varies from 14.0 to 4.05 nm. We employed distribution functions between sodium and sulfur, sulfur and sulfur, as well as mean square displacement data and population distributions for the surfactant length to analyze the effect of the frontal confinement on the surface aggregates. Our results suggest the presence of surface aggregate – surface aggregate interactions when the distance between opposing graphite surfaces is less than 10.0 nm. At separations

approaching twice the surface aggregate thickness we observe an effective attraction between head groups of surfactants adsorbed on the opposing surfaces. At separations above four times the surface aggregate thickness (> 8 nm) the surface structures do not seem to depend on the presence of surfactant aggregates on the opposing surface.

Within the limitations of the state-of-the-art computational facilities, which allow us to conduct all-atom molecular dynamics simulations for up to 10-20 ns in systems as complicated as those considered here, the morphology of the surfactant aggregates was studied in great detail. Our results show that when aqueous SDS surfactants are considered, counterion condensation is responsible for the formation of dense patches composed by surfactant heads and counterions. Because these patches are very dense, some hydrophobic surfactant tails remain exposed to water. When the sodium counterions are substituted with the larger cesium counterions, most of the surfactant tails are shielded from the aqueous solution and the self-assembled aggregate resembles perfect hemi-cylinder.

We conducted a parametric study on nonionic SDS-like surfactants to further unveil the role of counterion condensation on determining the morphology of the surfactant aggregates. We found a number of surface structures (layered structures, raising pancakes, and perfect hemi-cylinders) as the hydrophilicity of the surfactant head group was changed. The change of surface aggregate structure of SDS molecule from partial hemi-cylinder to perfect hemi-cylinder when sodium counterions are replaced by cesium counterions happened within ~2 ns in our simulations. The surface aggregate structure of nonionic model SDS surfactants with maximum hydrophilicity yields perfect hemi-cylinders. Even this phenomenon occurs in time scales accessible to

all-atom molecular dynamics, in this case ~2 ns. This suggests that the change in equilibrium configuration resulting with the change in force field parameters is often accessible with in 5 to 10 ns of all atom MD simulations. To test whether the imperfect hemi-cylinders correspond to the equilibrium configuration for SDS surfactants at the graphite-water interface we assigned electric charges to the model nonionic surfactants. Following this inverse procedure we obtained surfactant aggregates with morphological features statistically identical to those observed originally for SDS aggregates within 2 ns, further corroborating the correctness of the procedure employed in our simulations. The results presented here provide significant insights into the importance of counterion condensation in determining the morphology of surface aggregates of amphiphilic molecules, a phenomenon that could be employed to control self-assembly processes towards the production of structures with practical interest. Further, the distribution function provided can be used to develop coarse-grained models for studying surfactant self-assembly in larger systems.

4. Water Properties at Contact with Amphiphilic Surfaces

4.1. Abstract

Water, due to its role in biology, geology, and many industrial applications, has attracted and continues to attract extensive scientific interest. Results pertaining to bulk water as well as interfacial water are being regularly reported in the scientific literature. It has been suggested that density fluctuations near the substrates determine binding states in biology, slip conditions in fluid dynamics, and many other macroscopic phenomena. Although much is known about interfacial water, many fundamental questions still remain to be answered. In this study we report molecular dynamics simulations of water at contact with the amphiphilic molecules ionic sodium dodecyl sulfate (SDS) and non-ionic hexaethylene glycol monododecyl ether ($C_{12}E_6$). The surfactants are adsorbed at graphite-water and silica-water interfaces. We discuss density profiles of water molecules next to the various surfaces, the orientation of interfacial water molecules, and residence probability for water at contact with the various substrates. We compare our results to those previously obtained for water on silica. The goal of these simulations is to elucidate how amphiphilic molecules affect the properties of interfacial water. Our analysis will help explain the role of interfacial water structure in determining macroscopic properties such as surfactants adsorption and wettability of surfactant-covered surfaces.

4.2. Introduction

Surfactants/amphiphilic molecules are used to modify surface properties of substrates and interfaces.[5,138] The change in solvent properties close to the surface dictates resultant macroscopic substrate properties. Depending on the nature of the surfactant, its addition can result in the surface changing either into a more solvophobic or solvophilic one. Hydrophilic solid particles, and surfactant adsorption on these particles, are involved in applications ranging from mineral floatation, particle stability, detergency, deinking, etc.[76] In this study we employ the ionic sodium dodecyl sulfate (SDS) on graphite and on two silica substrates, and also the non-ionic hexaethylene glycol monododecyl ether ($C_{12}E_6$) on one silica substrate. We study the effect of the two surfactants on the behavior of the interfacial water molecules.

Water molecules next to different surfactant aggregates in the bulk have been studied experimentally[197-206] and through simulations.[117-118,188] The effect of different headgroups of self assembled monolayers on interfacial water was studied extensively.[140,207] On the contrary, the molecular level properties of water molecules next to surfactants at different solid-liquid interfaces did not get much attention. Surfactants can aggregate on a surface, causing a decrease in the density of interfacial water molecules. However, changes in local density do not necessarily imply changes in the properties of individual interfacial water molecules. Similarly, when surfactants do not completely adsorb on a surface, the density of interfacial water molecules can be unperturbed, but rotation, orientation, and translational dynamics of interfacial water molecules can differ significantly compared to the properties of interfacial water without surfactants.

Much is known about the aggregation of SDS on graphite and carbon nanotubes through experiments and simulations.[35,69-72,87,187,208] The aggregate morphology of cationic surfactants on silica has also been studied through experiments[209-212] and simulations.[185,213] Experimental results for the ionic and non-ionic surfactants at hydrophilic solid-water interface were reviewed in an article by Paria et al.[76] It is known from experiments that SDS does not adsorb significantly on like-charged oxide surfaces,[25,214-215] except when surfactant formulations are used.[40-41] No thorough molecular-level understanding has been obtained for SDS on charged oxide surfaces. Similarly, experimental studies for $C_{12}E_6$ and non-ionic surfactant mixtures on silica substrates are available,[81,89,216-217] but the molecular-level understanding of the aggregates structure as a function of surface protonation is currently lacking. This encouraged us to study the aggregation of amphiphilic molecules on silica surfaces. Further, understanding the change in the properties of water molecules near charged surfaces, like silica, due to the presence of surfactants will lead to better surface modification techniques, for applications involving super-hydrophobic or super-hydrophilic surfaces, and for the specific hydration of biological molecules and membranes.

Vibrational sum frequency generation (VSFG), and a few VSFG variants, have been widely used to study water at interfaces.[218] Adsorption[83,90] and scattering experiments[40,81,98,101,216,219-220] are performed to determine the structure of the adsorbed surfactant layers. Although water structure and adsorbed morphology of surfactants involve different time and length scales, we can evaluate both phenomena by conducting sufficiently long molecular dynamics simulations. Such calculations have

been performed to study separately, the aggregate structure of surfactant aggregates and the properties of interfacial water.[117-118] [69,208,221] We here show both aspects simultaneously.

Our results are quantified in terms of water density profiles near the various surfaces. Even though the peaks in density profiles cannot be used as signature for the hydrophobicity or hydrophilicity of the substrates,[140] the change in the density profiles in correspondence with surfactant adsorption will provide interesting information. We also report dipole moment distribution of water molecules next to the amphiphilic interfaces, residence probability for water molecules at the surface, and hydration structure of the headgroups of both ionic and nonionic surfactant.

4.3. Simulation Methodology

Molecular dynamics simulations were conducted using the Groningen Machine for Chemical Simulations (GROMACS) 4.0.5 simulation package.[133-135,222] Water was simulated using the extended simple point charge (SPC/E) model.[126] The force field employed for simulating $C_{12}E_6$ and SDS are described in our previous publications[208,223] and also in chapter 2 and chapter 3, respectively. SDS contains an anionic sulfate group with 4 oxygen atoms bearing partial negative charges. One oxygen atom connects the sulfur atom to the carbon of the tailgroup. The other 3 oxygen atoms are bonded only to the sulfur. The sodium ions are always dissociated. In $C_{12}E_6$, the ethylene oxide (EO) groups in the hexaethylene glycol headgroups are charged, the $-CH_2$ groups have a partial point charge of +0.25e, and the oxygen atom in the EO group has a partial charge of -0.5e. SDS surfactants were simulated on graphite, low density (LD) silica (~4.5 OH

/nm^2), and high density (HD) silica (~13.6 OH/nm^2) surfaces obtained from (1 1 1) β-cristobalite. $C_{12}E_6$ surfactants were simulated only at contact with the LD silica surface. As described previously by our group,[221,224] we can obtain surfaces with 13.6 (HD silica) or 4.5 (LD silica) non-bridging oxygen atoms per nm^2 by cutting the β-cristobalite crystal along the (111) face at different depths. Following Pellenq and Puibasset,[225] all the silicon atoms that are bonded to less than four oxygen atoms were removed, and the unsaturated non-bridging oxygen atoms (bonded to only one silicon atom) were saturated with one hydrogen atom positioned rigidly at 1 Å perpendicular from the surface. We simulated HD and LD silica surfaces with three degrees of surface hydrogen atoms or protonation (100%, 50%, and 20%). In the case of the HD silica, the three degrees of protonation correspond to 13.6, 6.8, and 2.72 OH/nm^2, respectively. On the LD silica they correspond to 4.5, 2.25, and 0.90 OH/nm^2. The various surfaces considered are denoted as LD_100, LD_50, LD_20, HD_100, HD_50, and HD_20. The surface density of the non-protonated non-bridging oxygen atoms are zero per nm^2 on HD_100 and LD_100 surfaces, 6.8 and 2.25 per nm^2 on HD_50 and LD_50 surfaces, 10.88 and 4.6 per nm^2 on HD_20 and LD_20 surfaces, respectively. For simulations involving partially protonated silica we introduce sodium ions to neutralize the total system charge. In all silicon surfaces all the atoms bear partial atomic charges. Silicon and hydrogen atoms are positively charged; bridging and non-bridging oxygen atoms are negatively charged. The partial charges and interaction parameters employed are those used previously by our group, as well as by others.[221,225] The graphite substrate was 3 graphene-sheets thick; the silica substrates were 2.0 nm thick.

The simulation protocol involves placing SDS surfactants perpendicularly to the solid substrate with the headgroups away from the surface. The sodium ions were placed close to the headgroups, and the water molecules above the sodium ions, away from the substrate. Above the water layer there was a slab (6.0 nm thick) of vacuum followed by a solid substrate. Detailed descriptions are provided in Ref [[70,208]]. For $C_{12}E_6$ surfactants on LD silica, the equilibrium configuration obtained earlier at the water-vacuum interface[223] was transferred to the silica-water interface and allowed to equilibrate. All simulations were conducted in the canonical ensemble in which the number of particles (N), the box volume (V) and the temperature (T) were kept constant. T was maintained constant using the Nose-Hoover thermostat with a relaxation time of 100 fs. All simulations were conducted at T=300 K.

Dispersive forces were computed using the Lennard-Jones potential with an inner cutoff of 0.8 nm and outer cutoff of 1.0 nm. Long range electrostatic interactions were treated using the particle mesh Ewald (PME)[137] method. Periodic boundary conditions were implemented in all three dimensions. The simulations were considered equilibrated when the density distribution of surfactants and water molecules obtained from two different 5 ns intervals during the same simulation showed no deviation. All the simulations were carried out for a minimum of 45 ns. The simulation trajectories from the last 5ns were used for calculating the results.

A box of size 5.041x5.267x22.00 nm^3 was used for SDS on silica, which resulted in an available surface area of ~0.48 nm^2 for each SDS. The distance between the non-bridging oxygen atoms of the two surfaces across the simulation box were 14.4 nm and 14.2 nm for simulations involving SDS on LD and HD silica, and 25.2 nm in

the case of $C_{12}E_6$. The box size of 10.082x9.605x31.00 nm^3 used for simulations involving $C_{12}E_6$ on silica resulted in ~0.54 nm^2 per each $C_{12}E_6$ surfactant. Simulation details for SDS surfactants on graphite are described in our previous publication.[70] The box size was selected such that the box length along each dimension is greater than twice the extended length of the surfactant. In Figure 4-i we show a typical simulation box with aqueous SDS surfactants on the HD silica surface. In the left panel it is shown the starting configuration and on the right the configuration obtained after 50 ns of simulation.

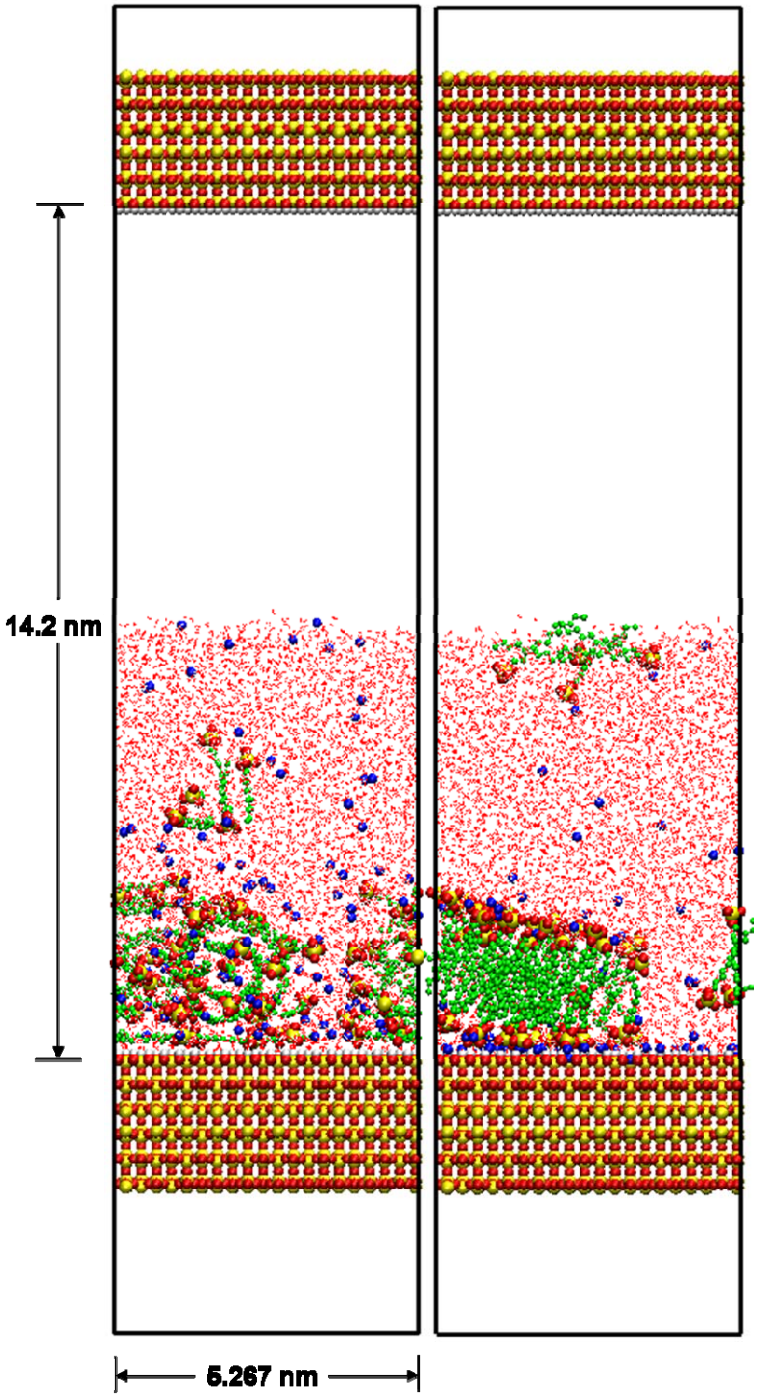

Figure 4-i: Typical simulation box. Left panel: starting configuration of aqueous SDS surfactants on HD_50 silica surface. Right panel: configuration after 50 ns of MD simulation at 300 K. Green, red, orange, yellow, white, and blue spheres represent methyl groups, oxygen, sulfur, surface silica, surface hydrogen, and sodium atoms respectively. Red lines are water molecules in the wireframe representation.

4.4. Results

4.4.1. Surfactant Aggregate Morphology

We report the surfactant aggregate morphology on the solid surfaces before we discuss the effect of the surfactants on the interfacial water. Results for SDS surfactant aggregates on graphite have been published before.[70-71,187,208] In short, SDS surfactants form hemi-cylindrical aggregates on graphite at coverages of 0.40-0.45 nm^2 per surfactant. At lower surface densities (e.g., 1.0 nm^2 per headgroup) SDS yields monolayers with most tailgroups oriented along the primary axis of graphite.[35,70-71,208] The structure of SDS and $C_{12}E_6$ aggregates on silica as obtained by simulations has not been previously reported. In Figure 4-ii, the density distribution of surfactant headgroups and tailgroups as a function of the distance perpendicular to the surface are reported for $C_{12}E_6$ on LD silica. The density distributions for headgroups, tailgroups, and sodium counterions for SDS on both LD and HD silica surfaces are also reported in Figure 4-ii. Headgroups and tailgroups are sulfate and dodecyl groups, hexaethylene glycol and dodecyl groups for SDS and $C_{12}E_6$, respectively. The density distributions showed in Figure 4-ii was computed considering the position of individual atoms/segments (-CH_3 or –CH_2 or –O or –S) in each tailgroup or headgroup and the resultant density was normalized with the number of segments in each headgroup (19 and 5 in $C_{12}E_6$ and SDS) or tailgroup (12 in $C_{12}E_6$ and SDS).

Unexpectedly, we find from Figure 4-ii (top left panel) that the majority of the hydrophobic $C_{12}E_6$ tailgroups are located next to the LD_100 surface. This result appears counter-intuitive because it was expected that the non-ionic hydrophilic headgroups of $C_{12}E_6$ would be attracted towards the hydrophilic LD_100 silica.[76] We

believe that the mismatch of spatial distribution of electrostatic charges on the silica surface and the ethylene oxide (EO) groups of $C_{12}E_6$ results in such aggregate morphology. The intensity of density distribution from 0 Å to 10.0 Å for $C_{12}E_6$ tailgroups on the LD_100 surface is higher than that observed for $C_{12}E_6$ tailgroups on LD_50 and LD_20 surfaces. The intensity of $C_{12}E_6$ tailgroups density is higher on the LD_50 and the LD_20 surfaces from 10.0 Å to 20.0 Å than on the LD_100 silica. The intensity of the first peak in the $C_{12}E_6$ tailgroup density profiles decreases with the decrease in the density of surface hydrogen atoms. Correspondingly, the $C_{12}E_6$ headgroups density distribution (top right panel in Figure 4-ii) shows the highest number of EO headgroups near the LD silica-water interface when only 20% of the non-bridging oxygen atoms are protonated. The density of EO headgroups close to the silica-water interface is the least on the LD_100 silica. Further, at 10.0 Å to 20.0 Å from the surface, the density of EO headgroups is the highest on LD_100 surface, indicating that on this surface the $C_{12}E_6$ headgroups are in part immersed in the aqueous phase.

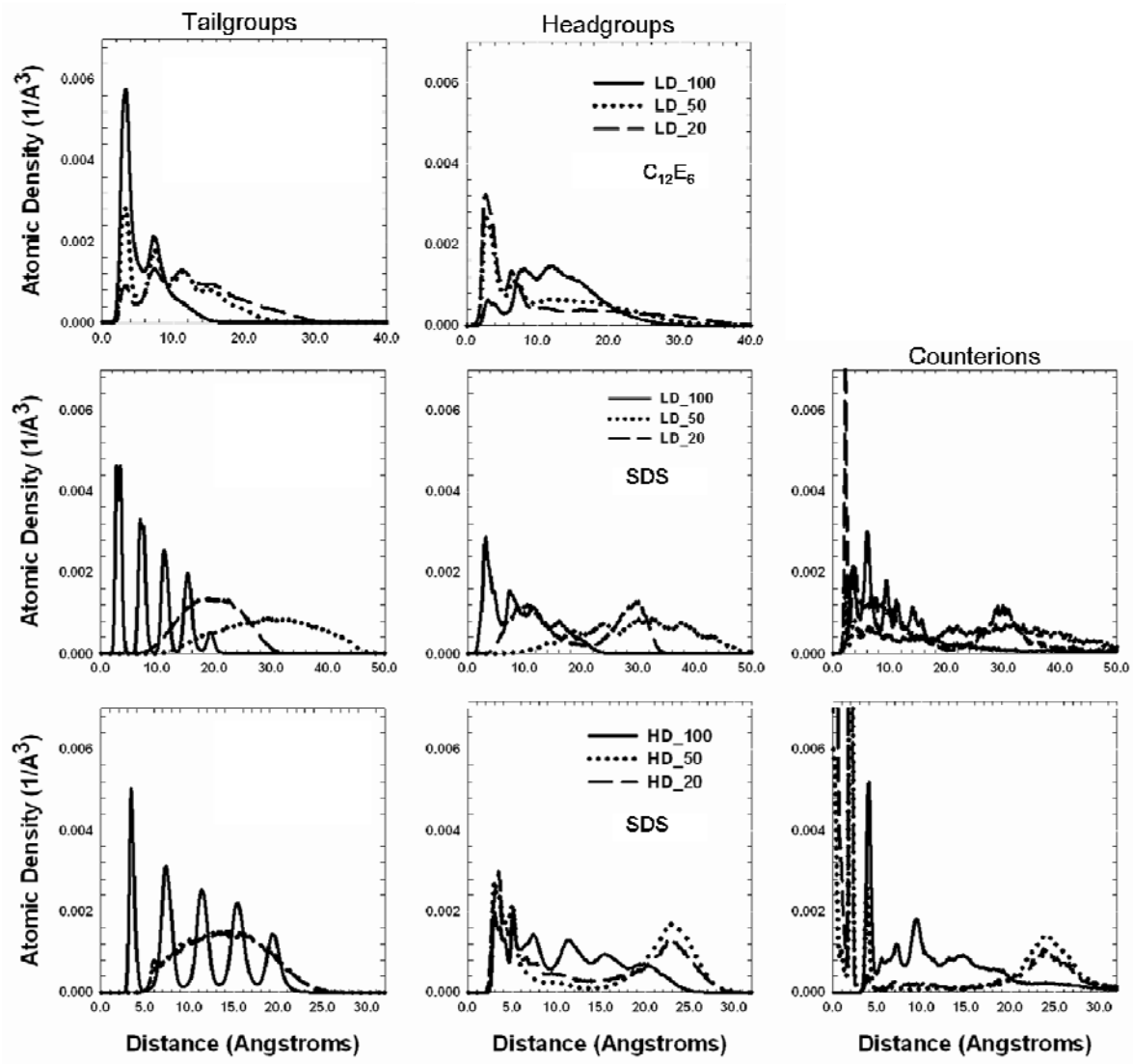

Figure 4-ii**:** Density distribution of tailgroups and headgroups away from the solid surface for $C_{12}E_6$ on LD silica (top panels), for SDS on LD silica (middle panels), and SDS on HD silica (bottom panels). Density profiles for counterions of anionic SDS surfactant are also reported in the bottom and middle right panels.

It is widely known that the anionic SDS does not adsorb on negatively charged surfaces, whereas it adsorbs on positively charged ones.[76] In agreement, we observe adsorption of SDS on completely hydroxylated HD and LD silica surfaces, where multiple layers are formed (see middle and bottom panels of Figure 4-ii). On LD_100 we observe multiple layers of SDS tailgroups (middle left panel of Figure 4-ii) oriented parallel to the surface. On LD_50 the surfactant aggregate assumes a globular structure

that remains within the water phase at ~10.0 Å away from the substrate. The homogenous distribution of tailgroups density from ~10.0 Å to ~45.0 Å, indicates the formation of micellar aggregate and that within the aggregate SDS tailgroups do not significantly overlap (extended length of SDS tailgroup is ~18.0 Å). The surface aggregate of SDS on LD_20 silica is closer to the surface compared to that observed on LD_50. The density distribution of the tailgroups from ~10.0 Å to ~30.0 Å (see center-left panel of Figure 4-ii) indicates that SDS yields a bilayer with overlapping tailgroups on this substrate. The formation of a bilayer with overlapping tails is confirmed by the peaks in the density distribution of headgroups on LD_20 surface (middle-center panel in Figure 4-ii) located at 10.0 Å and 30.0 Å. Although our result does not agree with experiments for SDS on silica surface,[226] surface aggregates similar to those obtained herein are observed for SDS on positively charged alumina.[18,227] We attribute this difference to the excessive sodium ions employed within the system to compensate for the surface hydrogen atoms. Those sodium ions render the surface positively charged at a few locations, enabling the adsorption of anionic SDS surfactants on LD_20 silica. The SDS headgroups density profiles on LD_100 and LD_50 are consistent with the formation of multiple layers and globular micellar structure on the two substrates.

The location of counterions on LD silica surfaces is shown in the middle-right panel of Figure 4-ii. On LD_50 and LD_20 surfaces, due to the net negative surface charge, sodium ions accumulate next to the solid, whereas on LD_100 the sodium ions are attracted towards the SDS headgroups. As mentioned in our previous articles, [70,208] the density profiles of SDS headgroups and sodium counterions exhibit similar trends, especially next to surfaces, because of counterion condensation phenomena.

On HD_100 SDS surfactants yield multi-layered structures similar to the ones observed on LD_100. On HD_50 and HD_20 surfaces, we observe structures resembling bilayers similar to the aggregates observed on LD_20. The SDS aggregates on HD_50 and HD_20 are closer to the surface than those on LD_20. SDS tailgroups and SDS headgroups are found closer to the LD_100 silica surface rather than the HD_100. On HD surfaces, the density of non-bridging oxygen atoms on the surface is higher than that on LD surfaces. Consequently short-ranged electrostatic repulsion between negatively charged sulfate headgroup of SDS and non-bridging oxygen atoms of silica compete with the electrostatic attraction between positively charged surface hydrogen atoms and oppositely charged surfactant headgroups.

The presence of sodium ions can attract surfactant headgroups to the surface on partially protonated silica surfaces. The surface charge density on the silica surface gradually decreases from being positive when all non-bridging oxygen atoms are protonated to neutral at point of zero charge, and it is negative on silica when none of the non-bridging oxygen atoms is protonated. The negative charge density is higher on HD surfaces than on LD ones. Consequently, more sodium ions accumulate on the HD surface and drag the surfactant headgroups closer to the surface. Because of the large number of Na^+ ions on both HD_50 and HD_20 surfaces, SDS aggregates obtained on these substrates are very similar to each other. The results just discussed seem to suggest that counterion condensation is crucial in determining the structure of SDS aggregates near charged substrates.

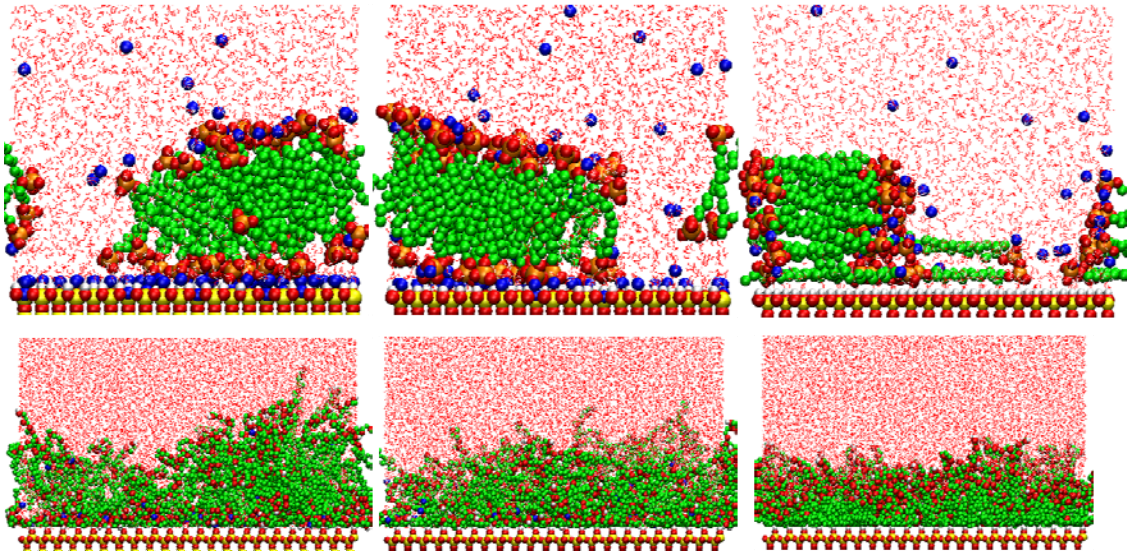

Figure 4-iii**:** Typical simulation snapshots for SDS and $C_{12}E_6$ aggregates on HD and LD silica (top and bottom panels, respectively). Left panels are for 20% hydroxylated, middle panels 50% hydroxylated, and right panels are completely hydroxylated silica surfaces. Green, red, orange, blue, yellow, and white spheres represent methyl groups, oxygen, sulfur, sodium, surface silicon, and surface hydrogen atoms respectively. Water molecules are shown in the wireframe representation (red lines).

In Figure 4-iii we show representative simulation snapshots of SDS on HD silica and $C_{12}E_6$ on LD silica surfaces that complement the information provided in the above discussion.

On HD silica we observe a patchy adsorption of SDS molecules, we also observe ~8% of SDS molecules migrating to the vacuum-water interface and remaining there for the entire period of the simulation. Since the surfactants headgroups are adsorbed on the surface due to the presence of sodium counterions on the surface, the dynamic displacement of the counterions and the patchy network of surface hydrogen atoms yield a patchy adsorption of SDS. A mechanism similar to the one just discussed has been proposed to describe the adsorption of anionic surfactants on alumina.[25,215] The number of SDS surfactants used in our simulation corresponds to that of full-monolayer coverage. However, as SDS surfactants form multiple layers we observe

patches of surface not covered by surfactants. On HD_100 and LD_100 silica we observe multiple layers with SDS surfactants parallel to the surface. SDS molecules remain perpendicular to the surface on partially protonated silica surfaces. This indicates that when the surface is completely protonated only two out of the three terminal oxygen atoms of the sulfate headgroup (the most negatively charged oxygen atoms in sulfate group) are adsorbed close to the surface hydrogen; on the contrary, when counterions adsorb on the surface (i.e., on partially protonated surfaces) all the three terminal oxygen atoms of sulfate headgroup are located next to the sodium ions. The differences in the electrostatic interaction between SDS headgroups and the surface atoms and sodium ions result in the observed changes in the morphology of SDS aggregates.

Representative snapshots of $C_{12}E_6$ aggregates on LD_20, LD_50 and LD_100 silica surface are also shown in Figure 4-iii. For $C_{12}E_6$ on LD_100 it is evident from snapshots that the tailgroups are adsorbed (bottom panels) on the LD_100 surface, whereas on LD_50 and LD_20 surfaces, we observe $C_{12}E_6$ headgroups on the surface and $C_{12}E_6$ tailgroups oriented away from it. The density of $C_{12}E_6$ headgroups close to the surface increases with the decreasing density of surface hydrogen atoms.

In Figure 4-iv, we show one enlarged view of the first layer of $C_{12}E_6$ surfactants on LD_100 and LD_20 surfaces to highlight the orientation of headgroups and tailgroups with respect to the surface hydrogen atoms. On LD_100 surface (left panel in Figure 4-iv), the $C_{12}E_6$ tailgroups (thick green lines) are found parallel to the surface hydrogen atoms (white spheres) and occupy the space between them. Visual inspection of simulation trajectories and density profiles indicate that SDS and $C_{12}E_6$ tailgroups are

mostly adsorbed only on LD_100 and HD_100 surfaces. On LD_20 (right panel) sodium ions (blue spheres) adsorb on top of non-bridging oxygen atoms (small red spheres). $C_{12}E_6$ headgroups coil around sodium ions so that the negatively charged oxygen atoms (large red spheres) in the $C_{12}E_6$ EO groups are close to the sodium ions and the cationic methyl groups (thick green lines in between the large red spheres) remain far from them. We would like to point out that we only observe coiling of $C_{12}E_6$ headgroups next to sodium ions when adsorbed on top of non-protonated non-bridging oxygen atoms, but never next to surface hydrogen atoms.

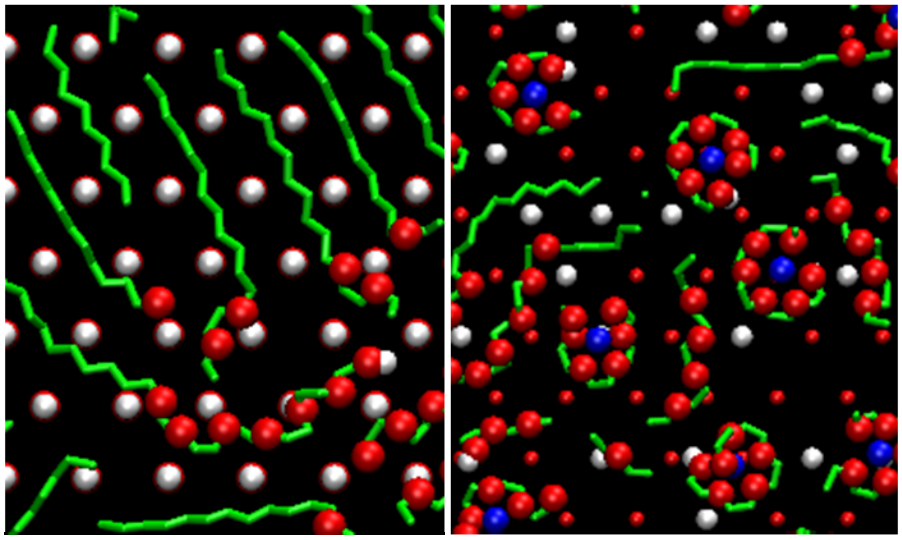

Figure 4-iv**:** Enlarged view of simulations snapshots for $C_{12}E_6$ surfactants on LD_100 (left) and LD_20 (right) surface. The color code is the same as that in Figure 4-iii. Surface silicon atoms are not shown for clarity and surfactant tailgroups are shown in the licorice representation. In the right panel smaller red spheres represent non-bridging oxygen atoms within the silica surface.

4.4.2. Orientation and Distribution of Water Molecules

In Figure 4-v we show the atomic density profiles for the oxygen atoms of water molecules (right panel) and the ensemble average of the z-component of their dipole

moment (M_z) as a function of the distance perpendicular from graphite (left panel). The dipole moment vector in our calculations is pointing away from the hydrogen atoms, i.e. towards the oxygen. M_z fluctuates around zero when the orientation of water molecules is isotropic. A positive M_z corresponds to hydrogen atoms of water molecules oriented towards the surface, and negative M_z indicate that water molecules are arranged with those hydrogen atoms pointing away from the surface. In the absence of surfactants (green dash-dot-dot line), we observe an intense peak for the density of oxygen atoms at ~3.3 Å, corresponding to a maximum in the z-component of the dipole moment. This indicates that most of the water molecules whose oxygen atoms are at ~3.3 Å from the surface adopt an orientation in which one hydrogen points towards the surface. This result is consistent with those reported in the literature.[221,228-229] As SDS surfactants adsorb on graphite, both density and orientation of interfacial water molecules change. At surface coverage close to 100.0 $Å^2$ per surfactant, SDS yields a monolayer. At this surface coverage, we observe a density peak for oxygen atoms of water molecules at ~3.5 Å (solid line in the right panel of Figure 4-v), although the overall density at the interface is much less than observed in the absence of the surfactants. The intensity of this peak decreases as the surfactant concentration increases, because as the SDS adsorbs water is expelled from the interfacial region.

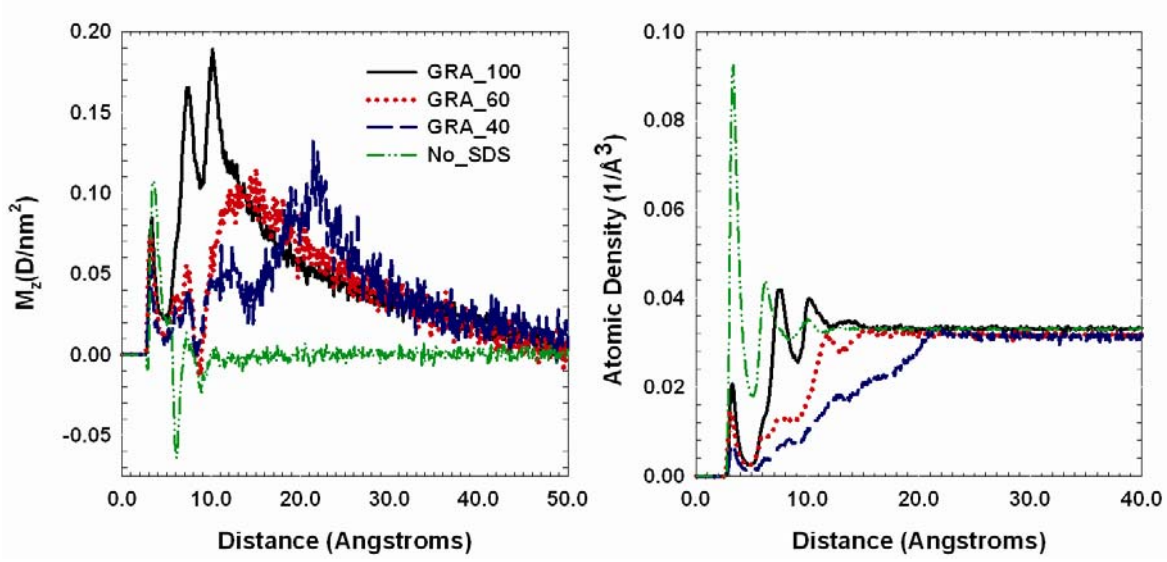

Figure 4-v**:** (Left panel) z-component of dipole moment vector of water molecules as a function of the distance away from graphite. (Right panel) Density profiles of oxygen atoms of water molecules. Results are shown at increasing concentration of SDS. GRA_X corresponds to graphite surface with X Å^2 available surface area per surfactant.

The presence of SDS phenomenally changes the orientational profile of interfacial water. In the absence of SDS, we observe structured layers of water molecules, i.e. a first layer with hydrogen-down (towards the surface) orientation, a second layer with hydrogen-up orientation. When SDS surfactants are present we do not observe any hydrogen-up orientation. Since adsorbed SDS surfactants are anionic, the negatively charged oxygen atoms of water are predominantly oriented away from the graphite surface. The positive peaks in the z-component dipole moments correspond to layers of water that form next to the SDS headgroups. These layers are spaced away from the graphite surface as the SDS surface concentration increases. These results can be explained when we recall that as the SDS aggregate morphology changes, with the increased SDS surface density, the location of SDS headgroups with respect to the surface also changes. Water molecules are strongly correlated to the SDS headgroups. From the z-component of the dipole moment, we observe that interfacial water

molecules show a perturbed orientation for up to 5.0 nm from the surface when SDS surfactants are present. This result is more impressive when we notice that in the absence of SDS water recovers bulk-like features at 1.0-1.5 nm from the graphite. Similar orientational effects were observed for water in the presence of anionic and cationic surfactants at the air/water interface.[230-231] The presence of SDS headgroups on graphite makes the surface charged, and it is known that charged surfaces have long range effects on the orientation of water and dipolar liquids.[232-233]

In Figure 4-vi, we report the density distribution and the z-component of the dipole moment for water molecules next to silica surfaces in the presence of either ionic or non-ionic surfactants. For comparison, in the insets of Figure 4-vi we show the density distribution and the orientation of water molecules on HD and LD silica substrates in the absence of surfactants as reported previously in Ref [[234]]. The surface coverage of SDS and $C_{12}E_6$ surfactants on the silica surfaces considered is ~1.8 surfactants/nm^2.

On bare HD_100, in the absence of surfactants, we observe two intense peaks in the density profile of water molecules (solid line in the inset of the top-left panel of Figure 4-vi) corresponding to the large number of interfacial water molecules on this hydrophilic surface. The properties of interfacial water on HD and LD silica surface have been described in details elsewhere.[224,234] The intensity of the first peak in the density profiles for water on LD_100 (dotted line in the inset of the top-left panel) is less than that observed on HD_100 even though both surfaces show macroscopic hydrophilic features.[235] On the top-left panel of Figure 4-vi we report the density profiles in the presence of SDS (on HD_100 and LD_100) and $C_{12}E_6$ (on LD_100). The

difference between the intensity of the first peaks in the density profiles on HD_100 in the absence and presence of SDS is ~16%, not very significant considering that 2.0 SDS surfactants per nm^2 are present on the surface. The difference in the intensity of the second peaks in the density profiles in the absence and presence of SDS is much more pronounced. One important observation is that the location of the peaks in the density profiles does not change with increasing SDS concentration. This can be explained by recalling that SDS does not significantly adsorb on HD_100, and hence cannot influence the interfacial water molecules. A depletion of water molecules is observed from 5.0 Å to 25.0 Å from the surface because of the presence of SDS. At larger distances the density of interfacial water approaches bulk values.

On LD_100, the first peak intensity in the density profile decreases by almost 50% when SDS is present. The intensity of the second peaks is also reduced by SDS. Even the peak positions change (compare the dotted line in inset of the top-left panel to the dotted line in the top-left panel).

On HD_100 (solid line in bottom-left panel of Figure 4-vi) we observe an insignificant decrease in the intensity of the first peak in M_z compared to the first peak in the inset, suggesting that the orientation of water molecules in the first layer does not change in the presence of SDS. The strong organization of water molecules within ~6.0 Å is preserved on HD_100 with SDS, whereas on LD_100 with SDS only water molecules in the first layer retain their orientation when compared to water molecules on bare LD_100. The hydrogen-up orientation observed on the bare LD_100 (~ at 3.0 Å) is absent when surfactants are present, indicating that SDS does effect the orientation of water molecules on LD silica.

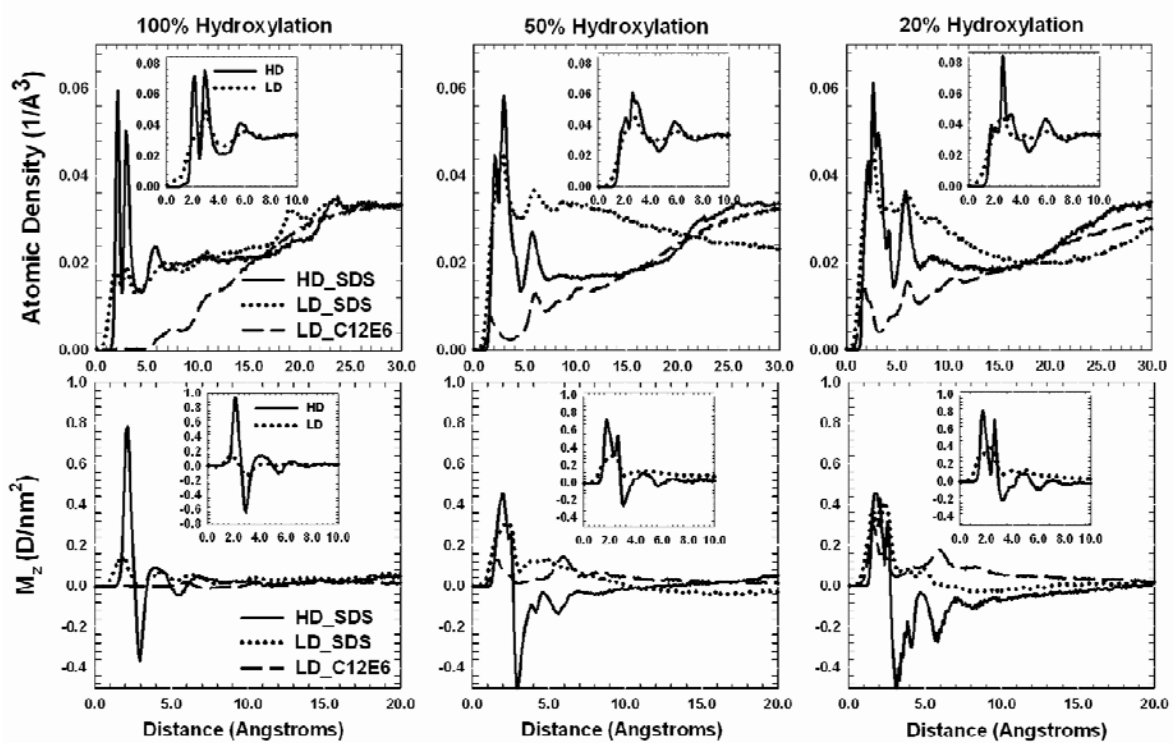

Figure 4-vi**:** (Top panels) Density profiles of water molecules away from the solid surface for aqueous SDS and $C_{12}E_6$ on HD and LD silica surfaces. Shown in the inset are the density profiles of water molecules on bare HD and LD silica surface. (Bottom panels) z-component of the dipole moment vector, normalized over the surface area, for interfacial water molecules as a function of distance from the surface for HD and LD silica with aqueous SDS and $C_{12}E_6$. Shown in the insets are the normalized z-component dipole moments of water molecules at HD silica-water and LD silica-water interfaces with no surfactants present. The left panels are for 100% protonated, middle panels for 50% protonated and right panels for 20% protonated HD and LD silica, respectively.

On HD_50, the second peak in the density profile (top-center panel of Figure 4-vi) shows a pronounced decrease due to the presence of SDS, while the first peak in the density profile shows little or no change. This result confirms that SDS does not affect the properties of water on HD silica at any degree of protonation. On LD_50 with SDS, the density of interfacial water is the same as that observed on bare LD_50 (compare dotted line in inset of top-center panel to the dotted line in top-center panel).

Farther away from the LD_50 surface, we observe a decrease in the density profile confirming the presence of SDS aggregates in water, as discussed above.

The results just discussed indicate that although the presence of SDS on HD_50 does not induce any significant density change in the interfacial layer, the change in the orientation of interfacial water molecules is pronounced. The M_z distribution for interfacial water on HD_50 with SDS has two major changes when compared to the M_z profile for interfacial water in the absence of SDS. The intensity of the first peak, signature of the hydrogen atoms of water pointing towards the surface, decreases. Because, the sodium counterions adsorb on the surface (from Figure 4-ii) the oxygen atoms of water molecules point towards the surface. The presence of sodium ions also results in the increased intensity in the negative peak at 3.0 Å (compare solid line in inset of bottom-center panel to the solid line in bottom-center panel of Figure 4-vi), indicating that the hydrogen atoms of water molecules are oriented away from the surface. The multiple positive peaks of M_z at ~2.0 Å for water on HD_50 surface almost vanishes with SDS. Instead, we observe multiple negative peaks at ~ 4.0-6.0 Å, where in the absence of SDS we observe a smooth transition from negative to positive peaks. The intense negative peak (solid line in the bottom-center panel in Figure 4-vi) corresponds to the peak in the density profile at ~3.0 Å other negative peaks correspond to shoulder and peak found at ~4.5 and ~6.0 Å respectively. On LD_50 silica the interfacial water molecules remain unperturbed in the presence of SDS, and the orientation of water molecules is similar to that observed on bare LD_50.

On HD_20 surface in the presence of SDS, we observe multiple peaks at multiple locations in the density profile (top-left panel in Figure 4-vi). High

concentration of sodium counterions next to the HD_20 surface results in the multiple peaks at 3.0 and 4.0 Å away from HD_20 surface (solid line in top-right panel of Figure 4-vi). On LD_20 surface with SDS, the oxygen density profile (dotted-line in top-left panel) is qualitatively similar to that observed on LD_50 surface in the presence of SDS, however with different peak intensities. The features in M_z profile of water molecules on bare HD_20 surface are similar to that observed on HD_20 surface with SDS (compare solid-line in the inset of bottom-left panel and the solid-line in the bottom-left panel), indicating that the presence of SDS has little effect on the orientation of the interfacial water molecules especially the first layer of water molecules on HD surfaces. However, we observe a rather insignificant enhancement in the structuring of water molecules at 4.0-6.0 Å away from the HD_20 silica. On LD_20, in the presence of SDS, the M_z profiles are not strikingly different from that observed on M_z profile of water molecules on bare LD_20.

We observe more pronounced change in the density profile when $C_{12}E_6$ is present on LD_100. As discussed before, we observe $C_{12}E_6$ tailgroups next to LD_100 silica, suggesting a depletion of water. On LD_100 in presence of $C_{12}E_6$, M_z profile as a function of the distance from the surface is close to zero suggesting no preferential orientation of the interfacial water molecules, except for a small perturbation at ~5Å. The near zero profile of M_z at distances away from the surface, where most of the $C_{12}E_6$ headgroups are located, also indicates that the presence of $C_{12}E_6$ headgroups does not preferentially orient the water molecules located next to them. On LD_50, in the presence of $C_{12}E_6$, we observe a significant depletion for interfacial water but not as pronounced when compared to that of the interfacial water on LD_100 with $C_{12}E_6$ (as

observed from the density profiles of Figure 4-vi). The density profile on LD_50 in the presence of $C_{12}E_6$ reaches that of the bulk water at ~30.0 Å from the surface. M_z profiles of interfacial water on LD_50 with $C_{12}E_6$ exhibits two positive peaks at ~2.0 and ~6.0 Å indicating hydrogen-down orientation. The location of these peaks corresponds to that of the peaks in the density profile (top-center panel). Hydrogen-bond between the water molecules located at ~2.0 Å and ~6.0 Å on LD_50 surface results in the hydrogen-down orientation for water molecules at ~6.0 Å. On LD_20, in the presence of $C_{12}E_6$, the M_z profiles are not strikingly different from that observed on M_z profile of water molecules on bare LD_20.

4.4.3. Residence Probability and Reorientational Dynamics

The residence probability function (P) is defined as the ratio of the number of water molecules present in the interfacial layer at time 't' to the number of water molecules in the interfacial layer at time zero (t = 0). The longer the water molecules stay in a layer, the more slowly P decays. For this analysis, only water molecules within a distance of 5.1 Å from the graphite and 3.3 Å from silica were considered. To assess the reorientational dynamics of water molecules we compute the dipole-dipole auto-correlation function (DACF), defined as

$$\text{DACF}= \left\langle \frac{\mu_w(t)\mu_w(0)}{\mu_w(0)\mu_w(0)} \right\rangle \qquad (4.1)$$

DACF is 1.0 at time zero and decays gradually as the water molecules rotate. Our calculations also discriminate P and DACF for water molecules simultaneously

present in the interfacial layer and in the hydration shell of surfactants. The 5.15 Å cut-off distance employed for the hydration shell of SDS surfactants is determined from the sulfur (SDS) - oxygen (water) radial distribution function. Radial distribution function calculations between centers of mass of $C_{12}E_6$ headgroups and oxygen atoms of water molecules yielded a cut-off of 7.95 Å for the hydration shell of $C_{12}E_6$. Water molecules re-entering into the interfacial layer or hydration shell are not considered in P and DACF calculations.

In the top panels of Figure 4-vii, we show P and DACF for interfacial water molecules on graphite with and without SDS. We observe that P decays fast for water molecules on graphite surface in the absence of SDS (dash-dot-dot line in the top-left panel). The slowest decay is observed for water molecules on GRA_100 (each SDS surfactant has an available surface area of 100.0 $Å^2$), i.e. when SDS yields a complete monolayer on graphite. When SDS surfactants form multiple layers or hemi-cylinders (surface area available per SDS are 60.0 $Å^2$ or ~40.0 $Å^2$, respectively), we observe that water molecules move out of the interfacial layer faster than observed on GRA_100, but more slowly than observed in the absence of surfactants.

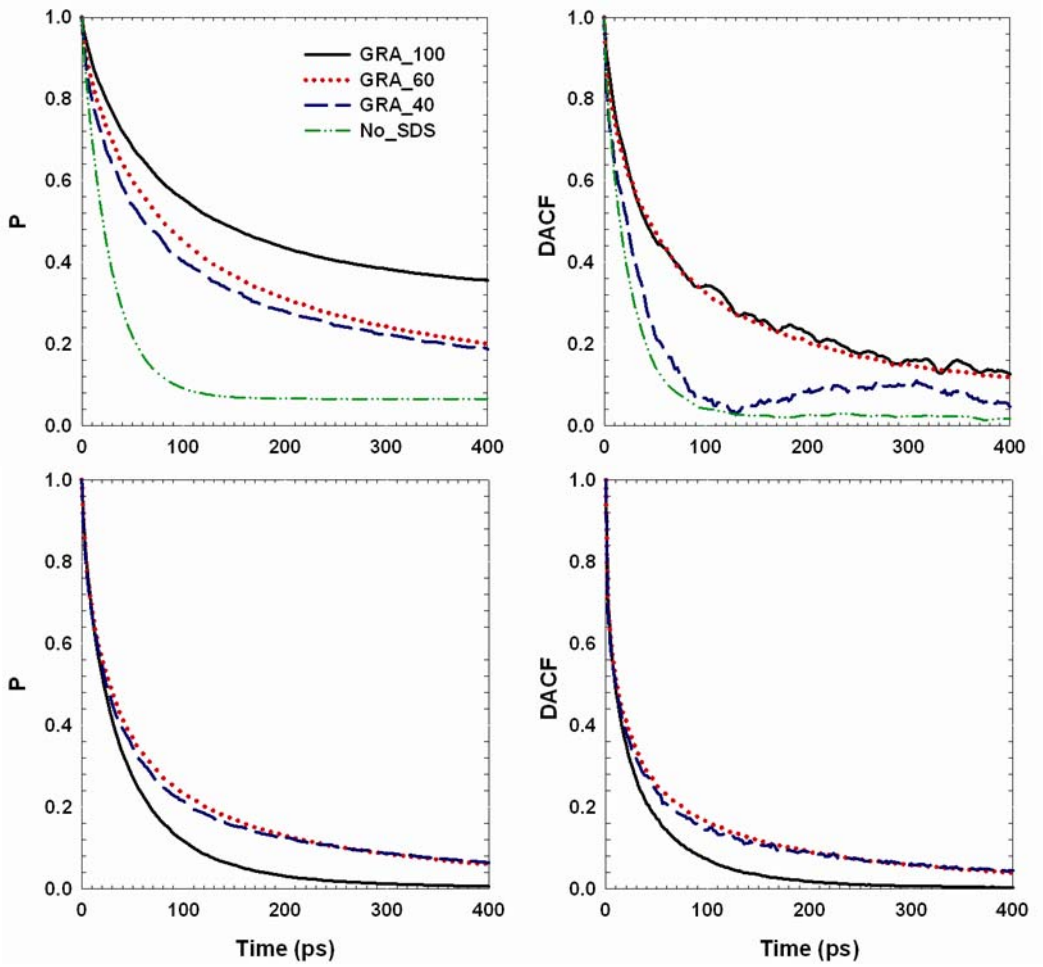

Figure 4-vii**:** (Top panels) Left: Residence probability function (P) for water molecules in the interfacial layer (within 5.1 Å from graphite). Right: Dipole-dipole auto-correlation functions for interfacial water molecules. (Bottom panels) P and DACF for water molecules simultaneously present in the interfacial water layer on graphite and in the hydration shell of SDS headgroups.

In the top-right panel of Figure 4-vii we show the DACF of interfacial water molecules on graphite. Surprisingly, we observe that P and DACF are qualitatively very similar for GRA_100 and GRA_60. P and DACF curves for water molecules on bare graphite and on graphite with a hemi-cylindrical surface aggregate decay at similar rates for the first 100.0 ps.

P and DACF results for water molecules simultaneously present in the interfacial layer and in the hydration shell of SDS headgroups are shown in bottom

panels of Figure 4-vii. Comparing P in top-left panel to that of bottom-left, we observe that P for water molecules simultaneously present in the interfacial layer and in the hydration shell decay faster than that for water molecules in the interfacial layer, indicating that water molecules next to SDS headgroups in GRA_100 move out of the hydration shell faster than they move out of the interfacial layer. Visual inspection indicates that water molecules exist in the interfacial layer in clusters, referred to as water clusters hereafter. We did not quantify the size and number of water molecules in these clusters. On both GRA_60 and GRA_100 we observe water clusters next to surfactant headgroups, since the clusters are located close to the bulk water in case of GRA_60, the P decay rate is enhanced. Water molecules next to SDS surfactant headgroups rotate faster than those in the interfacial layer and away from SDS headgroups (compare top-right and bottom-right panels of Figure 4-vii). Even though the water molecules next to ionic surfactant headgroups[118] form clusters and reorient slower than the bulk water, the observed reorientation is faster than that observed for clusters of water in confinement.[197,200,236] These results indicate that even though SDS surfactants introduce long range effects on the orientation of the water molecules away from the surface, at close proximities the effects of surface on water residence times and orientational dynamics is stronger than that of due to SDS headgroups, in part due to the substrate's rigidity.

In Figure 4-viii, we report P of water molecules next to silica surfaces without (inset of top panels) and with surfactants. The residence probability of water molecules on bare HD silica surfaces with different degrees of protonation decays to ~ 0.1 in 400 ps, although the curves are not identical. We observe a steep decay for P of water

molecules on bare HD_100 until P reaches ~0.5. Then the curve stays flat compared to results obtained for water molecules on HD_50 and HD_20. This suggests that the mechanism involving movement of water molecules from interfacial layer to the second layer varies with the change in the number of the surface hydrogen atoms. The anisotropic reorientation behavior of water molecules on these silica surfaces is discussed by Argyris et al.[234]

On HD_100, P for water molecules adjacent to the surface decays slowest in the presence of SDS surfactants. On LD_100 in the presence of either SDS or $C_{12}E_6$ P for water in the interfacial layer decays faster than that observed for P of water next to HD_100 surface with SDS as observed from top-left panel of Figure 4-viii. It is worth remembering that on LD_100 surface with $C_{12}E_6$ on surface, the water molecules present in the interfacial layer are few and hence we do not obtain a smooth curve. On all the silica surfaces with surfactants, P decays more slowly than that observed on bare silica surfaces without surfactants. In contrary to what has been observed for nano-confined water or for water in reverse micelles[197,200], the residence times and orientation of water molecules on silica are strongly related to the type of the surfactant used.

On partially protonated silica surfaces, P for water molecules on LD silica with $C_{12}E_6$ surfactants decays the slowest (top-middle panel) of all the curves in Figure 4-viii, indicating that the presence of $C_{12}E_6$ headgroups close to the surface enhances the residence times of interfacial water molecules on that substrate.

Interfacial water molecules that are not in the hydration shell of surfactants headgroups contribute to the slower decay of P (compare top panels of Figure 4-viii and central panels of Figure 4-viii) for water molecules in the interfacial layer of the

substrate with surfactants than that for water molecules which are simultaneously present in the interfacial layer and the hydration shell of surfactants headgroups. This indicates that water molecules diffuse out of the hydration shell of surfactants faster than the displacement of water molecules out of the interfacial layer.

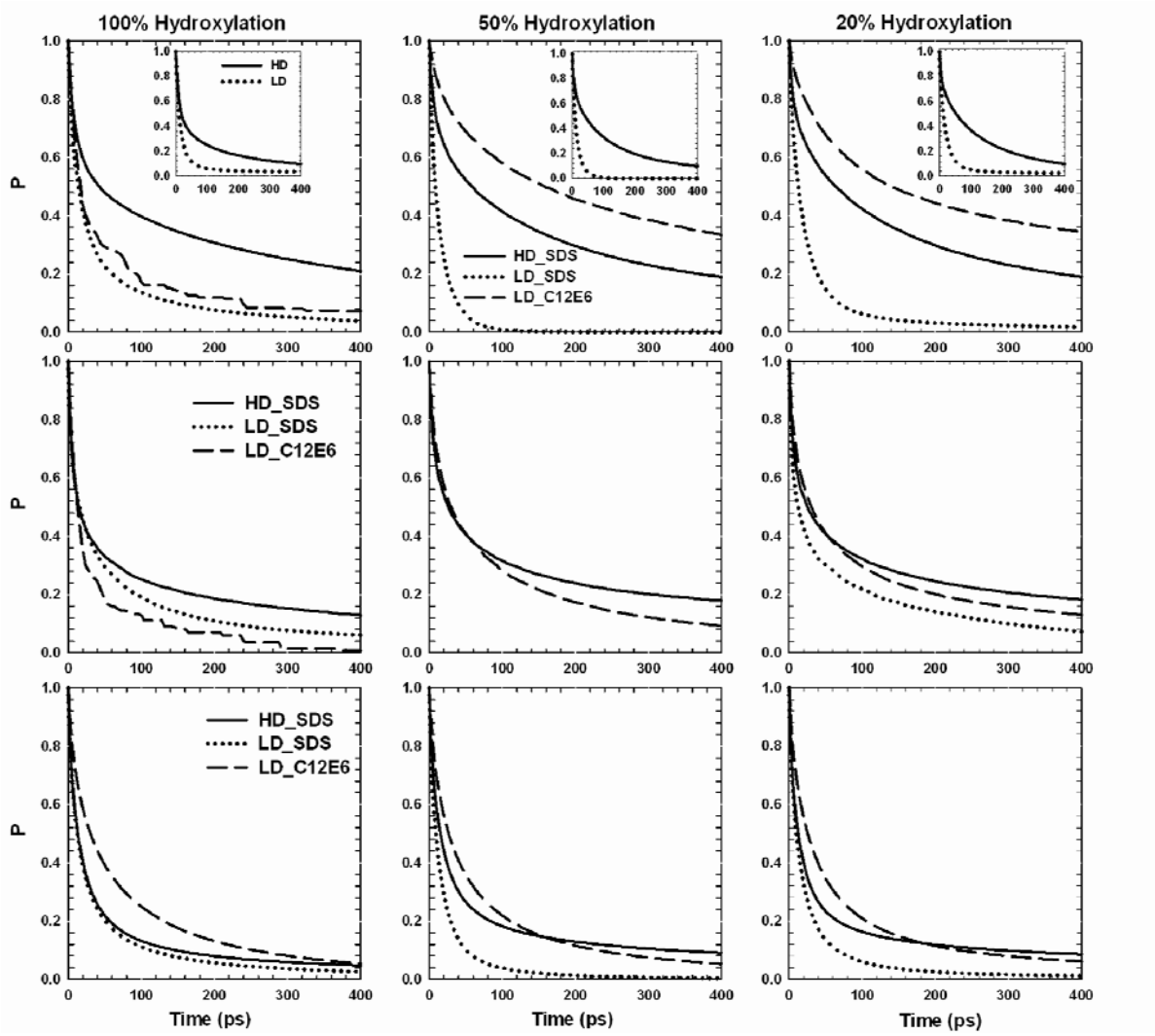

Figure 4-viii**:** (Top panels) Residence probability function (P) for water molecules in the interfacial layer on 100% (left), 50% (middle), and 20% (right) protonated HD with SDS, and LD silica with SDS, and LD silica with $C_{12}E_6$, respectively. (Middle panels) Residence probability function (P) of water molecules those are simultaneously present in the interfacial layer and in the hydration shell of surfactants headgroups. (Bottom panels) Residence probability function (P) of water molecules that are present in the hydration shell of surfactants headgroups.

The dynamics of water molecules in the hydration shell are slower than in the bulk.[197] The direct comparison of the dynamics of water next to surfactant headgroups and those that are next to surfaces in the absence of surfactants is not straightforward as the translation and rotation of surfactants molecules enhance the reorientational rate of water molecules within the hydration layer, whereas the rigidity of the substrate atoms reduces the rate of reorientation of water molecules next to the surface. When we only consider water molecules away from the surface and in the hydration shell of SDS surfactants on LD and HD silica we observe identical residence probability curves (not shown here for brevity), indicating that the differences we observe in Figure 4-viii are primarily due to the silica substrate. We find that water molecules that are simultaneously present in the interfacial layer and the hydration shell stay longer on HD silica with SDS rather than on LD silica with $C_{12}E_6$(centre panels of Figure 4-viii). However, water molecules stay longer in the interfacial layer and the hydration shell on LD silica with $C_{12}E_6$ than on LD silica with SDS. The differences arising due to the small compact ionic headgroup and long non-ionic headgroup plays an important role in determining the residence probability of water molecules next to substrates covered with different surfactants. The P curves for water molecules within the hydration shell of surfactants are reported in bottom panels of Figure 4-viii. The results indicate that the presence of $C_{12}E_6$ on LD silica strongly effects the residence times of water molecules than the presence of SDS on LD silica. Residence times of water molecules next to the partially protonated LD silica with $C_{12}E_6$ are comparable to that observed on HD silica adsorbed with SDS, indicating that $C_{12}E_6$ has retains water in the hydration shell for longer times.

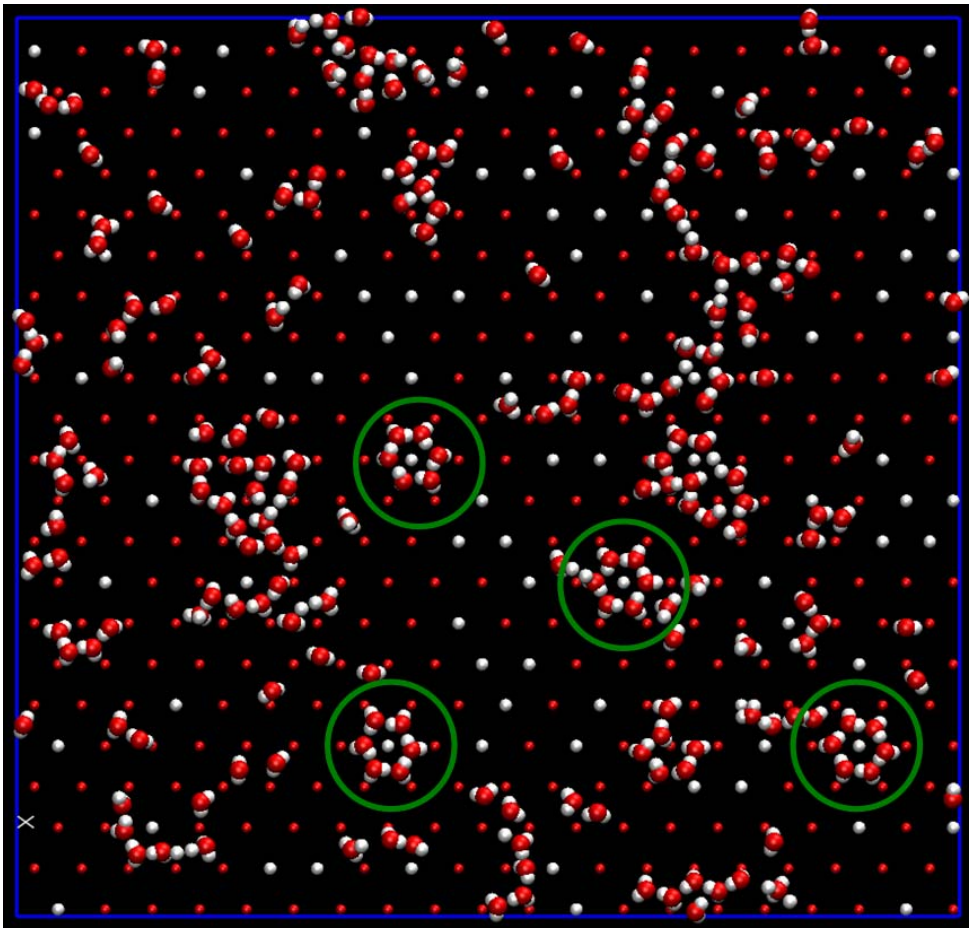

Figure 4-ix: Top view of water molecules within 3.3 Å from the non-bridging oxygen atom on LD_20 silica. Small red spheres are non-bridging oxygen atoms of silica, white spheres are surface hydrogen atoms, and large white and red spheres are hydrogen and oxygen atoms of water. Green circles highlight hydrogen bonded water molecules on top of surface hydrogen atom. We do not show $C_{12}E_6$ surfactants for clarity.

In Figure 4-ix we show one representative snapshot for water molecules on LD_20 within 3.3 Å from the non-bridging oxygen atoms. We observe the hexagonal clusters of hydrogen-bonded water molecules responsible for the slow decay of P for water molecules on LD_50 and LD_20 in the presence of $C_{12}E_6$. Within these hexagonal clusters, the oxygen atom of each water molecule is simultaneously hydrogen bonded to the surface hydrogen atom and to the hydrogen atoms of the adjacent water molecules. The hydrogen atoms of the water molecules within this hexagonal cluster

that are pointing away from the central surface hydrogen atom are hydrogen bonded to the non-bridging non-protonated oxygen atoms. We did not observe such hexagonal clusters on water molecules on LD_50 and LD_20 surfaces without surfactants or with SDS. We observe these hexagonal clusters only on LD_50 and LD_20 silica with $C_{12}E_6$ surfactants. The presence of surface hydrogen atoms surrounded by non-protonated non-bridging oxygen atoms of silica together with the tail-groups or coiled headgroups of $C_{12}E_6$ that do not strongly interact with adjacent water contribute to the formation of the hexagonal clusters of water molecules just discussed. These results indicate that, by carefully selecting a surfactant, wetting on charged substrates can be altered to obtain desired characteristics.

4.5. Conclusions

Structure and morphology of SDS surface aggregates on high density (HD) and low density (LD) silica surfaces with different degree of protonation, of $C_{12}E_6$ surface aggregates on low density (LD) silica surfaces with different degrees of protonation are studied using molecular dynamics simulations. $C_{12}E_6$ forms a monolayer on the 100% protonated LD silica with tailgroups close to the surface, whereas on partially protonated LD silica surfaces $C_{12}E_6$ headgroups are present adjacent to the surface. We observe coiled configuration of $C_{12}E_6$ headgroups on partially protonated silica surfaces. SDS forms a bilayer micellar-like structure on partially protonated LD and HD silica surfaces, whereas on completely protonated silica surfaces SDS forms a patchy multi-layer structure with tailgroups oriented parallel to the surface. Our results indicate that the surfactants adsorption on silica surfaces involves competing effects from charge distribution on surfactants headgroups, and also on the surface charge distribution.

Water molecules on graphite with a monolayer of SDS surfactants are found to have largest increase in residence probability when compared to SDS with hemi-cylindrical or multiple layers on graphite. We observe that the water molecules close to the headgroups have less residence times and faster reorientational dynamics than the water molecules away from the headgroups within the interfacial layer. On silica, $C_{12}E_6$ induces largest enhancement to the residence times of water molecules present in the LD silica-water interfacial layer. Reorientational dynamics of water molecules in the interfacial layer and hydration shell of surfactants, although not presented, follow the similar trends as observed for the residence probabilities. The results discussed above indicate that by introducing surfactants at the water-solid interface we can selectively change the wetting characteristics of a surface, tune the residence time of water in the interfacial regions, and disrupt the local structuring of interfacial water molecules.

5. Lateral Confinements Effects on the Structural Properties of Surfactant Aggregates: SDS on Graphene

The material presented below has submitted to the journal Physical Chemistry Chemical Physics in 2010.

5.1. Abstract

The effect of lateral confinement on the structures of surfactant surface aggregates has been studied using all-atom molecular dynamics simulations. Aqueous sodium dodecyl sulfate (SDS) surfactants aggregates were studied on 2.0 nm, 5.0 nm, and 10.0 nm circular graphene sheets and on 2.0 and 5.0 nm wide graphene nanoribbons. For the first time our results show that, because of lateral confinement provided by the graphene edges, SDS yields multiple layers, hemispheres, hemicylinders or multiple hemispheres depending on the graphene size and shape. Results are quantified in terms of morphology of the surfactant aggregates, order parameter of the adsorbed surfactant aggregates, and number of water molecules at contact with the carbonaceous support. Differences are explained in terms of the lateral confinement provided by the limited extensions of the graphene sheets. Our results are important for designing separation techniques to isolate graphene sheets of given size and shape.

5.2. Introduction

Because of their excellent properties, graphene sheets (GS) are receiving enormous scientific attention,[237-240] although their production and purification remain a significant hurdle. Liquid phase exfoliation that involves the use of surfactants has been exploited to produce graphene-like materials with optical and electrical properties comparable to those of graphene.[42,241] In a promising procedure, graphene flakes have been exfoliated using surfactants. Although surfactant remains on the exfoliated graphene affect performance,[42,241] surfactants enable density-gradient methods to separate single-layer GS from multi-layer ones.[242] In aqueous systems surfactants can provide ionic interactions that keep GS from self-aggregating.[43] Surfactants have been used as compatibilizers in the preparation of composite materials containing GS.[243-244] The grafting of polymer chains on the GS surface or edges may allow for greater entanglement and binding of graphene within nanocomposites, as suggested by molecular dynamics simulations,[245] as well as lower resistances to heat transfer in GS-based nanocomposites.[246] Surfactants can be used to graft polymer chains onto the graphene surface using admicellar polymerization[247] or similar techniques.[44,243-244] The primary step in most of the above processes is the adsorption of surfactants on the graphene surface.

Surfactants find vast applications in nanotechnology because they can direct the formation of structured aggregates on surfaces. The resulting supra-molecular structures are the direct result of self-assembly. The first step towards the aggregate formation is usually the adsorption of surfactants on the nano-particle surface. Because much is known about surfactant self-assembly on flat macroscopic surfaces,[36] it is tempting to

extrapolate the results obtained on macroscopic surfaces to those expected on nano-scale materials. However, due to their limited size, nanoparticles may constrain the adsorbed aggregates, yielding unexpected morphologies.[69-70] Within this work we address the following fundamental question: how do self-assembled surfactant aggregates formed on GS differ compared to those adsorbed on graphite?

We report molecular dynamics simulations of SDS surfactants on graphene sheets (GS) and graphene nanoribbons (GNRs) of different sizes. All simulations were performed at ambient conditions. Our results demonstrate the importance of lateral confinement, provided by 'edge effects', in determining the aggregate morphology. As the GS size increases, edge effects become less pronounced, but remain important in determining the performance of GS separation processes.

5.3. Simulation Methodology

Molecular dynamic simulations were conducted for circular graphene sheets (GS) of diameter 2.0, 5.0, and 10.0 nm, and for infinitely long graphene nanoribbons (GNRs) of 2.0 nm and 5.0 nm width in the presence of aqueous sodium dodecyl sulfate (SDS) surfactants. Water molecules were modeled using the extended simple point charge (SPC/E) model.[126] Carbon atoms in rigid graphene sheets were modeled as Lennard-Jones spheres and were not allowed to vibrate. The force field parameters for SDS were those used previously in our group.[69-70,77] The number of surfactants adsorbed on the GS surface yields an available surface area of 0.45 - 0.48 nm^2 per surfactant. At ~0.40 nm^2 surface area per molecule, SDS forms a hemicylindrical micelle on graphite.[35,187] Simulation boxes of size 6.0 x 6.0 x 8.0 nm^3 and 10.0 x 10.0 x 10.0 nm^3 were used for all systems except for the simulations involving GS of 10.0 nm

diameter, for which the box dimensions were 20.0 x 20.0 x 10.0 nm^3. The number of water molecules in the simulation box was varied to keep the density of the simulation box equal to the bulk density of water (~1.0 gm/cc). This resulted in 9500, 31734, and 125648 water molecules, and 16, 92, and 356 SDS surfactants in the simulations boxes containing 2.0 nm, 5.0 nm, and 10.0 nm graphene sheets, respectively. 8300 and 28805 water molecules, and 54 and 236 SDS surfactants were present within the simulation boxes used to study 2.0 nm and 5.0 nm wide GNRs. The simulation protocol consisted of 2 ns of simulation in the canonical (NVT) ensemble at 500 K, followed by 2 ns at 400 K and 2 ns at 300 K, also in the NVT ensemble. Then, for the production phase, the systems were simulated in the isobaric-isothermal (NPT) ensemble for 50 ns in all cases, except for GS of 10.0 nm diameter, for which only 25 ns of simulation were conducted. In the case of GNRs the production run was performed in the NVT ensemble. In the NVT ensemble the number of molecules (N), the volume of the simulation box (V), and the system temperature (T) are maintained constant during the simulation. In the NPT ensemble the system volume is allowed to fluctuate to maintain the pressure (P) constant. The system temperature was maintained constant using the Nosé-Hoover[248] thermostat. The pressure in NPT simulations was maintained constant using the Parrinello-Rahman[249] barostat. Relaxation time constants of 100 fs and 500 fs were used for temperature control and pressure control, respectively.[136] All results were obtained at 300 K and 1 bar.

The GROMACS 3.3.3[134,250-251] simulation package was used to integrate the equations of motion. All bonds and angles in water molecules were constrained using the SETTLE[127] algorithm. The equations of motion were integrated using the leap-frog

velocity integration scheme. The particle mesh ewald (PME)[252] algorithm was used to calculate long-range electrostatic interactions. Dispersive interactions, modeled as Lennard-Jones potential, were truncated at 1.0 nm.

Unsupported graphene sheets of micron size have been shown to have ripples on their surface.[253-254] The length and amplitude of such ripples increases as the GS size increases.[254] The height of surface ripples for 10.0x10.0 nm^2 GS can be ~1.0 nm.[255] To understand the effect of such structural features on the morphology of SDS aggregates, we simulated flexible 2.0 and 5.0 nm GS implementing the Tersoff-Brenner potential[256] to describe the interaction between carbon atoms. Because GROMACS does not support the Tersoff-Brenner potential, the molecular dynamics software LAMMPS[257] was used to perform these simulations. The configurations obtained at the end of the rigid GS simulations were used as initial configurations for flexible GS. The velocity-Verlet algorithm[258] was used to integrate the equations of motion and the Ewald summation algorithm was used to account for long-range electrostatic interactions. The simulations involving flexible graphene sheets were carried out for 10.0 ns in the canonical (NVT) ensemble.

5.4. Results

5.4.1. Structural Features

Visual inspection of simulation results shows that the GS size induces changes in the adsorbed SDS surfactant aggregate structure. Representative snapshots are reported in Figure 5-i. On 2.0 nm GS (left panels) the SDS surfactants form multiple layers with most of the surfactants either parallel or anti-parallel to each other. The GS

diameter (2.0 nm) is smaller than that of a SDS micelle in water, thus GS provides a constraint on the adsorbed SDS because it is not possible for all the SDS molecules adsorbed on the GS to thrust their headgroups towards the aqueous phase while maintaining all the tailgroups on the graphene surface. Consequently the surfactants stack on each other, yielding multiple layers, in an attempt to decrease the exposure of tailgroups and GS surface to water.

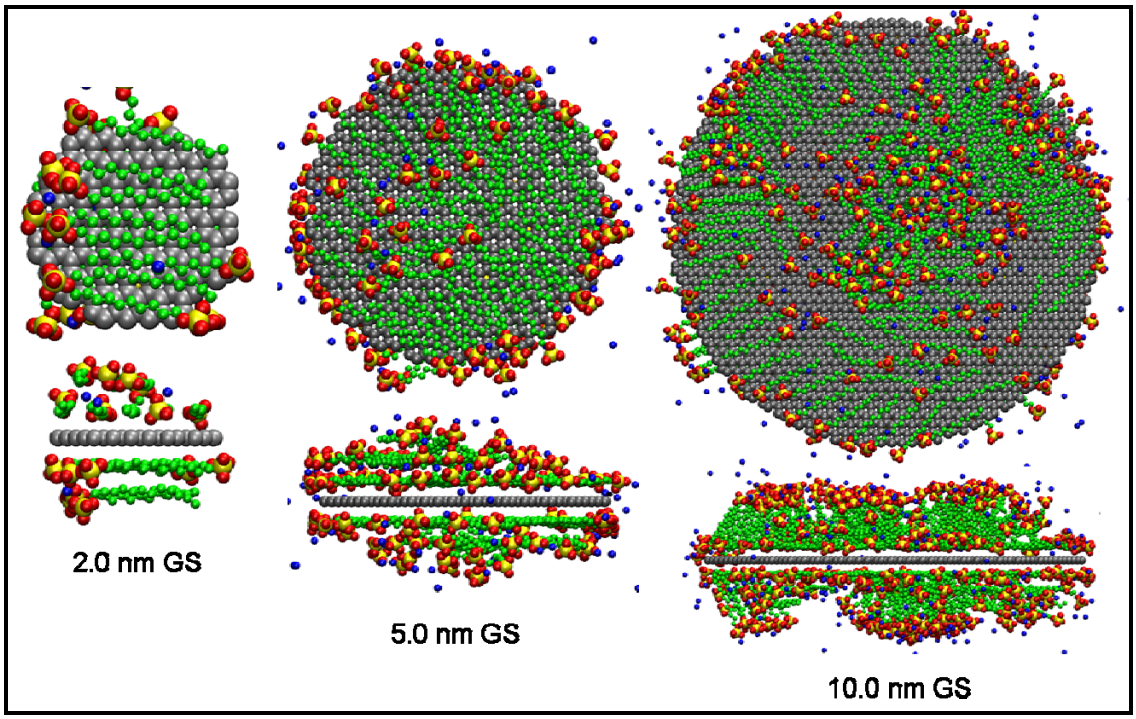

Figure 5-i**:** Top (top) and side views (bottom) of SDS aggregates on GS. Different GS sizes are considered, from left to right 2.0, 5.0, and 10.0 nm. Color code: methyl groups, sulfur, and oxygen in SDS are represented by green, yellow, and red spheres, respectively. Sodium ions are shown as blue spheres and carbon atoms in GS as grey spheres. Solvent molecules are not shown for clarity.

On 5.0 nm GS (central panels) we observe the formation of one hemi-sphere on each side of the GS (see side view, bottom panel). Although within this configuration most of the surfactant headgroups are exposed to water, it is important to point out that the surfactants are not oriented radially within the hemisphere. Instead, the hemisphere is formed by stacked layers of surfactants that remain parallel to the GS surface. Within

each layer the surfactants adsorb in a circular manner with their headgroups oriented towards the GS edge. The diameter of each layer decreases as the distance from the GS surface increases, and remains large enough to cover the tailgroups in the layer underneath, and small enough to allow the headgroups of the surfactants underneath to be exposed to water. The surfactant arrangement just described allows most of the headgroups to be exposed to water, while keeping most of the tailgroups, and GS surface, away from water.

Before analyzing the SDS structure formed on the GS of 10.0 nm in diameter we should point out that the diameter of this substrate is larger than the typical period of SDS surface aggregates on graphite, ~4.0-5.0 nm. On GS of 10.0 nm diameter (right panels in Figure 5-i) we observe a hemi-spherical structure with ~ 5.0 nm diameter at the center of the 10.0 nm GS. It is interesting to point out that this hemi-spherical structure is morphologically different from those observed on 5.0 nm GS in that several SDS molecules on 10.0 nm GS are oriented radially. Some portion of the GS surface remains exposed to water, as was observed in the case of SDS on graphite.[77] On the outer edge of the 10.0 nm GS SDS surfactants orient so that their headgroups project towards the water phase and all the tailgroups lie on the graphene surface. We conclude that the GS edge promotes the formation of a structure in which the SDS surfactant headgroups are pointing towards water, and the SDS tailgroups are ordered radially with respect to the GS. Because of excluded-volume effects, the rigidity of the SDS tailgroups, and the small diameter of the simulated GS, the surfactant aggregate structure is not uniform (e.g. note that the SDS structure on top of the 10.0 nm GS somewhat differs from that observed on the bottom). Similar morphological changes

within surfactant surface aggregates due to the change in surface size can be expected for other amphiphilic molecules, although adsorbed block copolymers will probably show much richer behavior.[259-260]

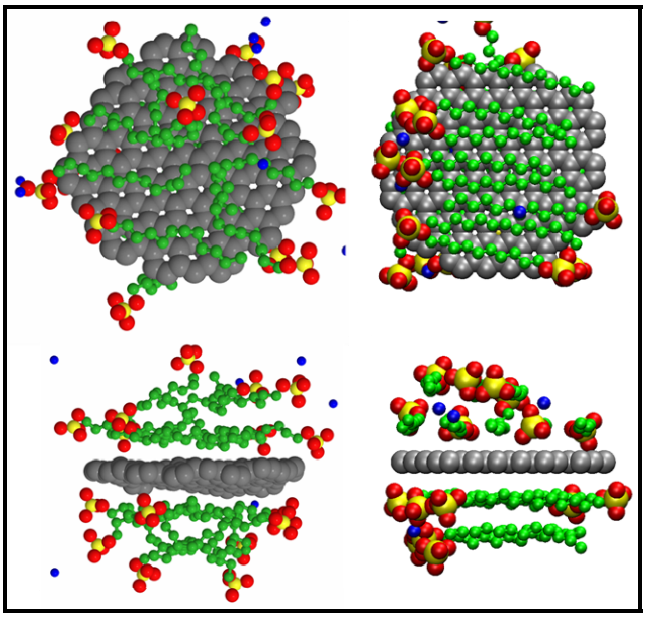

Figure 5-ii**:** Top (top) and side view (bottom) of SDS aggregates on rigid (right panels) and flexible (left panels) GS of diameter 2.0 nm. The color code is the same as that in Figure 5-i. Water molecules are not shown for clarity.

In Figure 5-ii, aggregates of SDS surfactants are shown on rigid (right) and flexible (left) GS of diameter 2.0 nm. The height of surface ripples on flexible 2.0 nm GS is ~0.5 nm. Due to these ripples we observe a small change in surface aggregate structure compared to the results obtained on rigid substrates. Some surfactants appear somewhat perpendicular to the GS surface, and the surfactant headgroups are distributed more uniformly along the z dimension. The change in surfactant morphology is due to thermal fluctuations experienced by the flexible GS. Despite these fluctuations, the overall morphology of the surface aggregate remains very similar to the one

observed on rigid GS. For rigid and flexible GS of 5.0 nm diameter we observed smaller differences on the surfactant aggregate structure than those reported for GS of 2.0 nm (results not shown for brevity; the ripples on the flexible 5.0 nm GS are of height ~0.6 nm). We speculate that as the GS size increases the results obtained on rigid substrates are more and more representative to those obtained on flexible ones, because the ripples height/GS diameter ratio decreases as the GS size increases.

Many production schemes yield elongated GS, sometimes nanoribbons (GNRs), rather than circular GS such as those considered above. In Figure 5-iii we show representative simulation snapshots for surfactants adsorbed on infinitely long GNRs of width 2.0 and 5.0 nm. In the case of 2.0 nm GNR, the length of the SDS surfactant (~1.8 nm) compares to the GNR width. It can be observed that all the SDS tails are oriented parallel to the GNR width, with the headgroups protruding into the aqueous phase. Our results suggest a pronounced ordering effect due to the GNR edges, which is consistent with simulation results for SDS adsorbed on a graphite surface with a step defect.[261]

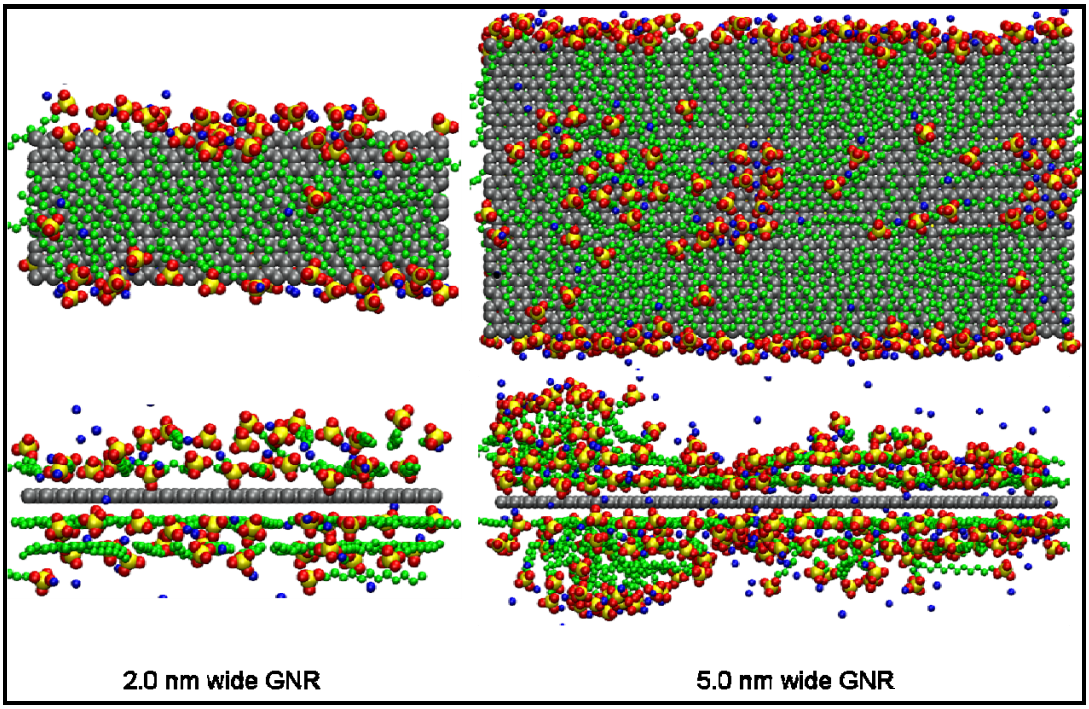

Figure 5-iii: Top (top) and side view (bottom) of SDS aggregates on GNRs of width 2.0 (left) and 5.0 nm (right). The color code is the same as that in Figure 5-i. Water molecules are not shown for clarity.

Our results indicate that the orientation of the SDS surfactants depends on the width of the GNR. On 2.0 nm-wide GNR, we observe that SDS surfactants are completely oriented along the width of the GNR because only in this way the headgroups can protrude into the aqueous phase. On 5.0 nm-wide GNR, we observe one row of surfactants oriented perpendicularly to each GNR edge, with their headgroups towards the aqueous phase. In the portion of the GNR surface far from the edges a few surfactants are oriented parallel to the GNR length, and others are perpendicular to the surface. The resultant morphology of the SDS aggregates is that of a few hemispheres, surrounded by flat SDS structures, and by some regions depleted of surfactants. By contrast, the surface of 2.0 nm-wide GNRs is completely covered by SDS. It is worth remembering that the structural features just discussed are obtained at surfactant surface

coverage of ~0.45 nm^2 per surfactant, at which conditions SDS surfactants on graphite yield hemicylinders.

5.5. Detailed Quantification of Surfactant Aggregate Structure

5.5.1. Density Profiles

In Figure 5-iv the density profiles of surfactant tailgroups, headgroups, and counterions are shown as a function of the distance *r* perpendicular to the graphene surface. In the case of SDS on GS, only those atoms that lie within a cylinder with radius 0.2 nm greater than that of the GS are included in the calculations. In the case of SDS on GNR, only those atoms that lie within a orthogonal box, centered on the GNR, with width 0.4 nm greater than that of the GNR are included in the calculations. In all density profiles shown in Figure 5-iv zero on the x-axis corresponds to the center of the graphene support. The tailgroups (headgroups) density profiles are calculated considering the position of each CH_3 or CH_2 (O or S) group in the surfactant tail (head). The tailgroups and headgroups density profiles are normalized by the number of segments in tailgroup and headgroup (12 and 5 respectively). The density profiles in Figure 5-iv help quantify the structural features described qualitatively in section 3.1.

In the tailgroups density profiles (top panels of Figure 5-iv) the pronounced first peaks at ~0.4 nm on GS and GNR indicate that the adsorbed surfactants form a well pronounced adsorbed layer, where they tend to be parallel to the substrate, as suggested by the simulation snapshots. The subsequent peaks correspond to additional layers formed on GS and GNR. For example, in Figure 5-i we observed two layers of SDS surfactants on GS of diameter 2.0 nm, correspondingly in the tailgroup density profile

(top left panel of Figure 5-iv) we observe two distinct peaks for tailgroups on 2.0 nm GS. All the tailgroups density profiles display distinct peaks at periodic intervals except for SDS on GS of 10.0 nm diameter. On the latter substrate one pronounced first peak is followed by a uniform distribution of tailgroups until a distance of 1.6 nm away from the GS is reached. The density profile gradually decays to zero as we move further away from the GS surface. This result is consistent with our previous analysis (se Figure 5-i), according to which SDS on 10.0 nm GS yield hemi-spherical aggregates.

The headgroups density profiles are more helpful in identifying those SDS molecules that are perpendicular to the graphene surface. The presence of peaks at ~ 2.0 nm away from the graphene surface (middle panels of Figure 5-iv), especially for GS of 10.0 nm diameter and GNR of 5.0 nm width, indicates that several surfactant molecules are perpendicular to these substrates. The length of one SDS is ~1.8 nm, and ~2.0 nm corresponds to the sum of the extended length of the SDS tailgroups and the radius of the one carbon atom in graphene surface. The headgroup density profiles for SDS on 5.0 nm GNR show four distinct peaks at 0.4, 0.8, 1.40, and 1.90 nm. This indicates that the surface aggregate is composed of multiple layers, and that only a few SDS molecules are perpendicular to the surface. On 10.0 nm GS we observe one pronounced peak at 0.4 nm, a second peak at 2.0 nm, and a uniform density distribution in between. This is consistent with the formation of hemispheres. On other substrates the headgroup density profiles show multiple peaks indicating the presence of multiple layers. These results confirm the analysis obtained from visual inspection of representative simulation snapshots.

In the bottom panels of Figure 5-iv we report the density profiles for counterions. In the system considered herein the counterions are positively-charged sodium ions. Due to counterion-condensation[77] effects, the counterions are often located close to the headgroups. Thus it is not surprising that the peaks observed in counterion density profiles are located in between the peaks observed in headgroup density profiles. In most cases the counterions are found sandwiched between the SDS headgroups, and contribute to the establishment of the morphological features discussed above for the adsorbed surfactant aggregates.

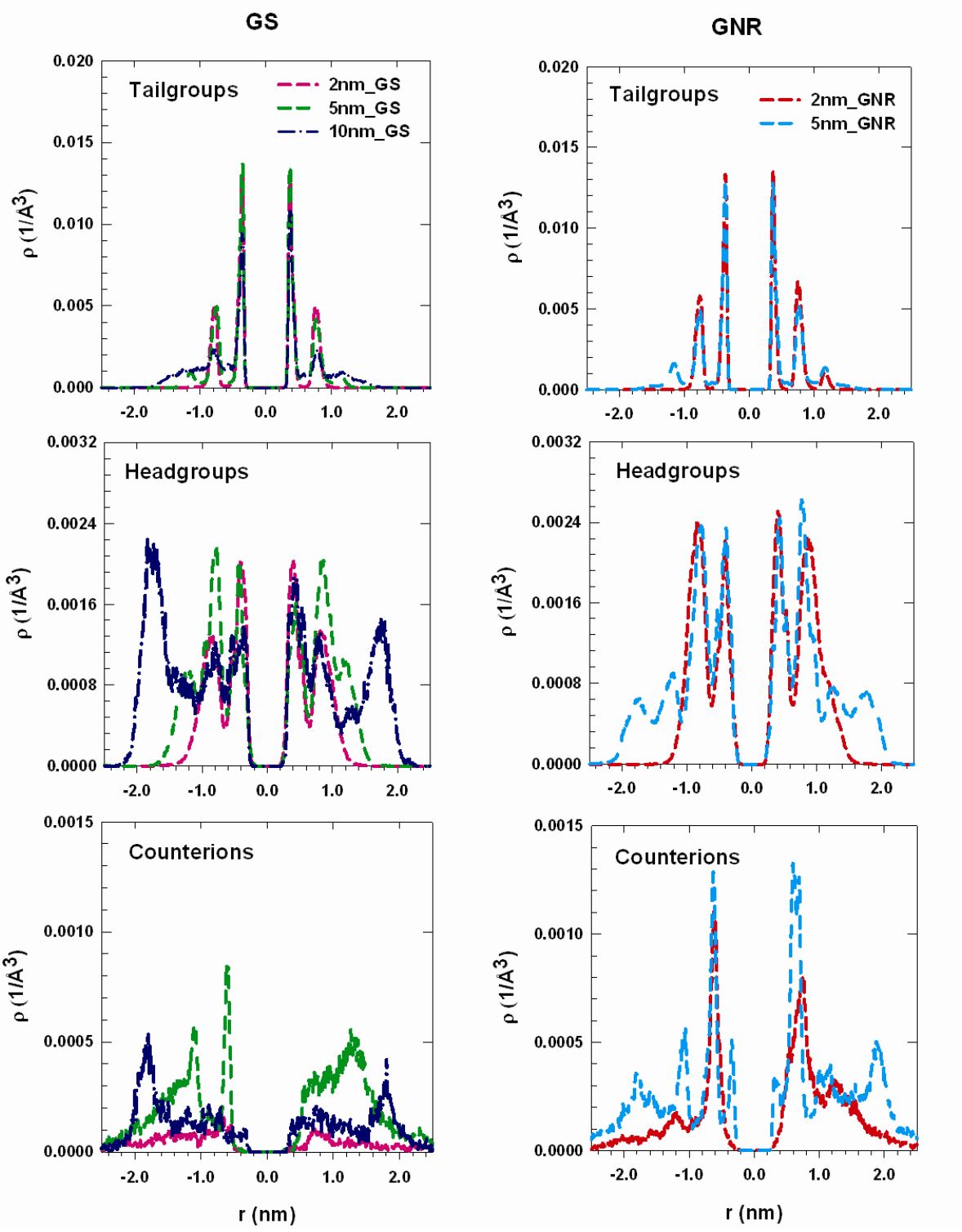

Figure 5-iv: Density profiles for surfactant tailgroups (top), headgroups (center), and counterions (bottom) in the direction perpendicular to the carbonaceous substrate for SDS on GSs (left panels) and GNRs (right panels).

5.5.2. Order Parameter

The nematic order parameter (S), which is based on the second Legendre polynomial of the cosine of the angle θ formed between the average orientational vector of all the surfactants on the surface (director vector) and the orientation vector of each individual surfactant is defined as[262]

$$S = \left\langle P_2(\cos\theta) \right\rangle = \left\langle \frac{3\cos^2\theta - 1}{2} \right\rangle \qquad (5.1)$$

The individual orientational vector for each surfactant is obtained from the position of the CH_3 group in the SDS tailgroup and that of the sulfur in the SDS headgroup. The average orientational vector, henceforth referred to as director vector, has been obtained following two different procedures. The first method, described elsewhere,[263-264] involves computing the largest eigenvalue corresponding to the inertia tensor of each surfactant molecule along the longest molecular axis. $\hat{e}_j$ is the normalized vector associated with the largest eigenvalue. The director vector is the eigenvector associated with the largest eigenvalue obtained after diagonalizing the tensor $Q_{\alpha\beta}$ defined as[263]

$$Q_{\alpha\beta} = \frac{1}{N}\sum_{j=1}^{N}\left(\frac{3}{2}\hat{e}_{j\alpha}\,\hat{e}_{j\beta} - \frac{1}{2}\delta_{\alpha\beta}\right) \qquad \alpha,\beta = x,y,z \qquad (5.2)$$

In the above equation $\delta_{\alpha\beta}$ is the Kronecker delta (i.e. the value of δ =1 when α=β and 0 otherwise) and $\hat{e}_j$ is the unit vector associated with the largest eigenvalue of the inertia tensor of each molecule considered. The ensemble average of the cosine of

the angle formed between the director vector and the individual orientational vector yields S (uniaxial order parameter).[263]

The second method involves four steps. In the first step the order parameter S is calculated, using the angle between individual orientational vector and an axis, separately for all three x, y, and, z axis of the simulation box. In the second step, S as computed in the first step is used to identify the axis along which most of the surfactants are oriented. In the third step the average orientational vector is computed by transforming the individual orientational vectors such that the orientational vector for each surfactant is oriented along the axis determined in the second step. This prevents the average vector from being cancelled out by parallel and anti-parallel orientations of surfactant molecules along the axis identified in the second step. Finally, the average orientational vector obtained from the third step is used to compute the order parameter S, using equation (1). The second method discussed has the advantage of being simple. Its accuracy for the system at hand has been verified by comparing selected results to those obtained implementing the first method. Because the results were comparable, in what follows we report the results obtained from the second method.

We computed the order parameter of the surface aggregates formed on both surfaces of single GS separately, and then we averaged them. The average results are shown in Figure 5-v. When $S = 0.0$ the surfactant orientation is isotropic, when $S > 0.4$ a nematic state is identified.[263] Our estimates for S suggest the presence of nematic phases for SDS aggregates adsorbed on both GS and GNR of size 2.0 and 5.0 nm. It is interesting to note that the order parameter results suggest the formation of nematic phases when the dimension of the graphene support (diameter for GS, width for GNR)

becomes comparable to the extended length of one surfactant molecule. Order parameter results suggest the formation of isotropic structures on GS of 10.0 nm diameter. Visual inspection of simulation snapshots shows well-defined structures. When analyzed in terms of surfactant-surfactant orientation, however, the simulation snapshots are consistent with rather disordered aggregates.

For comparison, in Figure 5-vi we show the order parameter for SDS adsorbed on graphite as a function of the SDS surface density. SDS is known to preferentially orient along the α symmetry axes of graphite.[71,265-266] Consequently, at low coverage (1.0 nm^2/surfactant) SDS molecules are aligned along the α symmetry axis of graphite[71,265] and S is ~0.45. As the surface area per head group decreases (and consequently as the surface coverage increases) S decreases, indicating the formation of structures in which the orientation of SDS molecules is likely isotropic.

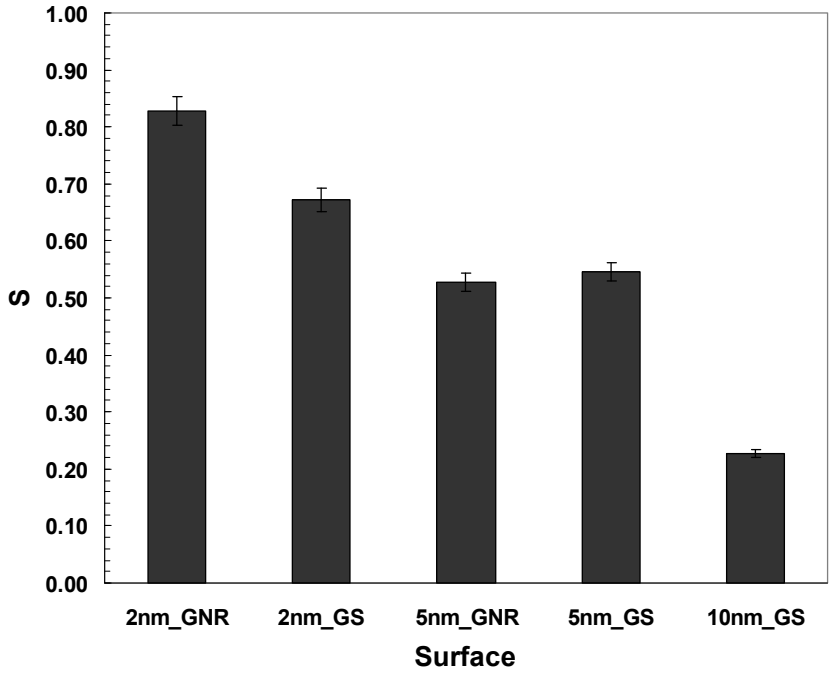

Figure 5-v: Nematic order parameter S for surface aggregates on the different graphene supports considered in this study.

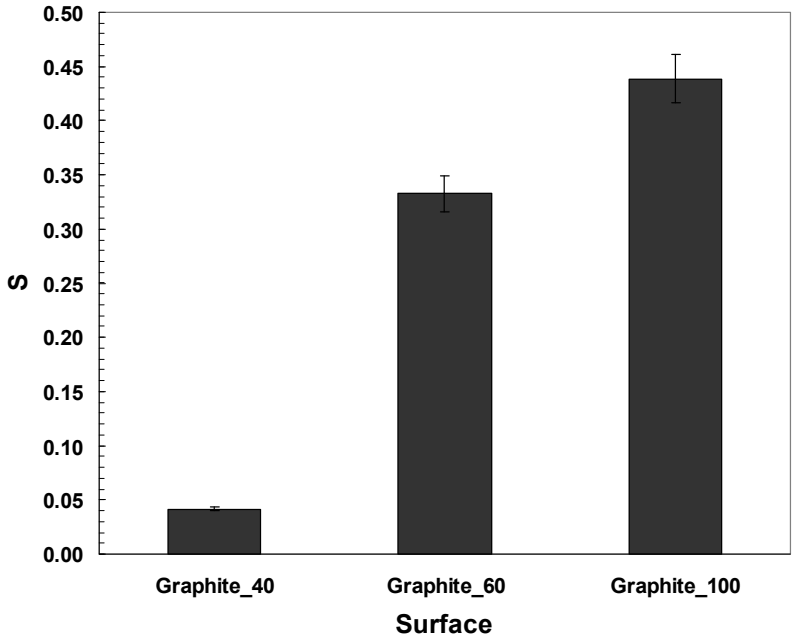

Figure 5-vi**:** Order parameter (S) for surface aggregates on graphite surface at different surface coverage. Graphite_40, Graphite_60, and Graphite_100 indicate systems with surface area per head group of 0.40, 0.60, and 1.00 nm^2, respectively.

5.5.3. Interfacial Water

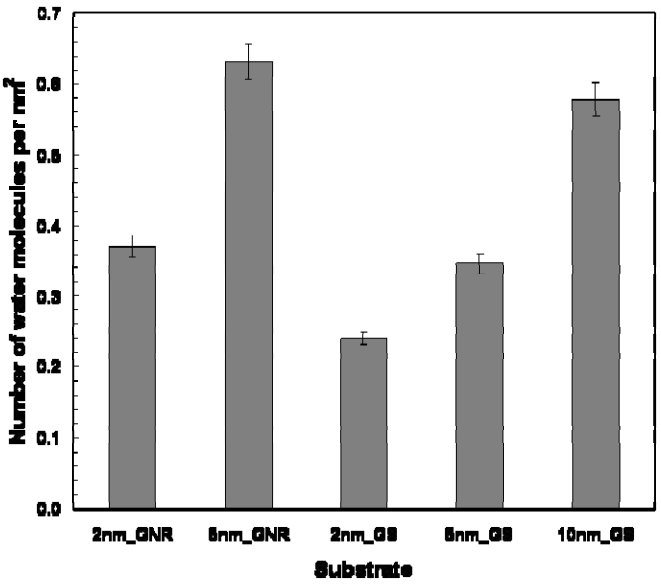

Figure 5-vii**:** Number of water molecules at contact with graphene covered by surfactant aggregates. The data are normalized by the surface area of the graphene substrate.

Hydrophobic effects are often invoked to explain the morphological properties of adsorbed surfactant structures. Thus it is important to quantify the number of water molecules that remain in contact with the graphene substrate even when SDS surfactant aggregates are present. In Figure 5-vii we report the number of water molecules found within 0.375 nm from the graphene surface normalized by area of the graphene surface. The distance of 0.375 nm corresponds to the thickness of the first adsorbed water layer formed at contact with a flat graphitic support.[267] From Figure 5-vii we observe that as the GS and GNR size increases, the SDS surfactants do not cover the entire graphene surface, even though their surface density remains constant in all our calculations. It is worth mentioning that on graphite covered with SDS at surface coverage of ~0.40 nm^2 per surfactant molecule, ~1.5 water molecules per nm^2 remain at contact with the carbon surface (at least twice as many as those found at contact with the graphene substrates considered here). It appears that the formation of aggregate structures with periodic structures results in excess water molecules in the vicinity of graphite surface, probably because the SDS headgroups, some of which remain at contact with graphite,[77] effectively bring water molecules near the hydrophobic substrate. On the contrary, the surfactant aggregate structures observed in our calculations form because most of the SDS headgroups are protruded towards the aqueous phase, while most of the SDS tailgroups cover the graphene surface. As the GS or GNR size increases we observe the formation of periodic structures rather than infinitely long multiple-layers, thus resulting in the increase of number of water molecules that remain close to GS and GNR surfaces.

5.6. Conclusions

The influence of lateral confinement provided by graphene sheet on surfactant surface aggregates has been studied using molecular dynamics simulations conducted at ambient conditions. At substrate sizes equivalent to the size of surfactant, very highly ordered surface aggregates are observed. When the substrate size is 2-3 times that of the surfactant molecules, hemispherical surface aggregates are observed, although they are often surrounded by flat aggregates, especially on graphene nanoribbons. On graphene substrates of any size the edge effects will be present. When graphene nanoribbons are of width ~10.0 nm (twice the size of periodic aggregate size of SDS on graphite surface), due to edge effects we observe one row of surfactants oriented along each edge, and hemispherical aggregates away from the edges. The atomistic description of surfactant aggregates self-assembled on graphene sheets and graphene nanoribbons provided herein is important to understand and optimize processes such as the density-gradient separation of graphene sheets, or in-situ polymerization processes used to stabilize graphene-polymer nanocomposites.

6. SDS Surfactants on Carbon Nanotubes: Aggregate Morphology

The material presented below has been published in volume 3, issue 3 of the journal ACS Nano in the year 2009.

6.1. Abstract

Although carbon nanotubes have attracted enormous research interest, their practical application is still hindered, primarily, by the difficulty of separating them into samples monodispersed in diameter, chirality, and length. Recent advances show that ultracentrifugating carbon nanotube dispersions stabilized by surfactants is a promising route for achieving the desired separation. For further perfectioning this procedure it is necessary to know how surfactants adsorb on nanotubes of different diameters, which determines the nanotube-surfactant aggregate effective density and the nanotube-nanotube potential of mean force. Because only limited experimental data are available to elucidate these phenomena, we report here an extensive all-atom molecular dynamics study on the morphology of sodium dodecyl sulfate (SDS) surfactant aggregates adsorbed on (6,6), (12,12), and (20,20) single walled carbon nanotubes at room conditions. Our calculations reveal that the nanotube diameter is the primary factor that determines the morphology of the aggregates because of a competition between the entropic and energetic advantage encountered by the surfactants when they wrap one nanotube, and the enthalpic penalty faced during this process due to bending of the surfactant molecule. The data are in qualitative agreement with the neutron scattering results reported by Yurekli *et al*. [J. Am. Chem. Soc. 126, 2004, 9902], and for the first

time provide an atomic-level description helpful in designing better separation, as well as stabilization techniques for aqueous carbon nanotube dispersions.

6.2. Introduction

Single-walled carbon nanotubes (SWNTs) have attracted vast research attention in the last two decades because of seemingly unlimited intrinsic properties.[268-271] Several methods are now available for producing this material,[272-275] and the last barrier that prevents the widespread application of carbon nanotubes consists in the difficulty of separating them into samples monodispersed in diameter, chirality, and length. Significant advances have been accomplished in the recent years. O'Connell *et al.*[276] managed to suspend SWNTs in aqueous solutions and to remove carbon nanotube bundles using sodium dodecyl sulfate (SDS) surfactants by implementing ultracentrifugation procedures. The technique has been improved by Arnold *et al.*[60], who, using bile salts such as sodium cholate in addition to SDS surfactants, demonstrated that it is possible to separate SWNTs based on their diameter and electronic structure. Nair *et al.*[85] demonstrated that the number of surfactant molecules adsorbed on each SWNT causes the effective nanotube-surfactant complex density to change, and that this density change causes the separation of nanotubes during ultracentrifugation. Further, recent data by Niyogi *et al*.[277] show that adding electrolytes to SWNTs-SDS systems improves the fractionation of SWNTs using density-gradient ultracentrifugation methods. Based on these recent advances, it is clear that understanding how surfactants adsorb on SWNTs of various diameters will lead to further advancements in this field.

Unfortunately, however, it is still not clear how surfactants self assemble on carbon nanotubes. It was postulated that the carbon nanotube – surfactant complexes resemble micelles in which the carbon nanotube forms the core and the surfactants extend radially from the core.[278-280] Another proposed morphology was one in which surfactant hemimicellar aggregates cover the carbon nanotubes.[281-282] The latter possibility has been challenged by energetic arguments discussed by Matarredona *et al.*,[84] and it seems unlikely to occur. To the best of our knowledge, the only experimental assessment on the morphology of surfactant aggregates adsorbed on carbon nanotubes is that reported by Yurekli *et al.*,[87] who used neutron scattering to characterize SWNTs dispersed in aqueous solutions with the aid of SDS surfactants at three concentrations. The experimental data do not support any ordered surfactant aggregate structure on the SWNTs, but rather suggest the formation of disordered aggregates. Because these results are at odds with the information available for the morphology of SDS aggregates on graphite,[71,77,283-284] they clearly indicate that the curvature of the solid support affects the morphology of adsorbed SDS aggregates. If this is the case, then the morphology of surfactant aggregates formed on SWNTs depends not only on surfactant concentration, temperature, and ionic strength, but also on nanotube diameter and chirality, possibly allowing for a precise separation of SWNTs dispersions into monodispersed samples. Further, it is likely that the molecular architecture of the surfactants (*i.e.*, linear alkyl chain *vs*. branched chain containing benzene rings) determines how individual surfactants adsorb on SWNTs of given diameter, which is the principle employed, *e.g.*, to design cyclic peptides to selectively stabilize SWNTs in aqueous suspensions.[285]

A detailed understanding of the equilibrium structure of surfactant aggregates adsorbed on SWNTs of various diameters is necessary for improving separation techniques. Such understanding will not only improve the ultracentrifugation technique of Arnold *et al.*,[60] but is also necessary for correctly predicting the effective potential of mean force between carbon nanotubes in aqueous surfactant solutions. For the purposes of predicting the nanotube-nanotube potential of mean force, Patel and Egorov[286] proposed a disordered, yet uniform along the nanotube axis, distribution of surfactants around one carbon nanotube. However it is possible that local density fluctuations affect the pair potential of mean force, as suggested for example by our recent simulations on colloidal systems.[245,287-289] More importantly, understanding and visualizing the molecular arrangement of surfactants adsorbed on SWNTs of various diameters will allow us to understand the driving forces responsible for determining the aggregate morphology, thus leading to the design of surfactants more effective for stabilizing aqueous SWNTs dispersions.

Because of the technical limitations typically encountered by experimental methods at the nanoscale, and because of the simplification necessary for applying density functional methods and coarse-grained simulations, molecular simulations conducted at the all-atom level offer the optimum compromise for securing progress in this field. One limitation typical for all-atom molecular dynamics simulations is due to the currently available computational resources, it is only possible to simulate large systems for a few tens of nanoseconds. This requires the number of surfactant molecules near one SWNT to be treated as an input parameter in the simulations. The

simulations are then conducted for a time sufficiently long to assess the equilibrium structure for the adsorbed aggregates.

We present here the first simulation results obtained for SDS surfactants adsorbed on (6,6), (12,12), and (20,20) SWNTs at room conditions, and we compare them to the structures proposed in the literature. Specifically, we analyze the effect of surface density and that of SWNT diameter on the aggregate morphology. The simulation results discussed herein are obtained from running all-atom molecular dynamics simulations for 50 ns. The results do not change over the last 30 ns of simulation time, and only those collected during the last 10 ns are presented in what follows. Simulation details are reported as Appendix to the text. The surfactant surface densities considered are consistent with the experimental data reported by Strano *et al.*,[290] Yurekli *et al.*[87] and by Matarredona *et al.*,[84] although precise surfactant adsorption isotherms on SWNTs monodispersed in diameter are at present not available.

6.3. Simulation Details

Aqueous SDS surfactants were simulated at contact with (6,6), (12,12), and (20,20) single-walled carbon nanotubes. Within these substrates, the carbon atoms, treated as Lennard-Jones spheres, were maintained rigid throughout the course of the simulations. Water molecules were modeled using the SPC/E model. The details of the force field employed are described in Ref. [[77]]. Dispersive attractions and repulsive interactions were treated with an inner cutoff of 0.8 nm and outer cutoff of 1.0 nm. Long-range electrostatic interactions were treated using the particle mesh Ewald (PME) method[252]. Bond lengths and bond angles in water were maintained fixed using the SETTLE algorithm.[291]

The simulation package GROMACS, version 3.3.3,[134,250-251] was employed to integrate the equations of motion. The number of particles (N), the simulation box volume (V), and the temperature (T) were maintained constant during our simulations. In all simulations the time step was 2 fs. The Nose-Hoover thermostat[258] with leap-frog algorithm[258] was implemented with a relaxation time constant of 100 fs. All simulations were conducted for 50 ns, and only the last 10 ns were used for data analysis. The systems are considered equilibrated because the results do not change during the last 30 ns of simulations. Although the length of the simulation, which approaches the limit of available computation resources, does not allow us to assess the number of surfactant molecules adsorbed at equilibrium as a function of bulk surfactant concentration, the number of surfactants simulated on each SWNT is consistent with available experimental data. In all the simulations considered one SWNT was placed in the center of the simulation box with the axis aligned along the Z direction. In the initial configuration the desired number of surfactant molecules were placed around the SWNT with their tails parallel to the nanotube axis. The number of water molecules in the box was adjusted to reproduce the bulk water density. Periodic boundary conditions were employed in X, Y, and Z dimensions. Further details are given in Table 6-A.

Table 6-A**:** Simulation details for the systems studied in this work.

Substrate	Number of SDS	Surfactant coverage (nm^2/head group)	Box size (nm^3)	Number of water molecules
(6,6)	16	0.98	7.0x7.0x6.1487	9900
(12,12)	32	0.98	7.0x7.0x6.1487	8640
(20,20)	53	0.98	7.0x7.0x6.1487	7700
(6,6)	36	0.44	7.0x7.0x6.1487	9000
(12,12)	64	0.49	7.0x7.0x6.1487	8450
(20,20)	64	0.81	7.0x7.0x6.1487	7700
(6,6)	64	0.25	7.0x7.0x6.1487	8800

6.4. Results and Discussion

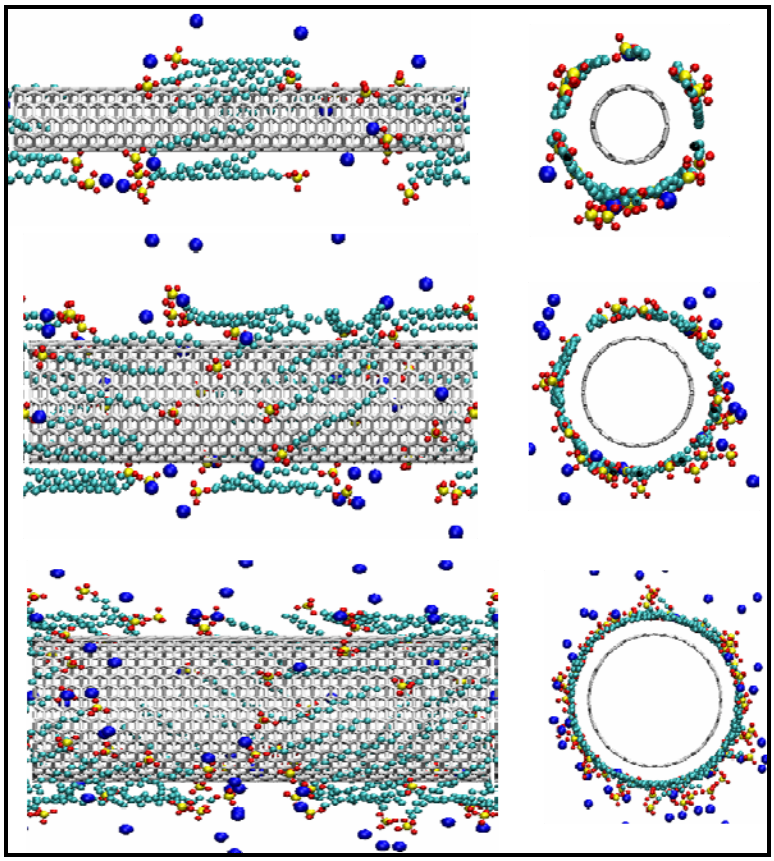

Figure 6-i: Side (left panels) and front views (right panels) of representative snapshots for (6,6) (top), (12,12) (center), and (20,20) SWNTs (bottom) covered by SDS surfactants at a surface density of 0.98 nm^2 per head group. Blue spheres are Na^+ ions. Cyan spheres are either CH_2 or CH_3 groups in the surfactant tails. Red and yellow spheres are oxygen and sulfur atoms in the SDS surfactant heads. Water molecules are not shown for clarity.

Representative simulation snapshots for (6,6), (12,12), and (20,20) SWNTs covered by SDS surfactants are shown in Figure 6-i and Figure 6-ii. In Figure 6-i the surface area per surfactant head group is 0.98 nm^2 in the three nanotubes considered. The surface area per surfactant head group decreases in Figure 6-ii, where it is 0.44, 0.49, and 0.81 nm^2 on (6,6), (12,12), and (20,20) SWNTs, respectively. Visual analysis suggests that the morphology of adsorbed aggregates depends on the surface coverage,

as expected, but also, and more significantly, on the SWNTs diameter. At low surface coverage (Figure 6-i) SDS surfactants on (6,6) SWNTs form 'rings' in which the surfactants lie parallel or anti-parallel to each other and parallel to the nanotube axis. As the SWNTs diameter increases the SDS surfactants still lie predominantly flat on the nanotube surface, but the surface coverage appears more uniform than that observed on the (6,6) SWNTs. The orientation of the adsorbed surfactants with respect to the nanotube axis also changes as the nanotube diameter increases, as discussed at length below.

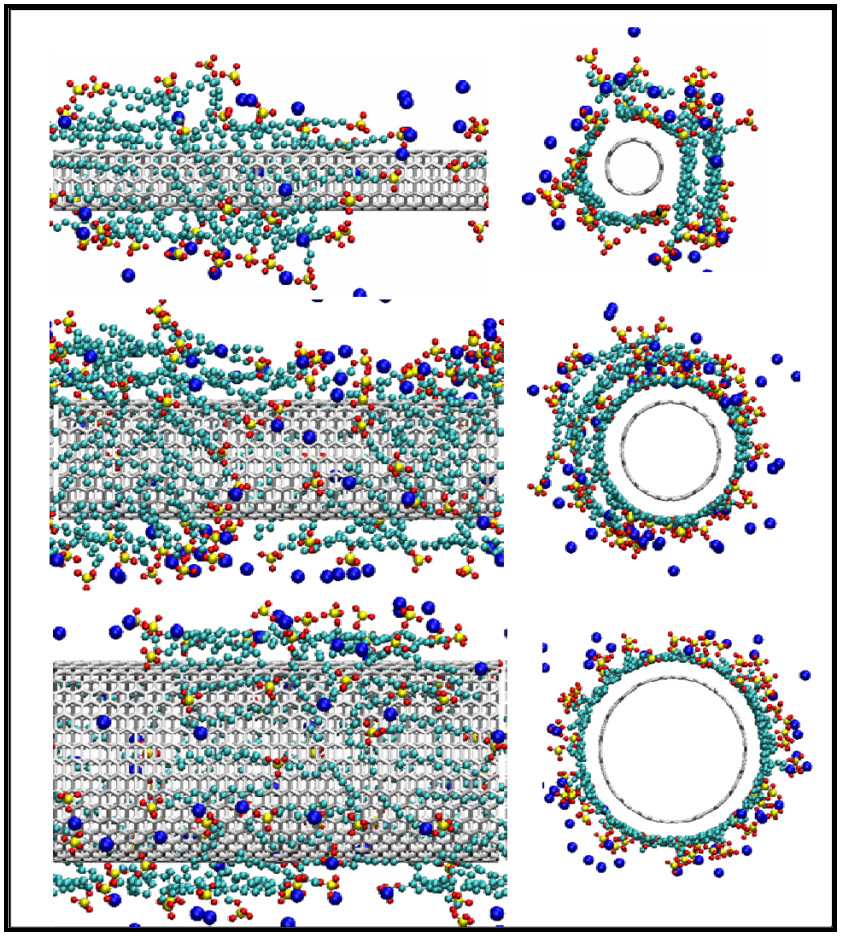

Figure 6-ii: Same as Fig. 1, but for SDS surfactants at a surface density of 0.44, 0.49, and 0.81 nm^2 per head group on (6,6), (12,12), and (20,20) SWNTs, respectively. Water molecules are not shown for clarity.

The different structures of the SDS assemblies on the SWNTs at high surface area per head group (Figure 6-i) are due to a competition between various factors, including surfactant-nanotube and surfactant-surfactant interactions. One of the leading effects seems to be the rigidity of the SDS molecule. SDS surfactants on graphite at low surface coverage (*i.e.*, high surface area per head group) preferentially lie along one of the three α symmetry axes to maximize the number of contacts between the surfactant tail and the carbon atoms in graphite.[71] Because the SWNTs are obtained by rolling one graphene sheet into one cylinder, in the SWNTs considered here one of the α symmetry axes is parallel to the SWNTs axes. Thus if the SDS surfactants lied along one α axes, they can be either parallel to the SWNTs axis, or they must wrap the nanotubes. Because of entropic reasons, both possibilities should occur. However, when one SDS molecule wraps around a narrow tube, it has to bend, encountering an energetic barrier (SDS is rather straight). Our simulations show that the entropic advantage of wrapping the nanotubes forming various angles with the nanotube axis is not sufficient to balance the energetic penalty encountered to bend the SDS molecule around the narrow (6,6) SWNTs. As the nanotube diameter increases, it becomes easier and easier for the adsorbed SDS to wrap the SWNTs not only because smaller bending of the SDS molecule is necessary, but also because the number of surfactant tail – carbon atoms contacts increases when the SDS surfactants lie along the β symmetry axes, which form an angle with respect to the nanotube axes. This latter effect is nanotube specific, *i.e.*, it occurs on the (20,20) SWNTs, but not on the other nanotubes considered here.

The morphology of the surfactant aggregates at high surface area per head group (Figure 6-i) is important because such aggregates provide a template to those formed at

higher densities (Figure 6-ii). On the (6,6) SWNTs the SDS surfactants adsorb on top of the rings formed at low density, and they yield admicelles that, although seem ordered at contact with the nanotube, lack any long-range order. Evidently, as the SDS coverage increases, the adsorbed aggregate structure depends predominantly on SDS-SDS interactions. It is also worth pointing out that some small regions of the (6,6) SWNT surface remains exposed to water even at this large surfactant surface density. This is probably due to the fact that the adsorbed SDS surfactants find it more favorable to maximize the SDS-SDS interactions than spread evenly on the SWNTs surface. In fact, because the SDS surfactants remain in large part parallel to the SWNTs, by spreading evenly on the SWNTs they would decrease the SWNT area in contact with water, but they would increase the tail area in contact with water, with no overall free-energy benefit. On the (12,12) SWNTs the SDS surfactants seem to form a continuous first layer of adsorbed surfactants at contact with the nanotube surface, and excess SDS molecules agglomerate forming a multi-layered structure. Although no long-range order is visible, each surfactant within these admicelles appears parallel or anti-parallel to its neighbors. On the (20,20) SWNTs the surface coverage was not large enough to provide complete coverage of the nanotube surface. Nevertheless, the surfactants would in some case prefer to agglomerate together rather than spread over the entire available surface.

The effects just described are due to a combination of tail-tail and tail-nanotube hydrophobic interactions. However also counterion-condensation phenomena, which, as we described earlier,[77] contribute in shielding the electrostatic repulsion between surfactant heads and effectively bring them close to each other, and intrinsic properties of the straight SDS molecules seem to play a major role in determining the morphology

of the adsorbed surfactant aggregates. It is worth pointing out that the structure of SDS aggregates formed on the SWNTs considered here are completely different compared to those obtained on flat graphite surfaces. As previously shown in the literature,[77,283,292] molecular dynamics simulations, in agreement with experimental AFM data,[284] for ionic surfactants on graphite yield hemicylindrical aggregates, in which it is possible that some of the hydrophobic tails are exposed to water.[77] Because the force fields implemented in this work are exactly the same as those used in our previous work for SDS on graphite, the morphology of the substrate (*i.e.*, cylindrical *vs*. flat) is the only possible cause for the differences observed in surfactant aggregates morphology. Clearly, the SWNTs curvature makes it energetically unfavorable for the SDS surfactants to form hemicylindrical admicelles. The results just discussed suggest that by appropriately designing surfactants at the molecular level it should be possible to completely wrap SWNTs of specific diameter. A similar approach has been successfully demonstrated by Ortiz-Acevedo *et al*.,[285] who designed circular peptides that selectively associate to carbon nanotubes of given diameter. Our results may also explain why bile salts tend to yield more stable aqueous SWNTs dispersions, although additional simulations are necessary.

In all the cases considered in Figure 6-i and Figure 6-ii the SDS aggregates do not show long-range order, in qualitative agreement with the experimental data of Yurekli *et al*.,[87] and certainly cannot be described in terms of the ordered micellar structures postulated earlier in the Literature.[84,278-279,281-282] In addition, we point out that the snapshots in Figure 6-i and Figure 6-ii do not agree with a completely disordered structure either, as it may be inferred from the interpretation of the neutron scattering

data of Yurekli *et al*. In fact, our simulations suggest that SDS surfactants cover the SWNTs sometimes only partially, and that a short-ranged order is present within the individual micellar structures. Because of a competition of forces, as described above, the individual SDS surfactants tend to lie on the SWNT surface, especially at low surface density. Additionally, the SDS surfactants adsorbed on the (6,6) SWNTs seem constantly parallel to the nanotube axis, whereas those adsorbed on the (20,20) SWNTs lie on the surface forming a slanted angle with the nanotube axis. This different orientation is more visible at low surface density (Figure 6-i), but it is nevertheless present at all conditions considered herein. In Figure 6-iii, top panel, we quantify the orientation of SDS surfactants adsorbed on the SWNTs at low surface density by reporting the probability density of observing various angles between the SDS surfactants and the SWNTs axis. When the angle is either 0° or 180°, the surfactants are parallel to the SWNTs axis, when the angle is 90° the surfactants lie perpendicularly to the nanotube axis. The results clearly show that while SDS surfactants lie parallel or anti-parallel to the (6,6) SWNTs axis, they form slanted angles on the other two nanotubes, and as the nanotube radius increases the preferred orientation seems to be along one of the three β symmetry axes of graphite. Note that in the SWNTs considered here the nanotube axis is parallel to one of the three α symmetry axes of the graphene sheet rolled up to form the nanotube. Because of the competition between the energetic advantage of maximizing the number of contacts between the SDS tail and the carbon atoms on the SWNTs surface, and the energetic penalty of bending the SDS molecule to wrap the SWNTs, it is likely that the ratio between the SWNTs diameter and the surfactant length is among the dominant parameters that determine how the SDS

surfactants orient with respect to the nanotube. In fact, as the SWNTs diameter increases the energetic penalty due to bending the SDS molecule around the SWNTs decreases. Also, when one SDS molecule lies along one of the β symmetry axes (which forms an angle of 30^{o} with respect to the SWNTs axes) the number of contacts between the methyl groups in the surfactant tail and the SWNT carbon atoms increases as the SWNT diameter increases, proving that it is energetically favorable for the SDS surfactants to wrap the (20,20) nanotubes, but not the narrower ones.

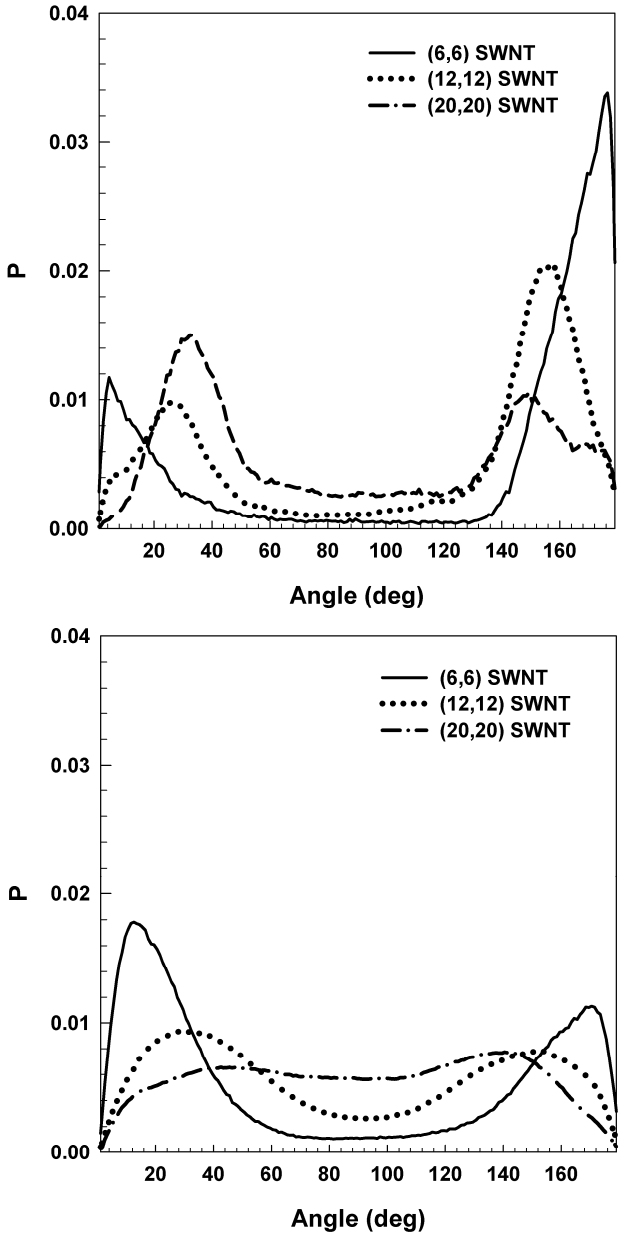

Figure 6-iii: Probability density for SDS surfactants orientation with respect to the SWNTs axis (top panel), and for SDS-SDS relative orientation (bottom panel). Results are obtained for the systems shown in Figure 6-i, in which the surfactants surface density is ~0.98 nm^2 per head group.

At low surface coverage the simulation snapshots of Figure 6-i suggest that the SDS surfactants are aligned not only with respect to the SWNTs axis, but also with respect to each other. In the bottom panel of Figure 6-iii we quantify this observation in

terms of probability density as a function of the SDS-SDS angle at low surfactant density (Figure 6-i). Angles of 0° and 180° represent SDS surfactants parallel, or anti-parallel to each other, respectively. The results indicate that the SDS surfactants on the (6,6) SWNTs are highly ordered with respect to each other, but as the nanotube diameter increases it becomes equally probable to observe SDS surfactants forming any angle with respect to each other. These data suggest that at low surface coverage the SDS surfactants prefer to assume random relative orientations, probably because of entropic reasons. However, on narrow SWNTs it is best for the surfactants to lie parallel / antiparallel with respect to each other to avoid the energetic penalties they would encounter should they bend to wrap the nanotubes.

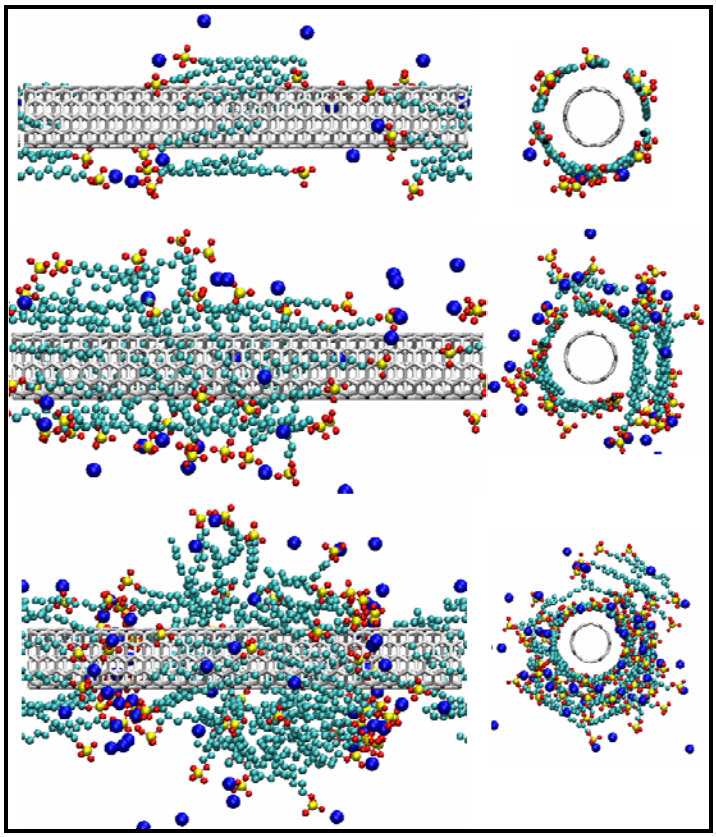

Figure 6-iv: Side (left panels) and front views (right panels) of representative simulation snapshots obtained for SDS surfactants adsorbed on SWNTs at increasing surface density. From top to bottom, the surface per surfactant head group is 0.98, 0.44, and 0.25 nm^2 respectively. Water molecules are not shown for clarity.

From the results shown in Figure 6-i it is also evident that the surfactant head groups in some cases are in contact with the hydrophobic SWNTs surface, which disagrees with the DFT data presented by Patel and Egorov.[286] However, it is likely that as the SDS surface density increases, the surfactant heads protrude more pronouncedly towards the aqueous phase. This possibility is suggested by the snapshots shown in Figure 6-ii, in which systems the surfactant density is larger than that considered in Figure 6-i. One clear difference between our results and the surfactant aggregate morphology commonly postulated is that the SDS surfactants do not uniformly cover the SWNTs. This becomes even more striking when we further increase the surface

density on the (6,6) SWNTs. Representative simulation snapshots at increasing SDS surface density are shown in Figure 6-iv.

Rather than distributing homogeneously on the SWNTs, the SDS surfactants form highly disordered admicelles on the nanotubes. These admicelles are not similar in any way to those proposed in 2002 by Poulin *et al.*,[282] or in 2003 by Islam *et al*.,[281] and those considered in the energetic calculations presented by Matarredona *et al.*,[84] but are in qualitative agreement with the neutron scattering data of Yurekli *et al*.[87] Our equilibrium simulations suggest that the pronounced curvature of the solid support prevents the formation of the ordered admicelles that form on graphite. It should however be pointed out that in our simulations the surfactant surface density is chosen arbitrarily. Because the simulations last only for 50 ns, the SDS surfactants may not have had sufficient time to leave the SWNTs, although we observed no evidence for such phenomenon to happen even at the highest surfactant surface densities considered.

Accounting for the actual surfactant aggregate morphology obtained from our realistic simulations should enhance theoretical predictions such as those reported by Patel and Egorov,[286] which are based on a uniform distribution of surfactant tails, surfactant heads, and counterions away from the carbon nanotube surface. However, accounting for non-uniform effects in either self-consistent theories or general theoretical models[293-296] is at present prohibitively expensive. Thus we provide in Figure 6-v the density distribution of surfactant head groups (top panels), surfactant tails segments (center panels), and counterions (bottom panels) around the SWNTs. These results correspond to time and space averages of the quantities of interest obtained during our simulations, and are a direct consequence of the aggregate morphology

discussed above. In the left panels we report the results obtained on the three SWNTs at low SDS surface density (as shown in Figure 6-i), on the right panels those obtained at high surface density (as shown in Figure 6-ii). In these figures the distance "r" is measured radially from the center of the carbon atoms forming the SWNTs. The surfactant head is defined as the center of mass formed by the oxygen atoms and the sulfur atoms in one SDS molecule. One tail segment is either one CH_2 or one CH_3 group in the surfactant tail. From Figure 6-v, our results suggest that the surfactant tail segments (center panels) accumulate near the hydrophobic SWNTs surfaces, as expected. At low surface density (left panel), we observe the formation of one layer of surfactant tail segments next to the SWNTs, and that the intensity of the peak depend on the nanotube diameter. As the surfactant density increases (right panel) our results suggest the formation of a second shell of surfactant tail segments around the nanotubes, as was indicated by the simulation snapshots of Figure 6-ii. In the case of SDS surfactants on the (12,12) SWNTs our results suggest the formation of up to three layers of surfactant tail segments around the SWNTs. Visual analysis of the simulation snapshots in Figure 6-ii, however, indicates that these layers are not uniform.

The density profiles obtained for the head groups (top panels) do not seem to depend significantly on the SWNT diameter, especially at low surfactant surface density (left panel). Our results indicate that the first peak in the density profile is found at ~0.4 nm from the center of the carbon atoms on the nanotube surface. When excluded-volume effects are considered, this distance corresponds to the head groups being at contact with the hydrophobic SWNTs surfaces, which was not an expected result. As the surfactant surface density increases (right panel) the surfactant heads extend towards

the aqueous phase, but our results indicate that a significant probability exists of finding SDS heads at contact with the nanotube surfaces at all conditions considered here, which is in partial agreement with our simulations for aqueous SDS surfactants on graphite.

The results obtained for the counterion density profiles (bottom panels) show a few unexpected features. The SWNTs are not charged, thus they should not attract ionic species. However, because of the SDS adsorption, it is natural for the counterions to be attracted by the surfactant heads. Indeed the first peak in the counterion density profiles is observed at slightly larger separations *r* than those at which the first peak in the head group density profile was observed. It is interesting to point out that the intensity of the first peak in the density profiles for counterions is approximately ½ of that for the first peak in the density profile for the surfactant heads. This happens because one counterion coordinates simultaneously with multiple surfactant heads, a manifestation of the counterion condensation phenomenon. It is also worth pointing out that the counterion densities show slowly decaying profiles as the distance *r* increases further from the first intense peaks. These results demonstrate that SWNT-SDS complexes can be thought of as polyanions, in which counterion condensation does not manage to neutralize the entire complex charge, as explained by Manning.[294-295,297] It has been recently demonstrated experimentally by Niyogi et al.,[277] that understanding how the density and the morphology of the adsorbed aggregates vary with the addition of electrolytes to the aqueous systems may lead to enhanced separation strategies.

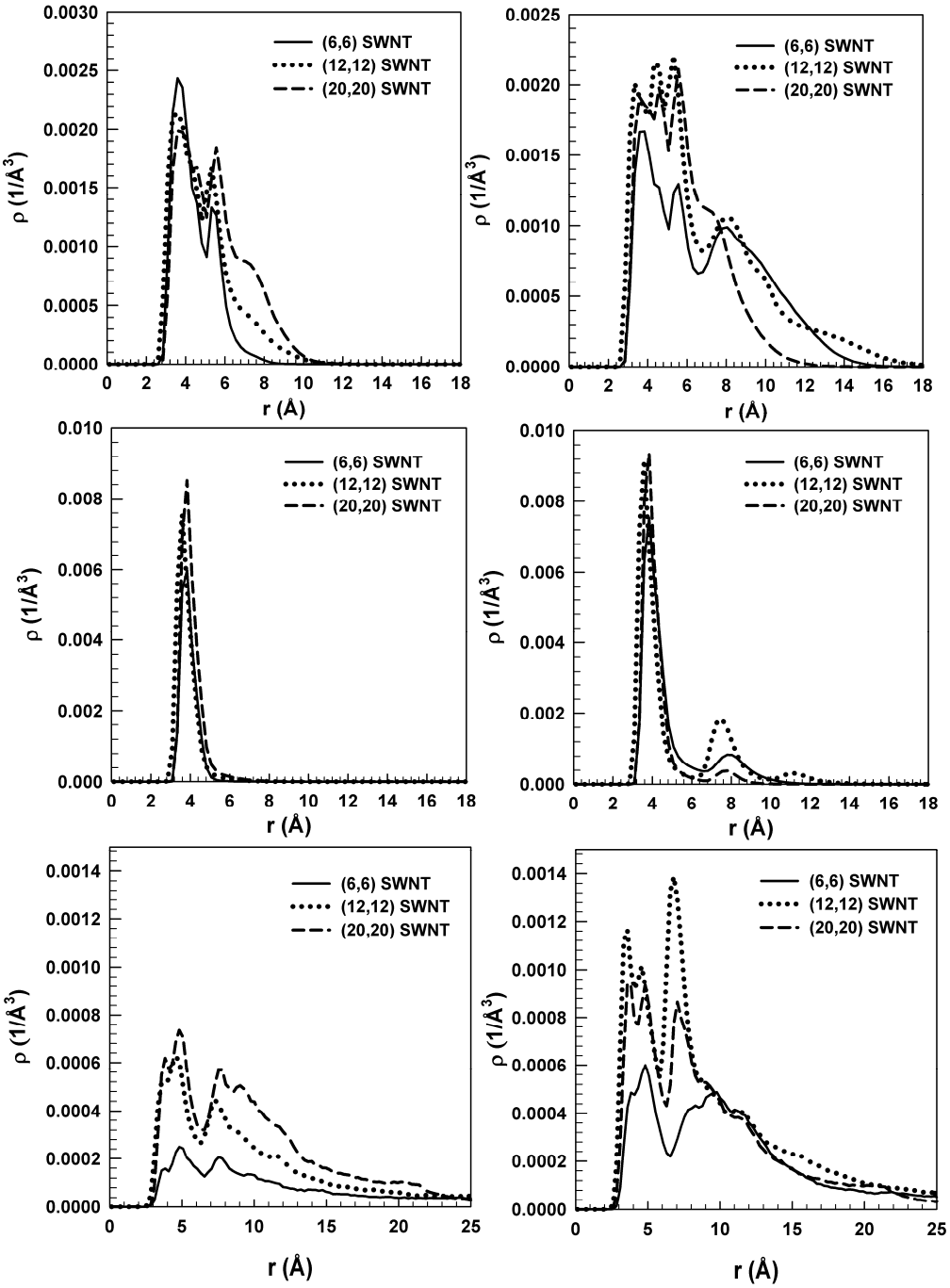

Figure 6-v: Density profiles of surfactant head groups (top panels), surfactant tail segments (center panels), and counterions (bottom panels) around the SWNTs. In the left panels we report the results obtained on the three SWNTs at low SDS surface density (shown in Figure 6-i), on the right panels those obtained at high surface density (shown in Figure 6-ii).

6.5. Conclusions

In conclusion, we reported the first detailed all atom simulation studies for the morphology of SDS surfactants adsorbed on (6,6), (12,12), and (20,20) single-walled carbon nanotubes. Our results agree with, and augment previous neutron scattering experimental data and show that the morphology of the surfactant aggregates strongly depends on the nanotube diameter, as well as on the surface coverage. The additional molecular-level information provided by our results (*i.e.*, density profiles for surfactant tails, surfactant heads, and counterions away from the nanotube surface) should be accounted for to better understand how adsorbed surfactants affect the effective carbon nanotube – carbon nanotube potential of mean force in aqueous solutions, so that to improve the stability of aqueous SWNTs dispersions and to design enhanced separation procedures such as ultracentrifugation. We demonstrated that intrinsic surfactant properties such as the flexibility of each individual surfactant molecule are important, in addition to surfactant-surfactant and surfactant-nanotube interactions to determine the equilibrium morphology of the adsorbed surfactant aggregates. Our results are useful for implementing coarse-grained models that will allow us to calculate the equilibrium adsorption isotherms for SDS surfactants on SWNTs of various diameters.

7. Curvature Effects on the Adsorption of Aqueous SDS Surfactants on Carbonaceous Substrates: Structural Features and Counterion Dynamics

The material presented below has been published in volume 80, issue 2 of the journal Physical Review E in the year 2009.

7.1. Abstract

The effect of substrate curvature on surfactant self-assembly has been studied using all-atom molecular dynamics simulations. We studied aqueous sodium dodecyl sulfate (SDS) surfactants on graphite, on the outer surface of single walled carbon nanotubes (SWNTs) and within SWNTs. Our results reveal that, although the chemical nature of the substrates is constant, the self-assembled structures change significantly as the curvature varies. For example, at large surface density SDS surfactants yield micellar structures on graphite, layered self assemblies outside SWNTs, and cylindrical lamellar structures inside SWNTs. Changes in substrate curvature as well as surfactant surface density affect significantly surfactant orientation and, more importantly, headgroup–headgroup distribution, headgroup-counterion packing, and counterion residence time next to the headgroups.

7.2. Introduction

The self-assembly properties of surfactants are employed in a variety of industrial and research applications [36], including detergents, oil-recovery, preparation of mesoporous and hierarchical materials for catalysis, self-healing of surfaces [298], stabilization of carbon nanotubes in aqueous dispersions [276], etc. The process of self-assembly under confinement [299-301], on rough surfaces [298,302-304], and on carbon nanotubes [305-307] has recently attracted scientific attention. For example, surfactants were thought to form cylindrical micellar structures with fully extended tails when adsorbed on carbon nanotubes [276]. On the contrary, it was found that SDS surfactants adsorbed on carbon nanotubes yield structures that lack long-range order, as shown by experiments [87], but that show support-specific features and sometimes short-ranged order as suggested by simulations [69,305]. Arai et al. [299] showed, employing dissipative particle dynamics (DPD) simulations, that different polymorphic phases can be obtained when surfactants are confined within nanotubes. The different phases obtained are related to the nature of the nanotube walls and also to the surfactant concentration inside the nanotube. With the aid of lattice Monte Carlo simulations, Zhang and co-workers [300] obtained surfactant morphologies within spherical confinement that had not been observed previously in bulk systems. The results just summarized clearly show that curvature plays a major role in determining the morphology of adsorbed surfactant aggregates. This stimulated our interest in conducting systematic molecular dynamic simulations to understand the effect of curvature on the morphology of self-assembled surfactant structures.

In this chapter we compare the morphology of the self-assembled aqueous aggregates of the anionic SDS surfactant when adsorbed on one (6,6) SWNT, within one (40,40) SWNT, and on graphite. We found that surface curvature strongly affects the aggregate morphology. As the surfactant concentration increases we observe a planar-to-hemi-cylindrical transition on flat surfaces, whereas on nanotubes we find a single-to-multilayer transition. Surfactants adsorbed inside nanotubes yield a completely different morphology; they form cylindrical lamellar structures even at low surface coverages. As expected because of hydrophobic considerations, we found that for SDS surfactants adsorbed on the outer surface of nanotubes, as well as on graphite, the hydrophobic tails lie on the support surface. However, when the SDS surfactants adsorb inside a carbon nanotube, the tails are never adsorbed completely on to the surface. Inside (40,40) SWNTs the surfactant tails extend into the aqueous solvent, and this phenomenon becomes more pronounced as the SDS density increases. We also found that the residence time of sodium counterions near the surfactant headgroups is inversely proportional to the substrate curvature.

7.3. Computational Details

Aqueous SDS surfactants were simulated at contact with (6,6) SWNT, (40,40) SWNT, and graphite surfaces. The chiral vector (n,m) represents the dimension, type (arm-chair vs. zigzag) as well as chirality of SWNTs. The diameters of (6,6) and (40,40) SWNTs, calculated as the distance between the center of carbon atoms comprising the nanotubes, are ~0.807 and ~5.42 nm, respectively. Within these substrates, the carbon atoms, treated as Lennard-Jones spheres, were maintained rigid throughout the course of the simulations. Water molecules were modeled using the SPC/E model [126]. The

details of the force field employed are described in Ref. [77]. The simulation package GROMACS [134,250-251] was employed to integrate the equations of motion. In our simulations the number of particles (N), the simulation box volume (V), and the temperature (T) were maintained constant. Orthorhombic simulation boxes were considered in all cases and periodic boundary conditions were implemented in the three dimensions. Graphite is always parallel to the x-y plane in the simulation box, and the carbon nanotube axis is always parallel to the z direction. In all simulations the time step was 2 fs. The Nose-Hoover thermostat [258] with leapfrog algorithm [258] was implemented with a relaxation time constant of 100 fs. All simulations were conducted at 300 K. Dispersive attractions and repulsive interactions were treated as Lennard-Jones potentials with an inner cutoff of 0.8 nm and outer cutoff of 1.0 nm. Long range electrostatic interactions were treated using the particle mesh Ewald (PME) [252] method. Bond lengths and bond angles in water were maintained fixed using the SETTLE algorithm [291]. All the simulations were conducted for 50 ns. Only the last 10 ns were used for data analysis. Other simulation details, including the number of molecules simulated and the size of the simulation boxes, are reported in Table 7-A. The labels given in Table 7-A are used throughout the text to refer to the respective simulated systems. The number of simulated molecules was chosen so that the density of the system corresponds to that in the bulk. For the simulation involving (40,40) SWNTs, surfactant and water molecules were present only inside the SWNT. Because GROMACS 3.3.1 does not allow us to simulate systems periodic in only one dimension, periodic boundary conditions were implemented in the three dimensions, but the SWNT was separated from its periodic replicas along the x and y directions by a

vacuum of thickness 5.4 nm. Increasing the vacuum thickness to 16.2 nm changes the total system energy by less than 0.5 %. For the system containing (6,6) SWNTs, one SWNT was placed at the center of the simulation box surrounded by surfactants and water molecules. In the case of graphite, either two opposing surfaces separated by more than 10.0 nm or one free standing surface covered by a thin aqueous film were considered. Our previous work [77] demonstrates that the results are independent on the configuration chosen. In most cases, SDS surfactants are separated by the periodic replica of the simulated system by at least 6.2 nm. Our previous work [77] guarantees that reliable results are obtained when such distance is larger than 4.5 nm. To further assess the reliability of our results, additional simulations were conducted within the NPT ensemble (P=1 bar) for SDS surfactants on (6,6) SWTNs (system 66-III in Table 7-A), and the results did not show appreciable differences compared to those shown herein (details can be found in the Pressure Effects section discussed later in this chapter). Note that in the implemented NPT ensemble the pressure was maintained constant by allowing the system volume to fluctuate along the x and y directions, while the z dimension was maintained constant because of the presence of the rigid SWNT. Other details of the simulation setup are described in our previous publication [69,77]. It is worth pointing out that the surface area available per each SDS headgroup shown in Table 7-A was calculated by considering excluded volume effects i.e., the SWNT diameter was increased/decreased by 0.3 nm to account for the size of carbon atoms. The value of 0.3 nm was chosen based on the results for density profiles, showed later, which indicate that no molecule can be found at distances less than ~0.3 nm from the center of the carbon atoms.

Table 7-A: Simulation box size, total number of SDS and water molecules, and surfactant coverage for each of the systems simulated.

Substrate	Label	Box Size (nm^3)	No. of SDS	No. of water Molecules	Surfactant coverage (nm^2/headgroup)
(6,6) SWNT	66-I	7.0x7.0x6.1487	16	9900	1.8
(6,6) SWNT	66-II	7.0x7.0x6.1487	36	9000	0.8
(6,6) SWNT	66-III	7.0x7.0x6.1487	64	8800	0.45
Graphite	GRA-I	9.102x4.26x20.0	38	7600	1.02
Graphite	GRA-II	6.15x3.124x25.34	32	5050	0.60
Graphite	GRA-III	3.936x2.556x25.0	25	3000	0.40
(40,40) SWNT [&]	I-4040	10.8x10.8x6.1487	89	3304	1.03
(40,40) SWNT [&]	II-4040	10.8x10.8x6.1487	108	3000	0.85
(40,40 SWNT)[&]	III-4040	10.8x10.8x6.1487	192	1680	0.48

[&]- SDS and water molecules are inside one (40,40) carbon nanotube.

7.4. Results and Discussion

7.4.1. Morphology of self-assembled aggregates

Ionic surfactants with 12 or more methyl groups are known to form hemi-cylinders at the water-graphite interface at high surface densities [37,80,284]. At low surface densities they form monolayers, the orientation of which depends on the length of the tailgroup [71,308]. We found that SDS molecules on graphite orient preferentially along the symmetry α-axes when the surface area available for each surfactant headgroup is ~1 nm^2. We compare here the aggregate morphology of SDS adsorbed on (6,6) SWNTs, graphite, and inside (40,40) SWNTs. To visualize the difference in surface aggregate

morphology, in Figure 7-i we show representative simulation snapshots of the 66-I, GRA-I, and I-4040 systems (see Table 7-A for details). The surface area available to each surfactant is 1.8 nm^2 in the case of surfactants on (6,6) SWNTs and ~1 nm^2 in the other 2 cases. For SDS on the (6,6) SWNT, the surfactants form a ring-like structure, similar to the one that has been observed from simulations of zwitterionic lysophosphatidylcholine on SWNTs [305]. Experimental TEM analysis, although performed on dry samples, corroborates the ring-like morphology for surfactants on narrow SWNTs [307]. From our simulations we notice that although most SDS molecules adsorb completely flat on the SWNT surface, some of the headgroups, and the methyl group closest to the headgroup, project into the aqueous phase. The fraction of SDS headgroups that protrude away from the hydrophobic surface is larger when SDS is adsorbed on graphite (GRA-I) and inside (40,40) SWNT. As discussed earlier [71], SDS at low surface densities on graphite yields a monolayer with a preferential orientation. In the right middle panel of Figure 7-i, we observe that SDS surfactants are uniformly distributed on the graphite surface and that the surfactant molecules are oriented parallel, anti-parallel, or at ~60^o to each other. When SDS surfactants are simulated inside (40,40) SWNTs, they yield a cylindrical monolayer-like structure with the SDS molecules oriented parallel to the axis of the nanotube. Within this structure, the headgroups of several SDS molecules protrude towards the aqueous phase at the center of the (40,40) SWNT.

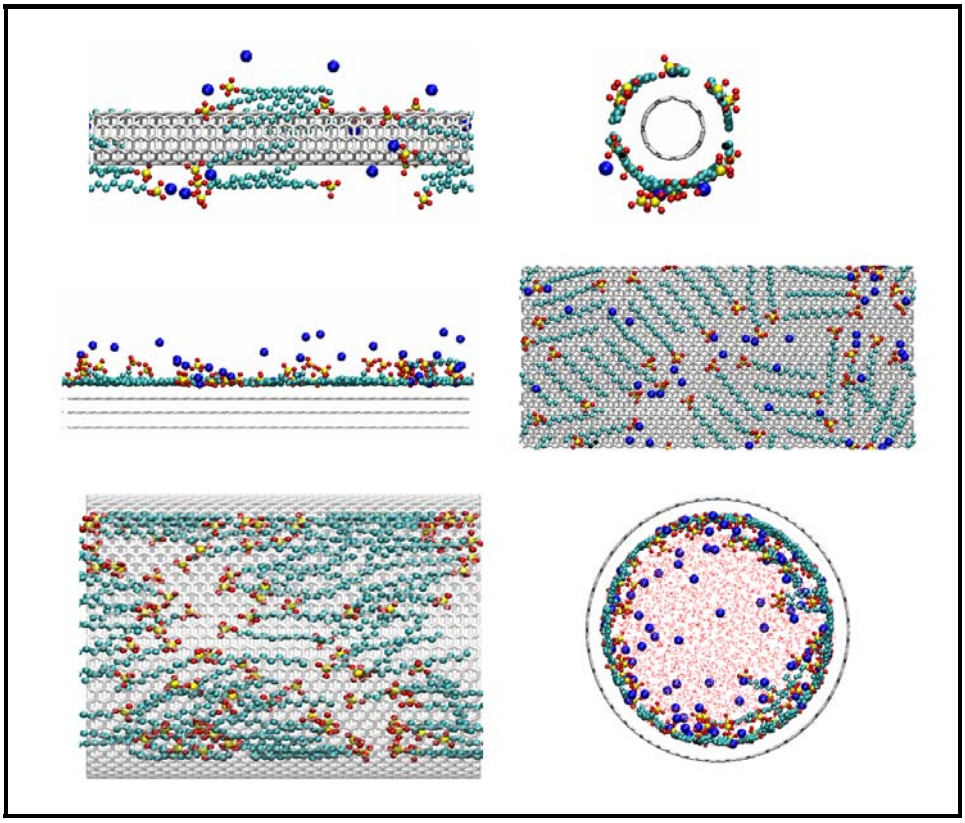

Figure 7-i: (Color online) Side and front view of representative simulation snapshots for SDS surfactants on (6,6) SWNTs (system 66-I, top), on graphite (system GRA-I, middle), and inside (40,40) SWNTs (system I-4040, bottom). Methyl groups, oxygen, sulfur, and sodium atoms are represented as cyan, red, yellow, and blue spheres respectively. Carbon atoms in graphite and carbon nanotubes are shown as bonded carbon atoms. Water, when shown, is represented according to the wireframe representation. All images are generated using the software VMD[309].

In Figure 7-ii we show representative simulation snapshots for the surface aggregates observed when the surface coverage of SDS surfactant exceeds that required to form one monolayer. On graphite (system GRA-II in Table 7-A, middle panel of Figure 7-ii), although the surfactant tails remain to some extent parallel to the α-axes, the adsorbed SDS surfactants yield multiple layers. The orientation of the SDS molecules adjacent to the graphite substrate not only depends on the SDS-graphite but also on SDS-SDS interactions.

SDS molecules on (6,6) SWNTs (system 66-II in Table 7-A, top panel of Figure 7-ii) aggregate without completely covering the surface. This suggests that SDS-SDS interactions dominate SDS-SWNT interactions.

Aqueous SDS surfactants within (40,40) SWNTs (system II-4040 in Table 7-A, bottom panel of Figure 7-ii), at surface density of 0.85 nm^2 per headgroup, yield a thread-like micellar structure. We found that the probability for the SDS headgroups to protrude away from the surface increase as the SDS surface density increases within (40,40) SWNTs (results not shown for brevity).

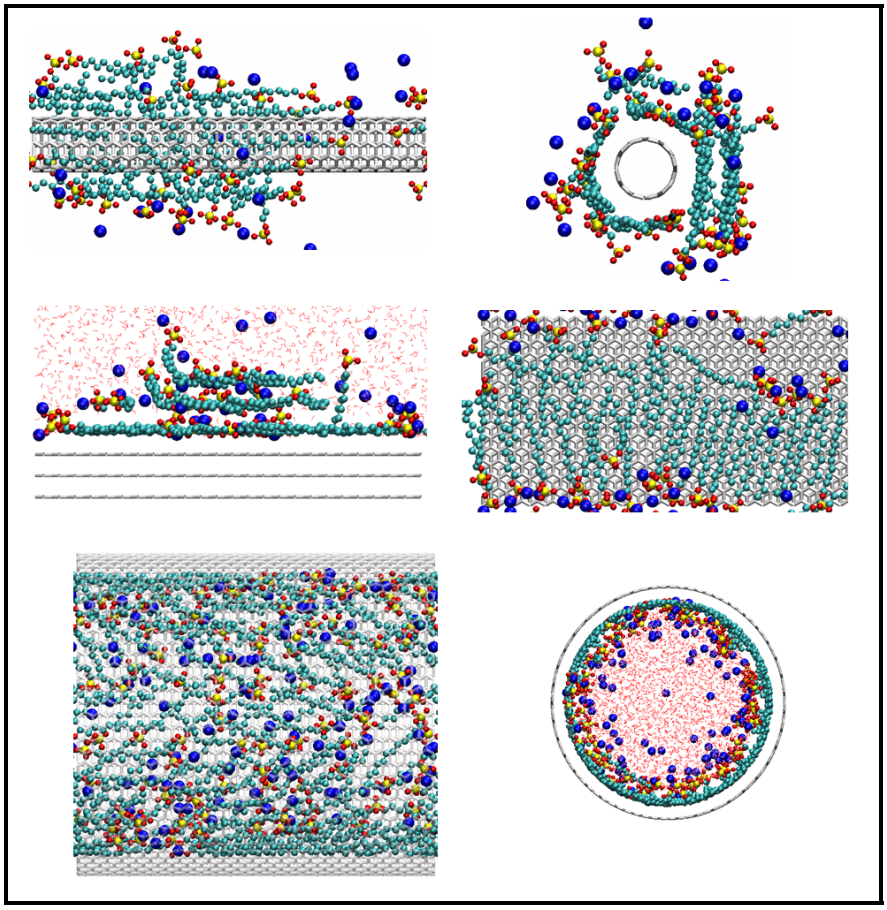

Figure 7-ii: (Color online) Representative simulation snapshots for SDS surfactants adsorbed on (6,6) SWNTs (system 66-II, top), on graphite (system GRA-II, middle), and inside (40,40) SWNTs (system II-4040, bottom). The color code is the same as in Figure 7-i.

At the highest surface density considered here (systems 66-III, GRA-III, and III-4040 in Table 7-A), SDS molecules form hemi-cylinders at graphite-water interface, in agreement with experiments [284] and simulations [77,283] (see middle panels in Figure 7-iii). As shown in Figure 7-iii, we find that on (6,6) SWNTs, adsorbed SDS yield multi-layer micellar structures. The morphology predicted from our simulations agrees with the experimental neutron scattering results of Yurekli et al. [87], as discussed at length elsewhere [69].

Inside (40,40) SWNTs (system III-4040 in Table 7-A), the aggregate morphology is reminiscent of reverse micelles. It appears that the hydrophobic nanotube provides the support for the hydrophobic surfactant tails. The aggregate resembles a cylindrical micelle, although the aggregate structure is not completely symmetric with respect to x and y axes, as observed in the bottom panel of Figure 7-iii, because the SDS tailgroups extend to different extents towards the center of the nanotube. The aggregate structure just discussed agrees with that reported by Arai et al. [299], who simulated coarse grained surfactants inside hydrophobic nanotubes. Those authors predicted that the thread-like micellar phase gives way to bi-layer micelles as the surfactant volume fraction within the nanotube increases. In addition, our all-atom simulations allow us to assess the structure of confined counterions and water molecules. We observe that water molecules yield a helical pattern between the surfactant headgroups along the length of the nanotube. The water molecules are strongly correlated with both SDS headgroups and sodium counterions, yielding a tightly packed structure due to electrostatic effects. We speculate that this cooperative effect involving headgroups, counterions, and water molecules becomes more significant as both the degree of confinement and the

surfactant density increase. Strong water-water association is not surprising, as it is well known that water-water hydrogen bonds become stronger under hydrophobic confinement [310-311]. Further, our results show that under confinement water is strongly attracted to charged species (i.e., the SDS headgroups) yielding both dense water-rich region and water-depleted regions, in agreement with the theoretical suggestions of Rasaiah et al. [311]

More details about the morphology of SDS aggregates on the three substrates are discussed in the SDS Orientation section later in this chapter.

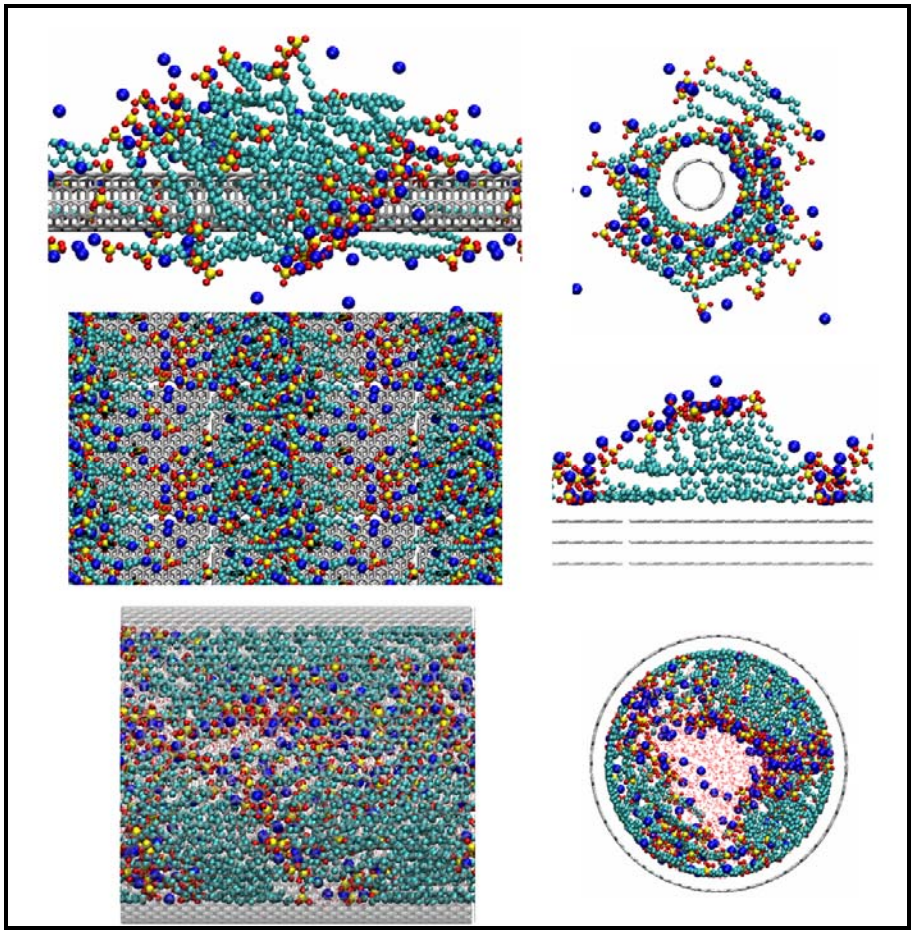

Figure 7-iii: (Color online) Representative simulation snapshots for SDS surfactants adsorbed on (6,6) SWNTs (system 66-III, top), on graphite (system GRA-III, middle), and inside (40,40) SWNTs (system III-4040, bottom). The color code is described in Figure 7-i.

To rationalize the results we invoke geometric arguments. The packing factor of Israelachvili for SDS is less than 0.33 and hence SDS form spherical micelles in aqueous bulk solutions at the critical micelle concentration [36]. In the presence of high concentrations of electrolytes, because of electrostatic shielding between headgroups, SDS yield long cylindrical micelles [4]. On planar graphite substrates strong tail-substrate interactions promote a preferentially oriented monolayer, which becomes a hemi-cylinder as the SDS surface density increases because of the strong tailgroup-tailgroup interactions. Curved substrates impair tail-substrate and tail-tail interactions considerably. For example, in the case of SDS within (40,40) SWNTs, should the surfactants extend radially towards the nanotube center with the tailgroups fixed at the nanotube surface, the distance between different surfactants would decrease as we move from the nanotube surface towards the center of the nanotube. Therefore confinement effects reduce the headgroup-headgroup distance. Equilibration of the consequent headgroup-headgroup electrostatic repulsion can only be achieved by tight packing of headgroups with counterions and water molecules. On a different scenario, should SDS on (6,6) SWNTs extend radially with their tails on the SWNT surface, the surfactant-surfactant distance would increase moving away from the nanotube. This would increase the hydrophobic surface area exposed to water, clearly an unfavorable phenomenon. Consequently, SDS surfactants on (6,6) SWNTs form randomly aggregated structures with multiple layers in which tail-tail contacts are maximized and tail-water contacts are minimized. These effects can be ascribed to changes in tailgroups effective volume and headgroups effective cross sectional area due exclusively to the substrate curvature.

7.4.2. Radial distribution functions

To understand the effect of curvature and surface coverage on headgroup-headgroup and headgroup-counterion structuring, we calculated sulfur-sodium and sulfur-sulfur radial distribution functions (RDFs). Sulfur-sodium and sulfur-sulfur RDFs are representative of surfactant head-counterion and surfactant head-surfactant head RDFs. To account for curvature effects in the calculation of RDFs we employed an algorithm similar to that proposed by Striolo et al.[312]; i.e., we normalize the distribution functions calculated in our simulations with the distribution functions obtained with molecular dynamic simulations involving ideal gas particles of density equal to that of SDS surfactants in the corresponding simulations. The results are shown in Figure 7-iv. The sulfur-sodium RDFs for surfactants on (6,6) SWNTs (top left panel) and on graphite surface (bottom left panel) are similar in terms of peak positions, but the peak intensities differ substantially. Both the RDFs at low surface coverage (compare 66-I and GRA-I systems) have an intense peak at ~4 Å and a small shoulder at 3.2 Å. The intensity of the shoulder at 3.2 Å increases as the surface coverage increases until a clearly discernable peak forms in the case of GRA-III and 66-III systems. The sulfur-sodium RDFs obtained inside (40,40) SWNTs (center left panel of Figure 7-iv) exhibit different behavior. Instead of the peak observed at 3.2 Å for sulfur-sodium RDFs on (6,6) SWNTs and graphite at high surface densities, a shoulder appears within (40,40) SWNTs. The intensity of the peaks at ~4.0 Å and ~5.5 Å for low and intermediate surface densities (systems I-4040 and II-4040), are almost identical, although the intensity of the peak at ~4.0 Å and of the shoulder at ~3.2 Å increase at the highest surface density studied (system III-4040). These data suggest that the high

surfactant concentration, coupled with the small amount of solvent available, promote packing between the headgroups and sodium counterions within (40,40) SWNTs.

Results from the sulfur-sulfur RDFs are more intriguing and clearly highlight the effects of the curvature on the local arrangement of the surfactant headgroups with respect to each other. On graphite, at low surface coverage the headgroup-headgroup attractions are minimal, as indicated by the first weak peak at ~6.5 Å (bottom right panel of Figure 7-iv). As the surfactant surface density increases, the counterion condensation phenomenon, described in our previous work [77], becomes more evident, as suggested by the S-Na RDFs shown in bottom left panels of Figure 7-iv. As a consequence, the headgroups associate more strongly, leading to more intense first peaks in sulfur-sulfur RDFs that are now located at ~4.0 nm (bottom right panel). This systematic increase of headgroup-headgroup packing is only observed on the flat graphite surface but not on the other substrates considered.

On (6,6) SWNTs, as discussed in previous sections, the surfactants form 'rings' at low surface density (66-I) around the nanotubes. Consequently the headgroups are spaced far apart from each other (see peak at ~7 Å in the top right panel of Figure 7-iv). When the surface density increases (system 66-II), the surfactant headgroups pack closer and the RDF intensity at ~7 Å decreases, the first RDF peak position shifts at shorter distances.

The sulfur-sulfur RDFs computed inside (40,40) SWNTs show very atypical behavior. The peaks in these RDFs show no systematic increases or position shifts as the surface density increases, suggesting that the local packing for SDS inside (40,40) SWNTs does not depend on surface coverage until a critical coverage is reached. At

high surfactant concentration the RDFs on different substrates show strong headgroup-headgroup packing.

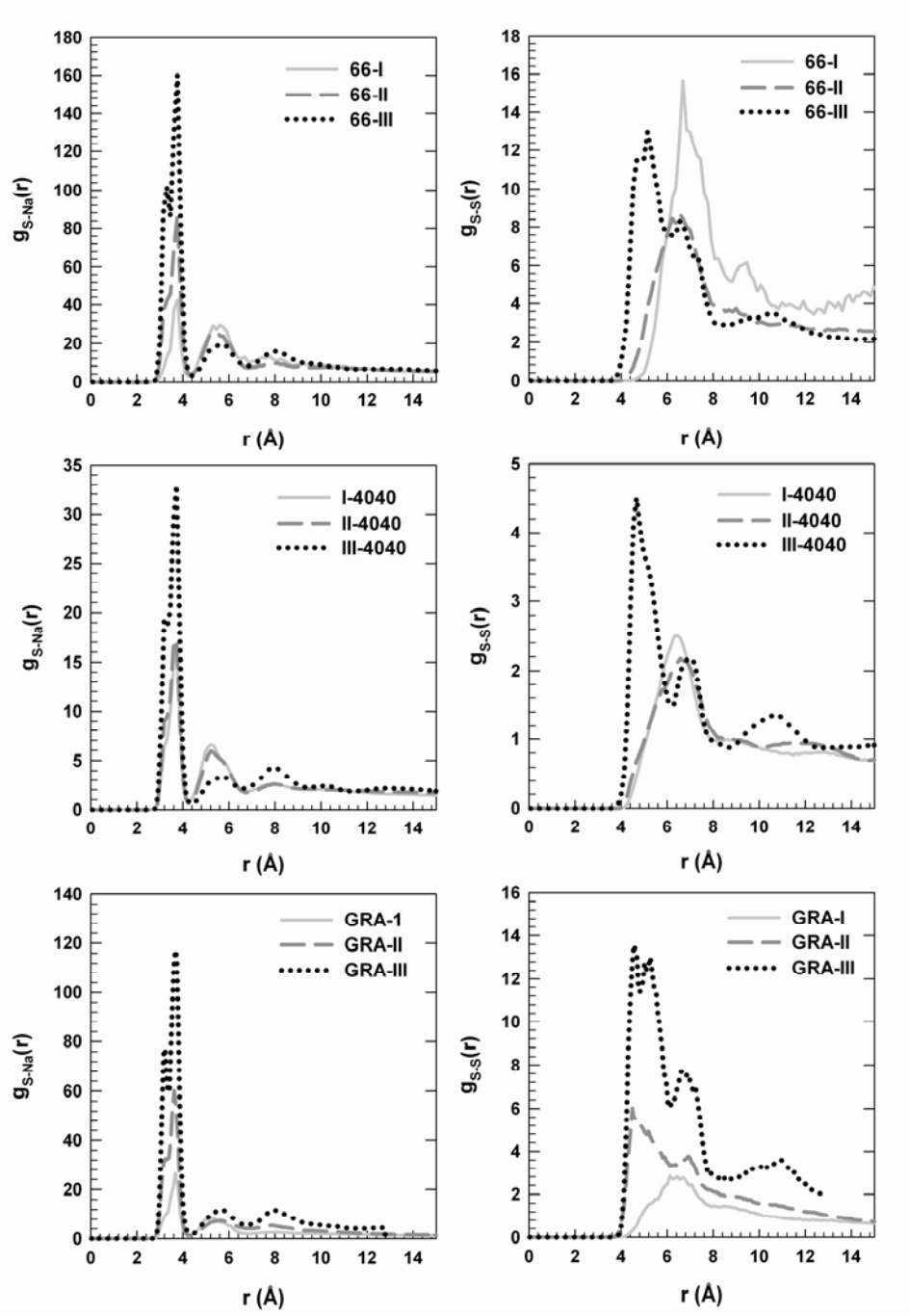

Figure 7-iv: Sulfur-sodium (left panels) and sulfur-sulfur (right panels) radial distribution functions. Top panels report results for SDS on (6,6) SWNTs, middle panels for SDS inside (40,40) SWNTs, and bottom panels for SDS on graphite. Results are shown at increasing surface coverage. Simulation details can be found in Table 7-A.

7.4.3. Density profiles

The density profiles of SDS headgroups, SDS tailgroups, and sodium ions away from the carbon-based substrates are shown in Figure 7-v. The center of mass of the sulfate group is used to calculate the density profile for surfactant headgroups. The headgroup density profile for I-4040 and GRA-I systems (top left panel of Figure 7-v) indicate that it is equally probable to find the headgroups at 0.35 nm and 0.55 nm away from the substrate surface. The peak at 0.55 nm and the shoulder at 0.75 nm show that a few headgroups project away from the carbonaceous substrate towards the aqueous phase. The density profiles of the tailgroups in 66-I, GRA-I and I-4040 display a strong first peak at 0.35 nm, as shown in the middle left panel of Figure 7-v, indicating that most of the tailgroups remain at contact with the substrate. Only a small fraction of tailgroups are not completely adsorbed as can be observed from the peak at 0.5 nm.

In the density profile of counterions shown in the bottom left panel of Figure 7-v, we observe that on (6,6) SWNTs (system 66-I) the counterions do not accumulate at the SDS–SWNT interface as much as they do on the other substrates considered. SDS adsorption on electrically neutral hydrophobic surfaces generates an electric charge density near the surface that promotes accumulation of the counterions. It is worthy to point out that at low surface density, for SDS adsorbed on graphite and within (40,40) SWNTs counterion density peaks are half the headgroup density peaks, whereas on (6,6) nanotubes the counterion density peak intensity is significantly less than half the peak intensity of headgroup density profile. Surface curvature affects the surfactant aggregate morphology, and hence also affects the density distribution of the counterions. At low surface coverage, when the adsorbed surfactants form a single

monolayer, it is possible to compare the results of counterion distribution simulated to those predicted by theoretical models such as Manning's condensation theory,[294,296] which invokes the Debye-Huckel approximation [297]. The Manning's condensation theory predicts that a spherical surface provides little or no counterion condensation, cylindrical surfaces tend to accumulate few counterions above a critical surface charge density, and flat surfaces accumulate the highest concentration of counterions [295]. The condensation theory assumes that the counterion density far away from the surface is negligible, thus direct comparison of the counterion distribution inside the (40,40) SWNT even at low surface coverage is not possible. Cumulative density profiles obtained from Figure 7-v (not shown for brevity) show that counterions in the GRA-I system do not completely accumulate on graphite, even when covered by SDS. Instead, we find that a few sodium ions remain in the bulk liquid and near the vacuum-water interface (in qualitative agreement with Ref. [313]). Counterion-condensation effects are more pronounced inside the SWNTs, due to confinement, than on graphite or on (6,6) SWNTs. The multiple peaks for counterions observed even at low surface density are consequence of excluded volume effects and of ion-ion correlations.

At high surface density, the density profiles for headgroups (top right panel of Figure 7-v) and tailgroups (middle right panel of Figure 7-v) are consistent with the formation of multi-layer structures on (6,6) SWNTs, hemicylindrical micelles on graphite, and reverse micelles within (40,40) SWNTs. In the counterion density profiles for systems 66-III, GRA-III, and III-4040 (bottom right panel of Figure 7-v), we observe that the density peaks are positioned at the same distance from the surface as observed for the density profiles of the surfactant headgroups, indicating close packing

of headgroups and counterions. In particular, at ~1.7 nm from each substrate the counterion density is almost equal to the headgroup density. These data, which support the conclusion that the morphology of surfactant aggregates strongly depends on the substrate curvature, cannot be easily compared to predictions from the Manning's condensation theory because the identification of a smooth interface is not unequivocal.

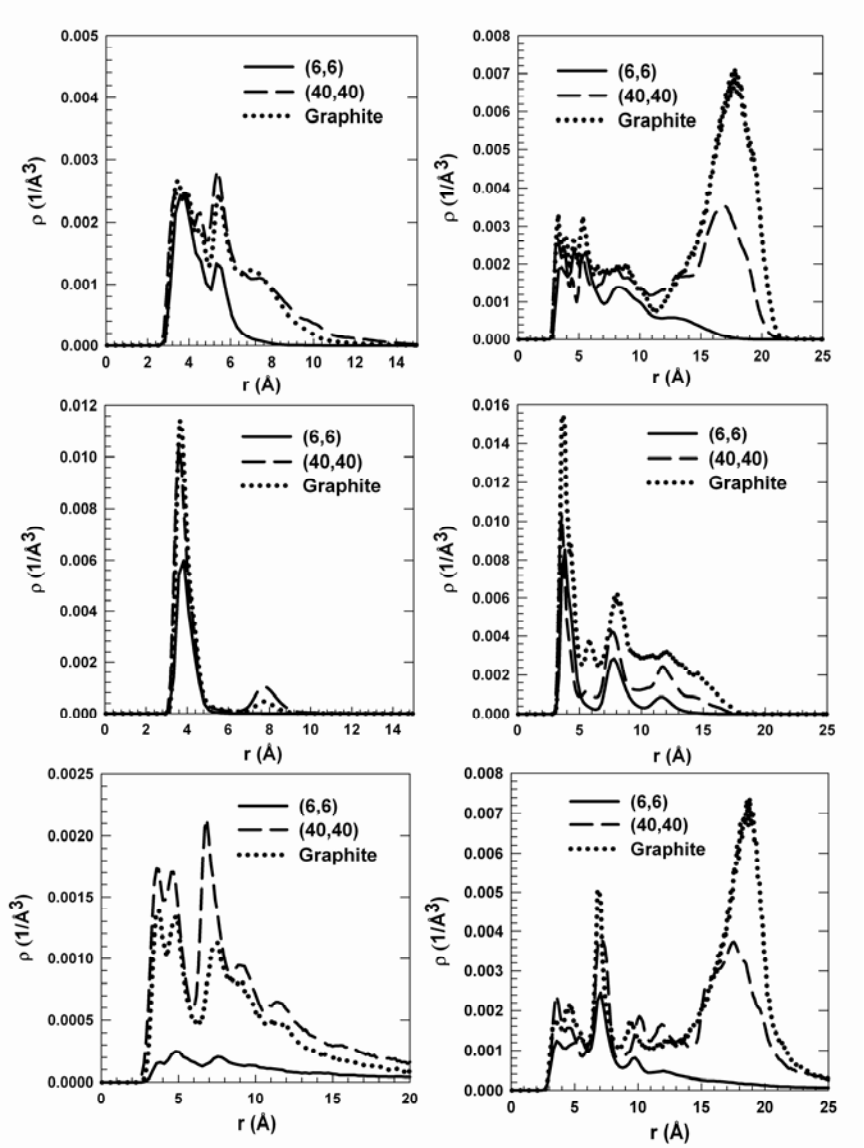

Figure 7-v: Headgroup (top), tailgroup (middle) and counterion (bottom) density profiles as a function of distance from the surface for the systems at low SDS surface density (systems 66-I, GRA-I, and I-4040, left panels) and at high SDS surface density (systems 66-III, GRA-III, and III-4040, right panels). See Table 7-A for simulation details.

7.4.4. Surfactant headgroup-counterion residence correlation functions

Because the results discussed above suggest that the counterions are strongly correlated to the surfactant headgroups, it is of interest to quantify how long each counterion resides in contact with any given surfactant headgroup. The corresponding residence correlation function is calculated herein as

$$C(t) = \left\langle \frac{\sum_{i=1}^{N} O_i(t) O_i(0)}{\sum_{i=1}^{N} O_i(0) O_i(0)} \right\rangle \quad . \tag{7.1}$$

In Eq. (7.1) angular brackets designate ensemble averages and the term $O_i(t)$ discriminates whether a sodium ion is or is not in the vicinity of one SDS headgroup (i.e., within a distance of 4.38 Å, which corresponds to the first minimum in the S-Na radial distribution function) at time t. $O_i(t)$ equals 1 when the sodium ion is in the vicinity of the surfactant head, 0 otherwise. The correlation function is expected to decay from 1 to 0 as time progresses in response to the movement of sodium ions. The slower the decay, the longer the counterions reside near the surfactant headgroups.

In Figure 7-vi we show the residence correlation function for the sodium counterions obtained during the different simulations. We observe that at similar surface coverage the sodium counterions stay longer near the SDS headgroups in the case of the I-4040 system compared to systems 66-I and GRA-I. On (6,6) SWNTs (top panel of Figure 7-vi) , when the surface area per each surfactant is ~1.8 nm^2, the correlation function decreases very rapidly. From Figure 7-i we had observed that at this surface coverage most of the surfactants adsorb on the nanotube and we could not detect

aggregation among SDS surfactants. The absence of aggregation allows for the effective screening between counterions and headgroups by water molecules, resulting in the fast decay of residence auto-correlation function. In fact, in all the plots showed in Figure 7-vi, we observe that the correlation functions decay faster for the simulations with low surfactant concentrations on all substrates. The correlation functions decay significantly more slowly at high SDS surface densities; i.e., upon the formation of surfactant aggregates. This observation further strengthens our previous results according to which counterion-condensation is an important phenomenon that contributes to determine the morphology of surfactant aggregates.[77] The system pressure would likely have an influence on the counterion dynamics, but the association between surfactant headgroups and counterions is the dominant phenomenon that dictates the results in Figure 7-vi, as demonstrated by additional simulations conducted in the NPT ensemble (P=1 bar) for SDS on (6,6) SWNTs, and others conducted in the NVT ensemble for SDS within (40,40) SWNTs in the presence of different amounts of water molecules. These results are described in later in this chapter.

Several experiments and simulations [69,77,87,284,299-301] suggest that self-assembled aggregates have different morphologies within confined regions vs. on flat surfaces, and a very well defined structure of surfactants adsorbed on SWNTs has not yet been observed. From the correlation functions just discussed, it is obvious that large residence times are indicative of formation of long-lasting aggregates. On the contrary, short residence times indicate very diffuse and possibly disordered surface aggregate structures. This result may lead to the design of experimental tools to discriminate, e.g., the effectiveness of a given surfactant to stabilize aqueous carbon nanotube dispersions.

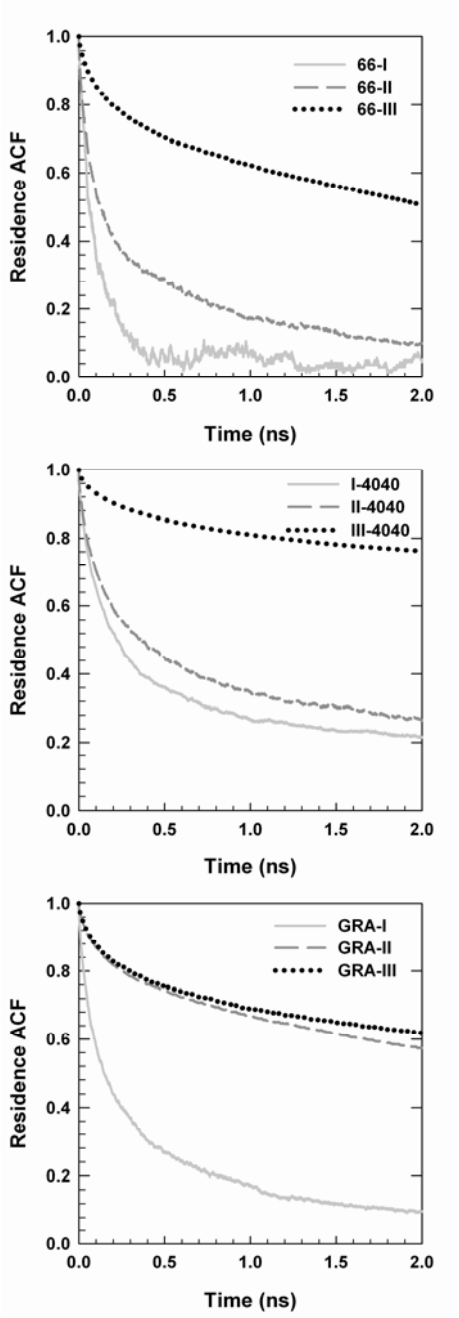

Figure 7-vi: Residence correlation functions for sodium ions in the vicinity of SDS headgroups. Results are shown for SDS surfactants on (6,6) SWNTs (top), inside (40,40) SWNTs (center), and on graphite (bottom) at three surface coverages. Simulation details are shown in Table 7-A.

7.4.5. SDS Orientation

From Figure 7-i it is clearly visible that the orientation of SDS molecules on (6,6) SWNTs is mostly parallel to the axis of the nanotube, whereas not all SDS molecules inside the (40,40) SWNTs are parallel to the nanotube axis. On graphite the SDS molecules adsorb preferentially along the α-axes. We quantify these observations in Figure 7-vii, where we show the probability distribution of the angle formed between the CH_3-S vector of SDS molecules and the nanotube axis when SDS molecules are adsorbed on SWNTs. Angles of 0^o and 180^o indicate that the SDS molecules are parallel to the nanotube axis. An angle of 90^o indicates that SDS molecules are perpendicular to the SWNT axis. For SDS on graphite, the angle shown in Figure 7-vii is the one formed by the CH_3-S vector of SDS and the α-axes of graphite [265]. It is worth remembering that the SWNTs used in the simulations are of the armchair type, thus the SWNT axis is parallel to α-axis of the graphite sheet rolled up to form the nanotube. In the case of graphite (as well as nanotubes), three symmetry α-axes are present, each separated by 60^o. Thus in Figure 7-vii the angles 0^o, 60^o, 120^o, and 180^o are all representative of α-axes, all equivalent in the case of graphite, but different with respect to the carbon nanotube axis. The angles 30^o, 90^o and 150^o correspond to β-axes.

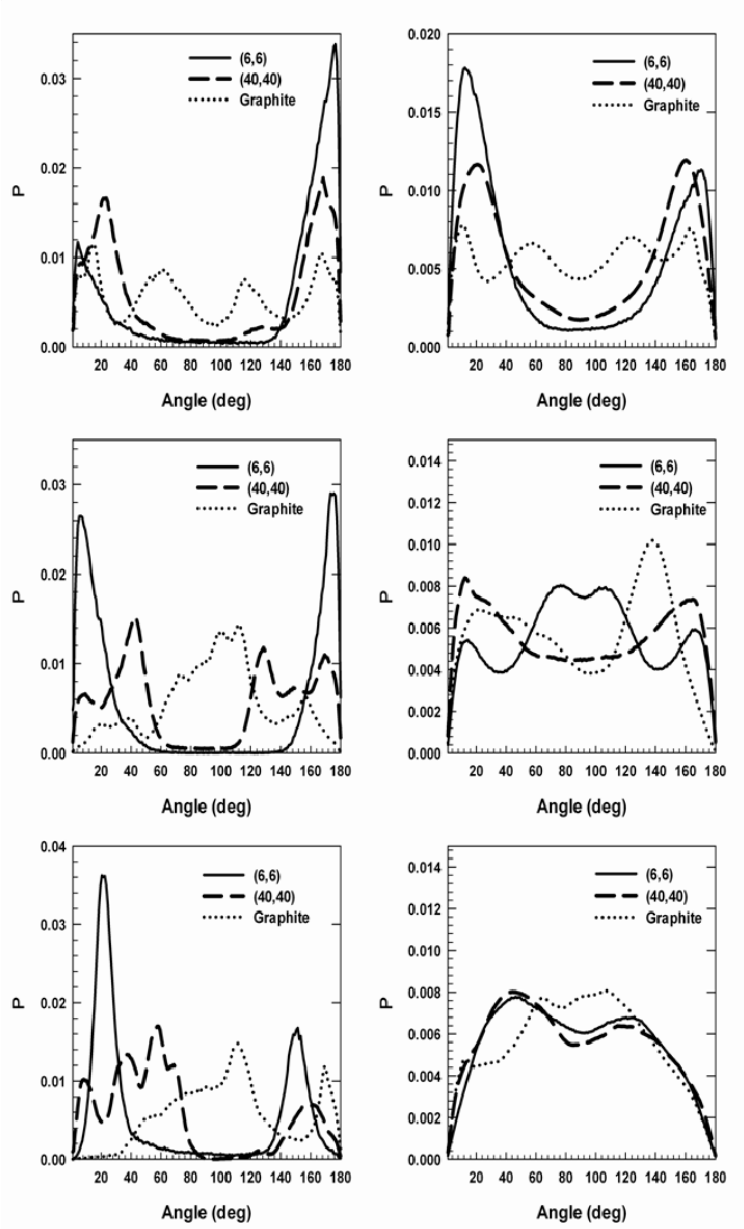

Figure 7-vii: Left panels: Orientation of SDS molecules in the first layer with respect to SWNT axis for (6,6) and (40,40) SWNTs and with respect to the α symmetry axis for graphite. Right panels: SDS-SDS orientation. Top panels report results for systems with low surface density (systems 66-I, GRA-I, I-4040), middle panels are for the results of medium surface densities density (systems 66-II, GRA-II, II-4040), and bottom panels are for the results of high surface densities density (systems 66-III, GRA-III, III-4040). Simulation details can be found in Table 7-A.

In the top left panel of Figure 7-vii we compare the population distribution of the orientation angle for SDS at low surface densities on the 3 substrates (systems 66-I, GRA-I, and I-4040). For SDS on graphite, the population distribution peaks at angles

that are multiples of 60^o. This preferential orientation is observed when the surface area per surfactant headgroup is ~1 nm^2, which corresponds to the formation of one complete monolayer.

The SDS surfactants are oriented parallel to the axis of the (6,6) nanotube. SDS surfactants within (40,40) SWNT are oriented parallel to the axis of the nanotube, but the fraction of the SDS molecules that are parallel is slightly less than that observed in the case of (6,6) SWNTs. In the middle left panel of Figure 7-vii we compare the orientation of SDS molecules whose headgroup is at distances less than 0.6 nm for systems 66-II, GRA-II, and II-4040. On (6,6) SWNTs SDS molecules remain parallel to the nanotube axis. On graphite one broad peak centered at ~100^o is observed, indicating that the SDS molecules undergo a reorientation upon increasing the surfactant density.

Within (40,40) SWNTs, the appearance of peaks at 40^o, 130^o and 170^o indicates that the SDS molecules close to the nanotube surface no longer assume a preferential orientation with respect to the nanotube axis. This happens because for the SDS within (40,40) SWNTs at this surface coverage at least 2 methyl groups in the tailgroup are not adsorbed on the nanotube surface, thus weakening the tail-substrate attractive interactions. This observation agrees qualitatively with previous reports that showed that surfactants or alkyl chains containing less than 12 methyl groups do not orient preferentially when adsorbed on graphite.[314-316]

In the bottom left panel of Figure 7-vii we show the probability distribution of the first layer of SDS molecules at the largest surface densities considered (systems 66-III, GRA-III, and III-4040). There is a small shift in the intensity of peak for SDS on 66-III compared to 66-II, i.e. the SDS molecules adsorbed on (6,6) nanotube are

oriented at ~20^{o} and 155^{o} with respect to the nanotube axis. In Figure 7-iii we had observed that there is a formation of a shapeless surface aggregate on (6,6) SWNTs at high surface density. The features of this aggregate are responsible for the change in surfactant orientation.

On graphite the probability distribution peaks at ~110^{o} and ~170^{o}, indicating that although some surfactants remain oriented along the symmetry axes of the graphite, the fraction of molecules oriented along the symmetry axes decreases considerably compared to GRA-I. Inside (40,40) SWNTs our results show that there is no particularly preferred orientation for the adsorbed surfactants. In the right panels of Figure 7-vii we show the orientation of SDS molecules with respect to each other. The data are calculated considering all the SDS molecules within each system. This information complements the results provided in the left panels of Figure 7-vii. For SDS on (6,6) SWNT at low surface coverage (system 66-I), SDS molecules orient either parallel to other SDS molecules or anti-parallel to them, as can be evinced from the peaks at ~10^{o} and 170^{o} in the top right panel of Figure 7-vii. For SDS on graphite (system GRA-I) we observe regular periodic peaks at multiples of 60^{o}. This information, combined with the results for GRA-I from the top left panel of the same figure, indicates that the SDS molecules orient along the symmetry axes of graphite.

The results for surfactants inside (40,40) SWNTs (system I-4040) at low surface coverage are similar to those on (6,6) SWNTs, i.e. SDS molecules are oriented either parallel or anti-parallel to each other.

At medium surface coverage as shown in the middle right panel of Figure 7-vii, for surfactants on (6,6) nanotube, the probability distribution of the SDS-SDS angle

peaks around 90^{o}. Using the complementary information from the SDS orientation angle presented in the left panels of Figure 7-vii, we deduce that surfactant molecules that are not within the layer closest to the nanotube are oriented at 90^{o} to each other or at 90^{o} to the molecules present in the layer adjacent to the nanotube. The presence of the first layer allows the subsequent layers to be oriented in any possible angle. For SDS molecules on graphite (system GRA-II), the SDS-SDS orientation peaks at ~140^{o}.

Interestingly, for SDS surfactants within (40,40) SWNT (system II-4040), the probability distribution exhibits two peaks at ~10^{0} and ~170^{o}. At even higher surface densities, the probability distribution of SDS-SDS angle does not have any distinct peaks, as can be observed in the bottom right panel of Figure 7-vii, indicating that the substrate no longer affects the orientation of the SDS surfactants with respect to each other.

7.4.6. Pressure Effects

In Figure 7-viii we compare the density profiles for the surfactant head groups on (6,6) SWNTs at the highest surface coverage considered (system 66-III) as obtained running our simulations in either the NVT or NPT ensembles (P=1bar). Within statistical accuracy, the results are very similar. Namely, the distribution of the head groups near the surface is almost identical at small distance (up to ~5 Å) from the SWNT surface. The density profiles differ somewhat at larger distances but only with respect to the intensity of the peak, while the peak positions are retained.

In Figure 7-ix we compare the SDS surfactant head group density profiles within (40,40) SWNTs (system III-4040) with different number of water molecules introduced inside the (40,40) SWNT. The system III-4040_II contains 668 water molecules; the

system III-4040 (discussed in the text above) contains 1680 water molecules. Even with this large difference in the number of water molecules inside the (40,40) SWNT, the results are almost identical at small distances from the nanotube surface, but at larger separations (> 10 Å) the peaks shift by ~1 Å. These results indicate that the counterion-head group association at close distances is insensitive to small changes of pressure in the surrounding fluid. The dynamics of such association however may be affected by the pressure, as the pressure directly affects the diffusion and packing characteristics of the particles within and around the surface aggregate.

In Figure 7-x we compare the residence ACF's for counterions close to the headgroups of SDS surfactants on (6,6) SWNTs at the highest surface coverage in the NVT and NPT ensembles. Once again, the results obtained in the two ensembles are very similar to each other, supporting the conclusion that the results discussed in the present manuscript are not affected by small changes in the system pressure.

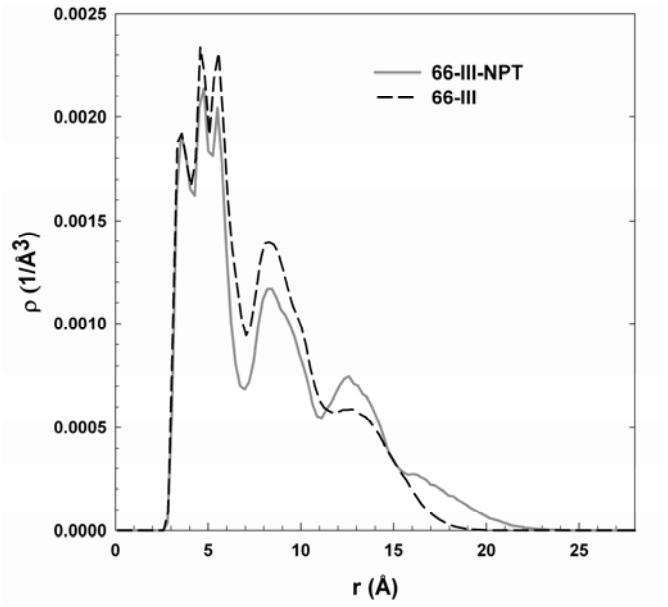

Figure 7-viii: Headgroup density profiles as a function of distance from the SWNT surface for the system 66-III in the NVT (dotted line) and NPT (solid line, P = 1 bar) ensembles.

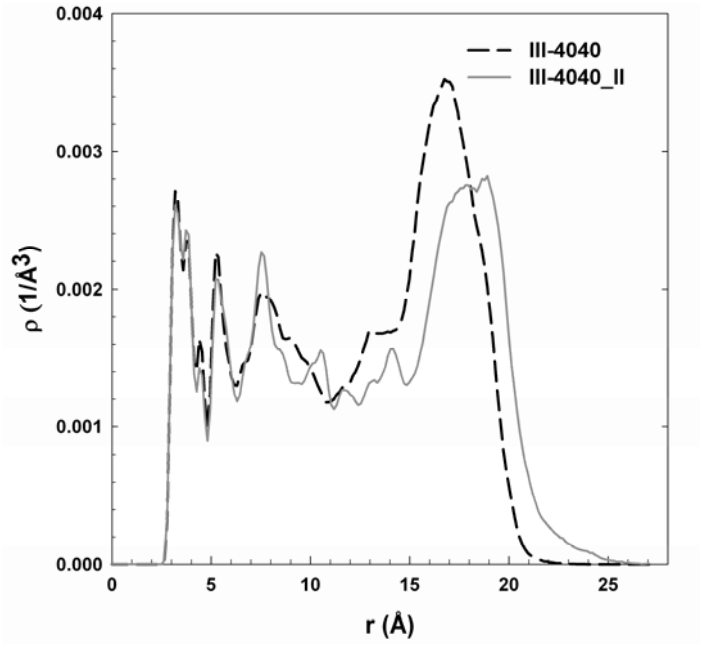

Figure 7-ix: Headgroup density profiles as a function of distance from the SWNT surface for the system III-4040 (dotted line), with 1680 water molecules, and for the system III-4040_II (solid line), with 668 water molecules.

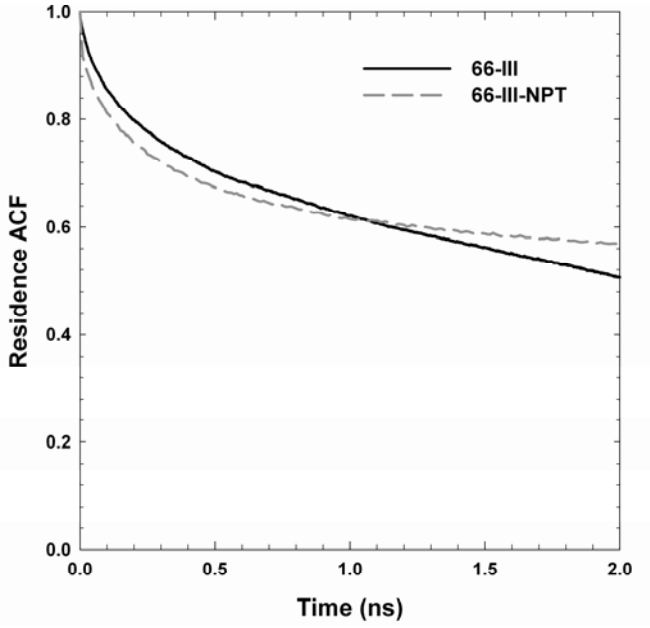

Figure 7-x: Residence correlation functions for sodium ions in the vicinity of SDS headgroups. Results are shown for SDS surfactants on (6,6) SWNTs at highest surface coverage in both NVT (solid line) and NPT (P = 1 bar, dotted line) ensembles.

7.5. Conclusions

Molecular dynamic simulations of SDS surfactants adsorbed on the outer surface of (6,6) SWNTs, on graphite, and within (40,40) SWNTs have been performed to assess the effect of curvature on the surfactant aggregate morphology. The changes in aggregate morphology were quantified using radial distribution functions and density profiles. The density profiles indicate that the probability of finding counterions close to headgroups increases with the increase in surfactant density, but decreases as the substrate curvature increases at equal SDS surface coverage. The results from residence correlation functions indicate that the mobility of counterions and curvature are inversely related. Especially for surfactants within the (40,40) SWNTs, counterions are packed strongly to the surfactant headgroups and reside for long times next to them.

The results presented confirm that counterion-condensation effects are important in determining the morphology of SDS surface aggregates. By promoting or impeding counterion-condensation phenomena, the substrate curvature is strongly reflected on the morphology of the supported surfactant aggregates.

8. Flavin Mononucleotide and Sodium Dodecyl Sulfate on Single-Walled Carbon Nanotubes: Insights from Molecular Dynamics Simulations

8.1. Abstract

Techniques for separating bundles of carbon nanotubes into homogenous dispersion are still under development, although a few methods have been successful at the laboratory scale. Understanding the effective interaction between carbon nanotubes in the presence of dispersing agents will provide the necessary information to develop better methods and also to refine the existing ones. We present here results from all-atom molecular dynamics simulations for aqueous flavin mononucleotide (FMN), which has been found experimentally to efficiently separate single-walled carbon nanotubes (SWNTs) based on diameter and chirality. We report results for the aggregate morphology of FMN on SWNTs of different diameters, as well as the potential of mean force between (6,6) SWNTs in the presence of aqueous FMN. The results are compared to the potential of mean force between SWNTs in aqueous sodium dodecyl sulfate (SDS). Our detailed analysis is used to explain the role of FMN, water, and sodium ions in providing a strong repulsive barrier between approaching SWNTs.

8.2. Introduction

Single walled carbon nanotubes (SWNTs) are one-dimensional materials with exceptional mechanical,[317] electrical, thermal[271] and electronic properties.[86] Application of single walled carbon nanotubes in electronics[318] or opto-electronics[319] devices requires their efficient separation based on chirality and diameter. Their use in therapeutics[74,320] and composites[321] requires homogenous dispersions within cellular environment or organic materials, respectively. Hence, separating and dispersing SWNTs continues to attract scientific attention. There has been success in separating SWNTs by density gradient centrifugation, especially at the laboratory scale, using a variety of surfactants.[60,67-68,84-86,277,290,322] Recently, DNA sequences that can selectively sort nanotubes based on chirality were discovered,[323] although their applicability to large-scale separations is not yet feasible. A simple gel-based method to separate metallic from semi-conducting SWNTs which appears to be easily scalable has also been reported.[324-325] Several excellent reviews are available concerning the state of the art of separating SWNTs after production, or of selectively growing SWNTs based on their chirality and diameter.[61,65,326-327]

Different surfactants yield a variety of molecular structures on SWNTs. These structures are thought to determine the buoyancy differences utilized in centrifugation-based separation methods. Scattering experiments[87] and molecular dynamics (MD) simulations can be used, complementarily, to investigate such structures.[69-70,280,305-306,328-329] It is known from experiments[87] and simulations[69-70,280,305-306,328-329] that sodium dodecyl sulfate (SDS) forms a variety of disordered aggregates on SWNTs at different surface densities. At low surface density aqueous SDS surfactants yield rings around

SWNTs. Increasingly order-less aggregates form with increasing surface density.[69-70,87,330] Using coarse grained simulations, researchers have found that many different aggregate morphologies are possible on SWNTs.[330] MD simulations for the aggregate structure of a SWNT covered with SDS at high surfactant coverage,[331] and the potential of mean force between SWNTs in the presence of SDS were recently reported.[331-332] The results show that the potential of mean force between the SWNTs is affected by the structure and morphology of the surfactant aggregates. Experimentally, it has been observed that excessive surfactant can result in flocculation of nanotubes,[333] but it is also known that surfactants at very low concentrations cannot efficiently disperse SWNTs[84-86,277,322] For biological applications the use of SDS, as well as that of sodium dodecyl benzene sulfonate (SDBS) may result in cytotoxicity.[334] Hence the use of biologically benign amphiphilic molecules like sodium cholate[60] and flavin mononucleotide (FMN)[67-68] has gained prominence. The presence of planar aromatic cyclic structures in the surfactants is considered to be the main reason for the observed effectiveness in dispersing and separating SWNTs. To design nanotube-specific stabilization processes it is necessary to determine the surfactant aggregate morphologies on SWNTs of various diameters. By comparing such results obtained for FMN to those available for SDS will allow us to better understand the effect of surfactant molecular structure on the effectiveness in dispersing SWNTs.

In this study we report the aggregate morphologies of FMN on SWNTs with different diameters as obtained via all-atom MD simulations. We also compute the potential of mean force (PMF) between two (6,6) armchair SWNTs in aqueous FMN and SDS at two surface densities. We compare the PMFs obtained from our study to

those available in the literature[331] to understand the effect of the amphiphilic surface density on the SWNT-SWNT PMF.

8.3. Simulation Methodology

The extended simple point charge (SPC/E) model[126] was used to describe water molecules in our MD simulations. The aggregate morphology of FMN was studied on (6,6), (8,6), (12,12), and (16,16) SWNTs. The center-to-center carbon-carbon distance across the nanotube diameter is 8.12 Å, 9.46 Å, 16.27 Å, and 21.70 Å, respectively, for the four nanotubes considered. SWNTs were maintained rigid during the course of the simulation. The force field parameters used for carbon atoms in the SWNT are identical to those used in our previous publications.[69-70] FMN molecules contain a tricyclic heteronuclear organic ring (isoalloxazine) and a d-ribityl phosphate group with affinity for polar solvents. FMN was modeled according to the AMBER force field.[147] In our model the two –OH groups bonded to the phosphorous atom in the d-ribityl phosphate group are dissociated.[335] We substituted each hydrogen atom of those –OH groups with sodium counterions. The force field parameters used for sodium ions have been reported previously, together with the models implemented to simulate SDS.[208]

The leap frog integration scheme within the GROMACS molecular dynamics simulation package[133-135,222] with a time step of 2 fs was used to integrate the equations of motion. A Berendsen barostat[336] with a time constant of 500 fs, compressibility of 4.5e-5 (1/bar), and reference pressure of 1 bar was used whenever the isobaric-isothermal ensemble (constant number of particles N, constant pressure P, and constant temperature T) was implemented. The canonical ensemble (constant number of particles N, volume V, and temperature T) was employed during the production phase. The

Nosè-Hoover thermostat[337-338] with a time constant of 100 fs was used to maintain T constant. The particle mesh Ewald method[137] with cutoff of 1.4 nm and Fourier grid spaced with 0.12 nm, tolerance of 1 x 10^{-5}, and fourth order interpolation was used to compute the long-range electrostatic interactions. A switch function starting at 1.2 nm was used such that the Lennard-Jones potential smoothly goes to zero at 1.4 nm. During the production phase one simulation configuration was saved every 2 ps for analysis of the aggregate morphology.

29 FMN molecules were concentrically placed around one SWNT as shown in Figure 8-i. 58 sodium ions, necessary to neutralize the 29 FMN molecules, were placed randomly throughout the simulation box. Water molecules were then used to fill the simulation box of size 8.0x8.0x6.15 nm^3. The NPT ensemble (P = 1 bar, T = 300 K) was used during the initial equilibration phase to bring the system at ambient conditions. This phase lasted generally for less than 5 ns. We conducted 30.0 ns of simulation in the NVT ensemble at 300 K, followed by 10.0 ns at 400 K, 10.0 ns at 500 K, and 20.0 ns at 300 K in the NVT ensemble. To ensure that the system was properly equilibrated all the groups bearing point charges in the FMN molecules were made neutral and the simulation was run for 20.0 ns in the NVT ensemble. This step was followed by reinsertion of charges and 30.0 ns of simulation in the NVT ensemble at 300 K. Thus each system was simulated for up to 120.0 ns. We compared the results computed from trajectories from 60.0 to 70.0 ns to those obtained from 100.0 to 110.0 ns. In all cases considered here we did not observe any significant difference in the aggregate morphology of FMN molecules before removing the charges and after reinserting the charges on all the FMN groups.

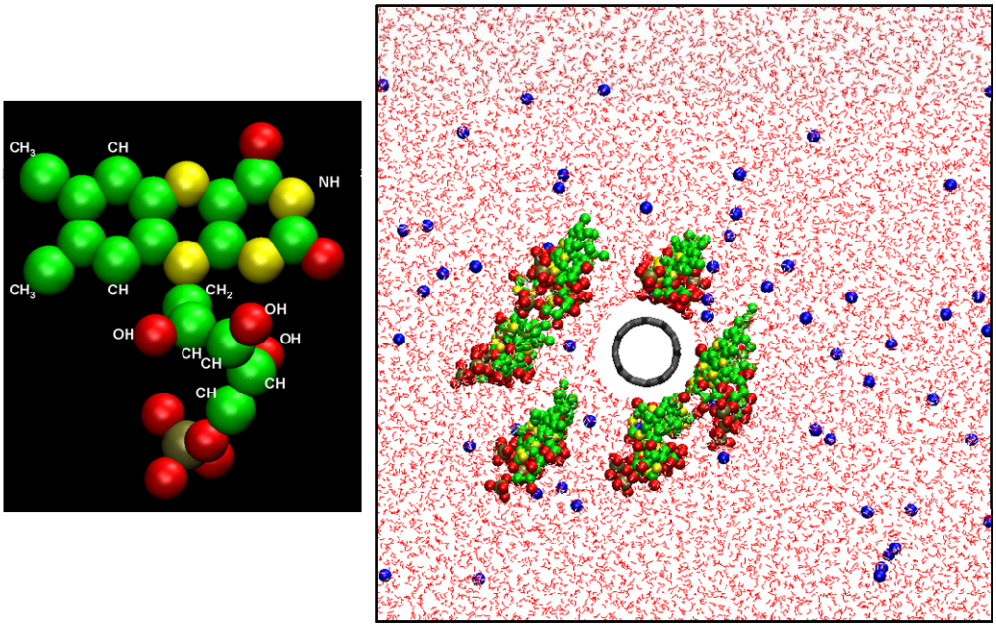

Figure 8-i: Left: FMN molecule. Green spheres represents aromatic carbon atoms, –CH, -CH_2 or –CH_3 groups; yellow spheres represent nitrogen and –NH; red spheres represent oxygen atoms in phosphate groups and isoalloxazine as well as –OH groups in the d-ribityl chain; tan spheres represent phosphorus atoms. Right: Initial configuration of FMN molecules around one (6,6) SWNT. The blue spheres represent sodium counterions. Water molecules are represented as red lines in the wireframe convention. The grey circle corresponds to the (6,6) SWNT. All images were prepared using the VMD visualization suite.[309]

We used the final equilibrium configuration of FMN on (6,6) SWNT and removed 7 FMN molecules and 14 sodium atoms to obtain a system with low FMN surface coverage. The surface area available for FMN is ~0.94 nm^2 and ~1.24 nm^2 for high and low surface coverage, respectively.

We used both the high and low surface coverage on (6,6) SWNT to study the PMF between two (6,6) SWNTs. The equilibrium configuration of the FMN-SWNT system was replicated. The replicated FMN-SWNT aggregate was inserted parallel to the original one in a simulation box of size 7.75x7.22x6.1487 nm^3. Water molecules and sodium counterions were randomly placed throughout the box. The NPT ensemble

was used to ensure that the system was simulated at ambient conditions. The simulation box was equilibrated for 20.0 ns. The final configuration was used as the starting configuration for 57 consecutive simulations, each conducted at a different separation between the SWNT centers of mass. The SWNTs were connected through a harmonic potential, following the umbrella-sampling technique.[258,339-340] The SWNT-SWNT separation distances employed ranged from 3.0 Å to 15.0 Å. The force constant used for the harmonic potential ranged from 5 kcal/mol nm^2 to 100 kcal/mol nm^2. We used 4.0 ns of equilibration at each separation followed by at least 3.0 ns of production phase in which the distance between the SWNTs centers of mass were recorded every 20 fs. We employed the weighted histogram analysis method (WHAM)[341-343] to extract PMF profiles from the simulation trajectories.

Armchair (6,6) SWNTs were modeled as rigid cylinders, composed of discrete carbon atoms, which can translate only along the x-direction (perpendicular to the SWNTs axis).

For SDS on SWNTs, the two equilibrium configurations reported in our previous publication[69] with coverages corresponding to 0.98 nm^2 and 0.44 nm^2 were used as starting configurations for PMF calculations. The PMFs were computed following the procedure described above, but within a simulation box of 8.5x7.57x6.15 nm^3, 5.0 ns equilibrium, and 5.0 ns production phase.

8.4. Results

8.4.1. Aggregate Structure

In Figure 8-ii we show representative simulation snapshots of 29 FMN molecules adsorbed on (6,6), (8,6), (12,12), and (16,16) SWNTs. The available surface area per each FMN is of ~0.94 nm^2, ~1.03 nm^2, ~1.48 nm^2, and ~1.84 nm^2 on (6,6), (8,6), (12,12), and (16,16) SWNTs, respectively. Because FMN molecules in the bulk can only self-aggregate forming dimers,[344] most of the FMN molecules simulated herein remain on the SWNT surface. In general our results show that the FMN isoalloxazine group remains for the most part adsorbed on the SWNT walls, while the d-ribityl phosphate group extends towards the aqueous phase. On SWNTs of diameter < 1.0 nm [(6,6) and (8,6) SWNTs], most of the SWNT surface is completely covered by the FMN molecules. Additional FMN molecules agglomerate in part within the bulk solution, while parts of the (12,12) and (16,16) SWNTs surfaces are exposed to water when there are same number of FMN molecules present on the SWNT surface. The formation of the helical 8_1 configuration, proposed[67-68,345] on (8,6) SWNT, requires a surface density of ~0.75 nm^2 per FMN molecule. Even though we employed ~1.03 nm^2 per FMN molecule on (8,6) SWNTs, we observe FMN molecules away from the SWNT surface (see Figure 8-ii). This suggests that the formation of 8_1 helical assemblies is hindered likely by large entropic barriers. It is possible that the process of ultra-centrifugation or very high bulk FMN concentrations, promote the formation of the helical structure observed via energy-minimization calculations. [67]

It should be pointed out that in the simulations supporting the formation of 8_1 helical assemblies,[345] pre-formed structures were compared. In the simulation presented

here the FMN aggregates form spontaneously depending on the evolution of the system, that obey the equations of motion. Because of the careful methodology implemented, we are confident that the aggregate structures shown in Figure 8-ii correspond to equilibrium structures, although, as always the case in simulations, the results strongly depend on the force fields implemented. It is possible that the force fields implemented herein, although widely used, are somewhat deficient to study the structure of FMN aggregate on nanotubes. From Figure 8-ii, it is also clear that sodium ions are strongly correlated to the phosphate groups, as expected because of electrostatic interactions.

To study the differences between the orientations of FMN molecules on SWNTs of different diameters we computed the angle between the vector formed by the two nitrogen atoms in the central ring of the isoalloxazine group (see Figure 8-i) and the SWNT axis (parallel to the z-axis of the simulation box). We also compute density distributions of isoalloxazine groups, d-ribityl phosphate groups, and sodium counterions away from the SWNT surface. We report these results in Figure 8-iii.

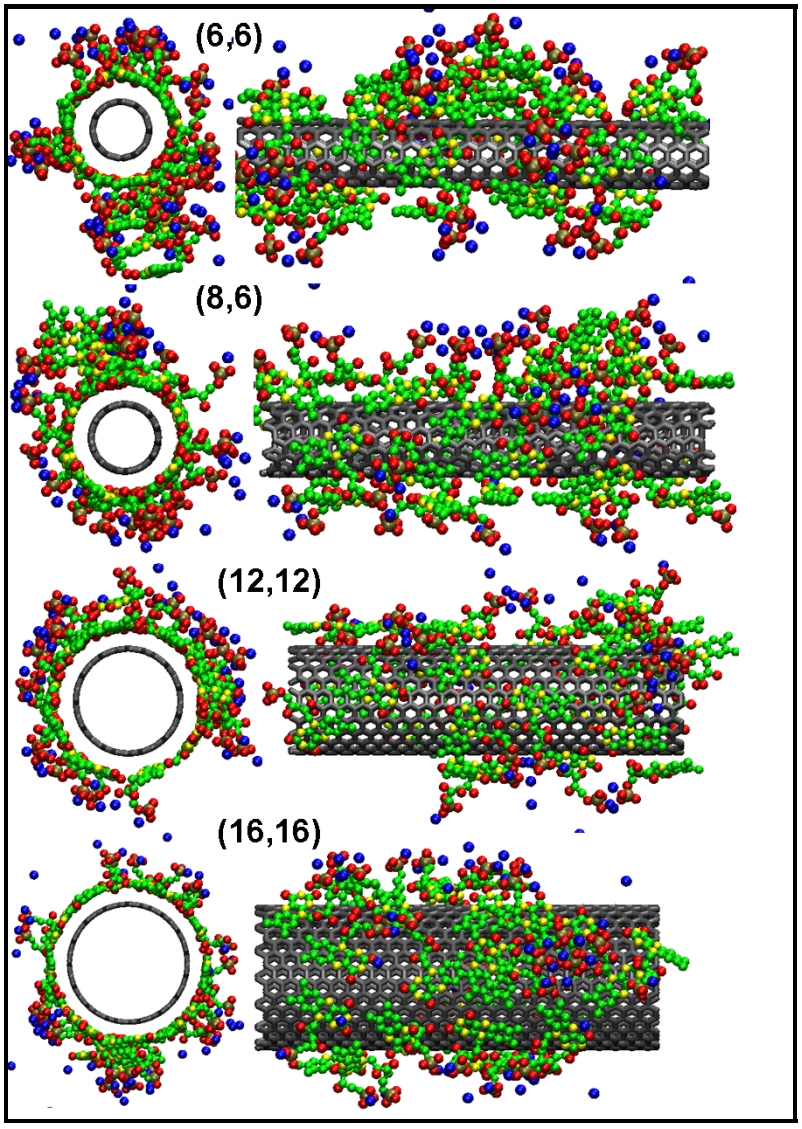

Figure 8-ii: Front and side view of representative simulation snapshots for FMN molecules on SWNTs of different diameters. From top to bottom the results are for (6,6), (8,6), (12,12), and (16,16) SWNTs, respectively. The color code is the same as that in Figure 8-i. Water molecules are not shown for clarity.

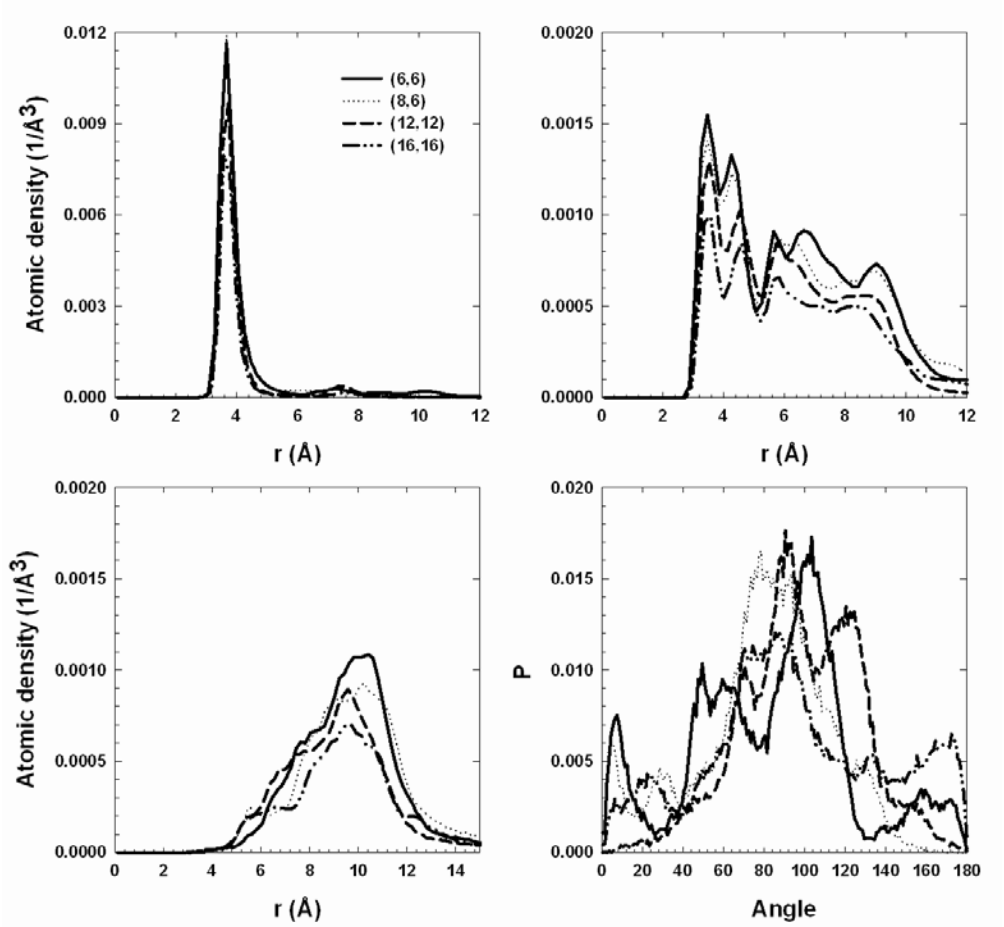

Figure 8-iii: Density distribution of isoalloxazine groups of FMN (top-left), d-ribityl phosphate groups of FMN (top-right), and sodium counterions (bottom-left). Orientation probability of isoalloxazine groups of FMN on SWNTs of different diameters (bottom-left). Different lines are for results obtained on SWNTs of different diameters.

The density distribution for isoalloxazine groups away from the SWNT surface is shown in the top-left panel of Figure 8-iii. We observe a strong peak at 4.0 Å, indicating that most of the FMN molecules are adsorbed on the nanotube surface with their isoalloxazine group lying on the carbon atoms. On (6,6) and (8,6) SWNTs we observe small peaks at 8.0 Å and ~10.0 Å, corroborating the observation from the representative snapshots in Figure 8-ii, according to which on these nanotubes a few FMN molecules remain away from the SWNT surface. The homogenous density

distribution of d-ribityl phosphate groups observed from ~ 3.0 Å to ~10.0 Å (top-right panel of Figure 8-iii) indicates that these groups extend away from the SWNT surface. The peaks observed on (12,12) and (16,16) SWNTs are less intense than those on (8,6) and (6,6) SWNTs because the FMN surface density is less on the former than on the latter tubes. The sodium counterions (bottom-left panel of Figure 8-iii) are strongly associated with the phosphate groups, as both density profiles show peaks located at ~10.0 Å from the SWNT surface.

For the calculation of the orientation probabilities (bottom-right panel of Figure 8-iii), only those isoalloxazine groups that are closer than 5.5 Å from the SWNT surface are considered. An angle of zero degrees indicates that the long axis of the isoalloxazine group is perpendicular to the SWNT axis. An angle of 90 degrees indicates that the long axis of the isoalloxazine group is parallel to the SWNT axis. On all the nanotubes we observe that the majority of the FMN isoalloxazine groups favor being parallel to the SWNT axis, which is consistent with the formation of 8_1 helical assembly.[67,345] However, even on smaller diameter SWNTs [(6,6) and (8,6)], we find a few FMN molecules with the long axis of the isoalloxazine group perpendicular to the SWNT axis. Such orientation is not consistent with the formation of helical assemblies and it is probably due to entropic effects. This result is consistent with data from tight-binding density functional methods, which show that the adsorption energy of flavin adenine dinucleotide (FAD) molecules is similar for both parallel and perpendicular orientation on semi-conducting (10,0) and metallic (5,5) SWNTs.[346] We find very few molecules oriented at 0 or 180 degrees on (12,12) SWNTs, whereas a few noticeable peaks in the orientation distribution corresponding to these angles can be observed on (16,16)

SWNTs. These results indicate that the FMN molecules yield aggregates with somewhat different morphologies on SWNTs of different diameter, which may result in the nanotube-specific properties that, for example, have been exploited experimentally for the purification of (8,6) SWNTs.[67] However, we point out that the differences observed on (6,6) or (8,6) SWNTs, which have similar diameter but different chirality, in terms of both density profiles and orientation of the adsorbed molecules are minimal. This is probably a consequence of the fact that in our simulations the electronic structure of the nanotubes (e.g. metallic vs. semiconducting) is not taken into consideration.

8.4.2. Potential of Mean Force

Potential of mean force (PMF) calculations show how one SWNT interact with another SWNT in the presence of water and adsorbed surface aggregates. A positive PMF indicates an effective repulsion; a negative PMF indicates effective attraction. Results for PMF between fullerenes and SWNTs in water have been reported.[347-348] Strong attraction at short separation (less than 5 Å) and water-induced repulsion due to hydrated layers at medium separations (~5-10 Å) are common features. The water-induced repulsion is not strong enough to hinder the agglomeration of SWNTs in water. Of course, the strength of the effective interactions predicted by simulations varies with changes in the interaction parameters implemented. These calculations remain however valuable in providing physical insights that could be used to design SWNT-specific dispersing agents. We compare the PMF profiles for flexible and rigid (6,6) SWNTs in water in Figure 8-iv. To model flexible SWNTs we employed the Tersoff potential.[349] The Lennard-Jones parameters used to model carbon-water interactions are σ_{CO} = 3.283

Å and ε_{CO} = 0.09303 Kcal/mol. Simulations with flexible SWNTs were conducted in the NVT ensemble using LAMMPS.[194]

The distance reported on the x-axis of Figure 8-ivFigure 8-v is that between the SWNT surfaces, measured as the distance between the centers of the carbon atoms on the nanotubes surfaces. One could obtain the corresponding SWNT-SWNT center-to-center distance by adding the diameter of the (6,6) SWNT (8.12 Å) to the distance reported on the x-axis.

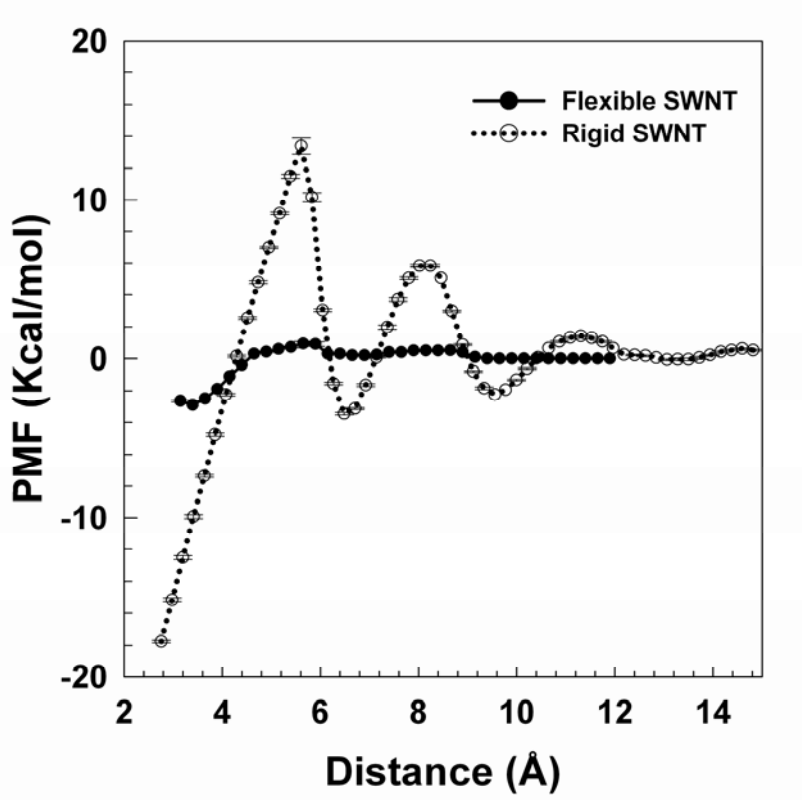

Figure 8-iv: Potential of mean force obtained from umbrella sampling calculations between rigid (empty symbols) or flexible (filled symbols) (6,6) SWNTs in water. Lines are guide to the eye.

We compare the PMF profiles of aqueous SWNTs (rigid and flexible) without amphiphilic molecules in Figure 8-iv. For rigid SWNTs in water we observe strong water-induced repulsion peaks at ~5.0 Å, ~8.0 Å, and ~12.0 Å, corresponding to one,

two, and three hydration layers. The rigidity of the tube allows for strongly hydrogen bonded water layers and hence the magnitude of the PMFs repulsion and attraction are far higher in the case of rigid SWNTs than it is for flexible SWNTs (see Figure 8-iv). We found more water molecules between two rigid tubes than between two flexible nanotubes (not shown for brevity), especially when the distance between the SWNT surfaces is 4-6 Å. For flexible SWNTs we observe that weak water-induced repulsion exists at ~4 Å to 6 Å, and ~7-9 Å. At farther distances the PMF is equal to zero, where water structuring is observed for rigid SWNTs.

In Figure 8-v we compare the PMF profiles of aqueous SWNTs in the presence of SDS at low and high surface coverage. The results are compared to those obtained in water. The PMF is set to zero at large separations between the SWNTs. For PMFs between SWNTs in aqueous SDS, we observe a weak repulsion between the SWNTs, at both SDS coverages, at distances larger than ~10.0 Å. At ~10.0 Å there is a rather strong repulsive barrier between SWNTs covered with SDS at high surface coverage (~10.0 kcal/mol). The repulsive peak is much weaker at low SDS surface densities (~3-4 kcal/mol). At both coverages, an attractive region is observed at ~11.0 Å, followed by a repulsion at ~13.0 Å and a small inflection in the PMF profile at ~16.0 Å (especially in the case of high surface coverage). The PMF profile between SWNTs at high SDS coverage is zero at separations larger than 18.0 Å. Recent results, obtained at much higher surface density than those considered herein, have reported the maximum in the repulsion between SWNTs at ~16.0 Å.[331] The PMF at d = ~3.0 Å (corresponding to SWNTs at contact with each other) is negative, indicating that it is thermodynamically

not possible to promote the dispersion of individual (6,6) SWNTs in aqueous systems using SDS at the conditions considered here.

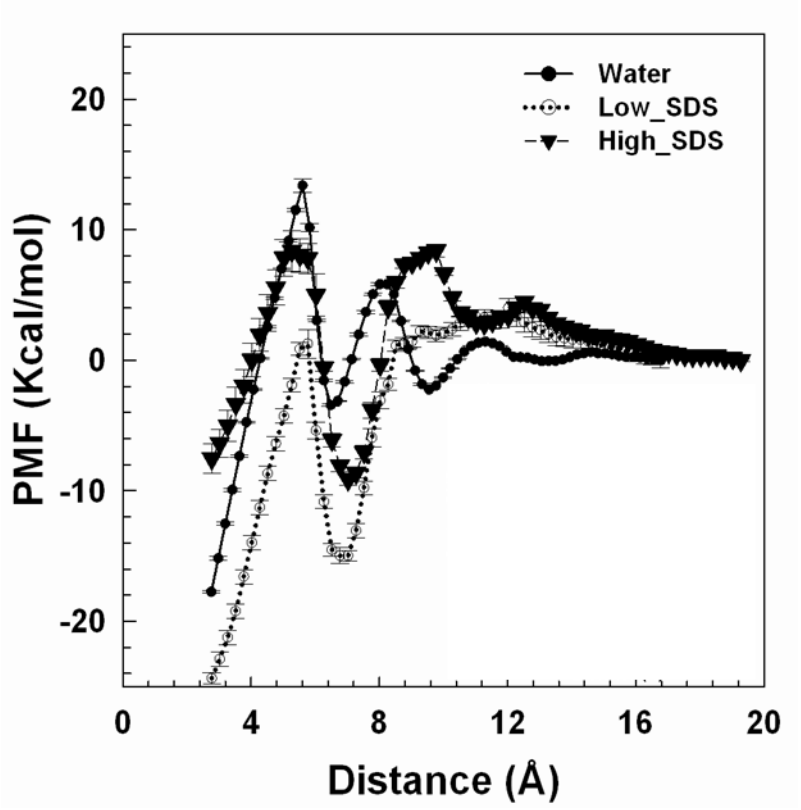

Figure 8-v: Potential of mean force between two rigid (6,6) SWNTs in water and in aqueous SDS.

All simulations indicate that the SWNT-SWNT PMF become repulsive when the SDS aggregates adsorbed on the nanotubes overlap. Consequently the PMF repulsive peak appears at ~10.0 Å and no strong SWNT-SWNT PMF is observed at distances greater than ~10.0 Å. At low SDS coverage a monolayer form in which SDS molecules orient parallel to the tube surface.[69-70] Our results indicate that SDS molecules at low coverage on SWNTs are very mobile. At short SWNT-SWNT distance they tend to accumulate in between the interacting tubes because in so doing one SDS molecule interacts with both SWNT surfaces simultaneously. Unfortunately

when this happens, a portion of the SWNT surface remains exposed to water, which may lead to nanotube aggregation. A snapshot is provided in Figure 8-vi to illustrate this situation.

When the SDS surface density is increased, the SDS molecules between approaching SWNTs provide a stronger repulsion (~10.0 kcal/mol) because it requires more work to disperse the SDS molecules aggregated on the SWNT surface. At even higher surface density, Xu et al., reported a repulsive barrier at ~16.0 Å of much greater magnitude than those observed in our simulations.[331] In our simulations we observe strong attraction at ~7-8 Å (as the 2 surfactant layers between SWNTs give way to only one surfactant layer). Similar oscillatory forces are often observed when solvent molecules form layers in between two approaching surfaces.[350-353] As a consequence of such effects, we observe a strong attractive peak located at ~7.0 – 8.0 Å, in agreement with DFT calculations by Patel and Egorov.[286] Even the results obtained by Xu et al. predict attraction at ~7.0 to 8.0 Å.[331] It is worth pointing out that the strongest attractive PMF between (6,6) SWNTs is observed at ~7.0-8.0 Å at high SDS coverage, and at ~3.0 Å at low SDS coverage. This suggests that a complex formed by two SWNTs and one layer of SDS surfactants in between can be more stable than SWNT bundles in the presence of SDS at high surface densities. This observation appears to be consistent, to some extent, with the experimental observation according to which SDS at high surface densities can keep SWNTs dispersed for some time.[86,277,322]

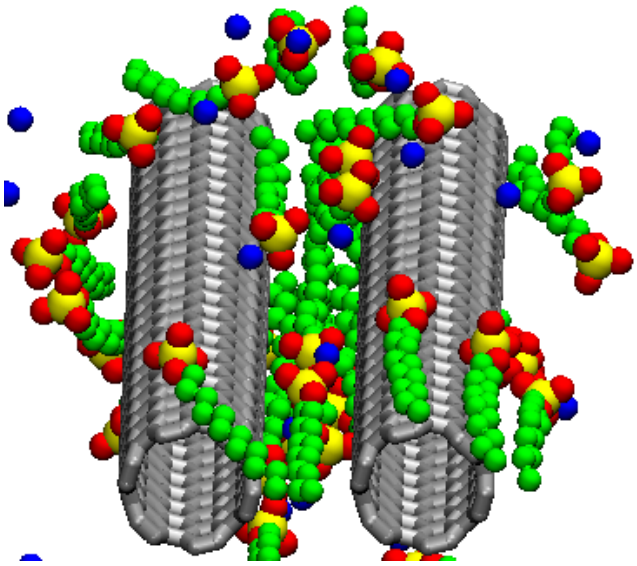

Figure 8-vi: Representative simulation snapshots for SDS aggregates on two approaching SWNTs at low SDS surface coverage. The SWNTs are separated by 6.90 Å. Green, red, and yellow spheres represent methyl groups, oxygen, and sulfur atoms of SDS, respectively. Blue spheres represent sodium ions. Carbon atoms in nanotubes are connected with bold grey lines. Water is not shown for clarity.

The PMFs between SWNTs at low and high FMN surface coverage are shown in Figure 8-vii, where the results are also compared to those obtained in water and aqueous SDS. It is evident from Figure 8-vii that adsorbed FMN molecules provide intense long-range step-wise repulsive barriers which becomes stronger as the distance decreases. Each step observed in the PMF corresponds to a reorganization of FMN molecules in the volume between the two approaching SWNTs, as discussed below. We could not sample the configuration corresponding to distances less than ~6.0 Å between SWNTs, as the expulsion of the last FMN molecule from the volume in between the approaching SWNTs is difficult. Hence, the PMF profiles between SWNTs in presence of FMN are not computed for distances less than ~6.0 Å. Because we do not have data for the PMF at contact between the (6,6) SWNTs, we cannot comment on the thermodynamic stability of aqueous dispersions of (6,6) SWNTs in the presence of

FMN, although the results in Figure 8-vii suggest that individually dispersed nanotubes may be thermodynamically stable. Certainly, the PMFs reported in Figure 8-vii in the presence of FMN are consistent with a substantial kinetic barrier that should prevent dispersed (6,6) SWNTs from aggregating.

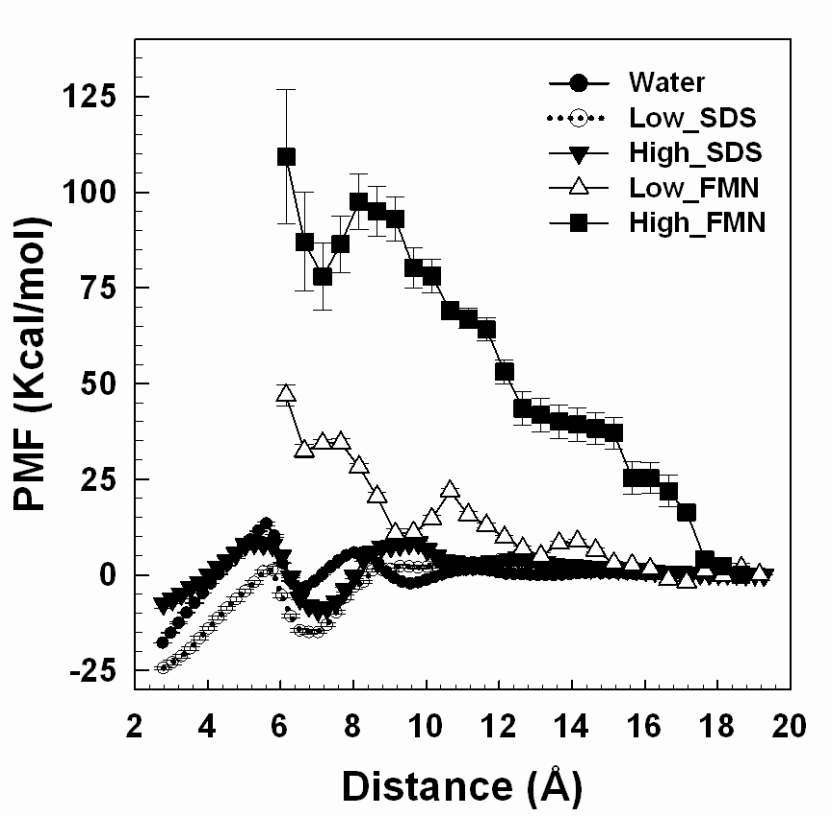

Figure 8-vii: Potential of mean force between two rigid (6,6) SWNTs in water, in aqueous SDS, and in aqueous FMN. For both surfactants results are reported at two surface coverages [low (0.98 nm^2/SDS and 1.24 nm^2/FMN) and high (0.44 nm^2/SDS and 0.94 nm^2/FMN)], respectively.

We discuss the rearrangement of FMN aggregates in conjunction with details of the PMF profile only at low FMN surface coverage since the changes in aggregate morphology with distance are more evident at such conditions. Representative simulation snapshots of FMN molecules assembled around the approaching SWNTs are shown in Figure 8-viii. When the distance between the SWNT surfaces is greater than

twice the extended length of the FMN d-ribityl phosphate groups, the SWNT-SWNT PMF oscillates around zero.

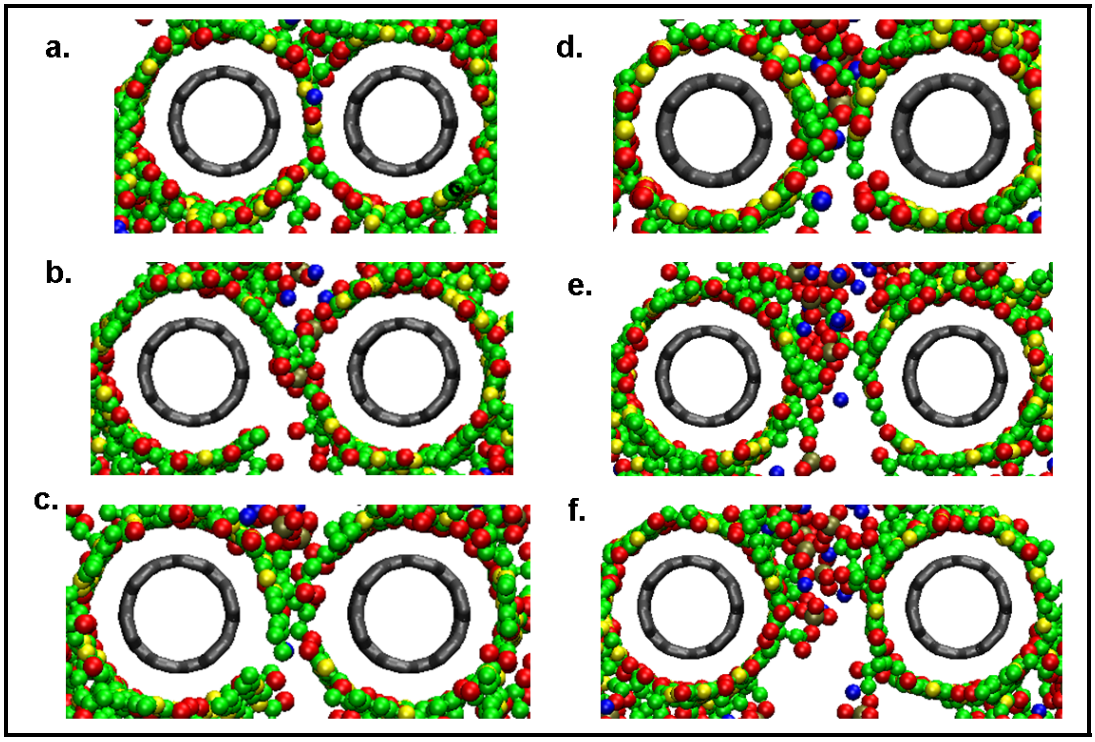

Figure 8-viii: Representative simulation snapshots for FMN aggregates on approaching SWNTs at low FMN surface coverage. Results are shown at various SWNT-SWNT separations, corresponding to steps in the PMF profile. SWNTs are separated by a.) 6.15 Å b.) 8.90 Å c.) 9.15 Å d.) 10.90 Å e.) 13.65 Å and f.) 14.90 Å, respectively. The color code is the same as that in Figure 8-i. Water is not shown for clarity.

Noticeable steps in the PMF profile occur at ~15.0 Å, ~13.0 Å, ~11.0 Å, ~9.0 Å, ~8.0 Å and ~6.0 Å. Decreasing the distance between the SWNTs to ~18.0 Å the phosphate groups and counterions from two interacting FMN-SWNT aggregates begin to overlap, causing the first repulsive step. The repulsive interaction increases until the phosphate groups of FMN on one of the two SWNTs are expelled out of the inter-tube separation, as observed in panel (f) of Figure 8-viii (d = ~14.0 Å). The phosphate groups continue to move out of the region between the interacting SWNTs as the distance decreases. The next step in the PMF profile occurs at ~13 Å, at which distance

we observe phosphate groups of FMN on only one SWNT in between the SWNTs [panel (e) in Figure 8-viii]. Decreasing further the SWNTs separation reduces the volume in between the tubes, and the d-ribityl phosphate groups adsorbed on both the SWNTs are expelled from the region [panel (d) in Figure 8-viii, d = ~11.0 Å], with related increase in steric repulsion. As the distance decreases further, the d-ribityl phosphate groups are expelled from the region between the SWNTs and the solvent enters into the inter-tube space. The PMF becomes less repulsive from ~11.0 Å to ~9.0 Å (see Figure 8-vii), indicating that the expulsion of water molecules in between the FMN-SWNT aggregates is energetically favorable. A representative snapshot of FMN-SWNTs aggregate at 9.15 Å separation between SWNTs is shown in panel (c) of Figure 8-viii. In this snapshot we observe a few isoalloxazine groups adsorbed on the two approaching SWNTs. Decreasing the distance between the SWNTs further involves expelling the last strongly adsorbed FMN molecules from the region in between the SWNTs. This process involves a strong energetic penalty and yields a step-wise increase in the PMF profile from ~9.0 Å to 6.0 Å. When the distance between the SWNTs is just greater than the distance required to fit one layer of isoalloxazine groups in between the SWNTs, we observe a plateau in the PMF profile. When the separation between SWNTs equals the sum of the excluded radii of SWNTs and isoalloxazine group [~6.0 Å, the snapshot shown in panel (a) of Figure 8-viii corresponds to 6.15 Å], we observe a strong repulsion.

To further quantify the phenomena discussed in Figure 8-viii we study the density of various components around and in between the approaching SWNTs. The density distribution of FMN moieties, sodium ions, and solvent molecules within a

rectangular box connecting the centers of mass of the two interacting SWNTs and extending over the diameter of the SWNT and their excluded radii are shown in Figure 8-ix and Figure 8-x. The two figures contain results at the various distances used in Figure 8-viii. Although the density distributions of d-ribityl phosphate groups does not convey any important information, we present them for completeness. Decreasing the distance between SWNTs from 14.90 Å to 13.65 Å we observe that the density of isoalloxazine groups between the nanotubes decreases (top-left panel of Figure 8-ix). The density of atoms in d-ribityl phosphate group is 5 times less than that observed for the atoms of the isoalloxazine group. This indicates there are not many d-ribityl phosphate groups in between the SWNTs at distances below 15.0 Å. The peaks in the density distribution of isoalloxazine groups (top-left panel of Figure 8-ix) correspond to the FMN molecules adsorbed on the SWNT surface along the line connecting the centers of mass of interacting SWNTs. At 10.90 Å, we observe a peak ~2.5 Å away from each SWNT, indicating that the FMN molecules on the SWNTs are compressed. In correspondence, a strong repulsion is observed in the PMF. The repulsion decreases as we further decrease the distance between the SWNTs. In most cases the number of the peaks in the density profiles for sodium ions correspond to the number of density peaks in density profile for water molecules (bottom-left and bottom-right panels of Figure 8-ix), providing evidence for water-ion correlations.[354]

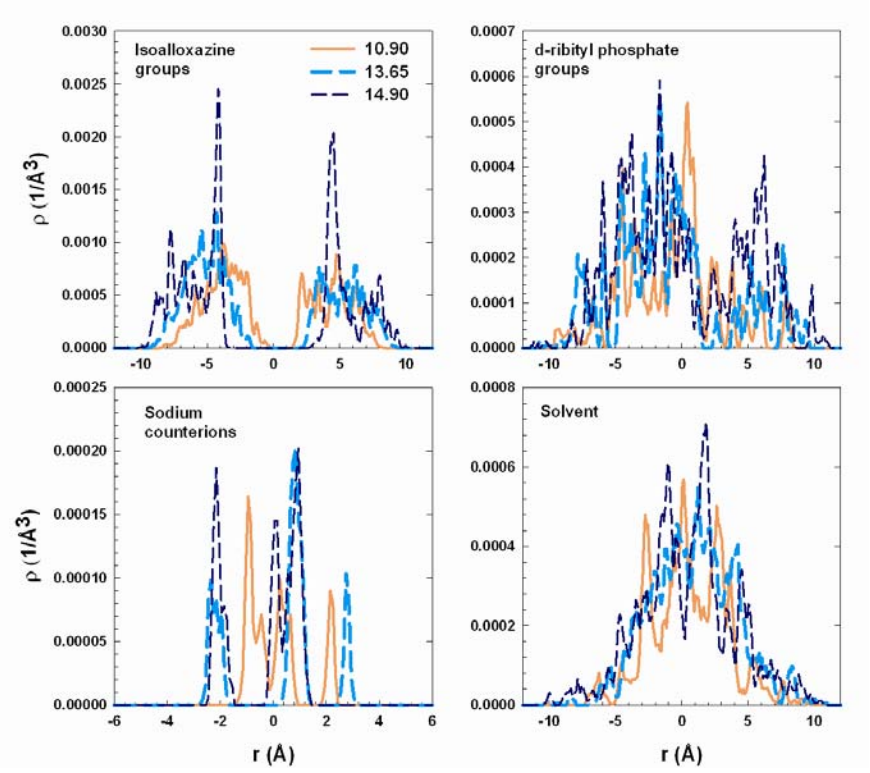

Figure 8-ix: Density distribution of isoalloxazine groups (top-left) and d-ribityl groups (top-right) of FMN molecules, sodium counterions (bottom-left), and solvent (water) molecules (bottom-right) at 10.90 Å (continuous line), 13.65 Å (thick dashed line), and 14.90 Å (thin dashed line) inter-tube separation between two (6,6) SWNTs at low FMN surface coverage.

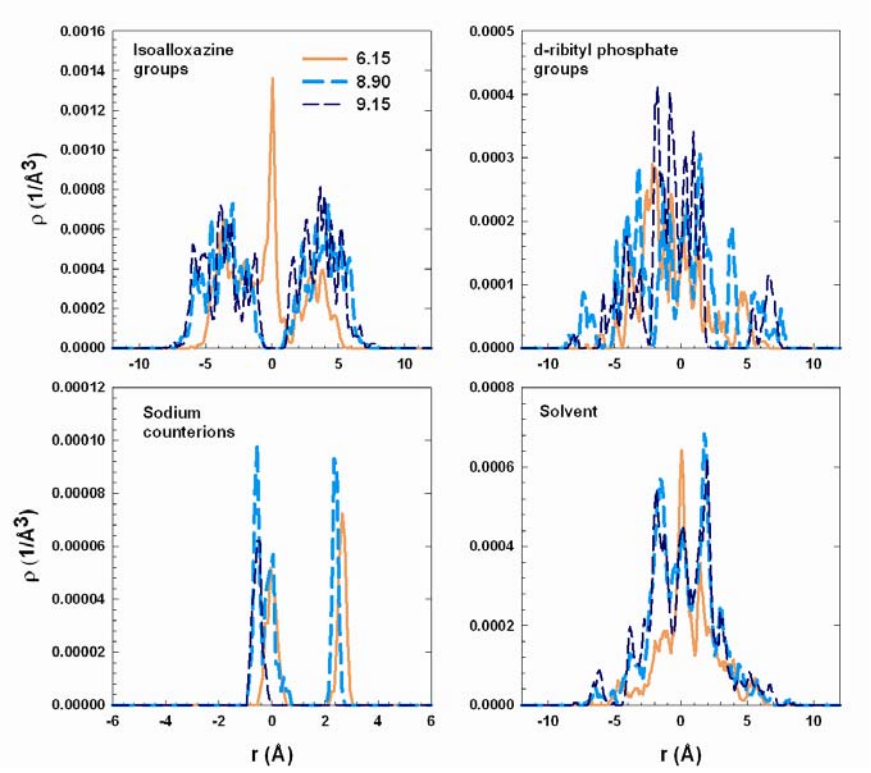

Figure 8-x: Same as Figure 8-ix, but at distances 6.15 Å (continuous line), 8.90 Å (thick dashed line), and 9.15 Å (thin dashed line).

The density profiles for FMN, sodium and solvent molecules at 9.15, 8.90, and 6.15 Å, are shown in Figure 8-x. We observe that at 9.15 Å and 8.90 Å separations between nanotubes, the density profile of water molecules in the volume between the nanotubes is almost identical. However, the density profile of sodium shows a single peak at 9.15 Å separation and multiple peaks at 8.90 Å; correspondingly we observe an increase in the repulsion in the PMF profile at those distances. For the density distribution of isoalloxazine groups, we observe a transition from multiple peaks at 9.15 and 8.90 Å SWNT-SWNT separations to a single peak at 6.15 Å, confirming the expulsion of isoalloxazine groups from the volume between the nanotubes in correspondence to the stronger repulsion observed in the PMF profile.

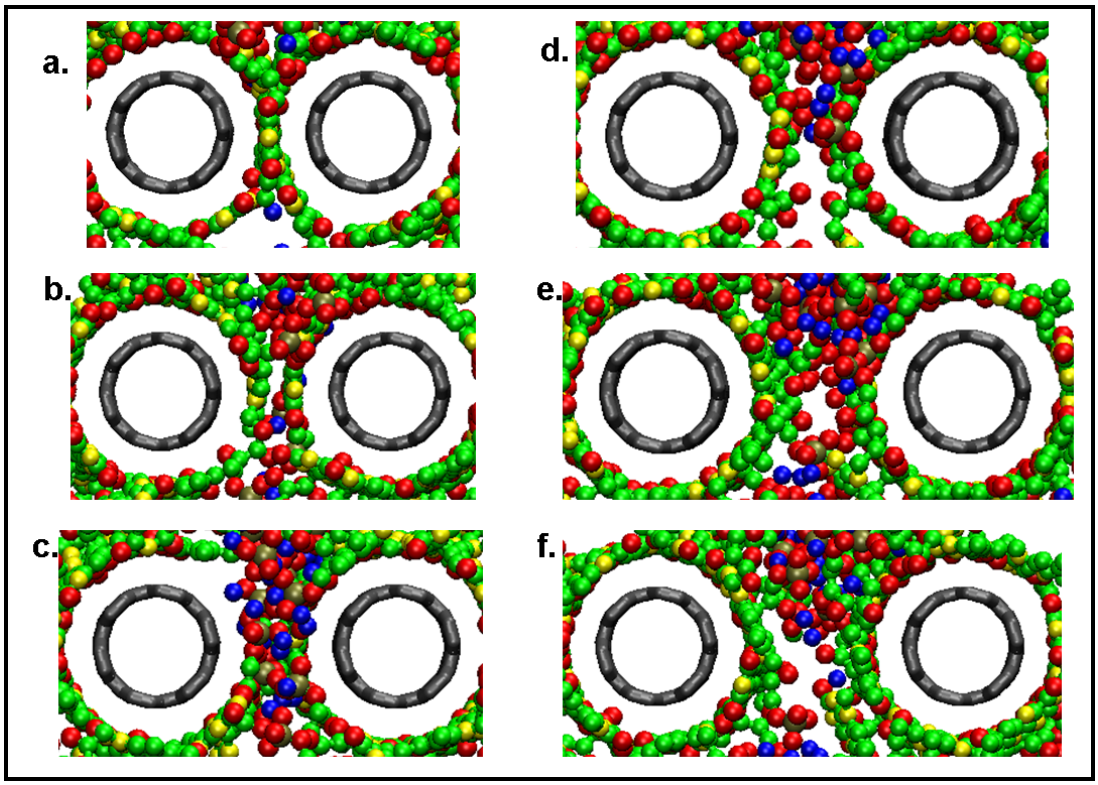

Figure 8-xi: Representative simulation snapshots for FMN aggregates on approaching SWNTs at high FMN surface coverage. Results are shown at various SWNT-SWNT separations, corresponding to steps in the PMF profile. SWNTs are separated by a.) 6.15 Å b.) 8.90 Å c.) 9.15 Å d.) 11.40 Å e.) 13.65 Å and f.) 14.90 Å respectively. The color code is same as that in Figure 8-i. Water is not shown for clarity.

The SWNT-SWNT PMF computed in aqueous FMN at high surface coverage shows about twice the repulsive barrier between SWNTs as compared to data at low surface coverage. The complete coverage of the SWNT surface with FMN molecules, and the presence of few FMN molecules in the surrounding water cause the enhanced repulsive barrier. However, the PMF profiles show a step-wise profile similar to that observed at low FMN coverage. At high FMN coverage the PMF profile either increases or remains constant at all distances, with the only exception observed at ~7.0-8.0 Å where the PMF decreases slightly. At similar separations we found plateau in the PMF profile at low FMN coverage. At high FMN coverage, decreasing the distance

between SWNTs from ~9.0 Å to 7.0 Å significantly decreases the number of FMN molecules at contact with the SWNT surface. When this occurs water molecules cannot enter the region between the nanotubes due to the high density of FMN molecules. The combination of these two reasons leads to a reduced repulsion between nanotubes, which appears to be due to depletion effects.

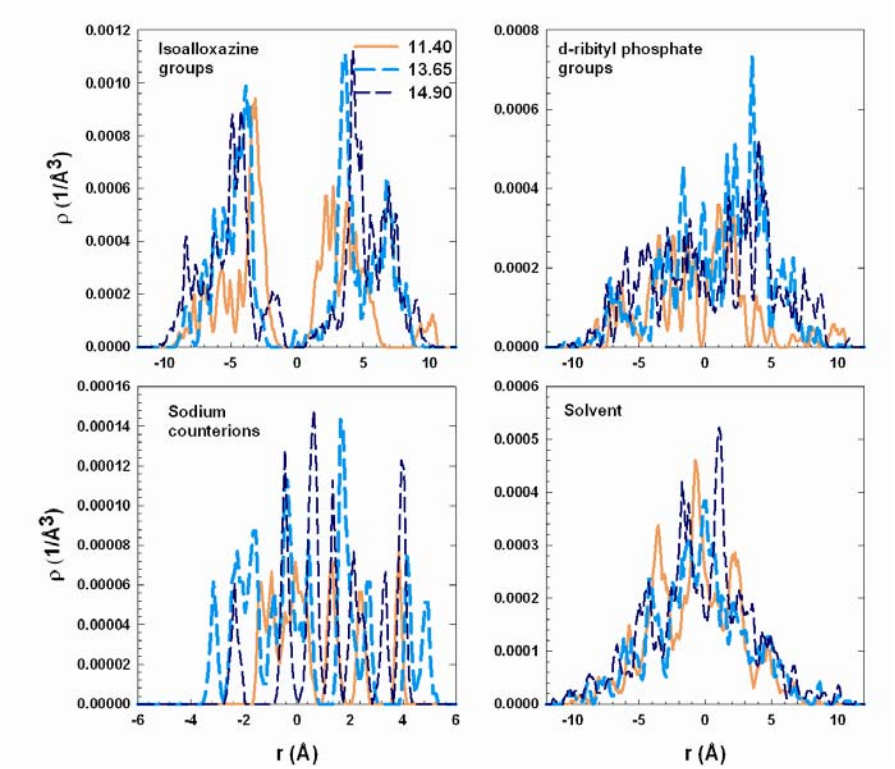

Figure 8-xii: Density distribution of isoalloxazine groups (top-left) and d-ribityl groups (top-right) of FMN molecules, sodium counterions (bottom-left), and solvent (water) molecules (bottom-right) at 11.40 Å (continuous line), 13.65 Å (thick dashed line), and 14.90 Å (thin dashed line) inter-tube separation between two (6,6) SWNTs at high FMN surface coverage.

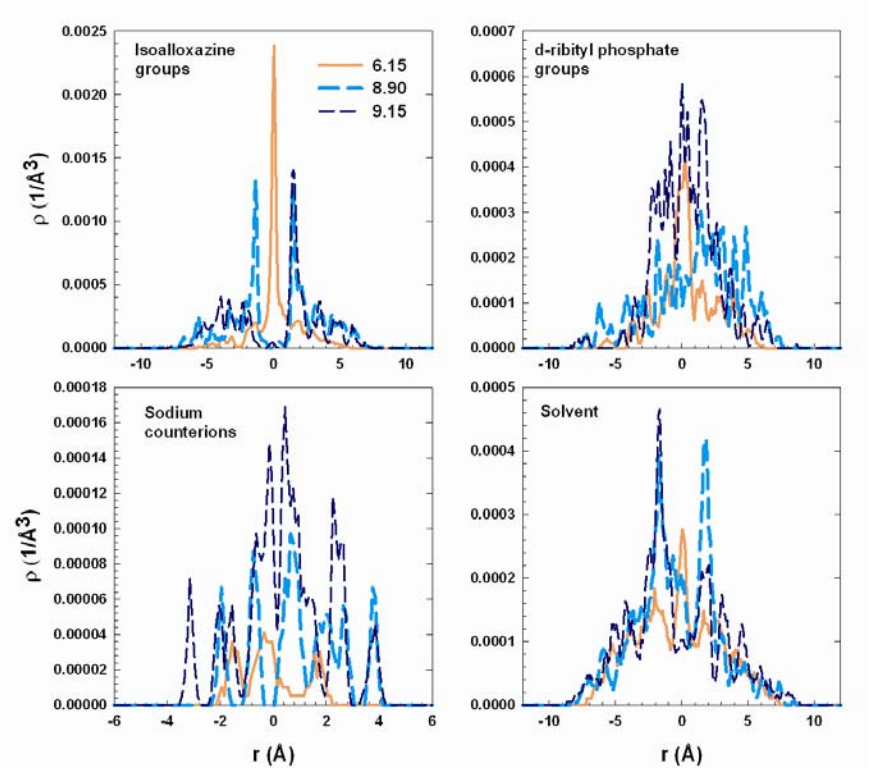

Figure 8-xiii: Same as Figure 8-xii, but at separations of 6.15 Å (continuous line), 8.90 Å (thick dashed line), and 9.15 Å (thin dashed line).

For interacting SWNTs at large FMN surface density we also report simulation snapshots (Figure 8-xi) and density distributions (Figure 8-xii and Figure 8-xiii) at various SWNT-SWNT distances. The molecular mechanisms responsible for the step-wise repulsive PMF shown in Figure 8-vii for high FMN coverage are analogous to those discussed at low FMN coverage. The only exception is that the effect of sodium counterions can be observed clearly at high FMN surface coverage. In the bottom-left panel of Figure 8-xiii we observe that the density of counterions decreases dramatically as the distance between SWNTs decreases from 9.15 Å to 8.90 Å. In correspondence, the PMF data show an increase in repulsive barrier in the PMF profile, suggesting that it is energetically not favorable to expel sodium ions from the region between the interacting SWNTs.

The density distributions showed in Figure 8-ix, Figure 8-x, Figure 8-xii, and Figure 8-xiii could be used to predict the effective interaction between SWNTs through classical density functional methods, such as those reported by Patel and Egorov.[286]

8.5. Conclusions

FMN molecules adsorb with the isoalloxazine group on the SWNT surface. We found that changing the SWNT diameter affects the orientation of FMN molecules and hence may enhance the separation of SWNTs based on diameter. We observed that increasing the surface density of FMN molecules increases the repulsive barrier between SWNTs. Based on the PMF profiles the results suggest that FMN molecules are superior to SDS to disperse and separate SWNTs. We also report the density of FMN molecules between the SWNTs at different distances, which explain the reasons for the increased repulsion with the increasing distance. The natural extension of this study is to calculate the PMF profiles between SWNTs of different chiralities and compare those with the PMF obtained between identical SWNTs as discussed in this study. The formation of helical assemblies on SWNTs of well defined diameter and chirality may be the reason for specific separation ability of FMN molecules, although more work needs to be done to fully understand the likeliness of formation of such helical assemblies.

9. Conclusions and Future Work

We studied the morphology of surfactant aggregates at water-vacuum and water-solid interfaces. At water-vacuum interface, non-ionic surfactants with long headgroups ($C_{12}E_6$) undergo gas-like to liquid-like phase transitions as the surfactant concentration increases. Anionic SDS surfactants with short sulfate headgroups pack more closely as the surfactant concentration increases and yield more ordered surface aggregates.

At the water-graphite interface, SDS yields hemicylinders due to counterion condensation. Because of changes in the effective size of the surfactant headgroups upon counterion-condensation phenomenon, the hemicylinders are imperfect in the presence of sodium counterions, perfect in the presence of cesium counterions. The hydration numbers of surfactant headgroups decrease in the presence of cesium counterions, further indicating that the size of counterions play an important role in determining the aggregate structure.

At water-silica interfaces SDS yields multiple-layers on completely protonated silica, and weakly adsorbed bilayer-like surface aggregates on partially protonated silica. $C_{12}E_6$ surfactants at the water-silica interface yield monolayers with the tailgroups oriented towards the surface on completely protonated surfaces. As the degree of protonation decreases the number of non-ionic headgroups adsorbed on the silica surface increases.

On graphene nanosheets (GNs) and graphene nanoribbons (GNRs) SDS yields multiple layers when the size of the graphene is comparable to that of SDS. On GNs and GNRs of size more than twice the length of SDS molecules, SDS surfactants yield

hemi-spherical aggregates. At all graphene sizes, we observe edge effects that determine the structure of surface aggregates.

On SWNTs, the nanotube diameter affects the SDS surface aggregate structure. Our results did not show differences depending on the nanotube chirality. However, since our MD simulations did not take into effect the change in electronic structure, we cannot accurately predict the effects of SWNT chirality on the surfactant aggregates. However our results suggest that it is possible to design surface aggregates of different shapes within SWNTs by matching the size/type of the surfactant to the curvature of the SWNTs.

SDS surfactants form lamellar structures inside large diameter SWNTs.

FMN molecules adsorb on SWNTs with the isoalloxazine moiety on the nanotube surface and d-ribityl phosphate groups extending away from it. Changing the diameter of nanotubes changes the orientation on FMN molecules. The effective interaction between two (6,6) SWNTs, computed through umbrella-sampling techniques, indicated that in the presence of FMN the effective repulsion between approaching SWNTs is much stronger than that observed in the presence of SDS, suggesting that FMN molecules are more effective in stabilizing aqueous dispersion of carbon nanotubes.

The limitations in our study can be categorized into three main groups. They are methodological limitations, force field limitations, and limitations arising from the availability of computational resources. Our MD simulations do not take into account the change in electronic structure or polarizability of nanotubes, or of surfactants. However, using computationally expensive ab-initio molecular dynamics (AIMD)

simulation techniques, one can enhance the accuracy of the simulations predictions. Currently such techniques can only be employed for up to 1000 atoms and hence studying many systems of interest is prohibitively expensive.

The accuracy of the available force fields limits the reliability of results in any kind of simulations. In all the simulations performed herein, the force fields employed resulted in experimentally consistent results except for the surface tension of $C_{12}E_6$. Computational time limitations prevent us from studying the exchange of surfactant monomers in the bulk with surfactant aggregates on various surfaces. To study such phenomenon one would have to simulate micro seconds in real time. No all-atom MD simulations, within current state of the computational resources, can reach such time scales. Coarse-grained models can attain such long time scales, but the atomic details used in all-atom MD are typically lost. Hence, one has to decide which are the important details and scopes of the project in order to settle on the simulations methods to use. Our aim was to study aggregate morphology of surfactants on different surfaces and understand the effect of different parameters such as curvature, lateral confinement, and hydrophilicity. We believe that all-atom MD simulations provide an elegant and powerful tool to study such effects.

In summary, the study of surfactant aggregate morphology on carbonaceous substrates of different sizes and different curvature effects multiple applications ranging from nano-patterning, surface modification, detergency, and colloidal dispersions of graphene and carbon nanotubes. The study of surface aggregation of surfactants on hydrophilic surfaces has implications in creating super-hydrophobic as well as super-hydrophilic surfaces, and can also help in the fundamental understanding of water

properties next to amphiphilic surfaces. The results from our studies can be extrapolated to understand the aggregation behavior of surfactants at many heterogeneous surfaces, and also that of nano-particles in different biological membranes.

The data from our all-atom simulations can be used to generate coarse grained potentials to study bundling and de-bundling of single walled carbon nanotubes. One could also use our results to enhance thermodynamic models to predict macroscopic properties of surfactants at many interfaces via the incorporation of curvature effects.

By studying the effective interactions between different carbon nanotubes and nanoparticles in the presence of surfactants with a variety of headgroups and tailgroups, it would be interesting and challenging to develop predictive tools to calculate the effective interactions between nanoparticles just by knowing the nature of the surfactants and the substrate.

References

(1) Beck, J. S.; Vartuli, J. C.; Roth, W. J.; Leonowicz, M. E.; Kresge, C. T.; Schmitt, K. D.; Chu, C. T. W.; Olson, D. H.; Sheppard, E. W. *Journal of the American Chemical Society* **1992**, *114*, 10834.

(2) Marquez, M.; Patel, K.; Carswell, A. D. W.; Schmidtke, D. W.; Grady, B. P. *Langmuir* **2006**, *22*, 8010.

(3) Marquez, M.; Grady, B. P. *Langmuir* **2004**, *20*, 10998.

(4) Rosen, M. J. *Surfactants and Interfacial Phenomena*; 3rd ed.; Wiley-Interscience: Hoboken, New Jersey, U.S.A, 2004.

(5) Hiemenz, P. C.; Rajagopalan, R. *Principles of Colloid and Surface Chemistry*; 3 ed.; Marcel Decker Inc.: New Yrok, 1997.

(6) Nagarajan, R.; Ruckenstein, E. *Journal of Colloid and Interface Science* **1977**, *60*, 221.

(7) Nagarajan, R.; Ruckenstein, E. *Journal of Colloid and Interface Science* **1979**, *71*, 580.

(8) Rao, I. V.; Ruckenstein, E. *Journal of Colloid and Interface Science* **1986**, *113*, 375.

(9) Nagarajan, R.; Ruckenstein, E. *Langmuir* **1991**, *7*, 2934.

(10) Blankschtein, D.; Thurston, G. M.; Benedek, G. B. *Physical Review Letters* **1985**, *54*, 955.

(11) Shiloach, A.; Blankschtein, D. *Langmuir* **1998**, *14*, 1618.

(12) Srinivasan, V.; Blankschtein, D. *Langmuir* **2003**, *19*, 9932.

(13) Stephenson, B. C.; Beers, K.; Blankschtein, D. *Langmuir* **2006**, *22*, 1500.

(14) Stephenson, B. C.; Goldsipe, A.; Beers, K. J.; Blankschtein, D. *The Journal of Physical Chemistry B* **2007**, *111*, 1025.

(15) Stephenson, B. C.; Goldsipe, A.; Beers, K. J.; Blankschtein, D. *The Journal of Physical Chemistry B* **2007**, *111*, 1045.

(16) Stephenson, B. C.; Beers, K. J.; Blankschtein, D. *The Journal of Physical Chemistry B* **2007**, *111*, 1063.

(17) Somasundaran, P.; Healy, T. W.; Fuerstenau, D. W. *The Journal of Physical Chemistry* **1964**, *68*, 3562.

(18) Somasundaran, P.; Fuerstenau, D. W. *The Journal of Physical Chemistry* **1966**, *70*, 90.

(19) Wakamats, T.; Fuerstenau, D. W. *Advances in Chemistry Series* **1968**, *79*, 161.

(20) Dick, S. G.; Fuerstenau, D. W.; Healy, T. W. *Journal of Colloid and Interface Science* **1971**, *37*, 595.

(21) Ball, B.; Fuerstenau, D. W. *Discussions of the Faraday Society* **1971**, *52*, 361.

(22) Trogus, F. J.; Schechter, R. S.; Pope, G. A.; Wade, W. H. *Journal of Petroleum Technology* **1979**, *31*, 769.

(23) Nunn, C.; Schecter, R. S.; Wade, W. H. *Journal of Colloid and Interface Science* **1981**, *80*, 598.

(24) Scamehorn, J.; Schechter, R.; Wade, W. *Journal of the American Oil Chemists' Society* **1983**, *60*, 1345.

(25) Scamehorn, J. F.; Schechter, R. S.; Wade, W. H. *Journal of Colloid and Interface Science* **1982**, *85*, 463.

(26) Somasundaran, P.; Middleton, R.; Viswanathan, K. V. *ACS Symposium Series* **1984**, *253*, 269.

(27) Viswanathan, K. V.; Somasundaran, P. *Colloids and Surfaces* **1987**, *26*, 19.

(28) Somasundaran, P.; Celik, M.; Goya, A.; Manev, E. *Society of Petroleum Engineers Journal* **1984**, *24*, 233.

(29) Levitz, P.; Van Damme, H.; Keravis, D. *The Journal of Physical Chemistry* **1984**, *88*, 2228.

(30) Levitz, P.; Van Damme, H. *The Journal of Physical Chemistry* **1986**, *90*, 1302.

(31) Levitz, P. *Langmuir* **1991**, *7*, 1595.

(32) Manne, S.; Cleveland, J. P.; Gaub, H. E.; Stucky, G. D.; Hansma, P. K. *Langmuir* **1994**, *10*, 4409.

(33) Warr, G. G. *Current Opinion in Colloid & Interface Science* **2000**, *5*, 88.

(34) Tiberg, F.; Brinck, J.; Grant, L. *Current Opinion in Colloid & Interface Science* **1999**, *4*, 411.

(35) Wanless, E. J.; Ducker, W. A. *The Journal of Physical Chemistry* **1996**, *100*, 3207.

(36) Israelachvili, J. N. *Intermolecular and Surface Forces*; Academic Press: London, 1992.

(37) Manne, S.; Gaub, H. E. *Science* **1995**, *270*, 1480.

(38) Patrick, H. N.; Warr, G. G.; Manne, S.; Aksay, I. A. *Langmuir* **1997**, *13*, 4349.

(39) Marquez, M.; Kim, S.; Jung, J.; Truong, N.; Teeters, D.; Grady, B. P. *Langmuir* **2007**, *23*, 10008.

(40) Penfold, J.; Staples, E.; Tucker, I.; Thomas, R. K. *Langmuir* **2002**, *18*, 5755.

(41) Penfold, J.; Tucker, I.; Staples, E.; Thomas, R. K. *Langmuir* **2004**, *20*, 7177.

(42) Lotya, M.; Hernandez, Y.; King, P. J.; Smith, R. J.; Nicolosi, V.; Karlsson, L. S.; Blighe, F. M.; De, S.; Wang, Z.; McGovern, I. T.; Duesberg, G. S.; Coleman, J. N. *Journal of the American Chemical Society* **2009**, *131*, 3611.

(43) Yanyu Liang, D. W. X. F. K. M. *Advanced Materials* **2009**, *21*, 1679.

(44) Bai, H.; Xu, Y.; Zhao, L.; Li, C.; Shi, G. *Chemical Communications* **2009**, 1667.

(45) Allen, E. C.; Rutledge, G. C. *The Journal of Chemical Physics* **2008**, *128*, 154115.

(46) Allen, E. C.; Rutledge, G. C. *The Journal of Chemical Physics* **2009**, *130*, 034904.

(47) Izvekov, S.; Voth, G. A. *The Journal of Chemical Physics* **2005**, *123*, 134105.

(48) Izvekov, S.; Voth, G. A. *The Journal of Physical Chemistry B* **2005**, *109*, 2469.

(49) Izvekov, S.; Voth, G. A. *The Journal of Chemical Physics* **2006**, *125*, 151101.

(50) Mirijanian, D. T.; Chu, J.-W.; Ayton, G. S.; Voth, G. A. *Journal of Molecular Biology* **2007**, *365*, 523.

(51) Liu, P.; Izvekov, S.; Voth, G. A. *The Journal of Physical Chemistry B* **2007**, *111*, 11566.

(52) Srinivas, G.; Klein, M. L. *Molecular Physics* **2004**, *102*, 883

(53) Srinivas, G.; Nielsen, S. O.; Moore, P. B.; Klein, M. L. *Journal of the American Chemical Society* **2006**, *128*, 848.

(54) Shinoda, W.; DeVane, R.; Klein, M. L. *Molecular Simulation* **2007**, *33*, 27

(55) Klein, M. L.; Shinoda, W. *Science* **2008**, *321*, 798.

(56) Shinoda, W.; DeVane, R.; Klein, M. L. *Soft Matter* **2008**, *4*, 2454.

(57) Chiu, C.-c.; DeVane, R.; Klein, M. L.; Shinoda, W.; Moore, P. B.; Nielsen, S. O. *The Journal of Physical Chemistry B* **2010**, *114*, 6394.

(58) Chan, E. R.; Striolo, A.; McCabe, C.; Cummings, P. T.; Glotzer, S. C. *The Journal of Chemical Physics* **2007**, *127*, 114102.

(59) Reith, D.; Pütz, M.; Müller-Plathe, F. *Journal of Computational Chemistry* **2003**, *24*, 1624.

(60) Arnold, M. S.; Green, A. A.; Hulvat, J. F.; Stupp, S. I.; Hersam, M. C. *Nat Nano* **2006**, *1*, 60.

(61) Hersam, M. C. *Nat Nano* **2008**, *3*, 387.

(62) Arnold, M. S.; Suntivich, J.; Stupp, S. I.; Hersam, M. C. *ACS Nano* **2008**, *2*, 2291.

(63) Green, A. A.; Hersam, M. C. *Nat Nano* **2009**, *4*, 64.

(64) Green, A.; Duch, M.; Hersam, M. *Nano Research* **2009**, *2*, 69.

(65) Liu, J.; Hersam, M. C. *MRS Bulletin* **2010**, *35*, 315.

(66) Chattopadhyay, D.; Galeska, I.; Papadimitrakopoulos, F. *Journal of the American Chemical Society* **2003**, *125*, 3370.

(67) Ju, S.-Y.; Doll, J.; Sharma, I.; Papadimitrakopoulos, F. *Nat Nano* **2008**, *3*, 356.

(68) Ju, S.-Y.; Kopcha, W. P.; Papadimitrakopoulos, F. *Science* **2009**, *323*, 1319.

(69) Tummala, N. R.; Striolo, A. *ACS Nano* **2009**, *3*, 595.

(70) Tummala, N. R.; Striolo, A. *Physical Review E (Statistical, Nonlinear, and Soft Matter Physics)* **2009**, *80*, 021408.

(71) Sammalkorpi, M.; Panagiotopoulos, A. Z.; Haataja, M. *J. Phys. Chem. B* **2008**, *112*, 2915.

(72) Sammalkorpi, M.; Panagiotopoulos, A. Z.; Haataja, M. *The Journal of Physical Chemistry B* **2008**, *112*, 12954.

(73) Verma, A.; Stellacci, F. *Small* **2010**, *6*, 12.

(74) Mutlu, G. k. M.; Budinger, G. R. S.; Green, A. A.; Urich, D.; Soberanes, S.; Chiarella, S. E.; Alheid, G. F.; McCrimmon, D. R.; Szleifer, I.; Hersam, M. C. *Nano Letters* **2010**, *10*, 1664.

(75) Lacerda, L.; Bianco, A.; Prato, M.; Kostarelos, K. *Adv Drug Deliver Rev* **2006**, *58*, 1460.

(76) Paria, S.; Khilar, K. C. *Advances in Colloid and Interface Science* **2004**, *110*, 75.

(77) Tummala, N. R.; Striolo, A. *J. Phys. Chem. B* **2008**, *112*, 1987.

(78) Wall, J. F.; Zukoski, C. F. *Langmuir* **1999**, *15*, 7432.

(79) Dong, J.; Mao, G.; Hill, R. M. *Langmuir* **2004**, *20*, 2695.

(80) Jodar-Reyes, A. B.; Lyklema, J.; Leermakers, F. A. M. *Langmuir* **2008**, *24*, 6496.

(81) Penfold, J.; Staples, E. J.; Tucker, I.; Thompson, L. J.; Thomas, R. K. *International Journal of Thermophysics* **1999**, *20*, 19.

(82) Gutig, C.; Grady, B. P.; Striolo, A. *Langmuir* **2008**, *24*, 13814.

(83) Gutig, C.; Grady, B. P.; Striolo, A. *Langmuir* **2008**, *24*, 4806.

(84) Matarredona, O.; Rhoads, H.; Li, Z.; Harwell, J. H.; Balzano, L.; Resasco, D. E. *J. Phys. Chem. B* **2003**, *107*, 13357.

(85) Nair, N.; Kim, W. J.; Braatz, R. D.; Strano, M. S. *Langmuir* **2008**, *24*, 1790.

(86) O'Connell, M. J.; Bachilo, S. M.; Huffman, C. B.; Moore, V. C.; Strano, M. S.; Haroz, E. H.; Rialon, K. L.; Bout, P. J.; Noon, W. H.; Kittrell, C.; Jianpeng, M.; Hauge, R. H.; Weisma, R. B.; Smalley, R. E. *Science* **2002**, *297*, 593.

(87) Yurekli, K.; Mitchell, C. A.; Krishnamoorti, R. *J. Am. Chem. Soc.* **2004**, *126*, 9902.

(88) Laughin, R. G. *The Aqueous Phase Behavior of Surfactants*; Academic Press: New York, 1994.

(89) Grant, L. M.; Tiberg, F.; Ducker, W. A. *The Journal of Physical Chemistry B* **1998**, *102*, 4288.

(90) Shi, L.; Ghezzi, M.; Caminati, G.; Lo Nostro, P.; Grady, B. P.; Striolo, A. *Langmuir* **2009**, *25*, 5536.

(91) Stalgren, J. J. R.; Eriksson, J.; Boschkova, K. *Journal of Colloid and Interface Science* **2002**, *253*, 190.

(92) Kjellin, U. R. M.; Claesson, P. M.; Linse, P. *Langmuir* **2002**, *18*, 6745.

(93) Lu, J. R.; Li, Z. X.; Thomas, R. K.; Binks, B. P.; Crichton, D.; Fletcher, P. D. I.; McNab, J. R.; Penfold, J. *The Journal of Physical Chemistry B* **1998**, *102*, 5785.

(94) Lu, J. R.; Li, Z. X.; Thomas, R. K.; Staples, E. J.; Thompson, L.; Tucker, I.; Penfold, J. In *The Journal of Physical Chemistry*; American Chemical Society: 1994; Vol. 98, p 6559.

(95) Lu, J. R.; Li, Z. X.; Thomas, R. K.; Staples, E. J.; Tucker, I.; Penfold, J. *The Journal of Physical Chemistry* **1993**, *97*, 8012.

(96) Lu, J. R.; Su, T. J.; Li, Z. X.; Thomas, R. K.; Staples, E. J.; Tucker, I.; Penfold, J. *The Journal of Physical Chemistry B* **1997**, *101*, 10332.

(97) Penfold, J.; Staples, E.; Tucker, I.; Thomas, R. K. *Journal of Colloid and Interface Science* **1998**, *201*, 223.

(98) Lu, J. R.; Marrocco, A.; Su, T. J.; Thomas, R. K.; Penfold, J. *Journal of Colloid and Interface Science* **1993**, *158*, 303.

(99) Lu, J. R.; Purcell, I. P.; Lee, E. M.; Simister, E. A.; Thomas, R. K.; Rennie, A. R.; Penfold, J. *Journal of Colloid and Interface Science* **1995**, *174*, 441.

(100) Lu, J. R.; Simister, E. A.; Thomas, R. K.; Penfold, J. *Journal of Physics: Condensed Matter* **1994**, A403.

(101) Penfold, J.; Thomas, R. K.; Simister, E.; Lee, E.; Rennie, A. *Journal of Physics: Condensed Matter* **1990**, SA411.

(102) Purcell, I. P.; Thomas, R. K.; Penfold, J.; Howe, A. M. In *Colloids and Surfaces A: Physicochemical and Engineering Aspects* 1995; Vol. 94, p 125.

(103) Dominguez, H.; Berkowitz, M. L. *The Journal of Physical Chemistry B* **2000**, *104*, 5302.

(104) Luo, M.; Dai, L. L. *Journal of Physics: Condensed Matter* **2007**, 375109.

(105) Elworthy, P. H.; Mysels, K. J. *Journal of Colloid and Interface Science* **1966**, *21*, 331.

(106) Dominguez, H.; Rivera, M. *Langmuir* **2005**, *21*, 7257.

(107) Hernáinz, F.; Caro, A. *Colloids and Surfaces A: Physicochemical and Engineering Aspects* **2002**, *196*, 19.

(108) Okamura, E.; Fukushima, N.; Hayashi, S. *Langmuir* **1999**, *15*, 3589.

(109) Rovillard, S.; Perez, E.; Ionov, R.; Voue, M.; De Coninck, J. *Langmuir* **1999**, *15*, 2749.

(110) Dhathathreyan, A.; Collins, S. J. *Langmuir* **2002**, *18*, 928.

(111) Rodriguez, J.; Clavero, E.; Laria, D. *The Journal of Physical Chemistry B* **2005**, *109*, 24427.

(112) Khurana, E.; Nielsen, S. O.; Klein, M. L. *The Journal of Physical Chemistry B* **2006**, *110*, 22136.

(113) Clavero, E.; Rodriguez, J.; Laria, D. *The Journal of Chemical Physics* **2007**, *127*, 124704.

(114) Yuan, S.; Ma, L.; Zhang, X.; Zheng, L. *Colloids and Surfaces A: Physicochemical and Engineering Aspects* **2006**, *289*, 1.

(115) Cuny, V.; Antoni, M.; Arbelot, M.; Liggieri, L. *Colloids and Surfaces A: Physicochemical and Engineering Aspects* **2008**, *323*, 180.

(116) Cuny, V.; Antoni, M.; Arbelot, M.; Liggieri, L. *The Journal of Physical Chemistry B* **2004**, *108*, 13353.

(117) Bandyopadhyay, S.; Chanda, J. *Langmuir* **2003**, *19*, 10443.

(118) Chanda, J.; Bandyopadhyay, S. *Journal of Chemical Theory and Computation* **2005**, *1*, 963.

(119) Schweighofer, K. J.; Essmann, U.; Berkowitz, M. *The Journal of Physical Chemistry B* **1997**, *101*, 3793.

(120) Andoh, Y.; Yasuoka, K. *Langmuir* **2005**, *21*, 10885.

(121) Rivera, J. L.; Predota, M.; Chialvo, A. A.; Cummings, P. T. *Chemical Physics Letters* **2002**, *357*, 189.

(122) Rivera, J. L.; Starr, F. W.; Paricaud, P.; Cummings, P. T. *The Journal of Chemical Physics* **2006**, *125*, 094712.

(123) Rivera, J. L.; McCabe, C.; Cummings, P. T. *Physical Review E* **2003**, *67*, 011603.

(124) Baoukina, S.; Monticelli, L.; Marrink, S. J.; Tieleman, D. P. *Langmuir* **2007**, *23*, 12617.

(125) Laing, C.; Baoukina, S.; Tieleman, D. P. *Physical Chemistry Chemical Physics* **2009**, *11*, 1916.

(126) Berendsen, H. J. C.; Grigera, J. R.; Straatsma, T. P. *J. Phys. Chem.* **1987**, *91*, 6269.

(127) Miyamoto, S.; Kollman, P. A. *Journal of Computational Chemistry* **1992**, *13*, 952.

(128) Martin, M. G.; Siepmann, J. I. *The Journal of Physical Chemistry B* **1999**, *103*, 4508.

(129) Briggs, J. M.; Matsui, T.; Jorgensen, W. L. *Journal of Computational Chemistry* **1990**, *11*, 958.

(130) Jorgensen, W. L. *The Journal of Physical Chemistry* **1986**, *90*, 1276.

(131) Berk, H.; Henk, B.; Herman, J. C. B.; Johannes, G. E. M. F. *Journal of Computational Chemistry* **1997**, *18*, 1463.

(132) Ryckaert, J. P.; Bellemans, A. *Chemical Physics Letters* **1975**, *30*, 123.

(133) Berendsen, H. J. C.; van der Spoel, D.; van Drunen, R. *Computer Physics Communications* **1995**, *91*, 43.

(134) Lindahl, E.; Hess, B.; van der Spoel, D. *Journal of Molecular Modeling* **2001**, *7*, 306.

(135) van der Spoel, D.; Lindahl, E.; Hess, B.; Groenhof, G.; Mark, A. E.; Berendsen, H. J. C. *Journal of Computational Chemistry* **2005**, *26*, 1701.

(136) Allen, M. P.; Tildesley, D. J.; Oxford University Press: Oxford, 1987.

(137) Essmann, U.; Perera, L.; Berkowitz, M. L.; Darden, T.; Lee, H.; Pedersen, L. G. *Journal of Chemical Physics* **1995**, *103*, 8577.

(138) Rosen, M. *Surfactants and Interfacial Phenomenon*; 3 ed.; Wiley Interscience: New York, 2004.

(139) Jamadagni, S. N.; Godawat, R.; Dordick, J. S.; Garde, S. *Journal of Physical Chemistry B* **2009**, *113*, 4093.

(140) Godawat, R.; Jamadagni, S. N.; Garde, S. *Proceedings of the National Academy of Sciences* **2009**, *106*, 15119.

(141) Garde, S.; Yang, L.; Dordick, J. S.; Paulaitis, M. E. *Mol. Phys.* **2002**, *100*, 2299.

(142) Stewart, E.; Shields, R. L.; Taylor, R. S. *The Journal of Physical Chemistry B* **2003**, *107*, 2333.

(143) Alejandre, J.; Rivera, J. L.; Mora, M. A.; de la Garza, V. *Journal of Physical Chemistry B* **2000**, *104*, 1332.

(144) Carless, J. E.; Challis, R. A.; Mulley, B. A. *Journal of Colloid Science* **1964**, *19*, 201.

(145) Dahanayake, M.; Cohen, A. W.; Rosen, M. J. *The Journal of Physical Chemistry* **1986**, *90*, 2413.

(146) Nath, S. K.; Escobedo, F. A.; de Pablo, J. J. *The Journal of Chemical Physics* **1998**, *108*, 9905.

(147) Cornell, W. D.; Cieplak, P.; Bayly, C. I.; Gould, I. R.; Merz, K. M.; Ferguson, D. M.; Spellmeyer, D. C.; Fox, T.; Caldwell, J. W.; Kollman, P. A. *Journal of the American Chemical Society* **1995**, *117*, 5179.

(148) Shelley, J. C.; Shelley, M. Y. *Current Opinion in Colloid & Interface Science* **2000**, *5*, 101.

(149) Rajagopalan, R. *Current Opinion in Colloids and Interface Science* **2001**, *6*, 357.

(150) Lokar, W. J.; Koopal, L. K.; Leermakers, F. A. M.; Ducker, W. A. *The Journal of Physical Chemistry B* **2004**, *108*, 15033.

(151) Koopal, L. K.; Leermakers, F. A. M.; Lokar, W. J.; Ducker, W. A. *Langmuir* **2005**, *21*, 10089.

(152) Leermakers, F. A. M.; Koopal, L. K.; Lokar, W. J.; Ducker, W. A. *Langmuir* **2005**, *21*, 11534.

(153) Leermakers, F. A. M.; Koopal, L. K.; Goloub, T. P.; Vermeer, A. W. P.; Kijlstra, J. *The Journal of Physical Chemistry B* **2006**, *110*, 8756.

(154) Behjatmanesh-Ardakani, R. *The Journal of Chemical Physics* **2005**, *122*, 204903.

(155) Wijmans, C. M.; Linse, P. *The Journal of Physical Chemistry* **1996**, *100*, 12583.

(156) Zhan, Y.; Mattice, W. L.; Napper, D. H. *The Journal of Chemical Physics* **1993**, *98*, 7502.

(157) Zhan, Y.; Mattice, W. L.; Napper, D. H. *The Journal of Chemical Physics* **1993**, *98*, 7508.

(158) Reimer, U.; Wahab, M.; Schiller, P.; Mogel, H. J. *Langmuir* **2005**, *21*, 1640.

(159) James J. Semler, J. G. *Macromolecular Theory and Simulations* **2004**, *13*, 219.

(160) Golumbfskie, A. J.; Pande, V. S.; Chakraborty, A. K. *Proceedings of the National Academy of Sciences of the United States of America* **1999**, *96*, 11707.

(161) Bratko, D.; Chakraborty, A. K.; Shakhnovich, E. I. *The Journal of Chemical Physics* **1997**, *106*, 1264.

(162) Seok, C.; Freed, K. F.; Szleifer, I. *The Journal of Chemical Physics* **2000**, *112*, 6443.

(163) Fleer, G. J.; Scheutjens, J. M. H. M. *Colloids and Surfaces* **1990**, *51*, 281.

(164) Semler, J. J.; Genzer, J. *The Journal of Chemical Physics* **2003**, *119*, 5274.

(165) Larson, R. G. *The Journal of Chemical Physics* **1989**, *91*, 2479.

(166) Larson, R. G. *The Journal of Chemical Physics* **1992**, *96*, 7904.

(167) Larson, R. G. *Chemical Engineering Science* **1994**, *49*, 2833.

(168) Care, C. M. *Journal of the Chemical Society, Faraday Transactions 1: Physical Chemistry in Condensed Phases* **1987**, *83*, 2905

(169) Brindle, D.; Care, C. M. *Journal of the Chemical Society, Faraday Transactions* **1992**, *88*, 2163

(170) Desplat, J. C.; Care, C. M. *Molecular Physics* **1996**, *87*, 441

(171) Rodrigues, K.; Mattice, W. L. *The Journal of Chemical Physics* **1991**, *95*, 5341.

(172) Wijmans, C. M.; Linse, P. *Langmuir* **1995**, *11*, 3748.

(173) Fodi, B.; Hentschke, R. *Langmuir* **2000**, *16*, 1626.

(174) Reimer, U.; Wahab, M.; Schiller, P. *Langmuir* **2001**, *17*, 8444.

(175) Cabral, V. F.; Abreu, C. R. A.; Castier, M.; Tavares, F. W. *Langmuir* **2003**, *19*, 1429.

(176) Zhan, Y.; Mattice, W. L. *Macromolecules* **1994**, *27*, 683.

(177) Wijmans, C. M.; Linse, P. *The Journal of Chemical Physics* **1997**, *106*, 328.

(178) Boecker, J.; Schlenkrich, M.; Bopp, P.; Brickmann, J. *The Journal of Physical Chemistry* **1992**, *96*, 9915.

(179) Shelley, J. C.; Patey, G. N. *Molecular Physics* **1996**, *88*, 385.

(180) Ibrahim, T. H.; Neuman, R. D. *Langmuir* **2004**, *20*, 3114.

(181) Cooper, T. G.; de Leeuw, N. H. *Langmuir* **2004**, *20*, 3984.

(182) Salaniwal, S.; Cui, S. T.; Cummings, P. T.; Cochran, H. D. *Langmuir* **1999**, *15*, 5188.

(183) Salaniwal, S.; Cui, S.; Cochran, H. D.; Cummings, P. T. *Industrial & Engineering Chemistry Research* **2000**, *39*, 4543.

(184) Salaniwal, S.; Cui, S. T.; Cochran, H. D.; Cummings, P. T. *Langmuir* **2001**, *17*, 1773.

(185) Shah, K.; Chiu, P.; Jain, M.; Fortes, J.; Moudgil, B.; Sinnott, S. *Langmuir* **2005**, *21*, 5337.

(186) Bandyopadhyay, S.; Shelley, J. C.; Tarek, M.; Moore, P. B.; Klein, M. L. *The Journal of Physical Chemistry B* **1998**, *102*, 6318.

(187) Dominguez, H. *The Journal of Physical Chemistry B* **2007**, *111*, 4054.

(188) Bruce, C. D.; Berkowitz, M. L.; Perera, L.; Forbes, M. D. E. *The Journal of Physical Chemistry B* **2002**, *106*, 3788.

(189) Greenwood, F. G.; Parfitt, G. D.; Picton, N. H.; Wharton, D. G. In *Adsorption from Aqueous Solution*; Weber, W. J., Matijevic, E., Eds.; American Chemical Society: Wahington, D.C., 1968, p 135.

(190) Cheng, A.; Steele, W. A. *The Journal of Chemical Physics* **1990**, *92*, 3858.

(191) Predota, M.; Zhang, Z.; Fenter, P.; Wesolowski, D. J.; Cummings, P. T. *J. Phys. Chem. B* **2004**, *108*, 12061.

(192) Smith, D. E.; Dang, L. X. *Journal of Chemical Physics* **1994**, *101*, 7873.

(193) Gao, J.; Ge, W.; Hu, G.; Li, J. *Langmuir* **2005**, *21*, 5223.

(194) Plimpton, S. *Journal of Computational Physics* **1995**, *117*, 1.

(195) Allen, M. P.; Tildesley, D. J. *Computer Simulation of liquids*; Oxford University Press: Oxford, 1987.

(196) Bitting, D.; Harwell, J. H. *Langmuir* **1987**, *3*, 500.

(197) Fenn, E. E.; Wong, D. B.; Fayer, M. D. *Proceedings of the National Academy of Sciences* **2009**, *106*, 15243.

(198) Moilanen, D. E.; Fenn, E. E.; Wong, D.; Fayer, M. D. *The Journal of Physical Chemistry B* **2009**, *113*, 8560.

(199) Moilanen, D. E.; Fenn, E. E.; Wong, D.; Fayer, M. D. *Journal of the American Chemical Society* **2009**, *131*, 8318.

(200) Moilanen, D. E.; Levinger, N. E.; Spry, D. B.; Fayer, M. D. *Journal of the American Chemical Society* **2007**, *129*, 14311.

(201) Piletic, I. R.; Moilanen, D. E.; Levinger, N. E.; Fayer, M. D. *Journal of the American Chemical Society* **2006**, *128*, 10366.

(202) Piletic, I. R.; Moilanen, D. E.; Spry, D. B.; Levinger, N. E.; Fayer, M. D. *The Journal of Physical Chemistry A* **2006**, *110*, 10369.

(203) Piletic, I. R.; Moilanen, D. E.; Spry, D. B.; Levinger, N. E.; Fayer, M. D. *The Journal of Physical Chemistry A* **2006**, *110*, 4985.

(204) Piletic, I. R.; Tan, H.-S.; Fayer, M. D. *The Journal of Physical Chemistry B* **2005**, *109*, 21273.

(205) Spry, D. B.; Goun, A.; Glusac, K.; Moilanen, D. E.; Fayer, M. D. *Journal of the American Chemical Society* **2007**, *129*, 8122.

(206) Zhao, W.; Moilanen, D. E.; Fenn, E. E.; Fayer, M. D. *Journal of the American Chemical Society* **2008**, *130*, 13927.

(207) Hummer, G.; Garde, S. *Physical Review Letters* **1998**, *80*, 4193.

(208) Tummala, N. R.; Striolo, A. *The Journal of Physical Chemistry B* **2008**, *112*, 1987.

(209) Fleming, B. D.; Biggs, S.; Wanless, E. J. *J Phys Chem B* **2001**, *105*, 9537.

(210) Atkin, R.; Craig, V. S. J.; Wanless, E. J.; Biggs, S. *Journal of Colloid and Interface Science* **2003**, *266*, 236.

(211) Atkin, R.; Craig, V. S. J.; Wanless, E. J.; Biggs, S. *Advances in Colloid and Interface Science* **2003**, *103*, 219.

(212) Velegol, S. B.; Fleming, B. D.; Biggs, S.; Wanless, E. J.; Tilton, R. D. *Langmuir* **2000**, *16*, 2548.

(213) Shah, K.; Chiu, P.; Sinnott, S. B. *Journal of Colloid and Interface Science* **2006**, *296*, 342.

(214) Atkin, R.; Craig, V. S. J.; Hartley, P. G.; Wanless, E. J.; Biggs, S. *Langmuir* **2003**, *19*, 4222.

(215) Scamehorn, J. F.; Schechter, R. S.; Wade, W. H. *Journal of Colloid and Interface Science* **1982**, *85*, 479.

(216) Penfold, J.; Tucker, I.; Thomas, R. K. *Langmuir* **2005**, *21*, 6330.

(217) Blom, A.; Warr, G. G.; Wanless, E. J. *Langmuir* **2005**, *21*, 11850.

(218) Nihonyanagi, S.; Yamaguchi, S.; Tahara, T. *Journal of the American Chemical Society* **2010**, *doi: 10.1021/ja910914g*.

(219) Lu, J. R.; Li, Z. X.; Thomas, R. K.; Staples, E. J.; Thompson, L.; Tucker, I.; Penfold, J. *The Journal of Physical Chemistry* **1994**, *98*, 6559.

(220) Purcell, I. P.; Thomas, R. K.; Penfold, J.; Howe, A. M. *Colloids and Surfaces A: Physicochemical and Engineering Aspects* **1995**, *94*, 125.

(221) Argyris, D.; Tummala, N. R.; Striolo, A.; Cole, D. R. *The Journal of Physical Chemistry C* **2008**, *112*, 13587.

(222) Hess, B.; Kutzner, C.; van Der Spoel, D.; Lindahl, E. *J. Chem. Theory Comput.* **2008**, *4*, 435.

(223) Shi, L.; Tummala, N. R.; Striolo, A. *Langmuir* **2010**, *26*, 5462.

(224) Argyris, D.; Cole, D. R.; Striolo, A. *Langmuir* **2009**, *25*, 8025.

(225) Puibasset, J.; Pellenq, R. J. M. *The Journal of Chemical Physics* **2003**, *119*, 9226.

(226) Huang, Z.; Yan, Z.; Gu, T. *Colloids and Surfaces* **1989**, *36*, 353.

(227) Lu, S.; Somasundaran, P. *Langmuir* **2008**, *24*, 3874.

(228) Yang, D.-S.; Zewail, A. H. *Proceedings of the National Academy of Sciences* **2009**, *106*, 4122.

(229) Gordillo, M. C.; Marti, J. *The Journal of Chemical Physics* **2002**, *117*, 3425.

(230) Benderskii, A. V.; Henzie, J.; Basu, S.; Shang, X.; Eisenthal, K. B. *The Journal of Physical Chemistry B* **2004**, *108*, 14017.

(231) Gragson, D. E.; McCarty, B. M.; Richmond, G. L. *The Journal of Physical Chemistry* **1996**, *100*, 14272.

(232) Xia, X.; Berkowitz, M. L. *Physical Review Letters* **1995**, *74*, 3193.

(233) Das, D.; Senapati, S.; Chandra, A. *The Journal of Chemical Physics* **1999**, *110*, 8129.

(234) Argyris, D.; Cole, D. R.; Striolo, A. *The Journal of Physical Chemistry C* **2009**, *113*, 19591.

(235) Ho, T. A.; Argyris, D.; Papavassiliou, D. V.; Lee, L. L.; Cole, D. R.; Striolo, A. *Molecular Simulation* **2010**.

(236) Tummala, N. R.; Striolo, A. *The Journal of Physical Chemistry B* **2008**, *112*, 10675.

(237) Park, S.; An, J.; Jung, I.; Piner, R. D.; An, S. J.; Li, X.; Velamakanni, A.; Ruoff, R. S. *Nano Letters* **2009**, *9*, 1593.

(238) Novoselov, K. S.; Geim, A. K.; Morozov, S. V.; Jiang, D.; Zhang, Y.; Dubonos, S. V.; Grigorieva, I. V.; Firsov, A. A. *Science* **2004**, *306*, 666.

(239) Ritter, K. A.; Lyding, J. W. *Nat Mater* **2009**, *8*, 235.

(240) Rao, C. N. R.; Sood, A. K.; Subrahmanyam, K. S.; Govindaraj, A. *Angew. Chem.-Int. Edit.* **2009**, *48*, 7752.

(241) Hernandez, Y.; Nicolosi, V.; Lotya, M.; Blighe, F. M.; Sun, Z.; De, S.; McGovern, I. T.; Holland, B.; Byrne, M.; Gun'Ko, Y. K.; Boland, J. J.; Niraj, P.; Duesberg, G.; Krishnamurthy, S.; Goodhue, R.; Hutchison, J.; Scardaci, V.; Ferrari, A. C.; Coleman, J. N. *Nat Nano* **2008**, *3*, 563.

(242) Green, A. A.; Hersam, M. C. *Nano Letters* **2009**, *9*, 4031.

(243) Jemma, L. V.; Avinash, J. P.; Stephen, M. *Advanced Materials* **2009**, *21*, 2180.

(244) RamanathanT; Abdala, A. A.; StankovichS; Dikin, D. A.; Herrera Alonso, M.; Piner, R. D.; Adamson, D. H.; Schniepp, H. C.; ChenX; Ruoff, R. S.; Nguyen, S. T.; Aksay, I. A.; Prud'Homme, R. K.; Brinson, L. C. *Nat Nano* **2008**, *3*, 327.

(245) Konatham, D.; Striolo, A. *Nano Letters* **2008**, *8*, 4630.

(246) Konatham, D.; Striolo, A. *Applied Physics Letters* **2009**, *95*, 163105.

(247) Carswell, A. D. W.; O'Rear, E. A.; Grady, B. P. *Journal of the American Chemical Society* **2003**, *125*, 14793.

(248) Nosé, S. *Molecular Physics* **1984**, *52*, 255

(249) Parrinello, M.; Rahman, A. *Journal of Applied Physics* **1981**, *52*, 7182.

(250) Berendsen, H. J. C.; van der Spoel, D.; van Drunen, R. *Comput. Phys. Comm.* **1995**, *91*, 43.

(251) van der Spoel, D.; Lindahl, E.; Hess, B.; Groenhof, G.; Mark, A. E.; Berendsen, H. J. C. *J. Comput. Chem.* **2005**, *26*, 1701.

(252) Essmann, U.; Perera, L.; Berkowitz, M. L.; Darden, T.; Lee, H.; Pedersen, L. G. *J. Chem. Phys.* **1995**, *103*, 8577.

(253) Carlsson, J. M. *Nat Mater* **2007**, *6*, 801.

(254) Fasolino, A.; Los, J. H.; Katsnelson, M. I. *Nat Mater* **2007**, *6*, 858.

(255) Thompson-Flagg, R. C.; Moura, M. J. B.; Marder, M. *Europhysics Letters* **2009**, 46002.

(256) Tersoff, J. *Physical Review B* **1989**, *39*, 5566.

(257) Plimpton, S. *Journal of Computational Physics* **1995**, *117*, 1.

(258) Frenkel, D.; Smit, B. *Understanding Molecular Simulations: From Algorithms to Applications*; Academic Press: San Diego, 1996; Vol. 1.

(259) Ouk Kim, S.; Solak, H. H.; Stoykovich, M. P.; Ferrier, N. J.; de Pablo, J. J.; Nealey, P. F. *Nature* **2003**, *424*, 411.

(260) Wang, Q.; Nath, S. K.; Graham, M. D.; Nealey, P. F.; de Pablo, J. J. *Journal of Chemical Physics* **2000**, *112*, 9996.

(261) Sammalkorpi, M.; Panagiotopoulos, A. Z.; Haataja, M. *J. Phys. Chem. B* **2008**, *112*, 12954.

(262) Wilson, M. R. *Journal of Molecular Liquids* **1996**, *68*, 23.

(263) McBride, C.; Vega, C.; MacDowell, L. G. *Physical Review E* **2001**, *64*, 011703.

(264) Eppenga, R.; Frenkel, D. *Molecular Physics: An International Journal at the Interface Between Chemistry and Physics* **1984**, *52*, 1303

(265) Saville, D. A.; Chun, J.; Li, J. L.; Schniepp, H. C.; Car, R.; Aksay, I. A. *Physical Review Letters* **2006**, *96*, 018301.

(266) Tummala, N. R.; Striolo, A. *Physical Review E* **2009**, *80*, 021408.

(267) Striolo, A.; Chialvo, A. A.; Cummings, P. T.; Gubbins, K. E. *Langmuir* **2003**, *19*, 8583.

(268) Milo S. P. Shaffer; Windle, A. H. *Advanced Materials* **1999**, *11*, 937.

(269) Vigolo, B.; Poulin, P.; Lucas, M.; Launois, P.; Bernier, P. *Appl. Phys. Lett.* **2002**, *81*, 1210.

(270) Cadek, M.; Coleman, J. N.; Barron, V.; Hedicke, K.; Blau, W. J. *Appl. Phys. Lett.* **2002**, *81*, 5123.

(271) Peters, J. E.; Papavassiliou, D. V.; Grady, B. P. *Macromolecules* **2008**, *41*, 7274.

(272) Nikolaev, P.; Bronikowski, M. J.; Bradley, R. K.; Rohmund, F.; Colbert, D. T.; Smith, K. A.; Smalley, R. E. *Chem. Phys. Lett.* **1999**, *313*, 91.

(273) Bronikowski, M. J.; Willis, P. A.; Colbert, D. T.; Smith, K. A.; Smalley, R. E. In *The 47th international symposium: Vacuum, thin films, surfaces/interfaces, and processing NAN06*; 4 ed.; AVS: Boston, Massachusetts (USA), 2001; Vol. 19, p 1800.

(274) Kitiyanan, B.; Alvarez, W. E.; Harwell, J. H.; Resasco, D. E. *Chem. Phys. Lett.* **2000**, *317*, 497.

(275) Iijima, S. *Nature* **1991**, *354*, 56.

(276) O'Connell, M. J.; Bachilo, S. M.; Huffman, C. B.; Moore, V. C.; Strano, M. S.; Haroz, E. H.; Rialon, K. L.; Boul, P. J.; Noon, W. H.; Kittrell, C.; Ma, J.; Hauge, R. H.; Weisman, R. B.; Smalley, R. E. *Science* **2002**, *297*, 593.

(277) Niyogi, S.; Densmore, C. G.; Doorn, S. K. *J. Am. Chem. Soc.* **2009**, *131*, 1144.

(278) O'Connell, M. J.; Boul, P.; Ericson, L. M.; Huffman, C.; Wang, Y.; Haroz, E.; Kuper, C.; Tour, J.; Ausman, K. D.; Smalley, R. E. *Chem. Phys. Lett.* **2001**, *342*, 265.

(279) Hagen, A.; Hertel, T. *Nano Lett.* **2003**, *3*, 383.

(280) Wallace, E. J.; Sansom, M. S. P. *Nano Lett.* **2007**, *7*, 1923.

(281) Islam, M. F.; Rojas, E.; Bergey, D. M.; Johnson, A. T.; Yodh, A. G. *Nano Lett.* **2003**, *3*, 269.

(282) Poulin, P.; Vigolo, B.; Launois, P. *Carbon* **2002**, *40*, 1741.

(283) Dominguez, H. *J. Phys. Chem. B* **2007**, *111*, 4054.

(284) Wanless, E. J.; Ducker, W. A. *J. Phys. Chem.* **1996**, *100*, 3207.

(285) Ortiz-Acevedo, A.; Xie, H.; Zorbas, V.; Sampson, W. M.; Dalton, A. B.; Baughman, R. H.; Draper, R. K.; Musselman, I. H.; Dieckmann, G. R. *J. Am. Chem. Soc.* **2005**, *127*, 9512.

(286) Patel, N.; Egorov, S. A. *J. Am. Chem. Soc.* **2005**, *127*, 14124.

(287) Striolo, A. *Phys. Rev. E* **2006**, *74*, 041401.

(288) Striolo, A. *Small* **2007**, *3*, 628.

(289) Striolo, A. *Nanotechnology* **2008**, *19*, 445606.

(290) Strano, M. S.; Moore, V. C.; Miller, M. K.; Allen, M. J.; Haroz, E. H.; Kittrell, C.; Hauge, R. H.; Smalley, R. E. *Journal of Nanoscience and Nanotechnology* **2003**, *3*, 81.

(291) Miyamoto, S.; Kollman, P. A. *J. Comput. Chem.* **1992**, *13*, 952.

(292) Bandyopadhyay, S.; Shelley, J. C.; Tarek, M.; Moore, P. B.; Klein, M. L. *J. Phys. Chem. B* **1998**, *102*, 6318.

(293) Anderson, C. F.; Record, M. T. *Annual Review of Physical Chemistry* **1982**, *33*, 191.

(294) Manning, G. S. *Acc. Chem. Res.* **1979**, *12*, 443.

(295) Manning, G. S. *J. Phys. Chem. B* **2007**, *111*, 8554.

(296) Marc Le Bret; Zimm, B. H. *Biopolymers* **1984**, *23*, 287.

(297) Manning, G. S. *J. Chem. Phys.* **1969**, *51*, 924.

(298) Schniepp, H. C.; Saville, D. A.; Aksay, I. A. *J. Am. Chem. Soc.* **2006**, *128*, 12378.

(299) Arai, N.; Yasuoka, K.; Zeng, X. C. *J. Am. Chem. Soc.* **2008**, *130*, 7916.

(300) Zhang, X.; Cao, D.; Wang, W. *J. Phys. Chem. C* **2008**, *112*, 2943.

(301) Jha, A. K.; Lee, J.; Tripathi, A.; Bose, A. *Langmuir* **2008**, *24*, 6013.

(302) Gutig, C.; Grady, B. P.; Striolo, A. *Langmuir* **2008**, *24*, 13814.

(303) Shi, L.; Ghezzi, M.; Lo Nostro, P.; Brian, P. G.; Alberto, S. *Langmuir* **2009**, *25*, 5536.

(304) Gutig, C.; Grady, B. P.; Striolo, A. *Langmuir* **2008**, *24*, 4806.

(305) Qiao, R.; Ke, P. C. *J. Am. Chem. Soc.* **2006**, *128*, 13656.

(306) Wu, Y.; Hudson, J. S.; Lu, Q.; Moore, J. M.; Mount, A. S.; Rao, A. M.; Alexov, E.; Ke, P. C. *J. Phys. Chem. B* **2006**, *110*, 2475.

(307) Richard, C.; Balavoine, F.; Schultz, P.; Ebbesen, T. W.; Mioskowski, C. *Science* **2003**, *300*, 775.

(308) Kiraly, Z.; Findenegg, G. H.; Mastalir, A. *J. Phys. Chem. B* **2003**, *107*, 12492.

(309) Humphrey, W.; Dalke, A.; Schulten, K. *Journal of Molecular Graphics* **1996**, *14*, 33.

(310) Tummala, N. R.; Striolo, A. *J. Phys. Chem. B* **2008**, *112*, 10675.

(311) Rasaiah, J. C.; Garde, S.; Hummer, G. *Annual Review of Physical Chemistry* **2008**, *59*, 713.

(312) Striolo, A.; Chialvo, A. A.; Cummings, P. T.; Gubbins, K. E. *J. Chem. Phys.* **2006**, *124*, 074710.

(313) Horinek, D.; Netz, R. R. *Physical Review Letters* **2007**, *99*, 226104.

(314) Holland, N. B.; Ruegsegger, M.; Marchant, R. E. *Langmuir* **1998**, *14*, 2790.

(315) Leggetter, S.; Tildesley, D. J. *Molecular Physics* **1989**, *68*, 519

(316) Gilbert, E.; Reynolds, P.; White, J. *Journal of Applied Crystallography* **2000**, *33*, 744.

(317) Huang, J. Y.; Chen, S.; Wang, Z. Q.; Kempa, K.; Wang, Y. M.; Jo, S. H.; Chen, G.; Dresselhaus, M. S.; Ren, Z. F. *Nature* **2006**, *439*, 281.

(318) Avouris, P.; Chen, Z.; Perebeinos, V. *Nat Nano* **2007**, *2*, 605.

(319) Avouris, P.; Freitag, M.; Perebeinos, V. *Nat Photon* **2008**, *2*, 341.

(320) Kostarelos, K.; Bianco, A.; Prato, M. *Nat Nano* **2009**, *4*, 627.

(321) Calvert, P. *Nature* **1999**, *399*, 210.

(322) Niyogi, S.; Boukhalfa, S.; Chikkannanavar, S. B.; McDonald, T. J.; Heben, M. J.; Doorn, S. K. *J. Am. Chem. Soc.* **2007**, *129*, 1898.

(323) Tu, X.; Manohar, S.; Jagota, A.; Zheng, M. *Nature* **2009**, *460*, 250.

(324) Tanaka, T.; Jin, H.; Miyata, Y.; Kataura, H. *Applied Physics Express* **2008**, *1*, 114001.

(325) Tanaka, T.; Jin, H.; Miyata, Y.; Fujii, S.; Suga, H.; Naitoh, Y.; Minari, T.; Miyadera, T.; Tsukagoshi, K.; Kataura, H. *Nano Letters* **2009**, *9*, 1497.

(326) Britz, D. A.; Khlobystov, A. N. *Chemical Society Reviews* **2006**, *35*, 637.

(327) Wang, H. *Current Opinion in Colloid & Interface Science* **2009**, *14*, 364.

(328) Nativ-Roth, E.; Shvartzman-Cohen, R.; Bounioux, C.; Florent, M.; Zhang, D.; Szleifer, I.; Yerushalmi-Rozen, R. *Macromolecules* **2007**, *40*, 3676.

(329) Angelikopoulos, P.; Gromov, A.; Leen, A.; Nerushev, O.; Bock, H.; Campbell, E. E. B. *The Journal of Physical Chemistry C* **2009**.

(330) Calvaresi, M.; Dallavalle, M.; Zerbetto, F. *Small* **2009**, *5*, 2191.

(331) Xu, Z.; Yang, X.; Yang, Z. *Nano Letters* **2010**, *10*, 985.

(332) Uddin, N. M.; Capaldi, F.; Farouk, B. *Journal of Engineering Materials and Technology* **2010**, *132*, 021012.

(333) Rastogi, R.; Kaushal, R.; Tripathi, S. K.; Sharma, A. L.; Kaur, I.; Bharadwaj, L. M. *Journal of Colloid and Interface Science* **2008**, *328*, 421.

(334) Lifeng, D.; et al. *Nanotechnology* **2008**, *19*, 255702.

(335) Schneider, C.; Sühnel, J. *Biopolymers* **1999**, *50*, 287.

(336) Berendsen, H. J. C.; Postma, J. P. M.; van Gunsteren, W. F.; DiNola, A.; Haak, J. R. *The Journal of Chemical Physics* **1984**, *81*, 3684.

(337) Hoover, W. G. *Physical Review A* **1985**, *31*, 1695.

(338) Nose, S. *The Journal of Chemical Physics* **1984**, *81*, 511.

(339) Roux, B. *Computer Physics Communications* **1995**, *91*, 275.

(340) Souaille, M.; Roux, B. *Computer Physics Communications* **2001**, *135*, 40.

(341) Kumar, S.; Bouzida, D.; Swendsen, R. H.; Kollman, P. A.; Rosenberg, J. M. *Journal of Computational Chemistry* **1992**, *13*, 1011.

(342) Kumar, S.; Bouzida, D.; Swendsen, R. H.; Kollman, P. A.; Rosenberg, J. M. *Journal of Computational Chemistry* **1995**, *16*, 1339.

(343) Kumar, S.; Payne, P. W.; Vásquez, M. *Journal of Computational Chemistry* **1996**, *17*, 1269.

(344) Grajek, H.; Gryczynski, I.; Bojarski, P.; Gryczynski, Z.; Bharill, S.; Kulak, L. *Chemical Physics Letters* **2007**, *439*, 151.

(345) Ogunro, O. O.; Wang, X.-Q. *Nano Letters* **2009**, *9*, 1034.

(346) Lin, C. S.; Zhang, R. Q.; Niehaus, T. A.; Frauenheim, T. *The Journal of Physical Chemistry C* **2007**, *111*, 4069.

(347) Walther, J. H.; Jaffe, R. L.; Kotsalis, E. M.; Werder, T.; Halicioglu, T.; Koumoutsakos, P. *Carbon* **2004**, *42*, 1185.

(348) Li, L.; Bedrov, D.; Smith, G. D. *The Journal of Physical Chemistry B* **2006**, *110*, 10509.

(349) Tersoff, J. *Physical Review B* **1988**, *37*, 6991.

(350) Pashley, R. M.; Israelachvili, J. N. *Journal of Colloid and Interface Science* **1984**, *101*, 511.

(351) Besseling, N. A. M. *Langmuir* **1997**, *13*, 2113.

(352) Raviv, U.; Klein, J. *Science* **2002**, *297*, 1540.

(353) Ho, R.; Yuan, J.-Y.; Shao, Z. *Biophysical Journal* **1998**, *75*, 1076.

(354) Argyris, D.; Cole, D. R.; Striolo, A. *ACS Nano* **2010**, *4*, 2035.